X-ray Crystallographic Investigations of the Structure and Function of Oxidoreductases

by

Ross Andrew Edwards

A dissertation submitted in partial satisfaction of the requirements for the degree of

Doctor of Philosophy

in the

Institute of Fundamental Sciences, Chemistry

at

MASSEY UNIVERSITY, NEW ZEALAND

1999

X-ray Crystallographic Investigations of the Structure and Function of Oxidoreductases

This thesis is dedicated to

The Venerable Fredrick John Ford

in tribute to his role in inspiring thoughtfulness and for sharing a fine understanding of the enjoyment of this adventure that is life.

Abstract

X-ray Crystallographic Investigations of the Structure and Function of Oxidoreductases

by

Ross Andrew Edwards

Doctor of Philosophy

Massey University, New Zealand

1999

Associate Professor Geoffrey B. Jameson, Professor Edward N. Baker, Supervisors

The structure and function of oxidoreductases were studied using the manganese-containing superoxide dismutase of *Escherichia coli* as the model system. The technique of single-crystal X-ray crystallography was used to determine the three-dimensional structure of this system. The structures of derivatives of this system, including iron-substituted manganese superoxide dismutase, and the five mutants Y34F, Q146H, Q146L, H30A and Y174F, were also determined. Analysis of these structures on a near-atomic scale revealed new structural aspects to the catalytic mechanism of this group of enzymes.

A structural basis for the inactivity of *E. coli* Fe-substituted MnSOD has been determined in the altered geometry of the metal site on substitution of the non-native metal. The change in geometry from active five-coordinate trigonal-bipyramidal to inactive six-coordinate distorted octahedral modifies both the kinetics and thermodynamics of superoxide dismutation at the enzyme's metal centre.

Gln146 is not essential for activity, but has an important role in optimising the reaction. Unlike the naturally active His146-containing MnSOD enzymes, the mutation of *E. coli*

MnSOD Gln146 to histidine largely inactivates the enzyme. The inactivity may be a consequence of the greater inflexibility of the mutated histidine when compared with its natural counterparts.

The lack of any change in both the primary and secondary coordination shells of the H30A mutant active-site, coupled with a 70 % reduction in catalytic activity, indicate an important role for His30 in optimising the catalytic mechanism.

It is likely that the 60 % reduction in catalytic activity of the Y174F mutant is due to a different orientation, and possibly different effective pKa of His30, although a loss of activity due to the slight differences of the primary and secondary coordination spheres can not be entirely ruled out.

Structural evidence supports a role for Tyr174 in orienting and possibly also modifying the pK of His30. The association of His30, in particular *via* its ND1 nitrogen, with aspects of the catalytic mechanism including interaction or protonation of substrate, can be postulated based on its structural behaviour.

Acknowledgments

This thesis is not the work of an individual, merely the end result of the influence of many, and I recognise those contributions here with gratitude.

I thank my supervisor, Associate Professor Geoffrey Jameson for generous contributions both scientifically and financially. Over the course of my PhD Geoff has only ever been supportive, open-minded and insightful. I wish to thank my secondary supervisor Professor Ted Baker, for his contributions, both financial and scientific. I acknowledge the foresight of my undergraduate Professor, Ward T. Robinson, who set me on this path over four years ago. This work was done in close collaboration with Drs. Jim and Mei Whittaker, who provided excellent biochemical and chemical results, enzyme and crystals.

I would also like to thank the numerous friendships made over the years both in and out of the Massey environment, that have shaped my experiences and given my life meaning:

Justin Corey, a most constant and great friend

Aaron Mikaere, David Fairley and Grant Samuels

Bryan, Andrew, Richard, Neil, Jakki and Paul, Rose, Catherine, Heather, Paul, Phil, Maria, Bin, Julian, Rebecca, Richelle, Rochelle, Todd

Dr. Stan Moore (the rudest Moose in the woods, mentor and fishing buddy)

Puck, of singular importance, thanks for keeping me sane in Hamburg - and for being yourself!

Katja, a close friend and great travelling companion, and Steffi

Esther

Saeid Miri, a generous friend

my flatmates, Sandy, Farah, Jeniffer, Carman, Adrian, Vitri and Sia who together share many great memories of 11 Keiller Place

John Ford (to whom this work is dedicated)

I especially thank my family for all their love and support:

Gloria, Graham, Peter and Nicola

Table of Contents

List of Figures

List of Tables

Abbreviations

ADP	adenosine diphosphate
ANIS	SHELXL specific command, refine atoms anisotropically
ATP	adenosine triphosphate
CCP4	Collaborative Computational Project, Number 4
CoSOD	cobalt superoxide dismutase
CuSOD	copper superoxide dismutase
CuZnSOD	copper, zinc superoxide dismutase
DESY	Deutsches Elektronen-Synchrotron
DMF	dimethylformamide
DNA	deoxyribonucleic acid
DORIS	Double Ring Storage (for synchrotron radiation)
EDTA	Ethylenediaminetetraacetic acid
EMBL	European Molecular Biology Laboratory
EPR	electron paramagnetic resonance
EXAFS	extended X-ray absorption fine structure
Fe_2MnSOD	iron-substituted manganese superoxide dismutase
FeSOD	iron superoxide dismutase
HOPE	SHELXL specific command, refine anisotropic scaling parameters
ISOR	SHELXL specific command, 'approximately isotropic' restraints
MPD	2-methyl-2,3-pentanediol
MnSOD	manganese superoxide dismutase
NADH	reduced form of nicotinamide adenine dinucleotide

NADPH	reduced form of nicotinamide adenine dinucleotide phosphate
NCS	non-crystallographic symmetry
NHE	normal hydrogen electrode
NMR	nuclear magnetic resonance
NiSOD	nickel superoxide dismutase
PDB	protein data bank
PEG	polyethylene glycol
RES	resolution
RMS	root mean square
SO	superoxide
SOD	superoxide dismutase
SWAT	SHELXL specific command, refine diffuse solvent parameter
UV	ultra-violet
WT	wildtype
apoFeSOD	iron-free iron superoxide dismutase
apoMnSOD	manganese-free manganese superoxide dismutase
hMnSOD	human mitochondrial manganese superoxide dismutase
redMnSOD	reduced manganese superoxide dismutase

Related Publications

The results presented in chapters two and three have been published in peer-reviewed journals.

R. A. Edwards, H. M. Baker, M. M. Whittaker, J. W. Whittaker, G. B. Jameson, and E. N. Baker. Crystal structure of *Escherichia coli* manganese superoxide dismutase at 2.1 Å resolution. *Journal of Biological Inorganic Chemistry*, **3**:161–171, 1998.

R. A. Edwards, M. M. Whittaker, J. W. Whittaker, G. B. Jameson, and E. N. Baker. Distinct metal environment in Fe-substituted manganese superoxide dismutase provides a structural basis of metal specificity. *Journal of the American Chemical Society*, **120**(37):9684-9685, 1998.

1 Introduction

Superoxide dismutases are a class of enzyme that catalyse the dismutation of superoxide into dioxygen and hydrogen peroxide. Superoxide, a high-energy, free-radical, oxygen species, is toxic to cellular function, and so must be removed by the organism. This is achieved most efficiently by employing superoxide dismutases to scavenge and dismutate superoxide into less harmful species. Superoxide dismutases are almost ubiquitous enzymes as almost all organisms utilize or are subjected to some level of dioxygen, and therefore require the defensive services this class of enzyme provides.

1.1. Superoxide chemistry

Superoxide (SO) is commonly written with the chemical formula of O_2^- or $O_2^{-\cdot}$, and also is referred to as the superoxide radical or superoxide anion. Superoxide is formed by the univalent (single-electron) reduction of dioxygen in a thermodynamically unfavourable reaction that gives $O_2^{-\cdot}$ higher energy and reactivity than molecular oxygen. Protonation of $O_2^{-\cdot}$ yields the perhydroxyl radical $HO_2^{\cdot}$, also called the hydroperoxy or hydroperoxyl radical. Two-electron reduction of dioxygen yields peroxide, O_2^{2-}. Protonation of peroxide yields the peroxy anion, HO_2^-, with further protonation forming hydrogen peroxide, H_2O_2.

1.1.1. Electronic structure

The electronic structure of the various states of dioxygen can be described by means of simple molecular orbital diagrams (see Figure 1-1 below). Ground-state dioxygen contains two unpaired electrons in the $2\pi_g$ orbital and is a triplet ($^3\Sigma_g^-$). The two unpaired electrons confer bi-radical nature. The other lowest energy excited states of dioxygen occur by there being three possible ways of aligning electron spins in the two degenerate $2\pi_g$ orbitals. The other two states are singlet states ($^1\Delta_g$ and $^1\Sigma_g^+$). Transitions from the singlet states to the triplet ground state are forbidden. Singlet states, therefore, have a relatively longer lifetime when compared with the other excited states of dioxygen which are allowed to decay *via* allowed transitions [13].

Superoxide, being formed by gaining a single electron during the univalent reduction of dioxygen, has an extra unpaired electron in one of the degenerate $2\pi_g$ orbitals. The

degenerate $2\pi_g$ orbitals are then split in a Jahn-Teller type distortion caused by the unequal occupancies of the orbitals [14].

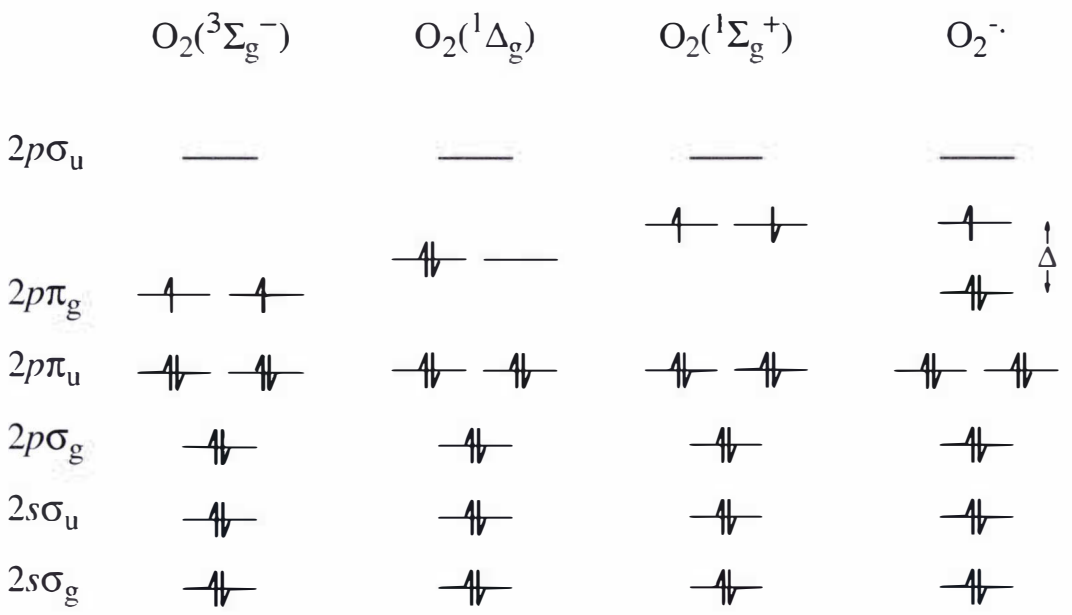

Figure 1-1. Molecular-orbital diagrams for oxygen and superoxide

Bond orders, as deduced from the molecular orbital diagrams, for dioxygen, superoxide and peroxide are 2, 1.5 and 1, respectively. The O-O bond lengths increase from 1.21 Å (O_2), to 1.34 Å ($O_2^{-\cdot}$), to 1.49 Å (O_2^{2-}), as successive electrons are added to the antibonding orbitals, consistent with decreasing bond orders [15].

Superoxide is paramagnetic due to the single unpaired electron in one of the $2\pi_g$ orbitals. This allows $O_2^{-\cdot}$ to be observed by using electron paramagnetic resonance (EPR) techniques. The unique EPR spectrum can be used for detection of $O_2^{-\cdot}$. EPR was the technique used to first show the presence of $O_2^{-\cdot}$ in a biological system [16].

Superoxide has an absorption band in the UV region with a maximum in the 240 to 260 nm range. The absorption has been assigned to a transition between the $2\sigma_g$ and the $2\pi_g$ orbitals [17]. The perhydroxyl radical also absorbs within this range [18, 19].

1.1.2. Redox reactions of superoxide

The superoxide radical is capable of acting as either a reducing agent (Reaction 1a, 1b) or an oxidising agent (Reaction 2). Superoxide is strongly solvated by water as confirmed by the shift of -0.44 V for the $O_2/O_2^{-\cdot}$ couple on going from water to dimethylfor-

mamide (DMF).

$$O_2 + e \rightleftarrows O_2^{-\cdot} \qquad E^{o\prime} = -0.137 \text{ V } \textit{vs.} \text{ NHE [20]}^1 \qquad (1a)$$

$$O_2 + H^+ + e \rightleftarrows HO_2^{\cdot} \qquad E^{o} (\text{pH } 0) = +0.12 \text{ V } \textit{vs.} \text{ NHE [12]} \qquad (1b)$$

$$O_2^{-\cdot} + 2H^+ + e \rightleftarrows H_2O_2 \qquad E^{o\prime} = +0.89 \text{ V } \textit{vs.} \text{ NHE [12]}^2 \qquad (2)$$

These two half-cell reactions yield the overall two-electron reduction of dioxygen to peroxide (Reaction 3).

$$O_2 + 2H^+ + 2e \rightleftarrows H_2O_2 \qquad (3)$$

The redox reactions are coupled with proton associations in water, conferring a pH dependence on the redox couples. The conjugate acid of $O_2^{-\cdot}$ is the perhydroxyl radical ($HO_2^{\cdot}$), which has a pK_a of 4.88 [21]. The perhydroxyl radical is the more powerful oxidising species of the $HO_2^{\cdot}/O_2^{-}$ pair whereas $O_2^{-\cdot}$ is the better reducing agent [11].

Hydrogen peroxide is a relatively weak acid with a pK_a for the first ionisation of 11.7 [22]. So in aqueous solution at pH 7, $O_2^{-\cdot}$ would be fully deprotonated and hydrogen peroxide would be fully protonated. Ionisations of dioxygen, superoxide and hydrogen peroxide are illustrated in Figure 1-2.

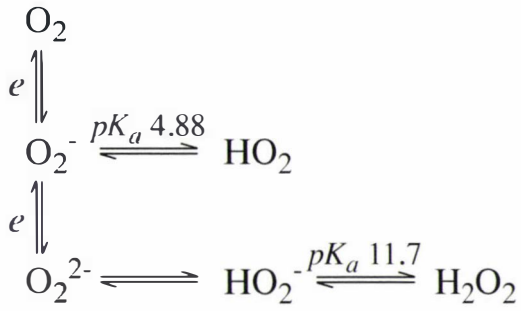

Figure 1-2. Ionizations of dioxygen, superoxide and hydrogen peroxide

Some debate still remains over the correct values of the two half-reactions of superoxide. The widely quoted value for the $O_2/O_2^{-\cdot}$ couple is $E^{o\prime} = -0.33$ V. This was calculated by Wood [23] on a system coupled to duroquinone, and also by Ilan, Meisel and Czapski

1. Other values measured include: $E^{o} = -0.33$ V *vs.* NHE [11], $E^{o\prime} = -0.16$ V *vs.* NHE [12], and E^{o} (in DMF) = -0.60 V *vs.* NHE [12].

2. Ilan *et al.* measure, $E^{o} = 1.00$ V vs. NHE [11].

[24, 11] from pulse radiolysis data on oxygenated solutions of duroquinone and indigo disulfonate. Barrette *et al.* [25] use the value of -0.16 V in their discussion that the optimum reduction potential value for SOD catalysis falls between those of the two half reactions of superoxide, quoting Stein *et al.* [26]. Vance and Miller [10], in a similar discussion, quote the value from Barrette *et al.* Stein *et al.* in fact did not measure or calculate this potential, but rather presented a figure giving the reduction potentials for both couples at acidic, neutral and basic pHs. The figure caption references Fee and Valentine [27], and Schwarzenbach [28]. Values abstracted from the figure of Stein *et al.* are: $E^{o}(O_2/O_2^{-})$, pH 0, -0.16 V; $E^{o'}(O_2/O_2^{-})$, -0.33 V; $E^{o'}(O_2^{-}/H_2O_2)$, +0.87 V. Fee *et al.* quote $E^{o}(O_2/O_2^{-})$ as -0.33 V (referencing both Wood and Meisel, and calculate a value for $E^{o}(O_2^{-}/H_2O_2)$ of +0.87 V. Most recently Petlicki and van de Ven re-evaluated literature data and found the standard redox potential for the oxygen/superoxide couple is -0.137 V at pH 7.0. Their analysis included re-evaluation of the data of Meisel and Czapski, concluding a new value of the dioxgen/superoxide couple from this data to be $E^{o'}(O_{2(g)}/O_2^{-}{}_{(aq)})$ -0.133 V. Using the value of -0.137 V and the calculation of Fee *et al.*, the value for the superoxide/hydrogen peroxide couple ($E^{o'}$) would be +0.67 V.

1.1.3. The dismutation reaction in aqueous solution

The overall dismutation reaction of $O_2^{-\cdot}$ in aqueous solution is very slow.

$$O_2^{-\cdot} + O_2^{-\cdot} + 2H^+ \rightarrow H_2O_2 + O_2 \qquad k<0.3\ M^{-1}s^{-1} \qquad (4)$$

However,

$$HO_2^{\cdot} + O_2^{-\cdot} + H^+ \rightarrow H_2O_2 + O_2 \qquad k=8.0\times10^{7}\ M^{-1}s^{-1} \qquad (5)$$

$$HO_2^{\cdot} + HO_2^{\cdot} \rightarrow H_2O_2 + O_2 \qquad k=8.0\times10^{5}\ M^{-1}s^{-1} \qquad (6)$$

So dismutation becomes more rapid at lower pH where the conjugate acid of superoxide will be more predominant. The overall rate of reaction at pH 7 is ~ $5.0\times10^{5}\ M^{-1}s^{-1}$.

1.2. Superoxide in biochemical systems

It is unnecessary to extol the essential role of the oxygen in the air we breathe to human life. Some forms of oxygen are decidedly more ambivalent in the role they play within living organisms. Oxygen radicals have a dual and seemingly contradictory role in cell metabolism, where they can act as either protector or provocateur. An example of the former role is the deliberate production of superoxide radicals during a process called the respiratory burst. Stimulus of neutrophils (granular white blood cells that participate in the immune response) produces quantities of superoxide radicals, which are an intermediate in the formation of more powerful oxidant species used by cells as microbicidal agents. Acting in the latter role, immoderate oxygen-radical production can have a dele-

terious effect on cell components, oxidising and modifying essential cell components leading eventually to cell death. In addition to being a source of oxidative damage to the cell, $O_2^{-\cdot}$ interacts with enzymes other than superoxide dismutases in an apparently beneficial way. It has been implicated as a controlled source of reduction/oxidation potential, an oxygenating substrate (particularly of ferric-heme proteins), an intermediate in the peroxidase-NADH oscillator, and a regulator (in *Escherichia coli*) of the SoxRs regulon.

1.2.1. Production of superoxide *in vivo*

In vitro, superoxide is produced by the univalent reduction of dioxygen, and is the first intermediate in the overall reduction of molecular oxygen to water. The overall process requires four electrons and proceeds by a further two intermediates: H_2O_2, a two-electron reduction, and the OH radical, a three-electron reduction ($O_2^{-\cdot}$ shown in its protonated state):

$$O_2 \xrightarrow[H^+]{e} HO_2^{\cdot} \xrightarrow[H^+]{e} H_2O_2 \xrightarrow[H^+]{e} HO^{\cdot} + H_2O \xrightarrow[H^+]{e} 2H_2O$$

This sequential, single-electron reduction process is necessary because the spin restriction of dioxygen creates a barrier to the divalent reduction of dioxygen [29].

Dioxygen is used by aerobic organisms in respiratory-chain phosphorylation where the energy generated by electron transport to oxygen is used in the formation of ATP from ADP and phosphate. The aerobic organism, whilst benefiting from the greater energy efficiency of aerobic respiration over anaerobic fermentation, must minimize the production of the partially reduced oxygen intermediates. It does this in part by using enzymes that mediate two or four-electron reductions without the release of the oxygen intermediates during the reduction [30]. However, because the univalent pathway is the most facile route for the reduction of dioxygen, single-electron autooxidations of cellular components can still occur, and are in fact the major source of superoxide within the cell. The autooxidation reactions are of the form:

$$[\text{cellular component}]^{+n} + O_2 \rightleftharpoons [\text{oxidised cellular component}]^{+(n+1)} + O_2^-$$

Examples of cellular components which have been shown to produce $O_2^{-\cdot}$ by autooxidation are hemoglobin, myoglobin, reduced cytochrome *c*, reduced ferredoxins, leukoflavins, tetrahydropterins, catecholamines and polyhydric phenols [31].

1.2.2. Superoxide as a damaging species

Superoxide could directly damage cellular components by acting as either a univalent reducing or oxidising agent, and there are of examples of $O_2^{-\cdot}$ acting in both of these capacities *in vitro* [31, 32]. Because of its relatively low redox potential, superoxide most

frequently acts as a reducing agent, and, as most cellular damage is due to oxidative damage, the $O_2^{-\cdot}$ form may cause little or no direct cellular damage. Instead superoxide causes more cellular damage indirectly by undergoing reactions whose products are even more powerful cellular toxicants.

Superoxide has been shown to directly inactivate various dehydratases including dihydroxy-acid dehydratase, fumarase A, fumarase B, and mammalian aconitase as expressed from *E. coli*. Dehydratases contain a [4Fe-4S] cluster which is oxidised by $O_2^{-\cdot}$ to an unstable oxidation state; Fe(II) is then released, and the cluster is degraded, inactivating the enzyme. The release of Fe(II) from the cluster initiates another series of oxygen-radical producing reactions, known collectively as the Fenton reaction [33]. In another direct interaction, but acting in a reductive capacity, $O_2^{-\cdot}$ mediates the reductive release of iron from ferritin [34]. During inflammation, $O_2^{-\cdot}$ and hydrogen peroxide are produced by stimulated polymorphonuclear leukocytes and macrophages. The iron released by the subsequent superoxide-mediated reduction of ferritin may potentiate the formation of the $OH^{\cdot}$ radical in inflammatory states [35], by catalysing its formation in the Haber-Weiss reaction [36]. Ferritin has also been found to promote the peroxidation of phospholipid liposomes, again by superoxide-stimulated iron release [37], although in this case initiation of lipid peroxidation does not occur *via* the iron-catalysed Haber-Weiss formation of $OH^{\cdot}$.

The indirect damage to cellular components by superoxide occurs because $O_2^{-\cdot}$ reacts to form further radicals. These radicals can have even greater oxidising power, and in some cases are better placed within the cell to take advantage of damaging particular cellular components.

The conjugate acid of superoxide, the perhydroxyl radical ($HO_2^{\cdot}$), is a more powerful oxidising species than $O_2^{-\cdot}$. Since the perhydroxyl radical is a neutral acid, its ionisation involves charge separation, which is more favourable in solutions with a higher dielectric constant. The movement of $O_2^{-\cdot}$ from water into environments within the cell with lower dielectric constants, e.g. lipid micelles, membranes or the interior of globular proteins, would be accompanied by its protonation. So it is likely that the reactive species in these environments would be the perhydroxyl radical rather than the superoxide radical [31]. At the physiological pH of 7.4, in aqueous polar environment, less than 1 % of any $O_2^{-\cdot}$ formed will be present as $HO_2^{\cdot}$ [38]. However, electrostatic forces concentrate protons adjacent to anionic interfaces so that the hydrogen ion concentration in the vicinity of biological membranes may be significantly higher than in bulk solution. Increased concentration of $HO_2^{\cdot}$ in such micro-environments can be expected. The perhydroxyl radical has been shown to react directly with linoleic, linolenic and arachidonic unsaturated fatty acids *in vitro* [39]. While $HO_2^{\cdot}$ reacts with linoleic acid at biologically significant rates,

its conjugate base $O_2^{-\cdot}$ does not [40]. This reaction takes place in the absence of metal catalysts or hydrogen peroxide, and, should it occur *in vivo*, could initiate oxidative damage to polyunsaturated phospholipids, leading to impairment of membrane function.

By far the most important mechanism of indirect damage to cells, mediated by superoxide, is the formation of the more reactive radical species, the hydroxyl radical. Any system generating $O_2^{-\cdot}$ will also produce H_2O_2. The combination of $O_2^{-\cdot}$ and H_2O_2 with catalytic concentrations of transition metals leads to the formation of the extremely reactive and powerful oxidising radical $HO^{\cdot}$.

This process, which involves the univalent reduction of hydrogen peroxide, was first proposed by H. J. H. Fenton [33] and by F. Haber and J. Weiss [36]. The metal ion acts as the redox catalyst of the catalase reaction, and the cycle of reactions (Equations 7 through 10) is known as the Haber-Weiss cycle.

$$Fe^{2+} + H_2O_2 + H^+ \rightarrow Fe^{3+} + HO^{\cdot} + H_2O \quad (7)$$

$$HO^{\cdot} + H_2O_2 \rightarrow HO_2^{\cdot} + H_2O \quad (8)$$

$$HO_2^{\cdot} + Fe^{3+} \rightarrow O_2 + Fe^{2+} + H^+ \quad (9)$$

$$2H_2O_2 \rightarrow O_2 + 2H_2O \quad (10)$$

Hydroxyl radicals are highly reactive and will react with most cellular components upon collision. Hydroxyl radicals generated in free solution are more likely therefore to react with expendable sugar phosphates, amino acids, nucleotides and other less critical components found in free solution. However, superoxide radicals are much less reactive and so can diffuse from their formation sites and react with transition metal ions in different parts of the cell. Because the catalytic metals are most likely to be found bound onto polyanionic DNA or cell membranes rather than in free solution, the hydroxyl radicals are more likely to be produced adjacent to, and hence react with, these more critical cellular components rather than those in free solution. This sequence of events has been termed the site-specific Haber-Weiss reaction [41, 42].

Superoxide has been implicated in damaging DNA *in vivo*. Enhanced mutation rates in bacterial DNA occur on the addition of the superoxide-generating drug paraquat [43], and strains that lack superoxide dismutase (SOD) show an increased rate of oxygen-dependent spontaneous mutagenesis [44]. The removal of either catalytic metals or H_2O_2 from systems that damage DNA fully protects DNA from superoxide [45]. This indicates that $O_2^{-\cdot}$ does not directly attack DNA, but instead is involved with hydrogen peroxide and metal catalysts in the production of the damaging species. The damaging species

could be the hydroxyl radical produced in the Haber-Weiss reaction. However, *in vitro* Fenton systems have been shown to generate damage which cannot be inhibited by hydroxyl-radical scavengers [46].

Studies of Fenton reactions in several systems [47, 48, 49] have led to the postulation of a "crypto-hydroxyl radical". That is, a hydroxyl radical that has a distinct character because it is complexed to a metal ion. Hence, the Fenton reaction might be postulated to include a crypto-hydroxyl intermediate such as the ferryl radical [46] (Equations 11 through 13).

$$Fe^{2+} + H_2O_2 + H^+ \rightarrow Fe^{3+}\text{-}HO^{\cdot} + H_2O \quad (11)$$

$$Fe^{3+}\text{-}HO^{\cdot} \rightarrow Fe^{3+} + HO^{\cdot} \quad (12)$$

$$Fe^{2+} + H_2O_2 + H^+ \rightarrow Fe^{3+} + HO^{\cdot} + H_2O \quad (13)$$

1.2.3. Cellular defence from oxidative damage

The protection of cells from oxidative damage is carried out by a number of mechanisms. The primary defence mechanism is the near ubiquitous enzyme superoxide dismutase (SOD), which catalyses the dismutation of superoxide to hydrogen peroxide plus dioxygen. However, one of the by-products, hydrogen peroxide is not only a strong oxidant but is also a precursor to even more powerful oxidising radicals, such as the hydroxyl radical ($OH^{\cdot}$), so a further defence mechanism involves the removal of hydrogen peroxide. Very low steady-state concentrations of hydrogen peroxide are maintained by catalases and peroxidases. Catalases dismutate hydrogen peroxide into water plus dioxygen. Peroxidases catalyse the reduction of hydrogen peroxide to water with the corresponding oxidation of an organic substrate which acts as the hydrogen donor. Further oxidative damage is controlled in part by antioxidants, such as alpha-tocopherol, which terminate free-radical reactions. And the final cellular response is the activation of repair systems in an attempt to repair any cellular damage.

1.2.4. The regulatory role of superoxide in *E. coli*

In *E. coli*, as part of the cellular defence against oxidative stress, $O_2^{-\cdot}$ plays a regulatory role by stimulating the SoxRS regulon. If $O_2^{-\cdot}$ concentrations within the cell increase, this group of regulated genes is activated [50, 51]. The products of the SoxRS regulon are a host of enzymes involved in the oxidative defence of the cell, including: MnSOD, to eliminate $O_2^{-\cdot}$; glucose-6-phosphate dehydrogenase, to ensure a supply of NADPH; endonuclease IV, to repair oxidatively damaged DNA; the stable form of fumarase *c*, to replace the superoxide-sensitive forms; ferredoxin reductase, to reductively repair oxida-

tively disassembled [4Fe-4S] clusters; micF, to decrease the porosity of the outer membrane; aconitase A, to replace superoxide-inactivated aconitase; and others [52]. SoxR is the redox sensor and activates SoxS, which turns on the regulon. In a similar way, another independent oxidative defence regulon, oxyR, is turned on in response to oxidative stress from H_2O_2.

1.2.5. Interactions with enzymes other than superoxide dismutases

Superoxide will also interact with enzymes other than superoxide dismutases, acting as an oxidant or reductant, an oxygenating agent, or an intermediate. It will reduce and/or oxygenate various ferric hemoproteins, including indoleamine-pyrrole 2,3-dioxygenase [53], catalase [54], myeloperoxidase [55], ferricytochrome *c* [56]. The physiological relevance of some of these interactions is still ambiguous. In some cases $O_2^{-\cdot}$ acts as a necessary redox step in the catalytic mechanism, e.g. in the reduction of ferricytochrome *c*, while in other cases $O_2^{-\cdot}$ will inactivate enzymes, e.g. catalases where $O_2^{-\cdot}$ converts the resting ferric enzyme to the poorly active ferro-oxy form. Superoxide is also an important chemical intermediate in the peroxidase-NADH biochemical oscillator [57, 58], where it oxidises peroxidase in one of the reaction steps of the oscillator.

1.3. Superoxide dismutase

Superoxide dismutases have the systematic name *superoxide oxidoreductase.* They catalyse the dismutation of the superoxide radical into hydrogen peroxide and dioxygen.

$$2O_2^{-\cdot} + 2H^+ \longrightarrow O_2 + H_2O_2 \qquad (14)$$

SOD is a ubiquitous enzyme in aerobic organisms, having an essential role in the biological defence against superoxide, and therefore against any reactive radical species derived from superoxide. Dismutation in the enzyme occurs at a transition metal-containing, superoxide binding site. The transition metals that have been found to catalyse the dismutation reaction at the active-site are Cu, Zn, Mn, Fe and Ni.

Dismutation of superoxide in aqueous solution is a rapid, spontaneous process, and it is therefore not immediately obvious why organisms require an enzyme to catalyse this reaction. The spontaneous dismutation reaction is second-order with respect to superoxide, and so the half-life of superoxide is dependent on the initial concentration. The superoxide dismutase-catalysed dismutation is first-order in $O_2^{-\cdot}$, and so the half-life is independent of $O_2^{-\cdot}$ concentration. The enzymic dismutation has been calculated to be 10^6-fold faster than the spontaneous reaction, if only due to fact that the likelihood of a collision between $O_2^{-\cdot}$ and SOD is much greater than the likelihood of a collision with another $O_2^{-\cdot}$ molecule [31]. This, and the fact that the reaction of $O_2^{-\cdot}$ with SOD is 10^4-fold faster than the spontaneous reaction, allows the enzymic process to eliminate super-

oxide 10^{10}-fold faster than the spontaneous process [31]. The benefits of SODs in the cellular environment are thus considerable.

Superoxide dismutases can be separated into two main classes based on biochemical and physical properties. The first class contain Cu and Zn (CuZnSOD) at their active-sites; the second class contain Mn (MnSOD), Fe (FeSOD) or Ni (NiSOD). The two classes are evolutionarily unrelated and have totally different primary, secondary and tertiary structures, but both classes show essentially the same catalytic activity for superoxide *in vitro*.

1.3.1. Historical perspective

CuZnSOD was first discovered unintentionally during the isolation of carbonic anhydrase in 1939. Carbonic anhydrase was suspected of containing copper so protein fractions derived from bovine hemolysate were being assayed both for the catalysis of the hydration of CO_2 and for copper content. Carbonic anhydrase in fact contains zinc and not copper, so the fractions isolated on the basis of their high copper content were not active when assayed for carbonic anhydrase activity. Since the activity of the isolated copper protein was not known the function of copper storage was assigned, and the protein named hemocuprein [59].

Hemocuprein was subsequently referred to as erythrocuprein. During the 1950's, hepatocuprein was isolated from liver [60], cerebrocuprein was isolated from brain [61], and human erythrocuprein was isolated from human erythrocytes [62]. The reduction of cytochrome *c* by xanthine oxidase and the inhibition of this reaction by carbonic anhydrase was studied [63]. Xanthine oxidase catalyses the aerobic oxidation of xanthine. In the process it generates the superoxide radical. The superoxide radical had been shown to reduce cytochrome c. A preparation of carbonic anhydrase from bovine erythrocytes inhibited this reaction by reducing the steady-state concentration of the superoxide radical, presumably by catalysing the dismutation of superoxide to hydrogen peroxide and oxygen. A note added in proof reported that the dismutation activity could be separated from carbonic anhydrase activity by column chromatography of the bovine erythrocyte carbonic anhydrase preparation. Inhibition was therefore not due to the carbonic anhydrase, but to an enzyme present in the carbonic anhydrase as an impurity.

In 1969 an enzyme from bovine erythrocytes was isolated and purified. The enzyme catalysed the dismutation of superoxide radicals and so was named superoxide dismutase. The properties of the enzyme were identical to the previously described copper-containing cupreins, and the connection was immediately obvious. Based on SOD activity, a manganese-containing SOD was isolated from *E. coli* [64], and soon after, the iron-containing SOD from the same species [65].

1.3.2. The copper-zinc superoxide dismutases

Copper-zinc superoxide dismutases are found primarily in the cytosols of eukaryotic cells. They have also been isolated from bacteria, and a glycosylated CuZnSOD has been characterised from extracellular fluids of vertebrates [66, 67]. In general, CuZnSODs form homodimers with a molecular weight of ~ 32000 Da per subunit. They contain one Cu^{2+} and one Zn^{2+} per subunit. The extracellular SOD is tetrameric with a molecular weight of 135000 Da.

1.3.3. The manganese, iron and nickel superoxide dismutases

These SODs share high amino acid sequence and structural homology. They have been isolated from a variety of prokaryotes. They tend to form homodimers with a subunit molecular weight of ~ 22000 Da. MnSODs from mitochondria, the mycobacteria and the thermophilic bacteria are tetrameric. Almost all FeSODs are dimeric. FeSOD from *Mycobacterium tuberculosis* is tetrameric [68], as is FeSOD from *Rhodococcus bronchialis* [69].

1.3.3.1. Transition metal binding

The active-sites of Fe, Mn and NiSODs are not specific for the binding of their native metal ion. This was first demonstrated *in vitro* by the reversible removal of manganese from *E. coli* MnSOD and its substitution with Co(II), Ni(II), and Zn(II), when present in 100mM excess over Mn [70]. However, none of these metal cations conferred superoxide dismutase activity on the enzyme. Given that *E. coli* has both a Mn-containing and a Fe-containing SOD, and that the amino-acid sequences of these two enzymes are almost identical at the active-site, Fe(II) could also be expected to bind to MnSOD. In fact iron can compete with manganese for binding to the active site in this enzyme both during reconstitution of the apo-enzyme [71] and during biosynthesis, yielding an inactive form of MnSOD, termed a proMnSOD [72, 30, 73, 74].

In vivo incorporation of metals other than the native metal, including Cu [75], and Co [76], has also been shown to occur if the *E. coli* is grown on media depleted in the native metal. Both zinc and copper have been found as constituent metals in SODs [77], again forming an inactive enzyme. FeSOD as purified from *Methylomonas* J on Fe-enriched media contained 1.04 mol Fe, 0.02 mol Mn, 0.05 mol Cu and 0.75 mol Zn per mole of dimer.

The presence of inactive isozymes of SOD, largely arising from *in vivo* competition, in otherwise purified protein solutions must be taken into account when comparing specific activities and metal contents [30, 78].

1.3.3.2. Metal-specific superoxide dismutases

The dismutase activity of almost all Fe and MnSODs characterised to date is dependent on the metal ion at their active-site. These enzymes share high amino-acid sequence identity. The Fe and Mn enzymes from *E. coli* share 45 % sequence identity based on a structural alignment [79] (see Figure 2-6). The ligand-metal geometries in their active sites are almost identical, and the secondary coordination sphere is similar in both. Yet despite these similarities, substitution of the native metal with the other inactivates the enzyme [80, 4, 81].

1.3.3.3. Metal-non-specific superoxide dismutases

Although the majority of SODs characterised show strict metal-ion specificity, several SODs isolated from bacteria are active with either Fe or Mn at their active-site: *Propionibacterium shermanii* [82]; *Bacteroides thetaiotaomicron* [77]; *Streptococcus mutans* [83]; *Porphyromonas gingivalis* [84]; *Methylomonas* J [85]; *Mycobacterium smegmatis* [9]; and *Bacteroides fragilis* [86]. These enzymes have been called 'cambialistic' [83] (from the Latin cambialis, suggesting change) to indicate enzymes capable of making a co-factor substitution.

All these cambialistic SODs have been shown by various analytical techniques, and most conclusively by complete protein amino-acid sequencing, to be derived from a single apo-protein [87, 75]. This is in contrast to bacteria containing metal-specific SODs, which are synthesised as independent Fe and Mn enzymes having different primary sequences. It appears that these cambialistic SODs will incorporate Fe or Mn depending on growth conditions and metal availability. In general, the cambialistic SODs purified from anaerobic bacteria grown on complex media produce FeSODs, whereas those from aerobic organisms or O_2-induced anaerobes produce MnSOD. Supplementation or deletion of either Fe or Mn from the media will produce a SOD incorporating the metal that is still available to it. SOD from *P. shermanii* was shown to incorporate Cu in the absence of Fe and Mn, and further in the absence of Fe, Mn and Cu to incorporate Co [75, 76, 78]. The activity of the CoSOD was not reported directly, and that of the CuSOD as showing 10 % of the activity of the native FeSOD.

Reported specific activities of cambialistic SODs vary considerably. The highest is 4546 U/mg[1] for the Mn-supplemented, aerobically grown MnSOD from *S. mutans*, and the lowest is 89 U/mg for the FeSOD of *Methylmonas* J. Any direct comparisons of specific

1. The definition of a unit of superoxide dismutase activity was originally defined by McCord and Fridovich in 1969 [198]. One unit of activity is defined as the amount of superoxide dismutase required to inhibit the rate of reduction of cytochrome *c* by 50 %, with the standard assay being carried out under set conditions.

activities should be careful to take into account the metal content of the purified enzyme, which also varies considerably.

1.3.3.4. Inactivation of FeSOD by hydrogen peroxide

In general, FeSOD is inactivated by hydrogen peroxide, whereas MnSOD is unaffected [88]. CuZnSODs are also inactivated by hydrogen peroxide with the associated loss of one histidine per subunit [89]. *Pseudomonas ovalis* FeSOD loses tryptophan and cysteine residues as well as histidine [90], whereas *E. coli* FeSOD loses iron and tryptophan but not histidine [91].

In CuZnSOD inactivation is preceded by bleaching of the active-site Cu(II). It has been proposed that peroxide reduces Cu(II) to Cu(I). Cu(I) could then undergo a Fenton type reaction with hydrogen peroxide to produce a strong oxidant capable of oxidising an adjacent histidine residue [92, 93, 89].

A similar mechanism has been proposed for the hydrogen peroxide inactivation of FeSOD [94], whereby an attacking oxidant is produced by reaction of hydrogen peroxide with Fe. In *E. coli* FeSOD the primary electron removal from a ligated imidazole could be immediately followed by electron transfer from a nearby tryptophan. This could explain why tryptophan is lost on inactivation, whereas histidine is not. In the case of *P. ovalis*, electron transfer to a tryptophan may be less efficient, resulting in loss of histidine as well.

E. coli FeSOD is only inactivated by hydrogen peroxide to a limit of 90 % [95]. The material associated with hydrogen peroxide-resistant activity had the electrophoretic mobility of FeSOD. This would appear to reflect an intrinsic activity of the hydrogen peroxide-modified FeSOD rather than either inadequate treatment with hydrogen peroxide, or an impurity of co-migrating, co-purifying, Mn-containing active FeSOD [94].

1.3.4. Evolution

The high number of similar or identical residues shared by MnSOD and FeSOD from different sources suggests a common evolutionary origin. The considerable differences between the CuZnSOD and the Mn and FeSOD classes in both primary and tertiary structure suggest independent evolutionary origins. Mitochondria contain a MnSOD while the cytosols of eukaryotic cells contain a CuZnSOD. The mitochondrial MnSOD is homologous to the MnSOD and FeSOD found in prokaryotes but is completely different from cytosolic CuZnSOD. This supports the endosymbiont hypothesis. However, two bacteria do contain CuZnSOD. These are *Photobacterium leiognathi* [96] and *Caulobacterium crescentis* [97]. Given that *P. leiognathi* is a symbiont, gene transfer from the host to the bacterium is the most likely explanation for the presence of a CuZnSOD

in *P. leiognathi* [98].

1.4. Structural aspects of Mn and Fe superoxide dismutases

1.4.1. Primary structure

The complete or almost complete primary structures of 39 Mn and FeSODs have been analysed [99]; 14 residues are invariant throughout, including the four involved in ligation to the metal ion. Two residues distinguish MnSODs from FeSODs. Residue 76 is a glycine in MnSODs and a glutamine in FeSODs. Residue 149 is an alanine in all FeSODs and either glutamine or histidine in MnSODs. SODs from species that are active with either metal ion at their active-site have the MnSOD sequence at these two positions. Structural studies have shown that residues 76 and 149 are in close proximity to the active-site and that the glutamine (or histidine) residue interacts with the strictly conserved Tyr34. Tyr34 is believed to be important for the function of the enzyme. Its hydroxyl group is pointing towards and is only 5.4 Å from the active-site metal.

1.4.2. Secondary and tertiary structure

Crystal structures of Mn and FeSODs from nine different species have been solved, the best to 1.35 Å resolution (see Table 1-1 below). The subunit tertiary structure is strongly conserved, as is the active-site geometry. Almost all variations occur within loop regions.

The basic subunit consists of two domains. The N-terminal domain is an all-alpha domain consisting of two anti-parallel, adjacent alpha-helices (A1, A2) connected by a loop region. There are two distinct conformations of this loop region. Human mitochondrial MnSOD (PDB ID: 1ABM) and MnSOD from *M. tuberculosis* (PDB ID: 1IDS) have a short connecting loop of three and six residues respectively. FeSOD from *E. coli* (PDB ID: 1ISA) and MnSOD from *Thermus thermophilus* (PDB ID: 3MDS) have an extended loop region, the extension arising from shortening of the two α-helices. The extended loop region (17- and 24-residues long respectively) has a 2-turn α-helix at its apex. The entire loop region is folded over ~ 180º relative to the ends of A1 and A2. The loop folds away from the active-site side of the α-helical pair. MnSOD from *E. coli* is similar to *T. thermophilus* enzyme, but has two single-turn, four-residue α-helices separated by 3 residues, in the loop region. These two, short helices are not given alpha-numerical designations in the schematic diagram of Figure1-3 (opposite).

A kink in A1 in a histidine-rich region has the effect of positioning a conserved tyrosine residue (Tyr34) closer to the metal centre [101, 100]. This places a phenolic hydroxyl within 5.4 Å of the metal centre. Ionisation of this phenolic hydroxyl may account for the activity-limiting ionisation (pKa ~ 9.5) responsible for a decline in activity with increas-

ing pH [102, 103, 104, 105, 106, 107, 108, 112].

The C-terminal domain is an alpha-beta domain. The core consists of three strands of anti-parallel beta sheet. The four α-helices of this domain lie on one side of the beta-sheet.

The active site containing the catalytic metal ion lies between the two domains. Two ligands are provided by each domain. Helices A1 and A2 each provide a histidine ligand coordinated through NE2. The end of the beta-sheet provides a histidine and an aspartate residue. The metal ion is five coordinate with the fifth ligand being an axially bound solvent molecule, either water or a hydroxide ion. The coordination geometry is a slightly distorted trigonal bipyramid.

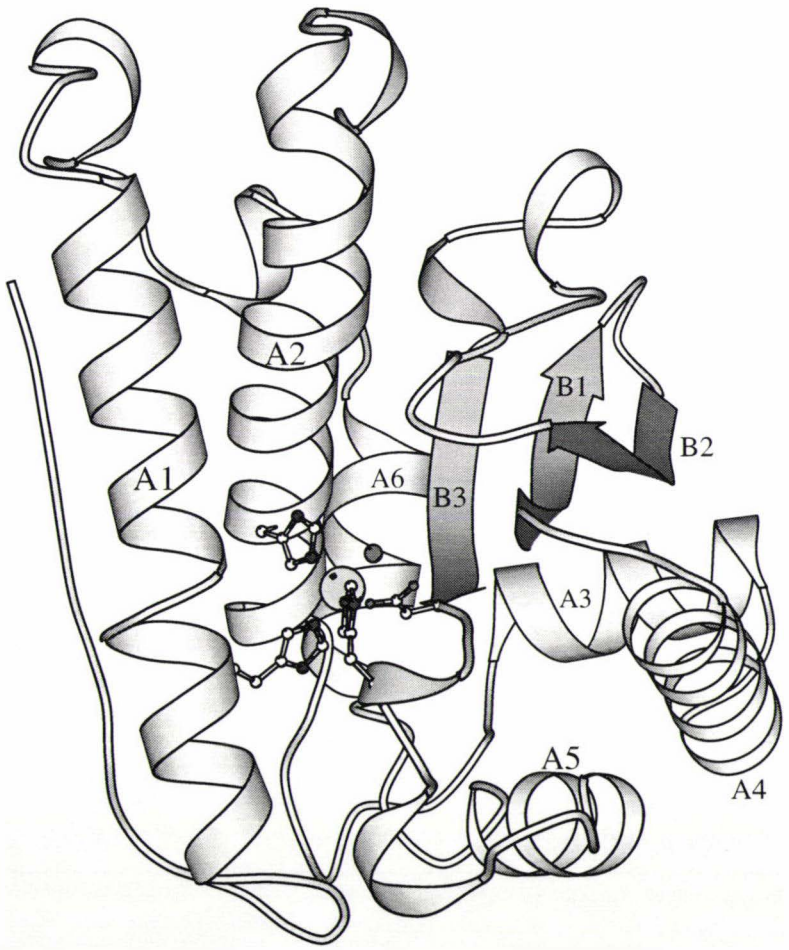

Figure 1-3. Schematic diagram of the *E. coli* MnSOD monomer

Schematic diagram of the *E. coli* MnSOD monomer, identifying secondary structure elements (helices as *ribbons*, β-strands as *arrows*). Figure drawn with MOLSCRIPT [1].

Table 1-1. X-ray crystal structures of Fe and Mn superoxide dismutases

Organism	Native metal	Crystallographic distinction	PDB ID	Author	Year	Res. (Å)
Aquifex pyrophilus	Fe	Fe(III)	1COJ	Lim	1997	1.9
Baccilus stearothermophilus	Mn	Mn(III)	-[1]	Parker	1988	2.4
Escherichia coli	Fe	Fe(II)	1ISA	Lah	1995	1.8
E. coli	Fe	Fe(III)	1ISB	Lah	1995	1.85
E. coli	Fe	Fe(III) + azide	1ISC	Lah	1995	1.8
E. coli	Mn	Mn(III)/Mn(II)	1VEW	Edwards	1998	2.1
E. coli	Mn	Fe(III)	1MMM	Edwards	1998	2.2
Human mitochondrial	Mn	Mn(III)	1MSD	Wagner	1993	3.2
Human mitochondrial	Mn	Mn(III)	1ABM	Borgstahl	1992	2.2
Human mitochondrial	Mn	Y34F orthorhombic form	1AP5	Guan	1998	2.2
Human mitochondrial	Mn	Y34F hexagonal form	1AP6	Guan	1998	1.9
Human mitochondrial	Mn	Q143N	1QNM	Hsieh	1998	2.3
Human mitochondrial	Mn	I58T	1VAR	Borgstahl	1996	2.5
Mycobacterium tuberculosis	Fe	Fe(III)	1IDS	Cooper	1995	2.0
M. tuberculosis	Fe	H145Q	-[1]	Bunting	1998	4.0
M. tuberculosis	Fe	H145E	-[1]	Bunting	1998	2.5
Pseudomonas ovalis	Fe	Fe(III)	3SDP	Stoddard	1990	2.1
Propionibacterium shermanii	Fe/Mn	Fe(III)	1AR4	Schmidt	1996	1.6
P. shermanii	Fe/Mn	Mn(III)	1AR5	Schmidt	1996	1.9
P. shermanii	Fe/Mn	Fe(III) + azide	1AVM	Schmidt	1998	1.55
P. shermanii	Fe/Mn	Fe(III) pH 6.1 + fluoride	1BS3	Schmidt	1999	1.55
P. shermanii	Fe/Mn	Fe(III) pH 8.1	1BSM	Schmidt	1999	1.35
P. shermanii	Fe/Mn	Fe(III) pH 10.0	1BT8	Schmidt	1999	1.85
Sulfolobus solfataricus	Fe	Fe(III)	1SSS	Ursby	1999	2.3
Thermus thermophilus	Mn	Mn(III)	3MDS	Ludwig	1991	1.8
T. thermophilus	Mn	Mn(III) + azide	1MNG	Lah	1995	1.8

[1] Coordinates not deposited in the PDB [2, 3].

The entire active-site environment is hydrophobic with three Tyr, three Trp and two Phe residues within 10 Å of the metal centre. This shell of hydrophobic residues may play a role in stabilising the Mn(III) which, because of its strong oxidising potential, would dismutate to Mn(II) plus $Mn(IV)O_2$ in water. These hydrophobic residues are conserved throughout Mn and Fe SODs. Ligation of the metal with residues from both domains allows the metal to provide for both structural stabilisation and catalysis. Removal of the

metal leaves the apoMnSOD as a dimer, whereas the apoFeSOD dissociates into subunits [4].

The crystal structures of Mn(II)SOD [109] and Fe(II)SOD [6] were compared with their corresponding trivalent state using difference Fourier methods. No difference in active-site geometry was observed. The crystals were reduced by soaking in dithionite.

Crystal studies of the active-site geometry in the presence of azide, a substrate mimic, have been carried out on both FeSOD from *E. coli* and MnSOD from *T. thermophilus*. Azide coordinates to Mn(III) at an in-plane site opposite the aspartate ligand. The His-Mn-His bond angle opens from 131º to 148º to accommodate the azide. The axial solvent ligand remains bound. The metal forms a six-coordinate, octahedral geometry. The azide binds to Fe(III) in essentially the same position but makes different non-bonding interactions.

1.5. Kinetics and the catalytic mechanisms of Fe and MnSODs

The first kinetic studies were undertaken on *E. coli* MnSOD in 1974 by Pick *et al.* [110]. These were followed by studies on *P. leiognathi* FeSOD [111], *Bacillus thermophilus* MnSOD [102, 112], *E. coli* FeSOD [103, 105], *Paracoccus denitrificans* MnSOD [106], and *P. ovalis* FeSOD [113]. Advances in kinetic techniques [105] produced more detailed studies on *E. coli* FeSOD [105], *T. thermophilus* MnSOD [7], *E. coli* Fe and MnSODs [114] and the cambialistic SOD from *P. shermanii* [115].

1.5.1. Kinetics of MnSODs

The kinetic studies of *E. coli* MnSOD [110] show a complicated reaction dependence between substrate and enzyme when compared with the subsequently revealed kinetics of CuZnSODs [116] and FeSODs [105]. When the initial concentration of $O_2^{-\cdot}$, $[O_2^{-\cdot}]_0$, is less than ten-times the initial concentration of *E. coli* MnSOD, $[E]_0$, the reaction is first-order in both $[O_2^{-\cdot}]$ and [E] with a rate constant of $1.5 \pm 0.15 \times 10^9$ $M^{-1}s^{-1}$. However, when $[O_2^{-\cdot}]_0/[E]_0 > 15$ a biphasic process occurs. Initially, approximately 15 $O_2^{-\cdot}$ radicals react per dismutase molecule at a relatively fast rate. The excess $O_2^{-\cdot}$ is removed by a less efficient reaction, first order in $[E]_0$ and nearly first-order in $[O_2^{-\cdot}]$, at a rate of $1.6 \pm 0.25 \times 10^8$ $M^{-1}s^{-1}$. These results were initially interpreted in terms of a series of four oxidation and reduction reactions, utilising four different valence states of Mn, and subsequently reevaluated by Bull *et al.* [7] in a more concise scheme that also fitted the kinetic data of *T. thermophilus* MnSOD. *Bacillus thermophilus* MnSOD showed similar behaviour having exponential decay of $O_2^{-\cdot}$ when $[O_2^{-\cdot}]_0/[E]_0 < 15$, a non-exponential decay when the ratio is between 15 and 100, and zero-order decay when $[O_2^{-\cdot}]_0/[E]_0 > 100$ [102]. This was interpreted as a fast cycle-slow cycle mechanism. The fast cycle is a

rapid one-electron oxidation-reduction cycle, and the slow cycle is a concurrent slower reaction that gives a superoxide-unreactive form of the enzyme which undergoes a first-order decay to regenerate fully active enzyme. Terech *et al.* [106] did not observe this behaviour in the MnSOD from *Paracoccus denitrificans.* Bull *et al.* [7] obtained kinetic data on the MnSOD from *T. thermophilus* with decay curves similar to those of MnSOD *B. thermophilus* showing three distinct phases: rapid disappearance of $O_2^{-\cdot}$ (the "burst" phase), a period of approximately zero-order $O_2^{-\cdot}$ decay (the "steady-state" phase), and a rapid depletion of $O_2^{-\cdot}$ at the end of the reaction. They determined that proton transfer is probably the rate-limiting step when the enzyme is saturated with $O_2^{-\cdot}$, and the reaction by which the inactive enzyme is converted to active enzyme is not limited by proton transfer. The reaction in the steady-state was slowed down by using D_2O at low temperatures (2-6ºC), allowing spectral changes of the metal ion to be monitored. The spectrum was assigned to the inactive form of the enzyme, which is postulated to be a cyclic peroxo complex of Mn(III) formed by oxidative addition of $O_2^{-\cdot}$ to Mn(II). A reaction mechanism (Figure 1-4) has been proposed to account for the kinetic behaviour of MnSODs, based largely on the reaction mechanism of *E. coli* FeSOD [105], and including the side reaction forming inactive enzyme, *X*.

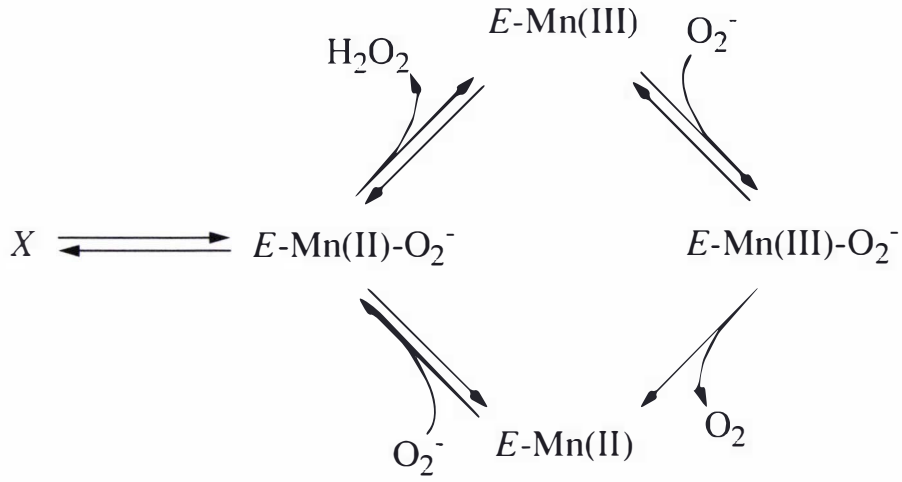

Figure 1-4. Proposed reaction scheme for MnSOD-catalysed superoxide dismutation [7]

Proposed reaction scheme for MnSOD-catalysed superoxide dismutation including two first-order rearrangements which lead from active enzyme (*E*) to inactive enzyme (*X*), and back to active enzyme.

Crystal structures of both Mn and Fe SODs show the metal ion at the active-site to have a five-coordinate geometry, changing to six-coordinate on binding of azide. Spectro-

scopic studies on MnSOD from *E. coli* [5] show five-coordinate geometry is retained on binding of azide to the Mn(III) form at room temperature. Variable temperature spectroscopy shows a thermal transition from five to six coordinate at around 200 K. Because both the native and azide complexes are five coordinate, the addition of the anion must be associated with loss of one of the other ligands. The ligand most likely to be involved is either the water ligand or the carboxylate group of the aspartate. The Mn-OD1 carboxylate bond distance increases by 0.4 Å (to 2.25 Å) when azide is bound to *T. thermophilus* MnSOD [6]. Dehydration would convert the complex to a square pyramid with either the solvent or His28 bound axially. The retention of the displaced ligand as a satellite in the outer sphere of the metal complex would account for the crystallographic detection of six atoms around the active-site Mn in the azide complex of *T. thermophilus* MnSOD. This is illustrated in Figure 1-5.

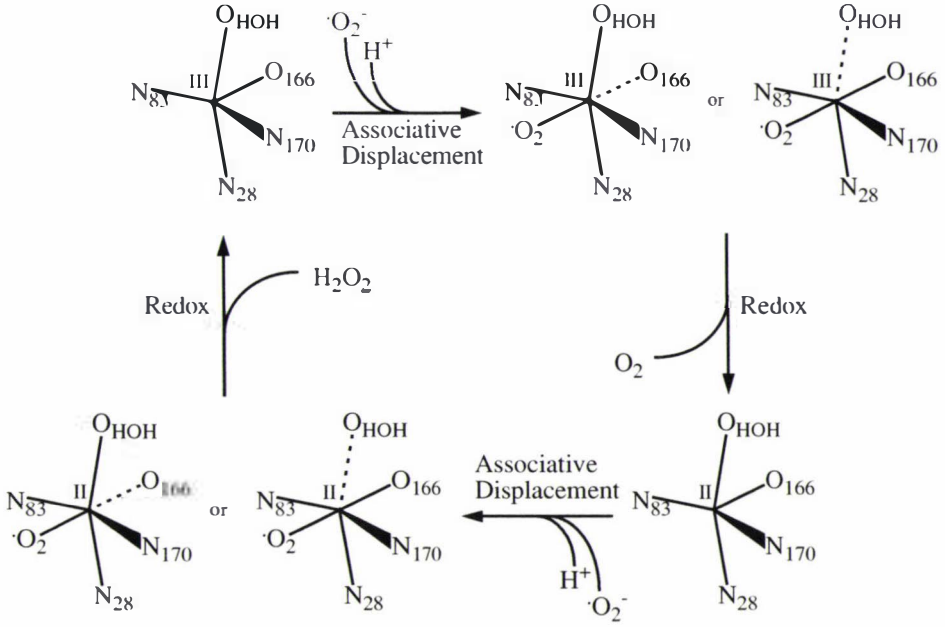

Figure 1-5. Reaction mechanism for MnSOD proposed by Whittaker *et al.* 1996 [8]

1.5.2. Kinetics of FeSODs

The most recently proposed mechanism for FeSOD catalysis, the "5-6-5 mechanism" [6], modifies schemes proposed by Bull and Fee in 1985 [105], and Stallings *et al.* in 1992 [117] and is presented below as Figure 1-6 along with a list of the salient points forming the basis of the mechanism. The geometries of the first three central species in the mechanism have been determined by X-ray analysis [6]. The X-ray structures show that the active site is not directly accessible to solvent. Ligands and solvent are proposed

to reach the iron because of thermal motions of Tyr34, His30, or because other residues provide a transient pathway [118, 117].

1. Fe in the resting oxidised enzyme coordinates an axial solvent ligand, postulated to be OH^- at neutral pH. A proton (1.1 ± 0.1) is taken up by the protein when it is reduced to the Fe(II) species in the pH range 7-10 [105]. An OH^- metal ligand in Fe(III)SOD is proposed as the acceptor of this proton. The proton acceptor should be close to the metal ion for the reduction to have an effect on its pK. Of the protein ligands, the aspartate is ionised and the three histidines are not charged at neutral pH so it would seem unlikely that any of the protein ligands acts as the proton acceptor.

2. Superoxide anion binds at the partly open coordination site opposite OD2 of Asp156 without substitution of ligated hydroxide anion, forming a distorted octahedron. This intermediate is modelled by the azide complex of Fe(III) SOD. Electron transfer then generates the dioxygen leaving group. Formation of Fe(III) innersphere complexes is associated with only small reorientations of the metal-ligand geometry. Reduction to Fe(II) produces virtually no change in the active-site geometry. The minimal perturbation required to form these catalytic intermediates is consistent with rapid turnover (~ 26000 s^{-1} at 25ºC for FeSOD [105]).

3. Protonation of the axial solvent ligand restores the net +1 charge on the cluster for the start of the second half reaction. Free reduced enzyme with trigonal bipyramidal coordination then accepts a second superoxide.

4. The coordinated superoxide anion is reduced and receives two protons, one shown as coming from the ligated HOH molecule, and leaves as hydrogen peroxide, with SOD returning to the resting state (1). There is no X-ray structure which models species (**4**). Neither azide nor OH^- has significant affinity for Fe(II)SOD [105]. However $NO^{\cdot}$ does form a stable complex with Fe(II)SOD indicating that a coordination position is available on the reduced metal [119]. Reduction of $O_2^{\cdot-}$ to form the doubly charged peroxide anion (O_2^{2-}) is likely to require direct ligation to the metal [120]. In the oxidative step, Fe(II)-O_2^{1-} is oxidised to Fe(III)-O_2^{2-}. This basic species is then protonated to Fe(III)-$^-$OOH and dissociated to form a hydroperoxyl anion. The most likely proton donor for this species is HOH, but there are no bound waters in the active-site other than the ligated solvent. Thus motions of Tyr34 and His30 may be required for protonation of the coordinated OH^- and peroxide anion, as well as for allowing access of the superoxide radical to the metal ion. To explain the pH dependence of the turnover number and a solvent deuterium isotope effect of ~ 3 [120], it is suggested that proton transfer from H_2O to developing basic centres is partly rate limiting when substrate is saturating.

5. A second OH^- ligand is bound at the sixth coordination site. Given that the solvent

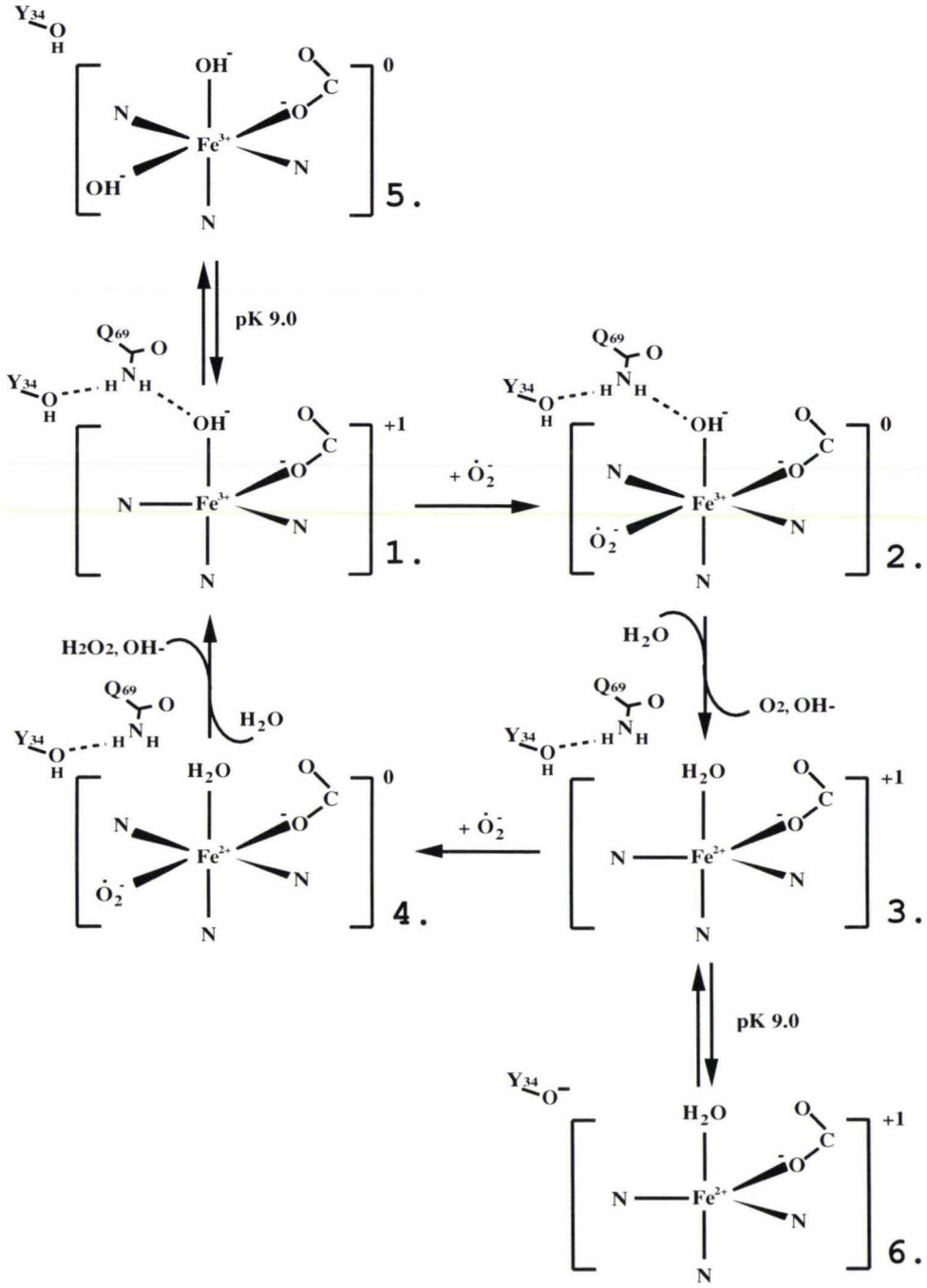

Figure 1-6. Scheme for the enzyme-catalyzed dismutation of superoxide as proposed by Lah *et al.* 1995 [6]

ligated to the Fe(III) is OH^- and not HOH at neutral pH, the metal associated pK_a of 9 is not due to ionisation of bound HOH, but instead due to binding of a second OH^- as a sixth ligand. The K_m for $O_2^{\cdot-}$ is influenced by the pK_a of ~ 9 in the ferric form and by an ionization in the reduced form that is not associated with the metal [105]. The pH dependence of K_m can be in part explained by competition between substrate (azide) and

OH^- for a binding site at Fe(III). Extended X-ray absorption fine structure (EXAFS) measurements [121] support both the ligation of OH^- and the six-coordinate Fe(III) species with the addition of a second OH^-.

6. Conversion of species (5) to species (6) occurs by the reduction of Fe(III) SOD at high pH. This step is accompanied by protonation of the axial ligand, loss of an OH^- ligand, and ionisation of Tyr34. In order for proton uptake to remain constant near pH 9 during reduction, there must be an ionisation at pH 9 in Fe(II)SOD that compensates the ionisation at pH 9 in Fe(III)SOD. The ligand that is titrated at pH 9 for Fe(II)SOD is most likely to be Tyr34. Mössbauer spectra show that the metal ligands do not ionize in the pH range 7 - 10.8 [119, 105]. The OH^- of Tyr34 is only 5.4 Å from the metal centre, and a hydrogen-bonding network links it with the metal centre. The components of this network are conserved, and Tyr34 is invariant in all known Fe and MnSOD structures [109].

1.5.3. Kinetics of cambialistic SODs

The only kinetic studies so far on this class of enzyme are those on the cambialistic FeSOD from *P. shermanii* [115]. Reaction rates determined were comparable to other metal-specific Fe- and Mn-containing SODs and were not decreased by D_2O. This is in contrast to the FeSOD from *E. coli,* which showed the rate-limiting step under saturating conditions was the transfer of a proton from a general acid (H_2O) to a basic centre that develops during catalysis [105]. In a similar fashion to the MnSOD from *Paracoccus denitrificans* [106], which shows comparable reaction rates and K_m, FeSOD from *P. shermanii* is not saturable by $O_2^{-\cdot}$ under physiological conditions.

1.5.4. The role of reduction-oxidation potentials on catalysis

The generally accepted scheme for catalysis of the dismutation reaction (Reaction 4), involves alternating reduction and oxidation of the metal ion in a ping-pong type mechanism.

$$O_2^- + SOD\text{-}M^{n+} \longrightarrow SOD\text{-}M^{(n-1)+} + O_2 \qquad (15)$$

$$O_2^- + SOD\text{-}M^{(n-1)+} \longrightarrow SOD\text{-}M^{n+} + H_2O_2 \qquad (16)$$

For a metal ion to be active as a superoxide dismutase, its standard reduction potential must fall between those of the two half-reactions of superoxide.

$$O_2 + e \rightleftarrows O_2^- \qquad E^{o\prime} = -0.137 \text{ V } vs. \text{ NHE} \quad (17)$$

$$O_2^- + e + 2H^+ \rightleftarrows H_2O_2 \qquad E^{o\prime} = +0.67 \text{ V } vs. \text{ NHE} \quad (18)$$

An optimum catalyst might be expected to have a reduction potential midway between

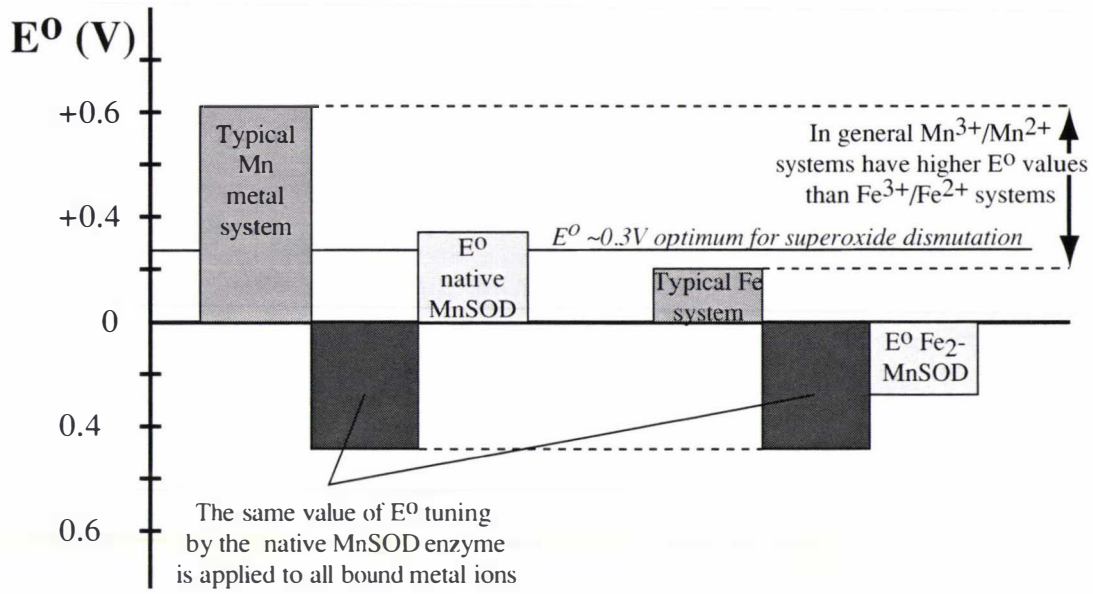

Figure 1-7. Reduction potential tuning of metal ions by SOD enzyme structure

Schematic diagram illustrating reduction potential tuning of the active-site SOD metal system by the enzyme, as proposed by Vance and Millar [10]. The native MnSOD enzyme tunes the reduction potential of the Mn metal ion to an optimum value for superoxide dismutation. The same amount of reduction potential tuning is applied by the MnSOD enzyme to the Fe metal ion in Fe_2MnSOD. However, because typical Fe metal systems have a lower reduction potential to start with, the reduction potential applied is too great causing the reduction potential of Fe_2MnSOD to be well below the optimum.

those for reactions 17 and 18; $(E^{o\prime}_{17} + E^{o\prime}_{18})/2 \sim +0.27$ V *vs.* NHE. The potentials for all the catalytically active SODs that have been measured so far fall in the range +0.23 V to +0.40 V *vs.* NHE [25]. It has been proposed that the inactivity of metal-substituted superoxide dismutases may be in part attributed to the fact that the standard reduction potential of the metal-substituted enzyme falls outside this range [10]. The standard reduction potential at pH 7.0 of *E. coli* Fe-substituted MnSOD was determined as -0.24 V *vs.* NHE. The Fe-substituted MnSOD should therefore, based on elementary redox chemistry, be unable to oxidise superoxide to oxygen in reaction 17, thereby halting catalysis. This was shown to be the case by *in vitro* potentiometric titrations. Vance and Miller [10] proposed a mechanism of reduction potential tuning of the metal ion by the enzyme (shown schematically in Figure 1-7). Mn systems in general have higher reduction potentials than those of Fe. Both have reduction potentials greater than the optimum for superoxide catalysis ($E^{o\prime} \sim +0.27$ V *vs.* NHE), and so the enzymes must depress or 'tune' the reduction potentials of their metal ions. It follows that the Mn-containing enzymes must depress the reduction potential of their metal ion to a greater extent than do the Fe-containing enzymes. When Fe is substituted into a MnSOD, the enzyme may 'tune' the non-native metal as if it were Mn, depressing it too far below the optimum,

leaving the Fe(III) centre unable to oxidise $O_2^{-\cdot}$ to oxygen. Similarly, if Mn is substituted into a metal-specific FeSOD, the enzyme cannot depress the reduction potential of Mn enough, and the reduction of $O_2^{-\cdot}$ to peroxide by Mn(II) cannot be achieved.

1.5.5. pH dependence of activity and inhibition

Fe and MnSODs, both metal-specific and cambialistic, exhibit a pH dependence for catalysis, reduction potential, spectral properties, and inhibition. *Bacillus stearothermophilus* MnSOD shows near-Nernstian behaviour for one proton coupled to the one-electron reduction, with $\Delta E_m/pH \sim 50$ mV [122]. *E. coli* MnSOD on the other hand exhibits a more complicated activity dependence on pH. It has a mid-point potential which changes little between pH 7 and pH 8, but which changes by 140 mV between pH 8 and 9. This is consistent with the catalytic rate constant which only shows a small change between pH 6.0 and pH 7.8, and decreases by about one-third between pH 7.8 and pH 8.5 [123]. The FeSODs from *Azobacter vinelandii* and *P. ovalis* show a similar a pH dependence of E_m [25], having a $\Delta E_m/pH$ of -60 mV, with E_m becoming independent of pH above ~ pH 9.5.

The activity, anion affinity and spectra of the Fe-substituted, metal-specific MnSOD from *Serratia marcescens* all show pH dependencies [199]. Activity increases with decreasing pH from 1 % of native at pH 8.1 to 10 % at pH 6.0 with a pK_a of 7. The affinity for azide also increases with decreasing pH from $K_d = 0.9$ mM at pH 8.2 to $K_d = 0.1$ mM at pH 6.2. The visible and EPR spectra of the active-site metal ion show pH-dependent changes with pK_a of 6.6 and pK_a of 7.2, respectively. Because the pK_a values derived from the absorption spectra and the affinity for azide are close to the pK_a for the pH-dependent activity, a change in the Fe environment with increasing pH must be related to the decreasing activity of the Fe-substituted MnSOD. Azide binding, spectral properties, and the Michaelis constant for superoxide in *E. coli* FeSOD are all affected by pH in a similar fashion, which is consistent with an ionizing group of $pK_a \sim 9$ [103, 104]. The same pH-dependent change in the metal environments of these two enzymes could control activity with different pK_a values [199]. The differing pK_a of the two Fe enzymes could be due to differences in their primary structure, or deprotonation of groups near the active-site such as coordinated water or histidine ligands. This change in the metal environment is proposed to be due to the binding of a hydroxide anion in the sixth coordination position [124, 117, 6, 199]. As O_2^- is also proposed to bind at this position [6], both azide and hydroxide would act as competitive inhibitors by this mechanism. This mechanism however, explains only part of the loss of activity of the Fe-substituted, metal-specific MnSOD from *S. marcescens,* as only 10 % activity is regained in the absence of these inhibitors at pH 6.0. A reaction scheme for Fe-substituted MnSOD from *S. marcescens* is presented in Figure 1-8 (opposite). The mechanism of metal ion tuning as pro-

posed by Vance and Millar [10] may also be applicable to this Fe-substituted enzyme.

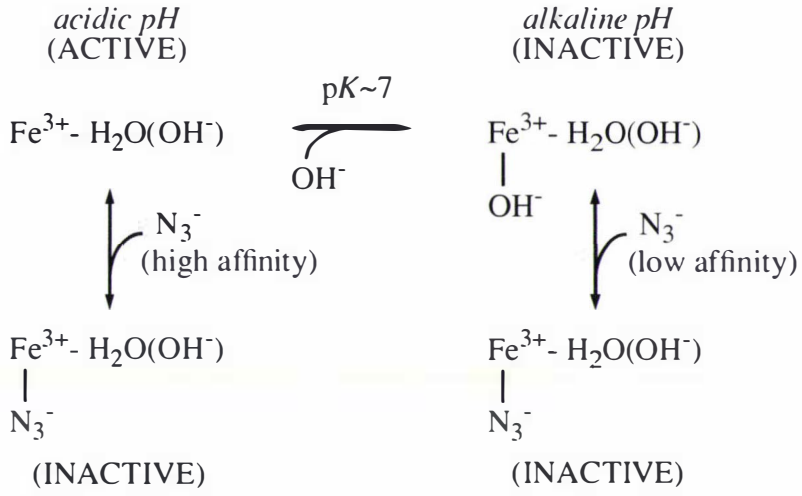

Figure 1-8. Reaction scheme for Fe-substituted MnSOD from *S. marcescens* [199]

Fe^{3+}-$H_2O(OH^-)$ represents coordinated solvent to the trivalent iron in Fe-substituted MnSOD. The inactive hydroxide form at alkaline pH represents species (5) in the 5-6-5 mechanism of Lah *et al.* [6].

Similar results have been obtained for the cambialistic FeSOD from *P. shermanii* [115, 125]. Reaction rates of both the Fe and MnSOD exhibit pH dependence. The activities of both increase by a factor of 3-4 on decreasing from pH 8.0 to pH 6.5 [115]. The native MnSOD shows no inhibition by azide or fluoride, whereas native FeSOD shows slight (23 %) inhibition by azide at pH 7.8 increasing to 80 % inhibition at pH 6.8 [125]. FeSOD also exhibits changes in its EPR spectra above pH 8, attributed to binding of OH^- in the sixth coordination position in an analogous fashion with *E. coli* FeSOD.

1.6. *E. coli* iron and manganese superoxide dismutases

FeSOD is constitutively expressed in *E. coli*. Specific activity decreases slightly on exposure of the growth medium to oxygen [126]. However, this is a result of there being less Fe available in the media due to induction of cytochromes and other Fe-containing proteins. Anaerobically grown *E. coli* produces an FeSOD. When *E. coli* is grown aerobically, MnSOD is induced, as well as a hybrid (see below). Very low levels of oxygen present in static cultures are enough to cause full induction of MnSOD but will not significantly induce the hybrid SOD or catalase. Agitation of the culture is sufficient to fully induce the hybrid SOD.

1.6.1. Hybrid superoxide dismutases

Aerobically induced hybrid ferrisuperoxide dismutase has been purified and characterised from *E. coli* [126, 127, 95]. The hybrid is dimeric and consists of a subunit of FeSOD and a subunit of MnSOD. The isolated hybrid, which originally contained both manganese and iron, could be subjected to metal removal. Activity was restored with either Fe(II) or Mn(II), and to an even greater extent with both metals. The hybrid could be produced *in vitro* by mixing purified MnSOD and FeSOD, and treating the mixture with 8-hydroxyquinoline in the presence of 2.5 M guanidinium chloride to remove the metal, followed by reconstitution with Fe and/or Mn [95].

Exposure of the *E. coli* hybrid SOD to hydrogen peroxide inactivated the enzyme, but not completely. Residual activity remained to a level of about 40 %. This is consistent with the hybrid being composed of both Fe and Mn subunits [95]. Partial inactivation of the hybrid by exposure to hydrogen peroxide was accompanied by a resegregation of subunits to form native Fe and Mn SOD dimers. Thus prior to hydrogen peroxide inactivation, hybrid SOD revealed a single band of activity and a single band of protein on a polyacrylamide electrophoresis gel, whereas after inactivation, two protein bands formed. One band showed activity and migrated as MnSOD, and the other inactive band migrated as FeSOD.

1.6.2. Manganese superoxide dismutase properties and features

MnSOD from *E. coli* is dimeric with two identical subunits each having 205 residues and a molecular weight of 22900 Da. Some general properties of MnSOD are given in Table 1-2 (opposite).

1.6.2.1. Metal ion

ApoMnSOD from *E. coli* retaining less than 0.2 % of the activity of the holoenzyme can be prepared by slight reversible denaturation followed by dialysis against a metal-chelating agent. The apoMnSOD can be reconstituted with Mn(II), with recovery of 70 % of the initial enzyme activity. Unlike apoFeSOD, apoMnSOD does not dissociate into subunits [4].

Co(II), Zn(II), Ni(II), Mg(II), Cr(III), Cu(II), Fe(II), In(II), and Mo(VI) have been tested for their ability to replace manganese. None restores activity to the apoenzyme. When present at a 100-fold molar excess over manganese, only Co(II), Zn(II) or Ni(II) were effective as competitors of manganese [70].

1.6.2.2. Redox forms

MnSOD as isolated from *E. coli* shows redox heterogeneity. Low-temperature EPR spec-

tra show a 60:40 ratio of Mn(III) to Mn(II) [5]. Homogeneous and stable Mn(III)SOD can be produced by oxidation with molybdicyanide without loss of metal or significant damage to the protein. Given that the redox potential of the Mn active-site is relatively low ($E^o = 0.31$ V *vs.* NHE) [122], oxidation by ferricyanide should be theoretically possible but does not occur. Oxidation with the slightly more powerful oxidant hexachloroiridate Na_2IrCl_6 appears to result in irreversible damage to the protein [5]. Mn(II)SOD can be formed by reduction with sodium dithionite, the purple colour of the oxidized enzyme being lost and a colourless solution obtained. No significant change in metal content or specific activity occurs upon reduction. Mn(II)SOD spontaneously reoxidises in air to give a mixture of Mn(II) and Mn(III) forms [5]. Crystals of MnSOD can be reduced by low concentrations of H_2O_2. Bleaching of the Mn(III) chromophore is readily apparent on reduction to Mn(II).

Table 1-2. Summary of general properties of MnSOD [4, 5]

$s^{20}(x10^{-13}\ s)$[1]	3.55 ± 0.3
R_s (Å)[2]	29.0 ± 1.7
R_{min} (Å)[3]	23.8
molecular weight (Da)	45800 ± 500
υ (mL/g)[4]	0.735
ε_{280}	$8.66x10^4\ M^{-1}cm^{-1}$
λ_{max}	478nm ($\varepsilon_{478}^{Mn} = 850\ M^{-1}cm^{-1}$)
$K_d(F^-)$[5]	25 mM, 1.1 M
$K_d(N_3^-)$	7.2 mM

1. Sedimentation velocity determined in 50 mM potassium phosphate (pH 7.8) buffer containing 100 µM EDTA.
2. Stokes radius.
3. Calculated by assuming a non-hydrated sphere of MW=45800 Da.
4. Partial specific volume calculated from the amino acid sequence.
5. Two-step binding.

1.6.2.3. Ligands

Both F^- and N_3^- bind to Mn(III)SOD from *E. coli*. Dissociation constants for both of these complexes have been extracted from the experimental data by non-linear regres-

sion against an equilibrium binding model [128], yielding K_d values of 25 mM and 1.1 M for two-step binding of F^-, and 7.2 mM for single-step N_3^- complexation [5]. Temperature-dependent absorption studies for anion complexes of MnSOD indicate a change in coordination number for the metal complex at low temperatures. At 295 K, the spectrum for the Mn(III)-azide complex is characteristic of five coordination. At low temperature, the spectrum reflects six coordination with a midpoint for the transition near 200 K [8]. This differs from the geometry of FeSOD from *E. coli,* for which X-ray and spectroscopic data show six-coordination at room temperature.

1.6.2.4. Functional inequivalence of Mn and Fe forms

It has been demonstrated that *E. coli* Mn and Fe SOD are not functionally equivalent. MnSOD is more effective than FeSOD in preventing damage to DNA, while the FeSOD appears to be more effective in protecting a cytoplasmic superoxide-sensitive enzyme [129]. MnSOD has been shown to bind non-specifically to DNA by electrophoretic mobility shift assay and nitrocellulose-filter binding methodologies. The equilibrium dissociation constants for interaction with a variety of double-stranded and single-stranded oligonucleotides range from 1.5 ± 0.2 to 8.4 ± 1.3 μM at 20ºC. *In vivo* binding of MnSOD to DNA was supported by colocalisation of MnSOD and the *E. coli* nucleoid in immunoelectron microscopy. Both MnSOD and DNA were inhomogeneously distributed in the cytosol, the concentration of each being higher in the centre of the cell and relatively low near the inner membrane. FeSOD was shown to only bind weakly *in vitro*, K_d > 40-220 μm. Association of MnSOD with DNA would localise the dismutase activity near a target of oxidative stress and increase protection of DNA from oxidative damage.

1.7. Research aims

There are many intriguing aspects of Mn and FeSOD biochemistry that remain to be investigated. Most of these revolve around the functional differences between the Mn and FeSODs and are necessarily related; the answers to one question may also provide the answers to others. Such questions include: the basis of the metal-ion specific nature of Mn and FeSODs; the mechanism of H_2O_2 inhibition of FeSODs but not MnSODs; the basis of the cambialistic nature of some SODs; features of the general mechanism of Mn and FeSODS including effects of pH and proton movements; the possibility of electron-transfer pathways linking active-sites; the role of hybrid FeMnSODs.

This research has two main focuses. The first is the determination of the subtle structural and chemical basis of the metal-ion specificity. Hence, the structures of *E. coli* MnSOD and Fe_2MnSOD were determined to provide structural comparisons with *E. coli* FeSOD. The second main focus involves elucidation of the mechanism of dismutation in more

detail, including the functional role of certain key residues as investigated in the site-directed mutagenesis studies.

2 Crystal Structure of *Escherichia coli* Manganese Superoxide Dismutase at 2.1 Å Resolution

2.1. Introduction

Several types of superoxide dismutase exist, which use metal ions to assist in the disproportionation reaction. These include the dinuclear Cu,Zn-superoxide dismutase that occurs primarily in eukaryotes, the iron-dependent superoxide dismutase (FeSOD) found in prokaryotes, the manganese-dependent enzyme (MnSOD) that is found in both prokaryotes and eukaryotes [30], and the nickel-dependent enzyme recently characterised from *Streptomyces* species [136].

The MnSOD and FeSOD enzymes both have a subunit size of about 22kDa (~ 200 residues) and share substantial sequence similarity, typically 30 - 40 % identity when compared on a pairwise basis [99]. Three-dimensional structures have been determined for several FeSODs [137, 6] and MnSODs [109, 100, 134, 138]. These enzymes are structurally homologous, and are quite distinct from the Cu,ZnSODs [139]. The Mn and FeSODs have a two-domain structure comprising an all-α N-terminal domain and an α/β C-terminal domain. In each case the metal site is located between the domains with the metal (Mn or Fe) bound by four protein ligands (3 His, 1 Asp), two being contributed by each domain. The catalytic mechanism involves alternation of the metal ion between the 3+ and 2+ oxidation states [102, 111, 112].

In spite of the high sequence similarity and structural homology between Mn and FeSODs, and the availability of high resolution structures from both classes, some curious and as yet unexplained differences exist. First, there is a distinct metal ion specificity in the two classes of enzyme: Fe(III) can substitute for Mn(III) (and vice versa), but only the native metal ion normally exhibits catalytic activity, despite the apparently identical metal binding sites [4]. A few cambialistic SODs have been reported which are completely active with either Mn or Fe at the active-site [82, 86, 83, 77, 84]. Secondly, some MnSODs are dimeric and others are tetrameric, but the factors that determine these differences have not been clearly identified. Finally, there is the fundamental biological question of why both manganese- and iron-dependent enzymes exist, often in the same

organism. For example, *Escherichia coli* has both MnSOD and FeSOD, both cytosolic, with 44 % sequence identity and identical rate constants [114]. The FeSOD is constitutive, whereas expression of the MnSOD is inducible, in response to oxidative stress [140, 126], but the question remains as to why both are needed. One possibility is that particular molecular properties of the two enzymes enable them to protect different targets of oxidative damage [129, 141], as suggested for example by the observation that MnSOD can bind to DNA [142].

E. coli MnSOD has been well studied spectroscopically [4, 5] and functionally [129, 143]. There are also several high resolution structures of Mn and FeSODs available from which meaningful comparisons can be made[1]. MnSOD from *E. coli* is dimeric, with subunit size of 22kDa (205 residues) and can thus be compared with the tetrameric MnSODs from *Thermus thermophilus* [109] and human mitochondria [134]. Moreover, since a high resolution crystal structure has been determined for FeSOD from *E. coli* [6], a direct comparison can be made between MnSOD and FeSOD from the same species to attempt to answer questions of metal-ion specificity and functional specificity with respect to interactions with DNA.

2.2. Structure determination

2.2.1. Purification

Mn superoxide dismutase was isolated from an *E. coli* strain (AB2463/pDT1-5) containing the sodA structural gene on an antibiotic-resistant plasmid [144]. MnSOD was purified as previously described [5] with the active-site metal ion in a redox heterogeneous form. The native enzyme was dialysed against water in preparation for crystallisation trials.

2.2.2. Crystallisation

Crystallisation trials were undertaken following previously published results [141]. Crystals were grown at room temperature using the hanging drop method. The hanging drops were suspended over 0.75 mL of well solution (16 - 30 % PEG 6000 and 0.05 M bicine titrated to pH 8.5) and consisted of 2 μL of well solution and 2 μL of protein solution (MnSOD at 12 mg/mL in water). Crystals were formed as needles or elongated blocks in space-group $C222_1$, with a = 100.72, b = 108.86, c = 181.87 Å. Crystals appeared after 1 - 3 days, the largest being approximately 0.2 mm x 0.2 mm x 0.6 mm.

1. *Thermus thermophilus* MnSOD (with azide bound), solved at 1.8 Å resolution, PDB ID: 1MNG [6]; *Homo sapiens* MnSOD (recombinant in *E. coli*), 2.2 Å, 1ABM [134]; *Escherichia coli* FeSOD (with azide bound), 1.8 Å, 1ISC [6]; *Mycobacterium tuberculosis* FeSOD, 2.0 Å, 1IDS [135].

The crystals have a faint magenta colour whose intensity varies with crystal volume, being more noticeable in larger crystals. Calculations based on the expected solvent content of protein crystals [145] gave a Matthews' coefficient, Vm, of 2.75 $Å^3$/Dalton (solvent content, Vsolv = 55 %) for a crystal having four SOD monomers in the asymmetric unit.

2.2.3. Data collection and processing

Native data were collected to a resolution of 1.9 Å at room temperature on a Rigaku R-Axis IIC image plate detector, using Cu-Kα radiation from a Rigaku RU-200B rotating anode generator. The native data set was collected from a single crystal over 30 hours after which the crystal began to deteriorate from radiation damage. The images were subsequently indexed and integrated to 2.0 Å using the program DENZO [146], and the program SCALEPACK [146] was used to scale and merge the resulting data.

A single image was indexed using the automatic peak-picking and auto-indexing facilities within DENZO. 1237 peaks between 40.0 and 2.5 Å resolution, and real-space vector lengths between 11.5 and 300 Å were used in auto-indexing. The highest symmetry lattice requiring the least distortion to match an equivalent symmetry restrained cell, was C centred orthorhombic. The metric tensor distortion index was 0.01 %, and the unrestrained cell was a = 100.86, b = 108.94, c = 182.11 Å, α = 89.99, β = 90.00, γ = 89.99º.

Detector and crystal parameters were then refined by the least-squares minimisation of the difference between the predicted and observed diffraction pattern. The crystal orientation and the position of the direct beam spot were first refined using only diffraction spots between 20 and 5.0 Å resolution. After convergence, the resolution was extended to 40 and 2.0 Å, and beam divergence and focusing (crossfire), image plate orientation, y scale, skew, cell and crystal to film distance were all refined. Appropriate spot shape, spot size, background box, mosaicity and profile fitting parameters were chosen and the detector and crystal parameters again refined to convergence. A circular region of the oscillation image corresponding to the beam stop shadow was ignored during processing. Correct indexing was confirmed by processing two further images, having phi angles 45 and 90º apart from the originally indexed image, using the same detector and crystal parameters. After all images were processed, the cell and mosaicity were post-refined in SCALEPACK. All images were then reprocessed with the cell fixed to that of the post-refined cell, and with the updated value for crystal mosaicity.

Scaling and merging of diffraction intensities were done using the program SCALEPACK. Initial scale factors and B-factors were calculated for each image, and the post-refined cell and mosaicity were reconfirmed. The value of χ^2 in each resolution bin was checked, and the values for the estimated errors in each resolution bin were adjusted

appropriately to improve the error model. Once the χ^2 values were approximately one, and therefore the error model most accurately reflected the actual errors in the data, reflections flagged as outliers were rejected. Multiple rounds of outlier rejection and rescaling were run until all outliers were removed from the data.

Table 2-1. Data collection and reduction statistics for native *E. coli* MnSOD[1]

Crystal	Native MnSOD, *E. coli*	Native MnSOD, *E. coli*
Space group	$C222_1$	$C222_1$
Z (Z')	32(4)	32(4)
Unit cell	*a*=100.718 Å	*a*=100.717 Å
	b=108.858 Å	*b*=108.857 Å
	c=181.869 Å	*c*=181.869 Å
V(m), Å^3/Da	2.77	2.77
Solvent content	55 %	55 %
Mosaicity	0.35º	0.35º
Data collection temperature	293 K	293 K
Data processing		
Resolution limits (of last shell)	50 - 2.1 Å (2.18 - 2.10)	40 - 2.0 Å (2.02 - 2.00)
Unique reflections	58757	67705
Observed reflections	324296	353625
Observed reflections after averaging	215051	234191
Observed reflections after averaging $I > 1\sigma_I$	212295	230617
Observed reflections after merging	56883	62514
Observations deleted manually	392	270
Redundancy	3.8	3.7
Completeness	96.8 % (77.0)	92.4 % (55.8)
R_{merge} on intensities[2]	0.056 (0.191)	0.059 (0.263)
Overall I/σ	22.0 (5.4)	20.0 (3.2)

[1.] The values in the first column of the table are those for the dataset used for the refinement, generating the coordinates in PDB ID: 1VEW, although by error the cell used for refinement was that previously reported (100.84,108.91,182.1Å) [79]. The values in the second column are those for a dataset processed from the same raw data but using the processing protocol described above.

[2.] $R_{merge} = \Sigma|I-\langle I\rangle|/\Sigma I$, where $\langle I\rangle$ is the mean of individual observations of intensities I.

The averaged intensities as output from SCALEPACK were converted to structure factor amplitudes using the procedure of French and Wilson [147] as encoded in the CCP4 program TRUNCATE [148]. Rather than simply taking the square-root of intensities, and setting any negative values to zero, the procedure of French and Wilson calculates a best

estimate of F from I, $\sigma(I)$, and the distribution of intensities in resolution shells. This has the effect of forcing all negative observations to be positive, and inflating the weakest reflections (less than about 3σ), because an observation significantly smaller than the average intensity is likely to be underestimated. TRUNCATE rejects reflections having intensities less than minus four standard deviations. The data were then put on an approximately absolute scale using the scale factor taken from a Wilson plot. Relevant data collection and processing statistics are given in Table 2-1 (opposite).

2.2.4. Structure solution

The structure was solved using molecular replacement. The structure of MnSOD from *T. thermophilus* solved to 1.8 Å [109] was used as a search model. MnSOD from *E. coli* and MnSOD from *T. thermophilus* share an amino-acid sequence identity of ~ 59 %. The search model dimer was modified by replacing all residues not conserved between the two amino-acid sequences with alanines. The program AMORE [149] was used to search for two copies of the dimeric search model, and a correct solution was found with a correlation coefficient of 0.44 and R-factor of 0.41 using data in the range 8 Å to 4 Å. Five cycles of rigid-body refinement were performed in TNT [130] using data in the range 10 Å to 3.1 Å, giving a starting R-factor for refinement of 0.456.

2.2.5. Model building and refinement

Refinement was carried out using the program TNT [130] by the method of restrained reciprocal space least-squares minimisation. Strict non-crystallographic symmetry (NCS) constraints were imposed on the four subunits of the asymmetric unit during the first stages of refinement. Poorly defined regions of the model were removed and rebuilt with the aid of the molecular modelling program TURBO-FRODO [150]. Several rounds of model building and refinement produced a model with an R-factor of 0.25 (R_{free} 0.26) at which time the NCS constraints were replaced with NCS restraints forcing similarity between the four molecules of the asymmetric unit. Further rounds of model building and refinement produced a model with 6528 protein atoms, 415 water molecules and four manganese ions. The R-factor is 0.188 (R_{free} 0.218) for 53872 reflections in the resolution range 50 to 2.1 Å. A bulk solvent correction, based on the scaling function suggested by Moews and Kretsinger [151], was applied to the low resolution terms using the program TNT [130]. Bond lengths and angles have RMS deviations of 0.011 Å and 1.2º, respectively, from the Engh and Huber target values [152]. Subsequent discussion is based upon the results of refinement using data to 2.1 Å (column one of Tables 2-1 and 2-2).

Table 2-2. Refinement and model statistics for native *E. coli* MnSOD[1]

Model		
PDB ID	1VEW	-
No. of residues	820	820
No. of protein atoms	6532	6512
No. of water molecules	415	411
No. of manganese ions	4	4
Average B-factors, Å^2		
Main-chain atoms	31.2	23.0
Side-chain atoms	35.7	23.9
Water molecules	47.9	31.7
Manganese ions	21.8	13.7
Overall	34.3	23.9
Refinement		
Refinement program	TNT [130]	CNS v0.5 [131]
Reflections used in refinement (no $I/\sigma(I)$ cutoff)	53872	59340
Reflections used in calculation of R_{free}	2873 (5.3 %)	3156 (5.3 %)
Resolution limits	50.0 - 2.1 Å	40.0 - 2.0 Å
RMS bond lengths	0.011 Å	0.005 Å
RMS bond angles	1.2º	1.2º
R-factor (all data)	0.188	0.176
R_{free} (all data)	0.218	0.197

[1] Columns of refinement and model statistics correspond with equivalent columns of data collection and reduction statistics in Table 2-1.

2.3. Structure description and discussion

2.3.1. Model validation

Details of the final model are given in Table 2-2. Of the 820 residues, 21 had sidechains which could not be suitably modelled due to poor electron density. In all four subunits, positions for Glu47, Asn50, Lys137, Lys186 and Lys205 sidechains were poorly defined as was Asp61 in subunit B. The electron density at the apex of the loop between the first two helices, A1 and A2, is also not well defined, especially around Pro52. Some disorder was apparent but could not be satisfactorily modelled. Almost 92 % of all residues fall within the sterically most favoured regions of a Ramachandran plot, as defined in PROCHECK [153]. Both Asn145 and Gln178 have normally disallowed phi and psi angles in each of the four subunits. Asn145 is the i+1 residue in a type II'(εα) β-turn (residues 144

- 147) between the β-strands B2 and B3. This β-turn includes the active-site residue Gln146. Likewise, Gln178 is the *i*+1 residue in another type II'(εα) β-turn (residues 177 - 180) which is positioned just before helix A5. Type II'(εα) β-turns that have (ϕ,ψ) angles around (60º,-120º) for the *i*+1 residue are relatively uncommon. In a study of β-turn types in proteins, only 3 % were found to be type II'(εα) β-turns [154]. The Asn146 εα β-turn is structurally conserved amongst the five Mn and Fe SOD structures from different species for which model coordinates are currently available, with the exception of the Ramachandrally challenged *Pseudomonas ovalis* FeSOD (PDB ID: 3SDP). The Gln178 εα β-turn is not strictly structurally conserved, however, with MnSOD from *Bacillus stearothermophilus* having a different combination of β-turns in this region.

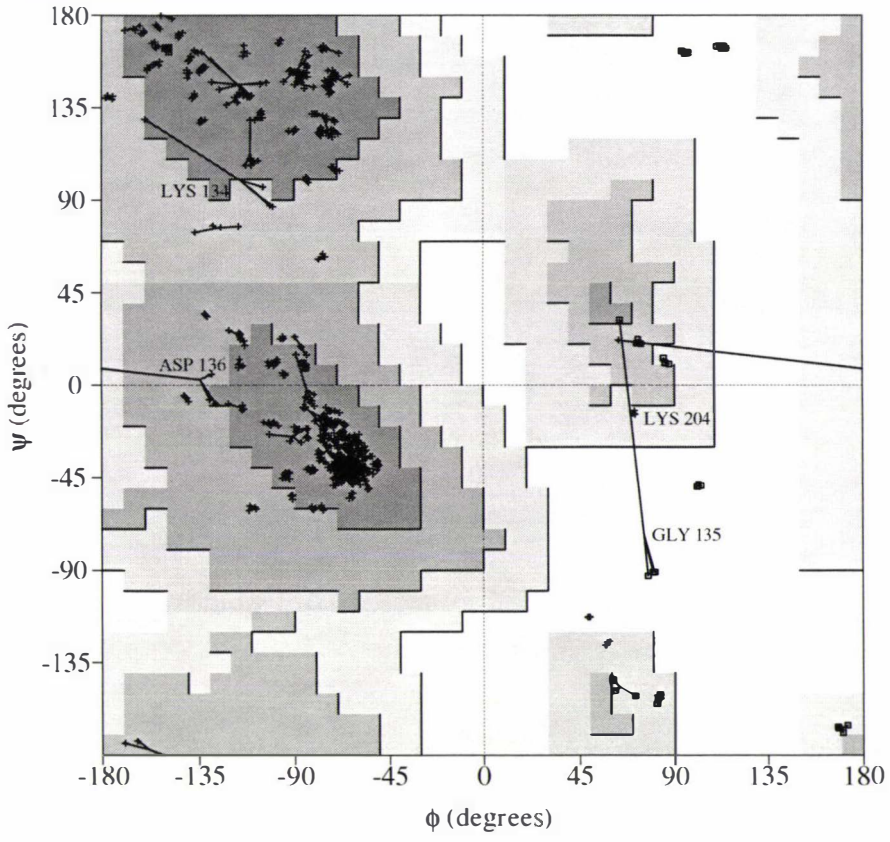

Figure 2-1. Multiple Ramachandran plot for native *E. coli* MnSOD

Ramachandran plots for each of the four subunits are shown superimposed on, and linked by solid lines to, the average Ramachandran plot for all four subunits. This has the effect of immediately highlighting any residues that have outlying phi or psi angles.

Several methods have been proposed [155] for assessing the similarity of NCS-related molecules to determine whether the differences between the molecules are truly signifi-

cant or artefacts of the building and refinement processes. Figure 2-1 (above) shows a multiple Ramachandran plot of all four subunits, and Table 2-3 gives the RMS deviations of mainchain and all atoms between the four subunits. Both the Ramachandran plot and the RMS deviations show that the four subunits of the asymmetric unit are essentially identical. The only significant difference among the subunits occurs in chain A for residues Lys134, Gly135 and Asp136. These residues form the loop between β-strands B1 and B2. The loop is distorted in chain A to provide a weak intermolecular crystal contact between the two dimers of the asymmetric unit with three hydrogen bonds being formed between subunit A of dimer 1 and subunit D of dimer 2. The RMS differences between main-chain atoms in a pairwise comparison range between 0.11 and 0.30 Å; between all atoms the values are 0.32 and 0.43 Å (see Table 2-3).

Table 2-3. RMS superpositions for subunits of native *E. coli* MnSOD[1]

	A	B	C	D
A	-	0.308	0.258	0.264
B	0.447	-	0.110	0.130
C	0.371	0.318	-	0.115
D	0.450	0.339	0.382	-

[1.] RMS superpositions of main-chain (above the diagonal) and all atoms (below the diagonal) of A, B, C and D subunits (Å).

2.3.2. Polypeptide chain conformation

The monomeric subunit of MnSOD from *E. coli* has 205 amino acids and a molecular weight of 22.9 kDa [4]. The overall tertiary structure is as found for the other Mn and Fe SODs whose structures have been characterised, with an all-α N-terminal domain and an α/β C-terminal domain. The MnSOD dimer is shown as a Cα plot in Figure 2-2 (opposite) and a schematic diagram of the monomer is shown in Figure 1-3. The Mn ion at the active site is bound between the two domains. The assignment of all secondary structure elements was done using the program DSSP [132] and these secondary structures can be seen in Figure 1-3.

The N-terminal domain has two long anti-parallel α-helices (A1, A2) having 23 and 22 residues respectively, which are connected by an extended loop region. The loop contains two one-turn α-helices and a one-turn 3_{10}-helix. A 19-residue N-terminal arm lies anti-parallel to helix A1. The C-terminal domain consists of two α-helices (A3, A4), followed by a central core of three strands of twisted anti-parallel β-sheet (B1, B2, B3), followed by two more α-helices (A5, A6). The four α-helices of this α/β domain lie on one

side of the β-sheet, with the other side of the β-sheet facing the N-terminal domain. Sidechains from this β-sheet thus contribute both to the hydrophobic core of the C-terminal domain and to the active-site and interdomain interface. The loop regions connecting the β-strands also contains two short (one-turn) α-helices and two 3_{10} -type turns.

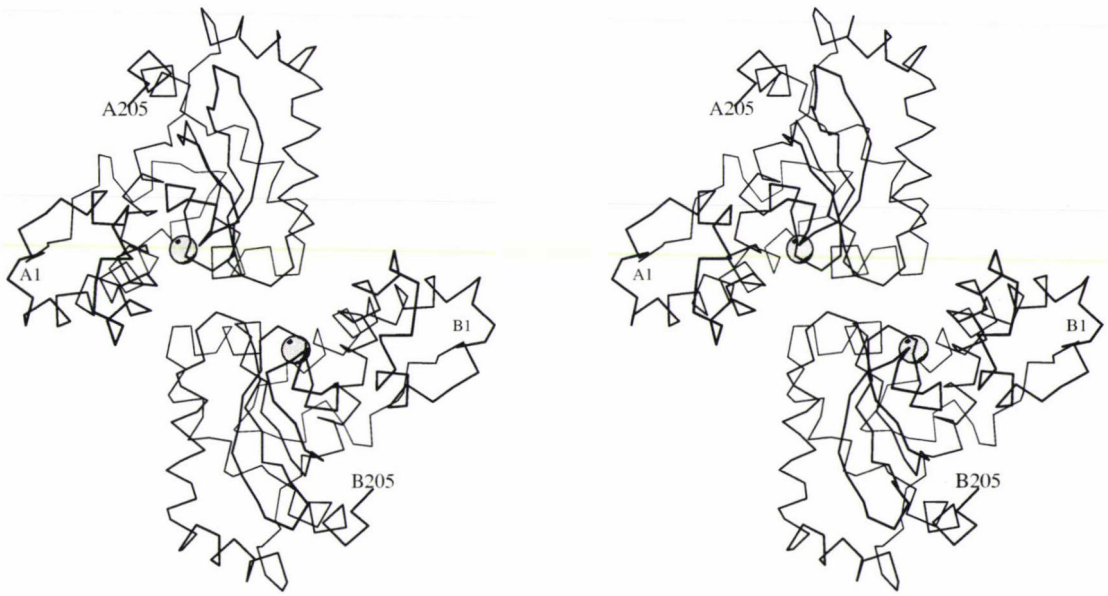

Figure 2-2. Stereo Cα plot for the native *E. coli* MnSOD dimer

The plot shows the polypeptide folding and the close proximity of the two active-sites in the dimer. The manganese atoms are shown as large shaded circles. Figure drawn with MOLSCRIPT [1].

The N-terminal arm lies anti-parallel to and forms various hydrogen bonds with helix A1. The sidechains of Asn39 at one end, His27 in the middle and Glu15, Asp19 and Thr22 at the other end are prominent in these interactions. Two proline residues in the N-terminal arm have unusual configurations. Pro8 has ϕ,ψ angles (-90º,20º) that depart from those usually expected for proline residues (ϕ ~ -65º; [156]), possibly because this residue, in all four subunits, makes close intermolecular symmetry contacts; these may impose steric constraints. Pro16 is preceded by a *cis*-peptide. This is a feature of all other MnSODs and FeSODs whose structures have been solved to date.

A characteristic distortion is found in the middle of helix A1 in all Mn and FeSODs, which involves widening of one turn to a π-type configuration. In *E. coli* MnSOD this distortion is centred on Lys29, which has ϕ,ψ angles (-110º,-60º), and creates a slight kink in the helix (the axes of the N- and C-terminal halves are at an angle of 176º) and a

displacement of the C-terminal half by approximately 2 Å towards the manganese centre. It is of critical importance to the active site as the active-site residues His26 and Tyr34 lie on either side of the distortion and His30 is in the middle.

The loop region (residues 43 - 64) between helices A1 and A2 has a primary structure that is highly variable amongst Fe and MnSOD species. The entire loop region folds over at the ends of A1 and A2 and lies alongside this α-helical pair on the opposite side to the active-site. There are two distinct conformations of this loop region amongst Fe and Mn SODs. Human mitochondrial MnSOD (PDB ID: 1ABM) and MnSOD from *M. tuberculosis* (PDB ID: 1IDS) have a short connecting loop of three and six residues respectively. FeSOD from *E. coli* (PDB ID: 1ISA) and MnSOD from *T. thermophilus* (PDB ID: 3MDS) have an extended loop region, the extension arising from the shortening of the two α-helices in the α-helical pair. MnSOD from *E. coli* has a similar extended loop region.

2.3.3. Quaternary structure

The crystals of *E. coli* MnSOD contain two dimers in the asymmetric unit. The buried surface area between the two subunits that comprise the MnSOD dimer is 850 $Å^2$ per subunit. Relative to the surface area of an isolated subunit (9600 $Å^2$), the fraction buried (9 %) is typical of strongly associated dimers [157]. The buried surface area involved in the crystal packing contact between the two dimers in the asymmetric unit is, by contrast, only 430 $Å^2$.

The program ASC [158, 159] was used to calculate the solvent-accessible surface area of residues firstly as a part of each subunit within the dimer, and secondly as part of the dimer as a whole. For point of comparison with the FeSOD, residues whose surface area decreased by more than 1.5 $Å^2$ upon dimerisation were taken to be a part of the dimer interface. A total of 19 residues fits this criterion in *E. coli* MnSOD, i.e. Gln21, Ile25, Lys29, His30, Tyr34, Asn73, Asn74, Phe124, Gly125, Ser126, Asn145, Gln146, Trp169, Glu170, His171, Tyr174, Leu175, Gln178 and Asn179. Interface residues for both *E. coli* Mn and FeSOD, along with their values for the decrease in surface area upon dimerisation, are given in Appendix B. Most of the contacts between the two monomers of the dimer are hydrophobic, and residues Asn73 and Phe124 form an amino/aromatic stacking type interaction across the dimer interface; the sp^2 N ... ring carbon distance is about 3.6 Å. However, there are also a small number of direct hydrogen bonds between protein atoms, across the dimer interface, and other hydrogen bonding interactions mediated by bridging water molecules.

The list of hydrogen bonds between the two monomers (Table 2-4 opposite) highlights one remarkable feature of the MnSOD dimer. This is the extent to which the active site is

linked with dimerisation. Among the residues of the dimer interface are five active-site-associated residues, i.e. His30, Tyr34, Glu170, His171 and Tyr174. Moreover, of the seven sidechain-sidechain hydrogen bonds across the dimer interface, three of the four unique bonds (the others are related by the non-crystallographic symmetry of the dimer) involve active-site residues, i.e. His30_NE2...Tyr174B_OH, His171_N...Glu170B_OE1 and His171_ND1...Glu170B_OE2. Exactly the same contacts are seen in the interface between the C and D subunits.

Table 2-4. Hydrogen bonding interactions in the dimer interfaces of Mn and FeSODs from *E. coli*[1]

MnSOD *E. coli*					FeSOD *E. coli*				
Residue (chain A)	Atom	Residue (chain B)	Atom	Dist (Å)	Residue (chain A)	Atom	Residue (chain B)	Atom	Dist. (Å)
His30	NE2	Tyr174	OH	2.59	His30	NE2	Tyr163	OH	2.70
His171	N	Glu170	OE1	2.90	His160	N	Glu159	OE1	3.02
His171	ND1	Glu170	OE2	2.79	His160	ND1	Glu159	OE2	2.88
Ser126	OG	Ser126	OG	2.83	Ser120	OG	Ser120	OG	2.76
Asn73		Phe124	Ar-ring	3.6	Asn65		Phe124	Ar-ring	3.7
Gln 178		No equivalent bond			Arg167	NH2	Glu21	OE2	2.88

[1]. There are no main-chain to main-chain hydrogen bonds across the interface.

2.3.4. The active site

The active site containing the catalytic manganese ion lies between the two domains in a substantially hydrophobic pocket which is characterised by a large number of aromatic sidechains. The four ligands which coordinate the manganese ion are invariant amongst Fe and MnSOD species. Two ligands are provided by each domain. The N-terminal domain provides His26 (in helix A1 below the kink) and His81 (in helix A2) both coordinated *via* their NE2 nitrogen. The C-terminal domain provides Asp167 (at the C-terminal end of B3) coordinated *via* its OD2 oxygen and His171 (in the 1-turn, 3_{10}-helix after B3) coordinated *via* its NE2 nitrogen. Additional density associated with the metal ion was interpreted as a solvent molecule bound to the manganese. When this was included in the model as an oxygen atom it refined to a value of 16 $Å^2$, comparable with the B-factors of the other ligands, which range between 15 and 25 $Å^2$. This is consistent with a full-occupancy water or hydroxide ion bound to manganese; given that the net charge of the other four ligands (3 His, 1Asp) is almost certainly 1-, it appears likely that it is a hydroxide ion that is bound to the Mn(III). The B-factor of the manganese ion (22 $Å^2$) implies that this site, too, is fully-occupied. The observed Mn-O separation of 2.24 Å is

consistent with a mixture of Mn(III)-OH and Mn(II)-OH moieties, the latter being favoured over an Mn(II)-OH_2 moiety due to the basic conditions for crystallisation (pH 8.5) and the hydrogen bonds made by this coordinated solvent species (see below). Moreover, the difference electron density for this site is spherical, indicating a relatively small difference between Mn(III)-O and Mn(II)-O separations.

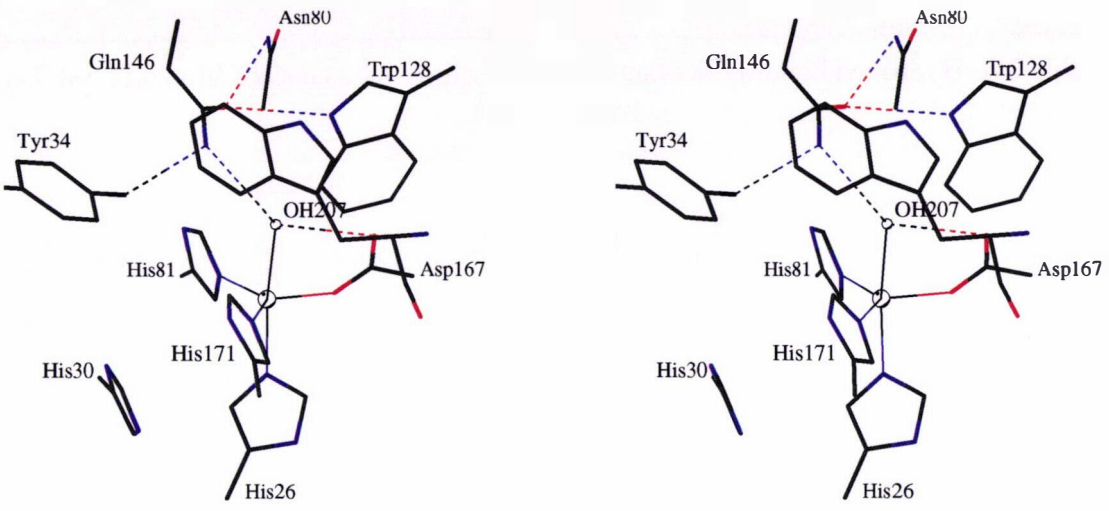

Figure 2-3. Stereo view of the metal site in native *E. coli* MnSOD

Stereo view of the metal site in MnSOD, showing the manganese coordination and the network of geometrically-favourable hydrogen bonds (broken lines) linking Gln146 and the metal-bound solvent molecule (filled circle). Covalent bonds formed with the manganese ion are, Mn-His26_NE2 2.19 Å; Mn-His81_NE2 2.25 Å; Mn-Asp167_OD2 2.05 Å; Mn-His171_NE2 2.19 Å; Mn-Ow207_O 2.24 Å. Hydrogen bond lengths are, OH207_O ... Asp167_OD1 2.75 Å; OH207_O ... Gln146_NE2 2.89 Å; Tyr34_OH ... Gln146_NE2 3.00 Å, Gln146_OE1 ... Asn80_ND2 3.33 Å; Gln146_OE1 ... Trp128_NE1 2.93 Å. Figure drawn with MOLSCRIPT [1].

Spectroscopic studies of *E. coli* MnSOD suggest a distorted trigonal bi-pyramidal environment around the Mn ion [5]. This is confirmed by the structural analysis, which clearly shows a five-coordinate manganese centre, with no suggestion of any low-occupancy six-coordinate species (Figure 2-3). The two axial ligands are His26_NE2 and Ow207, with the equatorial plane formed by His81_NE2, Asp167_OD2 and His171_NE2. The bond lengths and angles show a high degree of regularity in the geometry, with the His26_NE2-Mn-OW207 angle (175°) very close to the ideal 180°, and the Mn only 0.05 Å out of the equatorial plane, in the direction of His26. The principal distortion is in the equatorial plane, with the angle His81_NE2-Mn-NE2_His171 expanded to 129° (from the ideal 120°) and the angle His81_NE2-Mn-OD2_Asp167 reduced to

110°. This is a common feature of all Mn and FeSOD metal sites, and helps create an open face in the coordination sphere where N_3^- (and possibly O_2^-) may bind [6].

The ligands are for the most part tightly constrained by the surrounding structure. The non-coordinated ND1 atoms of His81 and His171 are hydrogen bonded respectively to Arg77_O (from the preceding turn of helix A2) and Glu170_OE2 (from the *other* subunit of the MnSOD dimer). The non-coordinating carboxylate oxygen of Asp167, OD1, is an acceptor of two hydrogen bonds, one from the metal-bound solvent molecule Ow207 (2.75 Å) and the other from the peptide NH of residue Trp169 (3.26 Å) in an n...NH(n+2) interaction (Figure 2-3 opposite), also known as an "Asx turn" [160, 161]. Only the His26 ligand is not directly constrained by any protein group, its ND1 atom being hydrogen bonded to a buried solvent molecule, Ow261, that is found to be conserved in most Mn or FeSOD structures.

The metal-bound solvent molecule (water or hydroxide) is firmly fixed in place by two hydrogen bonds, (Figure 2-3 opposite). It is the donor in the hydrogen bond with Asp167_OD1 and an acceptor of a hydrogen bond from NE2 of Gln146. Both hydrogen bonds are geometrically favourable with respect to length, 2.75 Å and 2.89 Å respectively, and angles; the N-H...O angle for the Gln146_NE2...Ow207 interaction is 159° (assuming trigonal geometry for the $-NH_2$ group of Gln146) and the Mn-Ow207...OD1_Asp167 angle is 85°, reasonably close to the tetrahedral angle of 109.5°. This implies that this bond is also approximately linear.

The hydrogen bonding network extends further from the metal-bound solvent through Gln146, which is also hydrogen bonded through NE2 to Tyr34_OH and through OE1 to Asn80_ND2 and Trp128_NE1. This emphasises the key role of Gln146 in the active site; its hydrogen bond potential is fully utilised and it appears firmly fixed in place. This in turn is consistent with the idea [6] that the metal-bound solvent is not displaced during catalysis.

The importance of a sidechain that can hydrogen bond with the coordinated solvent molecule is also evident from comparisons of both Mn and FeSODs. This sidechain (Gln146 in *E. coli* MnSOD) is, however, provided from a different position in the structure depending on the species. In the structures solved to date, the following pattern is observed. In MnSODs the residue occupying the position equivalent to Gln146 is always either a glutamine or a histidine, and the residue at the position equivalent to Gly77 is always a glycine. In FeSODs the position equivalent to Gln146 is either a histidine or an alanine, in which case the residue at the position equivalent to Gly77 is a glycine or glutamine, respectively. In this way a hydrogen bonding sidechain group is always structurally conserved, occupying a position within hydrogen bonding distance of the coordinated solvent water.

2.3.5. The wider active-site region

The residues making up the secondary coordination sphere were identified by measuring the increase in solvent-accessible surface area of residues around the active-site upon removal of the metal ion, ligated solvent molecule and ligand sidechains. The active-site pocket consists of 11 main residues (His30, His31, Tyr34, Gly77, Phe84, Trp85, Trp128, Gln146, Trp169, Ala172, Glu170B) and includes two waters (Ow261 and Ow1721) in addition to the metal ligands. Of these 11 residues, four (His30, Tyr34, Trp128, Glu170) are completely invariant and three (His31, Trp85, Trp169) are semi-invariant, having only one exception among the more than 50 sequences of Fe and MnSODs that were compared. The two waters in the active-site pocket are also conserved in the three MnSOD structures (*E. coli, T. thermophilus, Homo sapiens*), in the FeSOD from *M. tuberculosis*, and in the Fe/Mn cambialistic SOD (*Propionibacterium shermanii)*, but not in FeSOD from *E. coli*. Almost 60 % of the surface area of the active-site pocket is provided by non-polar, hydrophobic residues.

2.3.6. Solvent regions adjoining the active site

Most of the modelled solvent forms a monolayer around the protein surface. Two solvent regions deserve special mention, however. The first is the solvent-filled funnel that leads from the outside towards the manganese site of each monomer, and the other is an internal network of water molecules that lies behind the metal site starting at the ligand His26.

The funnel by which O_2^- could reach the metal centre has been described in detail for the MnSOD of *T. thermophilus* [109]. For each metal site the funnel is formed by residues from *both* monomers and leads towards the metal-bound solvent molecule. Thus, in *E. coli* MnSOD access to the metal centre of monomer A is *via* a funnel bounded by residues Asn37A, Asn73A, Asn74A, Phe124B, Asn179B and Arg181B at the entry, and residues His30A, Tyr34A, Trp169A and Glu170B nearer to the metal. Two hydrogen-bonding groups project into the funnel in a position where they could interact with incoming substrate, i.e. His30_ND1 and Tyr34_OH. His30 is oriented by a hydrogen bond with Tyr174_OH from monomer B, and Tyr34 is oriented by a hydrogen bond with Gln146; Tyr34 stretches across the funnel, its OH pointing directly at the aromatic ring of Trp169 and has been called a 'gateway' residue [162] because it is presumed to have to move to allow access to the metal site [118, 109]. The funnel is filled with some 17 solvent molecules (see Figure 2-4 opposite). Many of these have relatively high B-factors, implying mobility. However, three waters, Ow1251, Ow341 (which forms a hydrogen bond with the conserved Tyr34), and Ow1731, make multiple hydrogen bonds. This is reflected in their having B-factors considerably lower than the average.

On the inner side of the manganese, *trans* to the metal-bound solvent molecule, is another water cluster which lies between the N- and C-terminal domains. This begins at water Ow261, which is hydrogen bonded to ND1 of the ligand, His26. This water and its neighbour Ow1721 are in a hydrophobic pocket bounded by Phe18, Phe84 and Trp184, and do not use their full hydrogen bonding potential; Ow261 hydrogen bonds with His26_ND1, Met23_SD and Ow1721, and Ow1721 hydrogen bonds only with Ow261 and Ala172_O. These two waters appear to be a conserved feature of MnSODs. Beyond Ow1721 are found more buried waters, Ow191, Ow193, Ow1711 and Ow1741B which are more extensively hydrogen bonded, with three or four hydrogen bonds each to residues from both domains. These waters do not seem to have a functional significance except in so far as they contribute substantially to interdomain interactions.

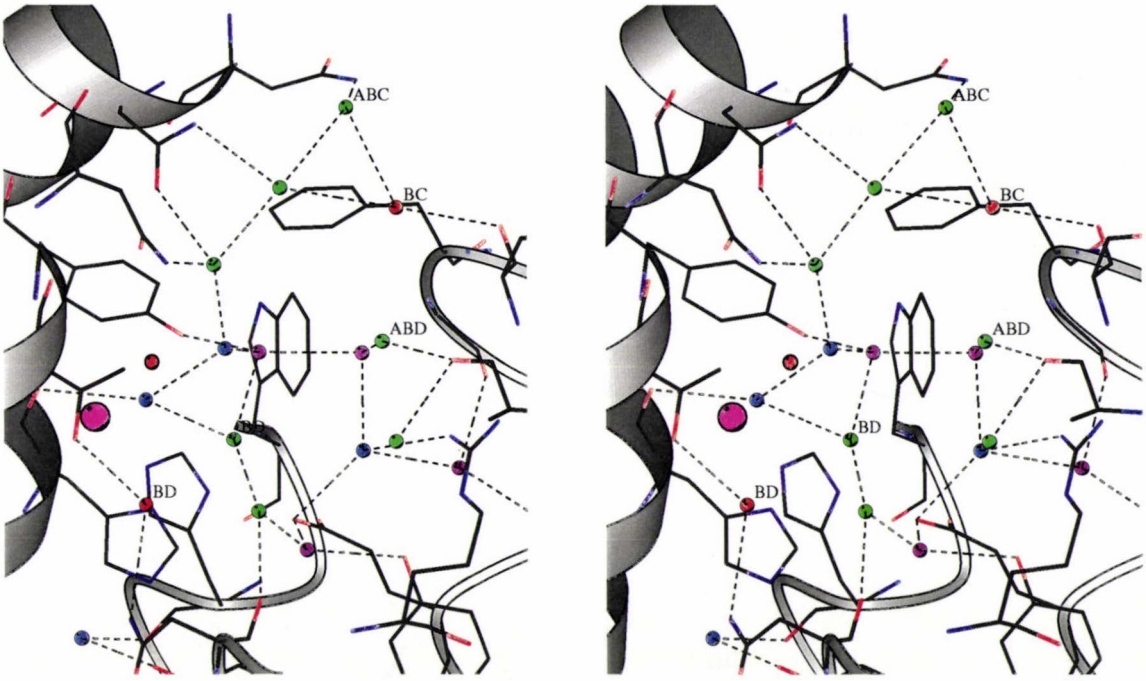

Figure 2-4. Stereodiagram of the solvent structure in the substrate-access funnel of MnSOD from *E. coli*

The 17 waters in the substrate-access funnel of the native structure are coloured by B-factor. B < 20 Å^2, purple; 20 - 30 Å^2, blue; 31 - 39 Å^2, green; > 40 Å^2, red. The average B for solvents in the protein is 32 Å^2, and for the 17 waters in the substrate-access funnel, 30 Å^2. The larger purple-shaded sphere represents the Mn atom. Some active-site ligands have been excluded for clarity. The ligated solvent OH207 is drawn as a smaller red sphere. Figure drawn with MOLSCRIPT [1].

2.3.7. The significance of the dimer

A striking feature of the MnSOD structure shared by all Mn and FeSODs is the extent to

which the active site of each monomer is linked with formation of a functional dimer. The dimer contributes a number of elements to the active-site. First, residues from both monomers are required in order to create the solvent-filled funnel through which the substrate is presumed to approach the metal site (see above). Second, His30, which is a 'gateway' residue projecting into the active-site funnel just above the metal site, and which may play an important role either as a proton donor/acceptor or in orienting the incoming substrate, is oriented by a hydrogen bond with Tyr174 from the other monomer of the dimer, as described above.

The third feature of the dimer is the bridge involving Glu170 which provides a connection between the two metal sites of the dimer [137]. The Mn...Mn distance is relatively long (18.4 Å) for communication between them. However, Glu170 of one monomer is hydrogen bonded to the manganese ligand, His171, of the other monomer; one carboxylate oxygen, OE1, is hydrogen bonded to the peptide NH of His171 and the other carboxylate oxygen, OE2, hydrogen bonds with ND1 of His171. This gives a three-residue bridge comprising 17 bonds that link one manganese to the other (Figure 2-5). Moreover, it is a double bridge because of the twofold symmetry of the dimer.

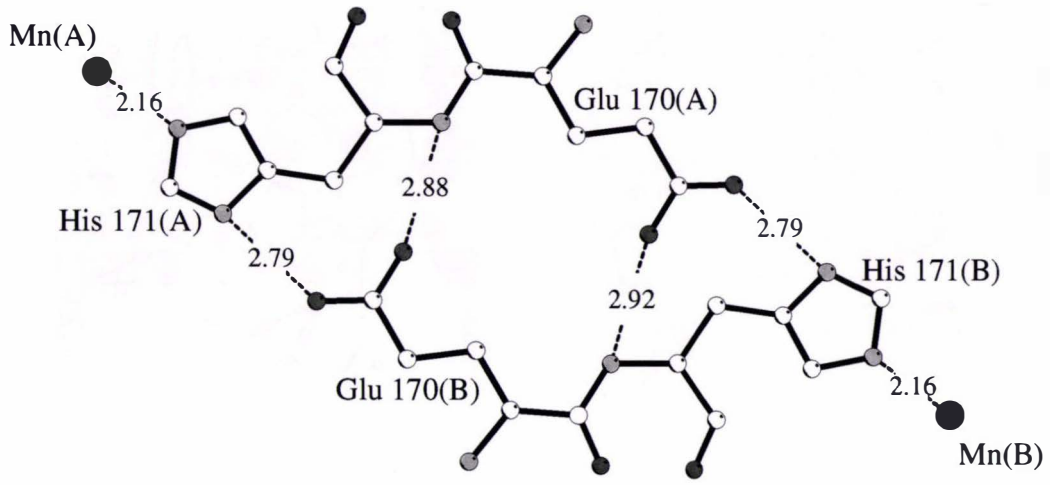

Figure 2-5. Glutamate bridge linking the two active sites of the MnSOD dimer

A schematic diagram of the 17-bond, three-residue, glutamate bridge linking the two active-sites of the MnSOD dimer. Hydrogen bonds are shown with broken lines.

Both Glu170 and His171 are absolutely conserved in all Mn and FeSODs, and this double glutamate bridge is thus likely to be a conserved structural feature. It may play a role in communicating between the two metal sites, either in communicating the redox or ligand-binding state of the metal centres, or in providing a pathway for electron transfer

between them, permitting recovery from oxidative damage when the metal is oxidised to a higher oxidation state, e.g. Mn(IV). A through-bond electron transfer pathway of this length is fully compatible with present ideas of electron transfer mechanisms [163].

2.3.8. Comparison with *E. coli* FeSOD

The availability of 3D structures for both MnSOD and FeSOD from *E. coli* allows comparisons to be made which may give insight into the different *in vivo* roles that these two enzymes play. Analysis of their secondary structures shows that the main secondary

Figure 2-6. A structure-based sequence alignment of *E. coli* manganese and iron superoxide dismutases

Residues absolutely conserved amongst Fe and MnSODs are shown in bold typeface. Secondary structure elements as calculated using the program DSSP [132] are shaded. Light shading, 3_{10}-helix; Medium-shading, α-helix; Dark shading, β-strands. Sequence insertions are indicated by a period (.). Insertions whose insertion points are ambiguous (~ 2 Å cutoff) are indicated by a tilde (~).

structural units and topology are highly conserved. This then allows the structures to be superimposed and a structure-based sequence comparison to be made (Figure 2-6 above). The Fe and Mn enzymes from *E. coli* share 45 % sequence identity based on this structural alignment.

A superposition of the structures based on the main-chain atoms (N, CA, C, O) of the conserved secondary structure elements, together with the active-site residues, gives an RMS difference of 0.6 Å (388 atoms) for superpositions of the monomeric chains. An almost identical RMS difference of 0.7 Å (776 atoms) is obtained for the superposition of the dimers. There is, therefore, no significant difference in the orientations of the monomers within the dimer between the Mn and Fe structures. Four areas of the polypeptide backbone deviate significantly, all of them in loop or turn regions. All the sequence insertions and deletions between the 205-amino acid MnSOD and 192-amino acid FeSOD are within these four areas. Residues 133 - 136 contain a single amino acid deletion in MnSOD relative to FeSOD with these four residues forming a type IV β-turn on the surface of the MnSOD enzyme (except for chain A which is distorted to a type I'(γγ) β-turn due to the dimer-dimer crystal packing contact). Residues 90 - 93 contain a two amino-acid deletion in MnSOD relative to FeSOD and, like the 133 - 136 region, this region is on the surface of the protein, well away from both the active-site and the dimer-dimer interface. The more significant differences occur in the regions 45 - 69 and 153 - 158. Residues 45 to 69 form part of the major loop region between A1 and A2. The loop in MnSOD has a seven-residue insertion (residues 61 - 67) relative to FeSOD. These residues form an extra loop which projects out from the surface and into the large hemicylindrical groove in the dimer formed between the two monomers. Residues 153 - 158 lie in the loop between B2 and B3 and contain a six-residue insertion relative to FeSOD. These extra residues also project out into the dimer groove, and because of the symmetrical nature of the dimer these two extra loops are present on both sides of the dimer groove (Figure 2-7 opposite). The sidechains in the loop 153 - 158 constrict the diameter of the hemicylindrical groove to around 14 Å. The sidechains of the positively charged residues Arg72, Lys118 and Arg123 form part of the surface of the dimer groove. In FeSOD the corresponding residues are Phe, Asp and Asn.

E. coli MnSOD has been shown [142] to bind non-specifically to various single- and double-stranded oligonucleotides with K_d in the range 1.5 - 1.8 μM. In contrast, interactions between FeSOD and the same oligonucleotides were much weaker with binding constants K_d > 40 - 220 μM. Given the markedly different surface properties in the dimer groove of MnSOD as compared with FeSOD illustrated in Figure 2-7 (opposite), it seems reasonable to suggest that the binding of DNA might occur within this region. There are a number of points favourable to the binding of DNA to MnSOD which are not emulated in FeSOD. The electrostatic potential at the surface of the dimer groove, as cal-

culated and viewed using the program GRASP [133], shows the MnSOD surface has an overall positive charge in the dimer groove (Figure 2-7a) whereas FeSOD has an overall negative charge (Figure 2-7b).

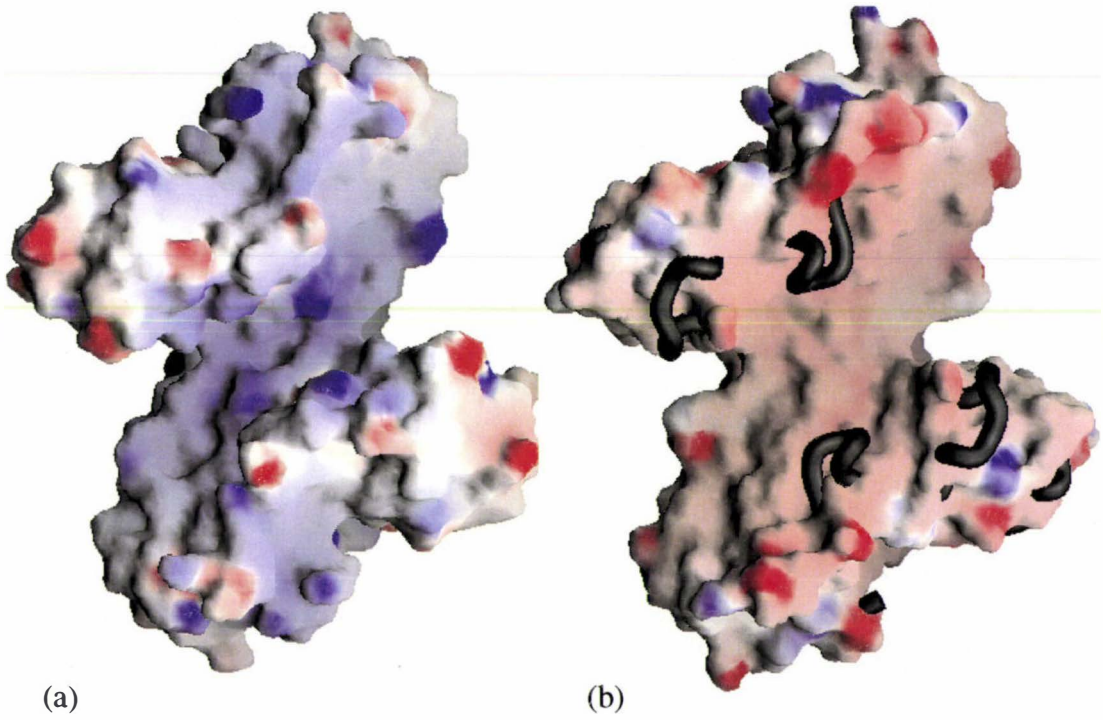

Figure 2-7. Surface comparisons of the *E. coli* FeSOD and MnSOD dimers

Comparison of the surfaces of the *E. coli* FeSOD and MnSOD dimers shaded according to electrostatic potential in the range -15 k_BT (red) to 15 k_BT (blue) (where k_B is the Boltzmann constant and T is the absolute temperature). In (a) the MnSOD surface is shown. In (b) the FeSOD surface is shown, with the MnSOD dimer superimposed on it; the four extra loops present in MnSOD (black) are shown as a Cα backbone worm, protruding on either side of the dimer groove. Note the positive charge of the MnSOD dimer surface (blue), compared to the negative charge of the corresponding FeSOD surface (red). Diagrams produced with GRASP [133].

A model for the interaction of standard B-DNA with the dimer groove of MnSOD is illustrated in Figure 2-8 (below). The two-fold axes of the dimer and duplex are approximately coincident. A total of ~ 3000 $Å^2$ of surface is buried by this interaction. Even without optimisation there are no unnaturally close contacts between the two molecules. In this model non-specific enzyme-DNA interactions are mediated *via* the positively charged residues on the surface of the dimer groove, and the negatively charged phosphates of the DNA. Additionally, the insertions in the sequence of MnSOD (relative to FeSOD) provide protrusions from the surface which are suitably placed for interacting

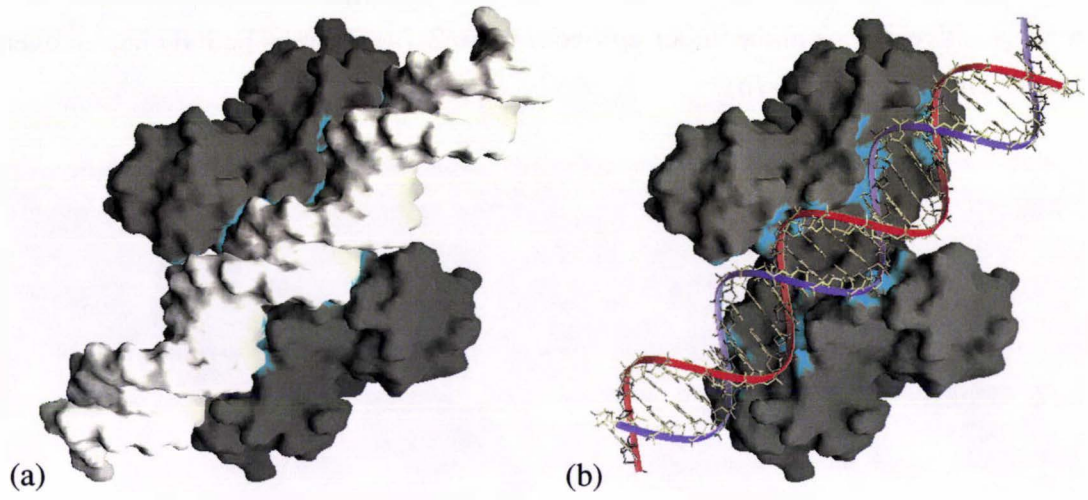

Figure 2-8. A model of the interaction of standard B-DNA with the dimer groove of native *E. coli* MnSOD

A surface representation of a model of the interaction of standard B-DNA with the dimer groove of MnSOD. The two-fold axes of the dimer and duplex are approximately coincident, and pass through the centre of the enzyme, perpendicular to the plane of the figure. The B-DNA model is shown in (a) as a solvent-accessible surface shaded in grey, and in (b) without the surface showing the underlying B-DNA structure. Areas of contact between the two surfaces within ~ 1 Å are highlighted in light blue. Diagrams produced with GRASP [133].

with the major grooves of DNA. Physical access to the active site is unimpeded by the binding of DNA, although there may be electrostatic consequences on superoxide-dismutase activity arising from proximity of the active site to the negatively charged DNA moiety. Other possible DNA-binding sites exist, but offer less extensive interactions with the protein. For example, DNA need not necessarily bind exactly parallel with the symmetrical dimer groove. The other region on the MnSOD surface of localised positive charge occurs at the C-terminus where three of the last six residues are positively charged; however, the number of possible interactions at this site is much less when compared to the number of interactions afforded by binding in the dimer groove. The MnSODs from human mitochondria and *T. thermophilus* also have a similarly positively charged dimer groove and DNA can be modelled into the dimer groove of MnSOD from *T. thermophilus* with only minor distortion of the DNA from its standard geometry. As structurally characterised, however, both human mitochondrial and *T. thermophilus* MnSODs are tetrameric. Within the tetrameric association, the dimer grooves face toward each other forming a tunnel. The tunnel has insufficient space for a double-stranded oligonucleotide without substantial rearrangement of the tetrameric structure. Thus, should tetrameric MnSODs also have a functional role in binding DNA by non-specific association, the binding would have to be at a site other than along the dimer

groove, or the functional unit would need to be dimeric.

Comparison of the active sites of the *E. coli* Mn and FeSODs shows a very high structural correspondence, confirming the view that their metal-ion specificity is more of a subtle chernical or electrostatic phenomenon than a distinct structural change [138, 162]. Superposition of the immediate metal sites (metal ions and ligands, 40 atoms) gives an RMS deviation of 0.2 Å, with the only significant difference being a slight rotation (11°) of the sidechain of His26, about its CB-CG bond (see Figure 2-9). This does not change the position of the coordinated NE2, relative to the metal, and so does not change the basic metal geometry, but could change M-N $d\pi$-$p\pi$ interactions. The slight movement is probably due to repulsion by the nearby Trp77 in FeSOD which is itself shifted relative to the equivalent residue (Trp85) in MnSOD.

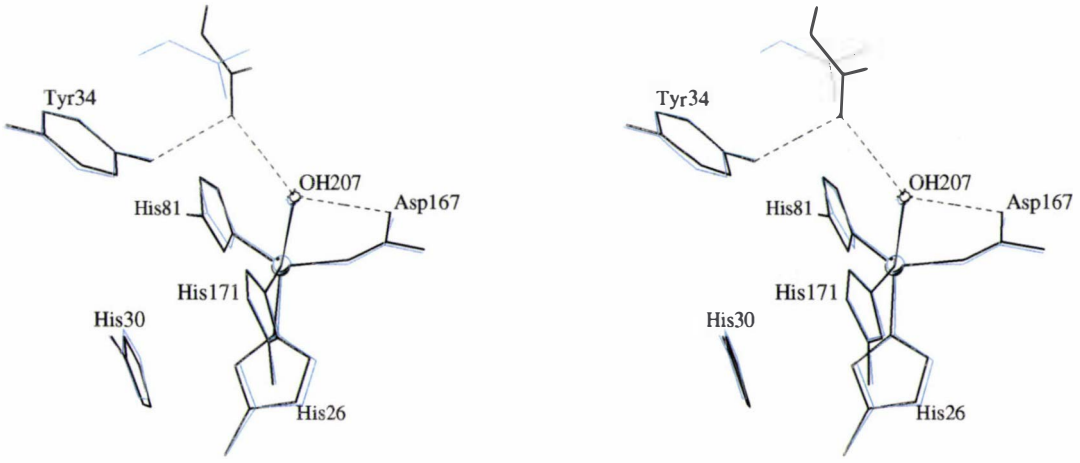

Figure 2-9. Stereodiagram of the metal environment of native MnSOD and FeSOD from *E. coli*

MnSOD in black lines and FeSOD in blue lines. Respectively, the axial angles are 175° and 174°, and the equatorial angles range from 111° to 129° and 113° to 127°. Figure drawn with MOLSCRIPT [1].

The MnSOD and FeSOD enzymes of *E. coli* are both homodimeric and structurally homologous but their solution properties are different, in particular with respect to their oligomeric state [4]. Apo-FeSOD undergoes dissociation into monomers at protein concentrations less than 150 µg/ml whereas apo-MnSOD does not. Given the close proximity of the metal ion to the dimer interface it is possible that differences in the dimer interface between the two enzymes, mediated through the loss of the metal ion, could account for the differing dissociation properties of the two enzymes.

Of the 19 residues in the *E. coli* MnSOD interface and 21 residues in the *E. coli* FeSOD interface, 14 are structurally conserved. The seven hydrogen bonds found in the MnSOD interface are also conserved in the FeSOD interface (Table 2-4 above). Of the residues that are not conserved within the interface, the most obvious change is the substitution of Gln178 in MnSOD by an arginine residue in FeSOD. This substitution allows the formation of a 2.93 Å salt bridge across the subunits at each side of the interface. The Asn73/Phe124 amino/aromatic stacking interaction is also conserved in the FeSOD dimer interface. Amongst other Fe and MnSODs two arrangements of this stacking interaction can be found. *T. thermophilus* MnSOD and *B. stearothermophilus* MnSOD have the same arrangement as the Mn and FeSODs from *E. coli*. In the second arrangement, which is found in *M. tuberculosis* FeSOD and human mitochondrial MnSOD, the asparagine is replaced by a phenylalanine, and the phenylalanine replaced by a glutamine. The extra carbon-carbon bond in the glutamine relative to the asparagine sidechain causes the amino nitrogen to lie further along the phenylalanine ring plane, weakening the amino/aromatic interaction. Like the Gln146/Gly77 interaction, this represents another example in Mn and FeSODs where a structural entity has been conserved by the complementary mutation of two residues. Tyr174 is the only invariant residue in the interface amongst Mn and Fe-SODs that is not also a direct part of the active-site pocket. However, Tyr174 forms a strong hydrogen bond with His30. This hydrogen bond is conserved in all structures which have main-chain dihedral angles acceptably sampling sterically allowed phi-psi space. This would suggest an important role in dimer formation or substrate access to the active-site.

2.4. Structure determination of an azide derivative

Various attempts were made to obtain the structure of the azide-bound native MnSOD. A summary of the preparation method and selected structure determination parameters of azide derivative wildtype MnSOD crystals is presented in Table 2-5 (opposite).

Method I: Pseudo-mother liquor (well solution with an extra 5 % w/v PEG 6 K) was prepared. A native crystal was then transferred and stabilised in this solution. The same pseudo-mother liquor, but with the addition of 100 mM sodium azide was prepared. The crystal was transferred directly into the azide-containing mother liquor and left to equilibrate for twelve hours before commencing data collection. Data were collected at ambient temperature.

Method II: Wild-type protein was first reacted with 200 mM sodium azide, then crystallised by seeding into sitting drops containing 200 mM sodium azide. Data were collected on crystals at ambient temperature and at 113 K. Crystals were frozen by flash freezing in a cryo-solution comprising 25 % PEG6K, 15 % MPD and 0.2 M bicine at pH 8.65. A

separate batch of crystals was prepared in a similar way but with all azide concentrations at 100 mM. Data on these crystals were collected at ambient temperature.

Method III: The oxidising agent $K_4Mo(CN)_8$ was prepared by a previously published method [164]. Wild-type crystals were stabilised in pseudo-mother liquor. The crystals were then transferred into a solution containing pseudo-mother liquor, oxidant and azide. The first crystal was soaked for one hour in an oxidising solution with an azide concentration of 100 mM. The second crystal was soaked for 24 hours, where the concentration of azide was 320 mM. Data were collected on both crystals at 113 K.

Refinement and inspection of all six structures revealed no azide had bound at the active site.

Table 2-5. Summary of potential azide derivative structures

Crystal	Method	Description	Temp. (K)	Res. (Å)	Refinement Program	R_{free} / R-factor
3	I	12 hour soak in 100mM NaN_3	293	3.0	CNS	
7	II	reacted/seeded in 0.200mM azide	293	2.2	TNT	0.213/0.184
8	II	reacted/seeded in 0.200mM azide	113	2.2	TNT	0.353/0.301
12	II	reacted/seeded in 0.100mM	293	2.3	TNT	0.268/0.237
14	III	~ 1hr soak in 100mM azide + $K_4Mn(CN)_8$	113	2.3	TNT	0.370/0.322
15	III	~ 24hr soak in 320mM azide + $K_4Mn(CN)_8$	113	2.7	TNT	0.297/0.237

2.5. Conclusions

This structural analysis identifies two factors that may be of importance for function. Firstly, the interdependence of the two active sites of the dimer emphasizes the importance of the dimer structure, and the double "bridge" between the two Mn centres, comprising the His171 and Glu170 residues of opposing monomers, may allow electron transfer between them as a means of recovering from oxidative damage. And secondly, significant differences in surface properties occur between the Mn and FeSOD enzymes from *E. coli* in the groove formed between the two monomers. The dimer groove may be a potential site for non-specific interaction with oligonucleotides, consistent with the evidence that MnSOD binds more tightly to oligonucleotides than does FeSOD.

Whilst this structural analysis of *E. coli* MnSOD does not in itself reveal the mechanism of metal-ion specificity, the structure does provide an important basis for further study of this problem, notably in comparisons with the Fe-substituted *E. coli* MnSOD presented in Chapter 3, and in the mutagenesis studies presented in Chapters 4 and 5.

3 Crystal Structure of Iron-substituted *Escherichia coli* Manganese Superoxide Dismutase at 2.2 Å Resolution

3.1. Introduction

One of the more intriguing properties of the manganese and iron superoxide dismutases is their metal-ion specificity. The dismutase activity of almost all Fe and MnSODs characterised to date is dependent on the metal ion at their active site: substitution of the native metal with the other inactivates the enzyme [80, 4, 81]. Given the different chemical properties of these two metal ions, it should not seem at all unusual that these Fe and MnSOD enzymes have adapted to more efficiently utilise their native metal ions. But one would expect that such adaptions would be apparent and conserved in the structures of these two types of enzyme, particularly at the active-site, or in the secondary coordination sphere so as to have an influence on activity at the active site. In fact, while differences have been observed, most notably in the position and type of residue involved in hydrogen bonding with the metal-coordinated solvent molecule, the ligand-metal geometries in the active sites of these two enzymes are almost identical, and the secondary coordination sphere is similar in both. Close scrutiny of the X-ray crystallographic structures of iron and manganese superoxide dismutase from different organisms [6], and more recently from the same organism [79], failed to reveal the structural nature of the specificity. The structural differences that influence the metal-ion specificity would thus appear to be subtle. The X-ray crystallographic structure of iron-substituted manganese superoxide dismutase (Fe_2MnSOD), presented here, is the first of any inactive form of the iron or manganese SODs. The aim of this structural investigation was to determine the structural nature of the metal-ion specificity by comparison between the structures of the active and inactive forms of *E. coli* MnSOD. This work complements the comparisons already made between the active forms of *E. coli* Fe and MnSOD [79].

3.2. Structure determination

3.2.1. Purification

Fe_2MnSOD was prepared and purified as for native MnSOD [5] except that the medium was supplemented with iron salts. Quantitative uptake of iron was confirmed by atomic absorption spectrometry.

3.2.2. Crystallisation

Crystallisation of Fe_2MnSOD was initially attempted by using a coarse screen based around the crystallisation conditions of the native enzyme. Sitting drops consisting of 1 µL of 10 mg/mL protein with 1 µL of well solution were prepared on micro-bridges. Well solution volumes were 1 mL, and contained 14 - 29 % w/v PEG 6000 in 3 % increments and 0.1 M bicine titrated to pH 8.0, 8.3, 8.6 and 9.0. Wells were covered using CRYSTAL CLEAR, a transparent plastic adhesive tape. After 2 - 3 days at 12ºC a heavy precipitate was formed in all wells. Further screening with reduced PEG concentrations (5, 10 % w/v PEG 6000) and otherwise similar conditions also failed to produce crystals. The trays were removed to stand at room temperature. The temperature change did not induce crystal growth.

As the crystallisation conditions for the native enzyme were not suitable for growth of crystals of the iron-substituted enzyme, it was decided to try various general crystallisation screens. The 'PEG Screen' [165] and the 'Crystal Screen' [166] were tested, and both produced crystalline material.

Of the four conditions in the 'PEG Screen' which produced results, all crystalline material was produced within three days, and none was suitable for testing by X-ray diffraction (see Table 3-1).

Table 3-1. Crystallisation conditions in the 'PEG screen' [165] in which crystalline material was produced

Run	Precipitant	Buffer	pH
11	21 % PEG 6000	0.2 M succinic acid/KOH	5.5
24	28 % PEG-mme 5000	0.2 M cacodylic acid/KOH	6.1
29	7 % PEG-mme 5000	0.2 M bis-tris propane/HCl	6.7
47	21 % PEG-mme 5000	0.2 M tris/HCL	7.9

The 'Crystal Screen' had four wells containing crystalline material (see Table 3-2 opposite). The crystals formed in Run 4 were salt crystals formed by dehydration. Crystals formed in the conditions of Run 6 have a very fast growth rate, and can be made to

appear almost instantly. They grow as a thick mass of very fine crystalline fibres, in some cases encompassing the entire drop, which when diluted and viewed under a microscope can be seen to be individual crystals. These individual crystals are too small for use in single-crystal X-ray diffraction experiments. Optimisation of this crystal form was aided by their fast-growing nature, which allowed for quick assessment of results and redesign of experiments.

Table 3-2. Crystallisation conditions in the 'Crystal screen' [166] in which crystalline material was produced

Run	Precipitant	Buffer	pH	Time
4	2.0 M Ammonium sulfate	0.1 M tris/HCl	8.5	13 months
6	30 % PEG 4000	0.1 M tris/HCl, 0.2 M Mg chloride	8.5	<1 hour
17	30 % PEG 4000	0.1 M tris/HCl, 0.2 M lithium sulfate	8.5	14 days
18	20 % PEG 8000	0.1 M Na cacodylate, 0.2 M Mg acetate	6.5	5 days

Initial optimisation experiments were designed to test requirements for the magnesium cation, the chloride anion, the effects of different precipitant concentrations, salt concentrations, pH, different ratios of protein and well solution in the drop, different protein concentrations, drop sizes, and the effects of micro and macro seeding.

Crystals would not grow if the concentration of magnesium chloride in the drop was <0.18 M, nor would they grow when magnesium sulfate or magnesium acetate were substituted for magnesium chloride. Crystals would grow between pH 7.5 and pH 9.0 in the tris buffer, and in buffer concentrations between 0.05 and 0.2 M. Higher pH seemed to favour slightly larger crystals. Crystals in sitting drops of 4 µL were larger than those in equivalent hanging drops. By decreasing the ratio of protein to precipitant in the drop, initial drop concentrations are closer to the well concentrations. This has the effect of reducing the density of crystals formed, but did not affect the size of crystals. Micro seeding was also effective at reducing density of crystals in drops but also helped form larger crystals. Macro seeding could also produce crystals of suitable diffraction size, but the results were quite variable with seed crystals seldom growing, and in some cases completely new crystals growing in the same drop.

The crystallisation conditions used to produce the crystals for which data were subsequently collected are listed in Table 3-3 (below). No crystals grown and tested after these diffracted, even though the crystal size and form appeared identical to the original diffracting crystals.

Table 3-3. Crystallisation methods and conditions of Fe_2MnSOD crystals

Fe_2MnSOD, room temperature, ~ 0.02 % w/v sodium azide			**3.0 Å**
30 % w/v PEG 4000	0.1 M tris/HCL pH 8.4	0.2 M $MgCl_2$	
Well volume was 1 mL. Hanging drops were formed under glass microscope cover slips, and consisted of 1 µL of protein solution at 10 mg/mL to which was added 1 µL of well solution. The resultant crystal used for data collection was ~ 0.005 x 0.01 x 0.50 mm. All crystallisation solutions contained ~ 0.02 % v/v sodium azide.			
Fe_2MnSOD, room temperature, ~ 0.02 % w/v sodium azide			**2.7 Å**
30 % w/v PEG 4000	0.1 M tris/HCL pH 8.5	0.2 M $MgCl_2$	
Well volume was 1 mL. Hanging drops were formed under glass microscope cover slips, and consisted of 1 µL of protein solution at 10 mg/mL to which was added 1 µL of well solution. The crystals grown at room temperature in this drop were then used for macro seeding. A single crystal was chosen and washed successively in solutions of 30, 25, 20 and 15 % w/v PEG 4000. The washed crystal was introduced into a sitting drop consisting of 10 µL of 10 mg/mL protein solution and 10 µL of well solution. The resultant crystal used for data collection was ~ 0.015 x 0.03 x 1.0 mm. All crystallisation solutions contained ~ 0.02 % w/v sodium azide.			
Fe_2MnSOD, 110 K, ~ 0.02 % w/v sodium azide			**2.2 Å**
19 % w/v PEG 4000	0.1 M tris/HCL pH 8.5	0.2 M $MgCl_2$	
Well volume was 1 mL. Sitting drops were formed in micro bridges, and consisted of 5 µL of protein solution at 10 mg/mL to which was added 5 µL of well solution. The crystals were grown at room temperature. All crystallisation solutions contained ~ 0.02 % w/v sodium azide.			
Fe_2MnSOD, 110 K, no sodium azide			**2.2 Å**
18 % w/v PEG 4000	0.1 M tris/HCL pH 8.7	0.2 M $MgCl_2$	
Well volume was 0.8 mL. Sitting drops were formed in micro bridges, and consisted of 3 µL of protein solution at 10 mg/mL to which was added 3 µL of well solution. The crystals were grown at room temperature.			

3.2.3. Data collection and processing

Four data sets were collected from crystals of Fe_2MnSOD. Data were collected on a Rigaku R-Axis IIC image-plate detector, using Cu-Kα radiation from a Rigaku RU-200B rotating anode generator. The Cu radiation was collimated using a 0.1 mm collimator. Using the smallest available collimator improved the signal to noise ratio of the data obtained from the small crystals by maximising the ratio of the radiation impinging on the crystal to the radiation passing by the crystal. The crystallisation methods and conditions of the four crystals for which data were collected are summarised in Table 3-3. Relevant data collection and processing statistics for three of these are given in Table 3-4 (opposite).

The first data collected were from a very small crystal with dimensions of ~ 0.005 x 0.01 x 0.50 mm. The crystal was sealed in a 0.1 mm glass capillary. The mother liquor was not completely drawn away from the crystal because of the difficulty in manipulating the very small crystal. Data were collected to 3.0 Å resolution, but proved difficult to process

because of changes in the crystal orientation as it moved slightly in the mother liquor. The data did, however, prove the crystal to be formed of protein, and also allowed the determination of the unit cell and crystal symmetry.

Table 3-4. Data collection and reduction statistics for *E. coli* Fe_2MnSOD

Crystal	Fe_2MnSOD R.T., trace N_3^-	Fe_2MnSOD 110 K, trace N_3^-	Fe_2MnSOD 110 K, no N_3^-
Space group	$C222_1$	$C222_1$	$C222_1$
Z (Z')	16(2)	16(2)	16(2)
Unit cell	*a*=47.234 Å	*a*=46.277 Å	*a*=46.190 Å
	b=90.164 Å	*b*=89.138 Å	*b*=89.040 Å
	c=208.379 Å	*c*=206.592 Å	*c*=206.671 Å
V(m), $Å^3$/Da	2.47	2.37	2.36
Solvent content	50 %	48 %	48 %
Mosaicity	0.27º	0.48º	0.31º
Data collection temperature	293 K	110 K	110 K
Data processing			
Resolution limits (of last shell)	50 - 2.7 Å (2.75 - 2.70)	50 - 2.2 Å (2.28 -2.20)	50 - 2.2 Å (2.28 -2.20)
Unique reflections	12796	22346	22227
Observed reflections	130893	265952	225177
Observed reflections after averaging	47915	77472	88015
Observed reflections after averaging $I > 1\sigma_I$	46809	74951	86464
Observed reflections after merging	12392	20089	20726
Observations deleted manually	45	72	422
Redundancy	3.8	3.7	4.2
Completeness	96.8 % (86.8)	89.9 % (68.6)	93.2 % (82.6)
R_{merge} on intensities[1]	0.113 (0.327)	0.080 (0.319)	0.090 (0.266)
Overall I/σ	8.9 (2.6)	13.8 (3.0)	14.0 (4.6)

[1] $R_{merge} = \Sigma|I-\langle I\rangle|/\Sigma I$, where $\langle I\rangle$ is the mean of individual observations of intensities I.

Data were collected on a second, larger crystal at room temperature. The crystal had dimensions of ~ 0.015 x 0.03 x 1.0 mm. The length of the crystal allowed three fragments to be mounted separately. The fragments were mounted in 0.1 mm glass capillaries. Excess mother liquor was drawn away from the crystal using very fine glass capillaries. Plugs of mother liquor at each end of the capillary ensured the crystal fragment remained hydrated, and each end of the capillary was sealed with wax. Data were

collected from all three fragments, with the first fragment being long enough to translate in the X-ray beam after significant radiation damage had accumulated. The crystal diffracted to 2.6 Å, and was subsequently indexed, integrated and scaled to 2.7 Å.

Fe_2MnSOD crystals are more susceptible to radiation damage than native MnSOD crystals. Whereas native MnSOD crystals only start to suffer significant radiation damage after 35 - 40 hours at room temperature, Fe_2MnSOD crystals exhibit the same level of damage in 20 hours or less. The combination of a long cell edge (~ 207 Å), small crystal size, and susceptibility to radiation damage at room temperature, effectively limits collecting data from a single crystal to about 2.6 Å resolution. To collect data to higher resolution on the R-Axis IIC, it is necessary to both increase the effective exposure time of oscillations and to swing out the two-theta stage of the detector. Both of these actions markedly increase the length of time needed for the data collection, and also therefore the number of crystals needed to collect a complete and redundant data set. Freezing a single crystal to around 110K effectively eliminates radiation damage, thus allowing collection of data to be limited by factors other than the lifetime of the crystal. Finding a suitable cyroprotectant for this crystal form was therefore fundamental to collecting higher resolution data. A summary of cryoprotectants tried is given in Table 3-5. The cryoprotectant giving the best results, the criteria being both diffraction to highest resolution and lowest mosaic spread, was a combination of 25 % PEG 4000 and 15 % MPD acting as the cryoprotectant, and 0.1 M tris titrated to pH 8.7 with HCl acting as a buffer to maintain the pH.

Table 3-5. Effects of different cryoprotectants on diffraction of Fe_2MnSOD

25 % PEG 4000, 15 % PEG 400	**+0.1 M tris/HCl pH 8.7**
Gave mixed results, with sometimes no diffraction and sometimes reasonable diffraction. Different soak times were trialed, 60 s, 1 - 2 min, 2 - 3 min, 10 min and 1 - 2 hour very slow equilibrations. The best results were from the quickest soaks of < 60 s. These quick soaks were tried on two different crystals; one diffracted to ~ 3 Å and the other did not diffract at all.	
25 % PEG 4000, 15 % Glycerol	**+0.1 M tris/HCl pH 8.7**
A single 60 s soak was tried resulting in very poor diffraction. Crystals dissolved in buffers and 40 % glycerol with no PEG.	
25 % PEG 4000, 15 % MPD	**+0.1 M tris/HCl pH 8.7**
This set of conditions consistently gave the best results. Short soaks of ~ 20 s and slow equilibrations of up to one hour both gave diffraction to ~ 3 Å. A combination of 20 % PEG 4000 / 30 % MPD with buffers resulted in higher mosaicity, and 30 % PEG 4000 / 10 % MPD with buffers did not diffract. Diffraction to 2.2 Å with a mosaicity of about 0.3° could be consistently achieved with ~ 60 s soaks in a cryoprotectant containing 25 % PEG 4000, 15 % MPD, and 0.1M tris/HCl pH 8.7.	

Two Fe_2MnSOD data sets were collected at 110 K, with both crystals diffracting to 2.2 Å. The first was from a crystal grown using solutions containing trace (0.02 % v/v)

sodium azide. The second was from a crystal grown from sodium azide-free solutions. The first of these frozen data sets suffers from both incompleteness (89.9 % overall, 68.6 % in the 2.28 - 2.20 Å shell) and a higher mosaic spread of 0.48º. The higher mosaicity increases the size of reflections, and therefore the possibility of overlapping reflections. The second frozen data set exhibited better mosaicity of 0.31º, and was both more redundant and more complete (93.2 % overall, 82.6 % in the 2.28 - 2.20 Å shell).

3.2.4. Structure solution

The structure of Fe_2MnSOD was solved by the technique of molecular replacement using the data from the room temperature, 2.7 Å resolution data set. The model of the native MnSOD dimer (subunits A and B) was used as the search model. All solvent molecules were removed from the search model. Calculations based on the expected solvent content of protein crystals [145] gave a Matthews' coefficient, Vm, of 2.36 $Å^3$/Dalton for a crystal having a single Fe_2MnSOD dimer in the asymmetric unit. The CCP4 [148] program AMORE was therefore used to search for one copy of the Fe_2MnSOD dimer in the rotation function. The highest peak in the rotation function had a correlation coefficient of 0.23. The translation function corresponding to this rotation was calculated, and the highest peak had a correlation coefficient of 0.76 and an R-factor of 0.30. Rigid-body fitting of the search model improved this to 0.82 and 0.28 respectively. Packing of the molecular replacement solution model was checked visually using the graphics program TURBO, and the model moved to an asymmetric unit comparable to that of the native MnSOD AB-dimer.

3.2.5. Model building and refinement

Refinement of the 2.7 Å resolution model was done using the program TNT [130]. The B-factors of all protein atoms in the starting refinement model were reset to 30.0 $Å^2$. The occupancy of the metal ion, metal ligands, Tyr34 and Gln146 were set to zero. Eight cycles of model building and refinement followed, including the addition of some 30 solvent water molecules and two molecules of azide. The azide molecules were initially modelled at half occupancy. The initial choice of occupancy was based on the peak height of the electron density in the difference map for the nitrogen atom of azide covalently bonding to the Fe. Peak heights for the other two atoms were progressively smaller. The partial occupancy was confirmed by the B-factors which were near the average of 30 $Å^2$ for the metal proximal nitrogen of the azide and increased to 50 $Å^2$ for the distal nitrogen.

The coordinates from the room temperature, model of Fe_2MnSOD at 2.7 Å resolution were used as the starting point for refinement of the azide-free, model at 2.2 Å resolution. The occupancies of the active-site metal and ligands were set to zero, and the B-fac-

tors of all atoms were reset to the Wilson B of 10.0 $Å^2$. Rigid-body refinement was performed using TNT, and improved the value of R_{free} from 0.393 to 0.323. Five further cycles of model building and refinement, including the addition of the active-site metal and ligands, and solvent water molecules reduced R_{free} to 0.274. Further refinement, in conjunction with model building, was carried out using CNS. Various NCS weighting schemes were tested to choose the optimal NCS weighting parameter. The effects on the pairwise RMS differences of mainchain atoms between the two NCS-related subunits, and the corresponding R_{free} and R-factor for various NCS weighting schemes, are shown in Table 3-6. The value of R_{free} was independent of the NCS weighting parameter chosen, but the R-factor showed considerable correlation with the weighting scheme, changing by over 2 % for the values tested. The R-factor increased when the NCS restraints were tightened, and decreased when they were loosened. A weighting scheme was chosen to give RMS differences tighter than those expected. Separate NCS weighting parameters of 300 and 100 were used for main-chain and side-chain atoms respectively, reflecting the added mobility of side-chains atoms. A peak in the electron density difference map ~ 2 Å from the active-site Mn in chain B was modelled as a covalently bound solvent molecule (see Figure 3-7 below). The final model has a value for R_{free} of 0.229 and an R-factor of 0.192.

Table 3-6. Effects of different NCS weighting schemes

CNS NCS weighting parameter	RMS difference (Å) of main-chain atoms		R_{free}	R-factor
	Selected atoms[1]	All atoms[2]		
none	0.176	0.361	0.253	0.215
10	0.132	0.238	0.252	0.219
25	0.096	0.154	0.252	0.222
50	0.062	0.090	0.252	0.226
75	0.045	0.064	0.252	0.229
100	0.038	0.055	0.252	0.229
300	0.019	0.027	0.253	0.233
500	0.013	0.019	0.253	0.233
1000	0.008	0.012	0.253	0.234

[1] A subset of all atoms is used in the calculation of the overall RMS difference. An atom pair is excluded if its distance deviates by more than 3 (overall standard deviation).

[2] Residues 1, 104, 136 and 202 - 205 were excluded because of large natural deviations due to crystal packing contacts.

Table 3-7. Refinement and model statistics for native *E. coli* MnSOD

Model	Fe_2MnSOD R.T., trace N_3^-	Fe_2MnSOD 110 K, trace N_3^-	Fe_2MnSOD 110 K, no N_3^-
PDB ID	-[1]	-[2]	1MMM
No. of residues	410		410
No. of protein atoms	3262		3256
No. of water molecules	155		284
No. of Fe ions	2		2
Average B-factors, Å^2			
Main-chain atoms	10.2		13.1
Side-chain atoms	12.2		13.9
Water molecules	15.5		16.6
Fe	13.1		13.1
Overall	11.4		13.8
Refinement			
Refinement program	TNT v5e [130]		CNS v0.5 [131]
Reflections used in refinement	11764		19132
Reflections used in calculation of R_{free}	597 (4.8 %)		1557 (7.0 %)
Resolution limits	50.0 - 2.7 Å		50.0 - 2.2 Å
RMS bond lengths	0.018 Å		0.006 Å
RMS bond angles	0.47º		1.25º
R-factor (all data)	0.225		0.196
R_{free} (all data)	0.275		0.235

[1] Refinement of this model is not complete as indicated by the tightly constrained bond angles and relatively high R_{free}

[2] No model has been refined for this data.

3.3. Structure description

3.3.1. Model validation

Details of the final models for two of the three data collections are given in Table 3-7, no model has been refined against the 2.2 Å, trace azide data. Of the 410 amino-acid residues five had sidechains which could not be suitably modelled due to poor electron density. All five, Gln21, Gln47, Asn50, Lys137 and Lys205 are in chain B, and are solvent-exposed residues on the enzyme surface. Almost 91 % of all residues fall within the sterically most favoured regions of a Ramachandran plot, as defined in PROCHECK [153]. As in the structure of *E. coli* MnSOD, Asn145 and Gln178 have normally disallowed phi

and psi angles in each of the subunits, and the peptide conformation of Pro16 is *cis*. Figure 3-1 shows a multiple Ramachandran plot of the two subunits of the dimer.

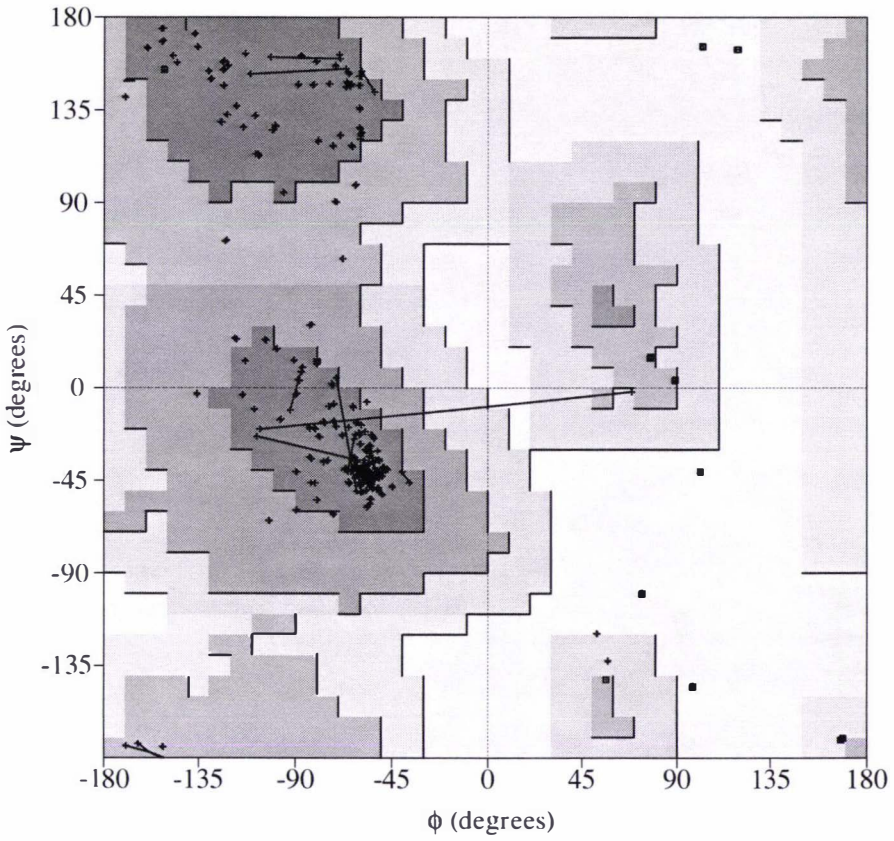

Figure 3-1. Multiple Ramachandran plot for *E. coli* Fe_2MnSOD

Ramachandran plots for each of the two subunits are shown superimposed on, and linked by solid lines to, the average Ramachandran plot for the two subunits.

3.3.2. Secondary, tertiary and quaternary structure

The tertiary structure of the A and B subunits of the dimer are similar. Significant deviations do exist between the two subunits in residue 1 at the N-terminus, in residues 63 - 67, and in residues 204 - 205 of the C-terminus. All of these deviations are caused by crystal packing contacts. Figure 3-2 (opposite) shows an overlay of the Cα-traces of the two subunits for the azide-free Fe_2MnSOD structure. The RMS difference between main-chain atoms in a pairwise comparison for the two subunits is 0.70 Å, for all 820 main-chain atoms, and 0.16 Å for a subset of 800 mainchain atoms excluding residues 1, 63 - 66 and 204 - 205. Fifteen residues have significantly different chi1 and chi2 side-chain torsion angles between the A and B subunits. All fifteen residues are either in the

naturally variable regions of the N-terminus, the A1 - A2 loop, and the C-terminus, or are involved in crystal packing contacts.

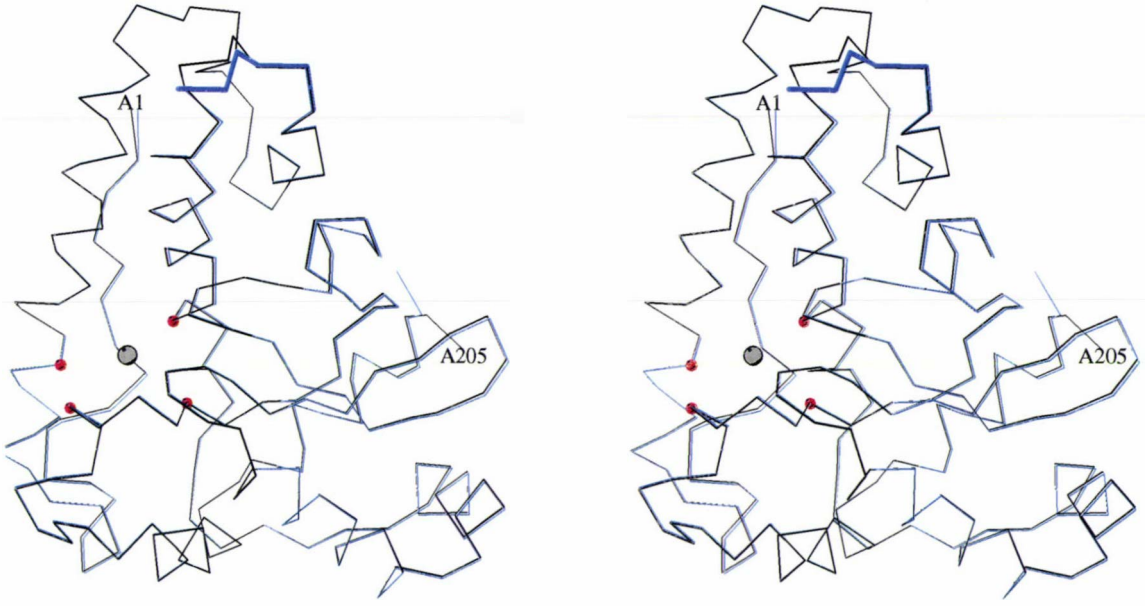

Figure 3-2. An overlay of the Cα-traces of the A and B subunits of *E. coli* Fe_2MnSOD

Subunit A is drawn in black, and subunit B in blue. Residues 63 - 67, whose main-chain differs significantly in subunit B due to a crystal packing contact, are drawn with a thick blue line. The metal ion is indicated by a grey sphere, and red spheres highlight the Cα atoms of the four metal-binding amino-acids. Figure drawn with MOLSCRIPT [1].

3.3.3. Active site of azide-free Fe_2MnSOD

The active sites of the azide-free Fe_2MnSOD dimer are dissimilar. Coordination of the iron in the active site of subunit B is six-coordinate, compared with that of subunit A which is five-coordinate. A water/hydroxide has been modelled as the sixth ligand, OH208, in subunit B. Ignoring this sixth ligand, the stereochemistry of the two active sites appear identical, both having a slightly distorted square-pyramidal geometry. The distortion arises in the non-linearity of the His81_NE2 - Fe - His171_NE2 axis, the angle being 148° instead of 180° for a regular square-pyramid.

Figure 3-3 (below) is a stereodiagram showing an overlay of the A and B subunit active-sites. Small rotations and shifts in active-site ligands can be observed, most being within the error limits of the model and superposition. There are, however, two coupled movements, possibly caused by the addition of the second solvent molecule to the coordination sphere of the Fe in subunit B, which may be noted. The first is a rotation in Asp167

about its chi2 side-chain torsion angle of ~ 15°. This makes the Asp167_OD2-Fe - OH208 angle of subunit B more linear (177°) than if the rotation did not occur (171°). This rotation may be coupled to the linearisation of the OH207 - Fe - His26_NE2 angle (178° in subunit B, and 174° in subunit A), with the shortening of the Asp167_OD1 ... OH207 hydrogen bond by ~ 0.3 Å, to 2.85 Å. The second coupled movement occurs between His81 and Trp128. The side-chain of His81 rotates ~ 10° around its chi2 torsion angle (chi2, subunit A = 83°; chi2, subunit B = 72.7°). This has the effect of positioning the His81B_CE2 carbon atom ~ 0.3 - 0.4 Å closer to Trp128B_CZ. Trp128 rotates away from His81, undergoing a rotation of ~ 5° in chi1 (chi1, subunit A = -65.2°; chi2, subunit B = -70.4°). Due to the length of the tryptophan side-chain, this amounts to a significant shift in the position of the CZ atom, maintaining an otherwise 3.2 Å His81B_CE2 ... Trp128B_CZ interaction at 3.5 Å.

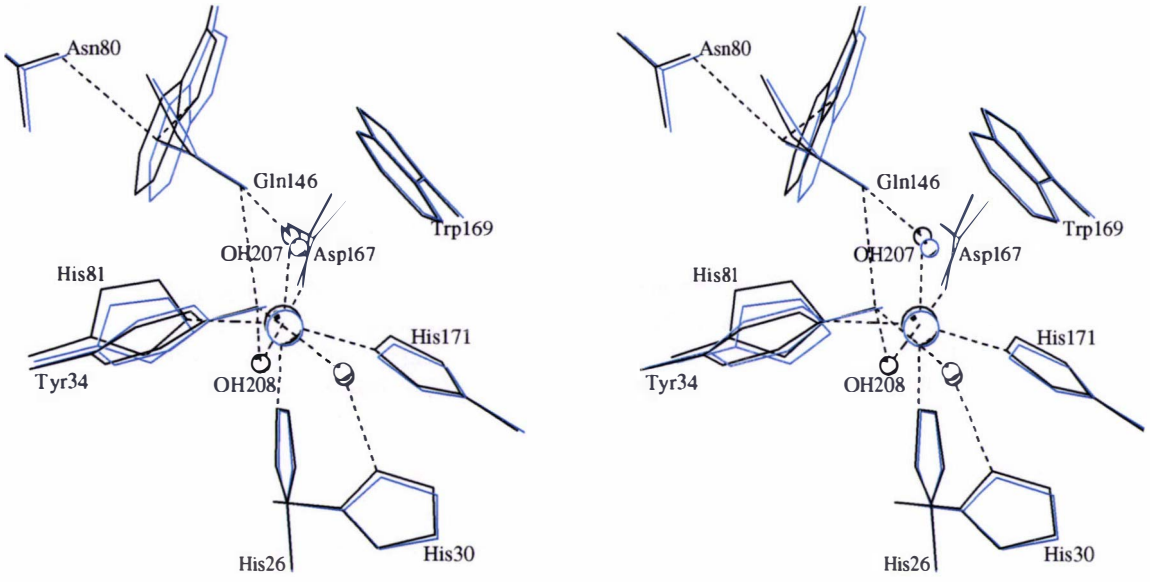

Figure 3-3. A stereodiagram showing an overlay of the two active-sites of the Fe_2MnSOD dimer

The active site of subunit A (drawn in blue lines) is five-coordinate. That of subunit B (drawn in black) is six-coordinate. Figure drawn with MOLSCRIPT [1].

The B-factors of the metal ions in the two active sites (12.1 $Å^2$ in subunit A and 14.1 $Å^2$ in subunit B) are 50 to 100 % higher than the B-factors of their ligated amino-acids (see Table 3-8 opposite). The higher B-factors of the metals may indicate a higher thermal motion due to static disorder of the metal position, particularly if the metal is in a mixed valency state. The higher B-factor may also be representative of partial occupancy of the

metal ion. In subunit B, the B-factor of OH208 (16.1 $Å^2$) is over three times higher than that of the other metal bound solvent OH207 (4.5 $Å^2$). Again this is likely due to either partial occupancy or higher thermal motion.

Table 3-8. Selected B-factors ($Å^2$) at the active site of Fe_2MnSOD[1]

Residue	B-factor subunit A	B-factor subunit B
Fe	12.1	14.1
OH207	7.5	4.5
OH208	-	16.1
His26_NE2	5.7 (5.9)	8.8 (7.3)
His81_NE2	8.6 (8.6)	11.0 (10.8)
Asp167_OD2	10.8 (8.9)	7.7 (9.7)
His171_NE2	9.9 (9.7)	8.8 (8.3)
Gln146_NE2	9.5 (7.0)	8.4 (10.4)
Tyr34_OH	18.4 (12.4)	16.0 (13.8)

[1]. Average value for side-chain given in brackets.

Some disorder is apparent in the secondary coordination sphere of subunit A. Tyr34, which is ordered in subunit B, is disordered in subunit A. The disorder, which could not be satisfactorily modelled, is represented by a total lack of electron density around the CE2 carbon of Tyr34A (see Figure 3-4 below). Simulated-annealing $|F_o|-|F_c|$ omit maps, calculated by omitting residues within 3 Å of Tyr34 (see Figure 3-7 below), have been calculated for subunits A and B. In subunit B, electron density contoured at 3.0σ and -2.5σ is indicative of an ordered Tyr34, and OH208. The corresponding map for subunit A shows the tyrosine to be disordered, and no electron density is apparent for an equivalent OH208.

3.3.4. Comparison with native MnSOD *E. coli*

The tertiary and quaternary structures of dimeric Fe_2MnSOD are very similar to that of native MnSOD (see Figure 3-5 below). The RMS differences for a pair-wise overlay of the native AB and CD dimers of MnSOD on the AB dimer of Fe_2MnSOD range between 0.49 and 0.51 Å for 1624 main-chain atoms, and between 0.29 and 0.34 Å for a subset of ~ 1400 main-chain atoms. Comparison of phi and psi poly-peptide torsion angles on a per residue basis for the monomeric subunits of MnSOD and Fe_2MnSOD reveal significant deviations in residues 1 - 3, 63, 67, 134 - 136, 204 - 205. All can be attributed to crystal packing contacts in subunits of either MnSOD or Fe_2MnSOD. Residues showing significant deviations in chi1 and chi2 side-chain torsion angles between MnSOD and

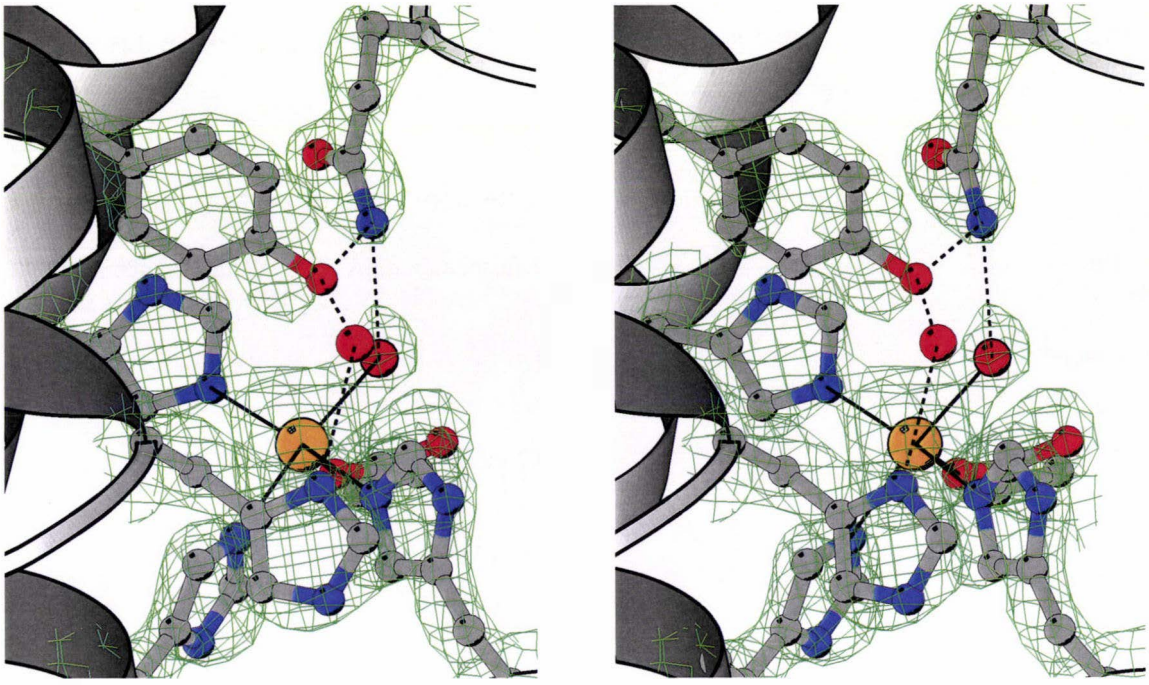

Figure 3-4. A stereodiagram showing electron density around the disordered Tyr34 in subunit A of Fe_2MnSOD

Stereoview of the sigma A-weighted ($2|F_o|-|F_c|$) electron density map around Tyr34 and the active-site of subunit A, contoured at 2σ. The disorder of Tyr34, as represented by the lack of electron density around the CE2 carbon, is apparent. The iron is represented by the orange-coloured sphere. Covalent bonds between the iron and its ligands are represented by solid lines and hydrogen bonds by dashed lines. Figure drawn with MOLSCRIPT [1].

Fe_2MnSOD either show similar variation within their own subunits, are affected by crystal packing contacts, or are solvent-exposed surface residues. The dimer interface of Fe_2MnSOD is identical to that of native MnSOD, with the buried surface area between the two subunits being 850 $Å^2$ per subunit, and the same 19 residues being buried in the interface.

Contrasting to the similar nature of the tertiary and quaternary structures of Fe_2MnSOD and native MnSOD is the marked difference in their active sites. Native MnSOD is five-coordinate and has trigonal-bipyramidal geometry, whereas Fe_2MnSOD is five- or six-coordinate and for the five ligands in common has distorted square-pyramidal geometry (see Figure 3-6 below). In the rearrangement from trigonal-bipyramidal to square-pyramidal, the His81-metal-His171 angle opens by ~ 16° from an average of 131.4° in MnSOD to 148.0° in Fe_2MnSOD. This geometry, though still distorted from square-pyramidal, allows for the coordination of a sixth ligand opposite Asp167_OD2, as seen in subunit B of Fe_2MnSOD. The Asp167_OD2-Fe-OH208 angle is 177.1°, and the axial His26_NE2-Fe-OH207 angle is 176.0°. The rearrangement to distorted square-pyramidal

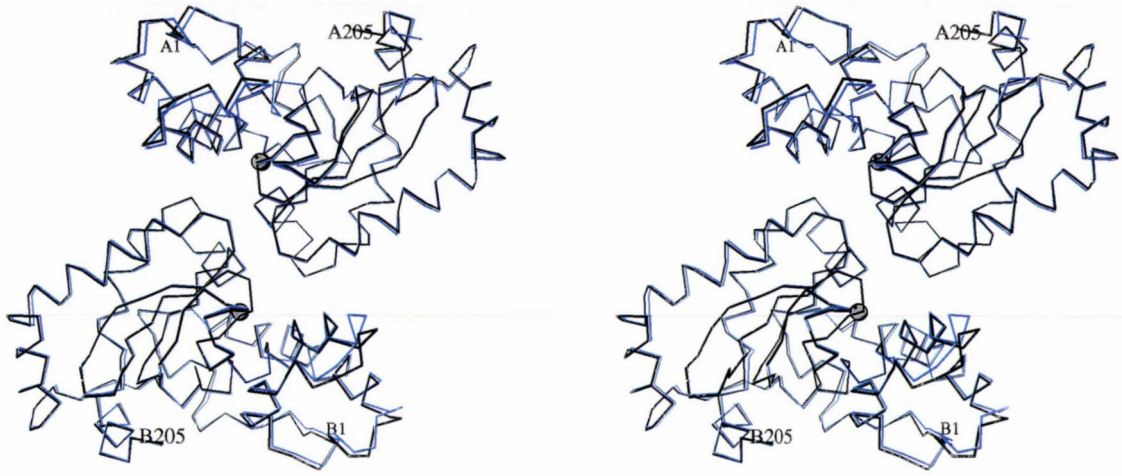

Figure 3-5. A stereodiagram showing an overlay of the Fe_2MnSOD dimer on the AB dimer of native MnSOD

Native MnSOD in black lines, and Fe_2MnSOD in blue lines. The metal ions are indicated by grey spheres. Figure drawn with MOLSCRIPT [1].

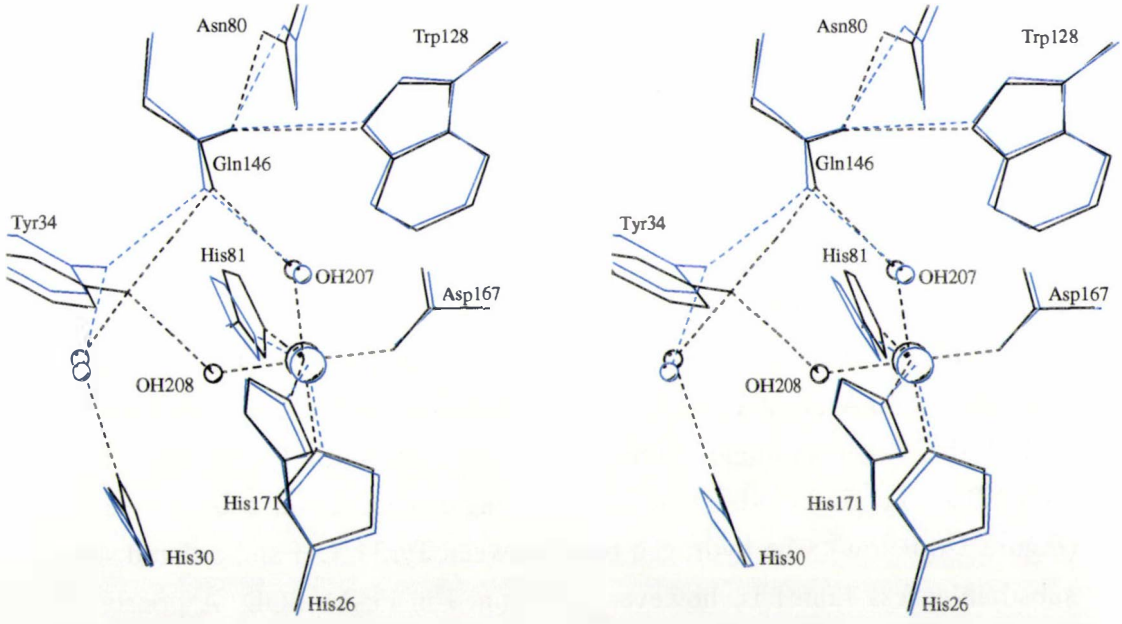

Figure 3-6. A stereodiagram showing an overlay of the Fe_2MnSOD subunit B active-site on that of native MnSOD

Native MnSOD (subunit A) in blue lines, and Fe_2MnSOD in black lines. The metal environment of Fe in subunit A is similar to that for chain B, with the largest exception being the absence of OH208 (see Figure 3-3). Figure drawn with MOLSCRIPT [1].

geometry in Fe_2MnSOD is not a consequence of the coordination of the sixth, metal-bound solvent, but rather is the geometry imposed by the binding of the Fe to the enzyme, as subunit A maintains the same geometry in the absence of the sixth ligand. Metal-ligand bond lengths, averaged over subunits, differ by between 0.02 and 0.13 Å. The largest shifts in Fe_2MnSOD bond lengths relative to MnSOD, occur in the His26_NE2-Fe bond (-0.13 Å) and the OH207-Fe bond (-0.11 Å). The hydrogen bond between Gln146_NE2 and OH207 shortens by nearly 0.3 Å, from 2.91 Å in MnSOD to 2.63 Å in Fe_2MnSOD.

The hydrogen-bonding network of the active site, linking OH207 to solvent in the substrate-access funnel *via* Gln146_NE2 and Tyr34_OH, is maintained in Fe_2MnSOD. An additional 2.88 Å hydrogen bond is formed in subunit B between OH208 and Tyr34_OH (see Figure 3-7 opposite). The tyrosine undergoes a rotation of approximately 5° about its chi1 side-chain torsion angle (MnSOD, chi1 = -65.4°; Fe_2MnSOD, chi1 = -61.0°), the side-chain rotation moving the phenolic oxygen by ~ 1.0 Å to form the hydrogen bond. Tyr34 of subunit A undergoes a similar rotation, although it is disordered and does not form the hydrogen bond with OH208 because of the absence of the latter in subunit A.

The rotation of the Tyr34 side-chain causes rearrangements of the ordered solvent structure in the substrate-access funnel. Of the 17 ordered waters in the substrate-access funnel of Fe_2MnSOD, 13 correspond to ordered waters in native MnSOD, two correspond with a single ordered water in MnSOD near the lip of the substrate-access funnel, and two undergo both positional movements of 1.4 and 1.0 Å and rearrangement of hydrogen bonds, due to the rotation of the tyrosine side-chain.

In all four subunits of the native structure, a water in the substrate-access funnel forms a hydrogen bond (2.9 Å) with Tyr34_OH. This water has an average B-factor of 18 $Å^2$, compared with the average solvent B-factors in the structure and the substrate-access funnel of 32 and 30 $Å^2$, respectively. In Fe_2MnSOD, because of the large spatial shift of Tyr34_OH, this water no longer forms a hydrogen bond with Tyr34_OH, and instead moves ~ 1.0 Å to optimise other hydrogen-bonding contacts in the substrate-access funnel (Figure 3-8 below). The hydrogen bond between Tyr34_OH and ordered solvent in the substrate-access funnel is, however, maintained in Fe_2MnSOD. A poorly ordered (average B-factor of 39 $Å^2$) water found in only the B and D subunits of the native structure, moves ~ 1.4 Å in the Fe_2MnSOD structure to form a hydrogen-bond bridge between Tyr34_OH and His30_ND1. This bridging water in Fe_2MnSOD is found in both subunits and has an average B-factor of 17 $Å^2$. In the native structure His30_ND1 forms no hydrogen bonds because the position of Tyr34_OH does not allow for a water to adopt a suitable geometry for hydrogen bonding to His30_ND1.

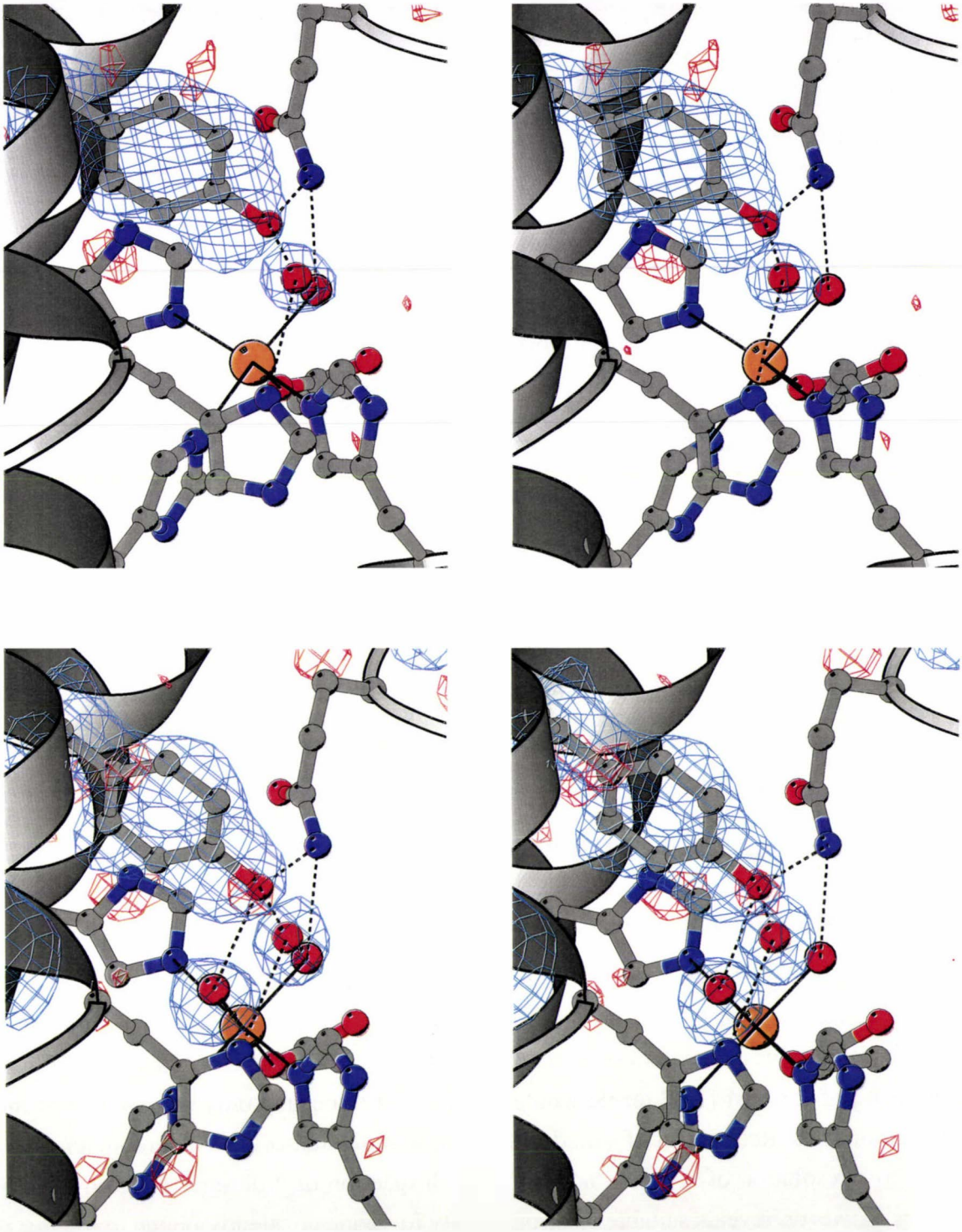

Figure 3-7. Stereodiagrams showing simulated-annealing omit maps of selected residues in the active-sites of Fe_2MnSOD

Stereoview of the sigma A-weighted ($|F_o|-|F_c|$) electron density map around Tyr34 and the active-site of subunit A (top), and subunit B (bottom) contoured at 3σ (blue) and -2.5σ (red). The disorder of Tyr34, as represented by the lack of electron density around the CE2 carbon, is apparent in subunit A. The iron is represented by the orange-coloured sphere. Covalent bonds between the iron and its ligands are represented by solid lines and hydrogen bonds by dashed lines. Figure drawn with MOLSCRIPT [1].

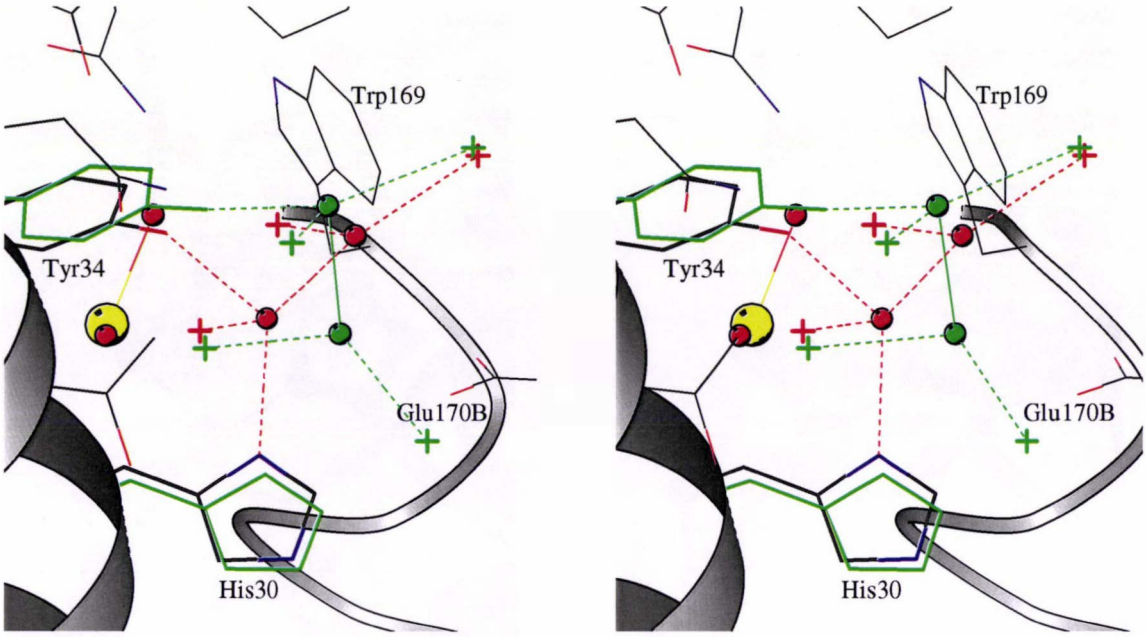

Figure 3-8. A stereodiagram showing the movement of waters in the substrate-access funnel of Fe_2MnSOD relative to those of native MnSOD

Fe_2MnSOD structure (subunit B) coloured by atom-type, and native structure (subunit A) in green. The iron is represented by the larger yellow sphere, and covalently-bonded solvent molecules OH207 and OH208 by smaller red spheres. The other metal ligands are omitted for clarity. Conserved substrate access funnel waters near the gateway are represented by crosses. The two substrate access funnel waters at the gateway that occupy different positions in the Fe-substituted structure are represented by small spheres. Figure drawn with MOLSCRIPT [1].

3.4. Fe_2MnSOD-azide complex

Data were collected from two crystals possibly containing enzyme-azide complexes. The azide was introduced into the crystallisation conditions by its inclusion as an anti-bactericide in crystallisation solutions at concentrations of 0.02 % w/v. Given that Fe_2MnSOD has a K_d of 0.3 mM [162], azide would be expected to occupy only around 1 % of the metal ion sites. Refinement of a model using the first dataset, collected at room temperature to a resolution of 2.7 Å, is not complete. Inspection of difference electron-density maps, however, reveals suitable electron density for azide covalently bound to the metal ion at an occupancy of < 20 %. A model is yet to be refined using the data collected at 110 K to a resolution of 2.2 Å. Crystallisations under the same conditions but with all traces of azide removed from crystallisation solutions initially proved successful and led to the azide-free structure of Fe_2MnSOD at 2.2 Å reported above. Considerable effort was made to repeat these crystallisations in order to produce a higher occupancy enzyme-azide complex by controlled soaking. Crystals were produced under the same conditions and having the same habit, but these crystals would not diffract.

3.5. Discussion

The mechanism of the metal-specific nature of Fe and MnSOD activity has been the focus of many investigations on these enzymes since first noted [70]. Theories on the basis of this mechanism were initially focused on proposed differences in the primary or secondary coordination sphere as a result of differences in the primary sequences of these enzymes. Although conserved differences between the primary structures of Fe and MnSODs have been observed, most notably the Gln/His/Ala substitutions at positions 76 and 146 (*E. coli* MnSOD numbering scheme) as discussed in Section 1.4.1, none have been related chemically to the metal specificity. More recent biochemical studies showed the metal-specific activity to be dependent in part on the pH of the enzymic environment [167, 9, 162]. Further, the redox potential of the metal ion has been determined as a cause of the inactivity of metal-substituted SODs [10]. However, the structural factors that cause these chemical effects have yet to be identified. Comparisons of the enzyme structures as determined by X-ray crystallography, including the native Fe and MnSODs from *E. coli* [79] have failed to determine the necessarily subtle structural factors underpinning the inactivity. The X-ray crystallographic structure of the inactive iron-substituted form of MnSOD from *E. coli* has been solved with the aim of determining the structural basis of the inactivity.

The structure of Fe_2MnSOD revealed two major differences from those of native Mn and FeSOD. Firstly, the geometry at the active site is distorted square-pyramidal compared with the trigonal-bipyramidal geometry of the native structures. Secondly, a sixth ligand was shown to bind to the Fe, albeit at partial occupancy, and only in one subunit of the enzyme.

Various pKs associated with the pH dependence of a number of properties of Fe_2MnSOD have been measured. There is considerable variation between measured values, but in general they fall around either a low pH or high pH transition. Reported values for the low pH pK lie between 6.4 and 7.2, and for the high pH pK between 8.5 and 9.1.

The Fe_2MnSOD from *S. marcescens* exhibits a pH dependence for activity (pK 7.0), optical absorption spectra (pK 6.6), EPR spectra (pK 7.2) and for azide affinity (pK 7.0) [199]. The high pH transition is yet to be observed for this enzyme.

The Fe_2MnSOD from *E. coli* shows a pH dependence in activity (pK 6.4) and optical absorption spectra A_{400} (pK 6.4) [162], A_{370} (pK 6.7 and 8.5), ^{1}H NMR (pK 9.1), EPR spectra (pK 8.5) and azide affinity (pK 7.0) [200].

E. coli FeSOD also shows a pH dependence at both low (pK 5.1) and high (pK 8.6-8.9) pH, with the high pH transition affecting activity, optical and EPR spectra, and substrate analog binding [104, 105]. The high pH transition is proposed to be either the loss of a

proton by the deprotonation of a bound water [105], or the binding of OH^- to the Fe(III) metal centre to form a six-coordinate complex [124, 121]. Because the same pH-dependent changes in spectra, activity and azide affinity of Fe_2MnSOD occur also for FeSOD, it has been proposed that these changes reflect the same chemical transition but with the pK shifted downward in Fe_2MnSOD (pK ~ 7) relative to FeSOD (pK ~ 9). In addition, in an analogous fashion to FeSOD, OH^- can act as a competitive inhibitor of superoxide binding to Fe_2MnSOD, but with inhibition occurring at a pH closer to the biological pH. Competitive inhibition by OH^- could therefore partly account for the loss of activity of the Fe_2MnSOD at a pH where the native enzyme is most active.

Since the report of the previously undetected high pH transition in *E. coli* Fe_2MnSOD, it remains unclear as to whether the binding of OH^- is associated with the higher or lower pH transition. The pH of crystallisation of this structural study was ~ 8.5, and as such falls close to the pK of the high pH transition. Inaccuracies in the crystallisation pH, and the possibilities of partial metal-ion occupancy in the enzyme or redox non-homogeneity make it difficult to assign the binding event to a pK based solely on the crystallographic occupancy of the OH^-. An X-ray crystallographic investigation at a range of pHs around or near the reported transitions, and taking careful account of redox state, pH and metal-ion occupancy, could provide supporting evidence for assigning this transition.

Vance *et al.* 1998 note the possibility that the lower pK of 6.7 may not be associated with OH^- binding to Fe(III), but may represent the prebinding of substrate analog to a protein site near the Fe in analogy with the two-step binding of N_3^- to FeSOD [200]. The process associated with the lower pK appears to affect substrate-analog binding, as seen by the large changes in the optical spectra at A_{370}, but has a more subtle effect on the EPR spectra.

The group responsible for the pK of 6.7 is not Tyr34 as the Y34F mutant of Fe_2MnSOD retains the optical signature of the pK but at a modified pK value [162, 200]. The group is likely to interact with Tyr34, however, due to its effecting a shift in the pK of the mutant. A possible candidate for this group is His30. His30 lies at the entrance to the active-site in the substrate-access funnel. The pK of His30 should be similar to that of typical histidine residues as the micro-environment of His30 is not extraordinary and is solvent-exposed, although His30 is involved in a strong hydrogen bond with the absolutely conserved Tyr174. The solvent-exposed ND1 nitrogen of His30 lies near to Tyr34. In the native *E. coli* MnSOD structure, no hydrogen bonds are formed to this nitrogen. However, due to the movement of Tyr34 in the Fe_2MnSOD structure, a suitable geometry exists for a water to form bridging hydrogen bonds between His30 and Tyr34. A change in the protonation state of His30 could account for observed effects on negatively charged substrate-analog interactions with the enzyme. Azide affinity for Fe_2MnSOD is

20-fold weaker at pH 7.8 than pH 7.0 [162], possibly due to changes in protonation states of adjacent residues or due to competition with H_2O/OH^- for the vacant sixth site.

Significant asymmetry occurs between the active-sites in the two subunits of the *E. coli* Fe_2MnSOD dimer, being most evident in the different coordination numbers of the metal ions. Crystallographic subunit A is five-coordinate and subunit B is six-coordinate, with both having a square-pyramidal metal-ligand geometry. Additional asymmetry occurs in the disorder of Tyr34 seen only in subunit A, whereas Tyr34 of subunit B is well ordered. The disorder of Tyr34 is most likely coupled to the absence of OH208 in subunit A. The partial occupancy of OH208 in subunit B can be caused by a number of factors including redox non-homogeneity of the metal, incomplete occupancy of the metal, and the affinity of the ligand for the metal. These reasons can not be used to explain why OH208 is not occupied (partially or otherwise) to the same extent in subunit A as that of B.

It is not uncommon for structural entities in crystallographically different but biologically identical subunits to have differing spatial orientations. These differences are usually caused by the different crystal-lattice packing environments of the subunits. While such effects are generally seen at the surface of proteins where the crystal-packing contacts occur, it is none the less possible for such a contact to be transmitted through the structure, either electrostatically or sterically, to affect the buried metal centre. At the resolution of this study such an effect would be difficult to detect.

Active-site coupling could also explain the asymmetry. Although the two active sites are separated by more than 18 Å, a three-residue, 17-bond bridge links the active sites (Section 2.3.7 and references [137, 79]). This connection could allow the communication of ligand or redox state between the metals.

Despite the difference in coordination number, both active sites maintain the same resting-state geometry. The disorder of Tyr34 in subunit A could not be modelled discretely. The single conformation modelled represents an average position of the real dynamic locations of this residue. This average position is similar to that of Tyr34 in subunit B, and the hydrogen bond to Gln146 is maintained. The absence of OH208 in subunit A, and therefore the hydrogen bond between Tyr34 and OH208, may make this residue more flexible, leading to the observed disorder.

The standard reduction potential of *E. coli* Fe_2MnSOD has been measured as -0.24 V [200]. This is considerably lower than the standard reduction potentials of *E. coli* FeSOD (+ 0.22 V) and *E. coli* MnSOD (+ 0.23 V). Because $E^{o'}$ of Fe_2MnSOD is lower than that of the O_2/O_2^- couple ($E^{o'}$ = -0.133V), $Fe(III)_2$MnSOD is unable to oxidise superoxide in the first step of the catalytic redox cycle. The lowered $E^{o'}$ of Fe_2MnSOD is consistent with thermodynamic stabilisation of its active site relative to that of the native MnSOD

enzyme. The observed change from five- to six-coordinate geometry is consistent with this stabilisation. The factors causing the change in geometry could not be identified.

3.6. Conclusions

A structural basis for the inactivity of *E. coli* Fe-substituted MnSOD has been determined in the altered geometry of the metal site on substitution of the non-native metal. The change in geometry from active five-coordinate trigonal-bipyramidal to inactive six-coordinate distorted octahedral (subunit A) and square pyramidal five-coordinate (subunit B) modifies both the kinetics and thermodynamics of superoxide dismutation at the enzyme's metal centre. Coordination of a sixth exogenous ligand blocks direct substrate access to the metal, a kinetic factor controlling activity. The predisposition for a geometry favouring stabilisation of six-coordinate adducts provides evidence in support of the observation that the redox potential of Fe in Fe_2MnSOD (but not in native FeSOD) lies below that required to oxidise superoxide ion - a crucial thermodynamic factor in controlling activity. The structural and chemical factors that lead to the altered metal geometry could not be identified from this X-ray crystallographic structure.

4 Crystal Structures of Active-site Mutants of *Escherichia coli* Manganese Superoxide Dismutase

4.1. Introduction

The extended active-site region of manganese superoxide dismutases when compared across species is generally highly conserved with some 65 % of the twenty-four residues within 8 Å of the active-site having sequence identity or sharing high sequence similarity. From the time that the first X-ray crystallographic structures of both iron and manganese superoxide dismutase revealed their location, two of these highly conserved residues, Tyr34 and Gln146, have been implicated as playing an important role in the catalytic fine-tuning of these enzymes. This structural implication in catalytic activity has been largely based on their position in the secondary-coordination sphere of the metal, and on the conserved hydrogen-bonding pattern in which these residues are involved. Tyr34 is absolutely conserved in iron and manganese superoxide dismutases. The phenolic oxygen of Tyr34 lies only 5.4 Å from the metal centre and is consistently found to form a hydrogen bond to the amide nitrogen of Gln146 (or its structurally equivalent residue). Tyr34 has been described as a gateway residue [162], however, because of its proximity to the active site, its interactions with Gln146 and potentially with substrate coordinated to the metal, Tyr34 is included here as an active-site residue. The amide nitrogen of Gln146 lies 4.7 Å from the metal, and forms another hydrogen bond to a solvent molecule that is covalently bonded to the metal. This solvent molecule, H_2O or HO^- depending on the redox state of the metal ion, completes a hydrogen-bonding relay extending from the solvent surrounding the enzyme to the metal ion *via* Tyr34, Gln146, and the metal-bound solvent. Proton involvement in the mechanism of superoxide dismutation is important as two protons are required in the overall reaction. The hydrogen-bonding relay may function to deliver protons to oxyanion intermediates during turnover [162]. In fact, it is the NH (nitrogen-hydrogen) moiety and not Gln146 that is the strictly conserved component of the hydrogen-bonding relay. In MnSODs, this functional group can be provided by either a glutamine or a histidine. In FeSODs, the NH nitrogen is only ever provided by a glutamine, with the added twist that the glutamine residue is part of a different secondary structure element. In FeSOD the

glutamine is provided from part-way along the second alpha-helix, A2, typically four residues before the active-site residue His81. In MnSOD the glutamine or histidine is at the beginning of the loop between the beta-strands B2 and B3. In either case a nitrogen atom always occupies the same position relative to the metal coordination geometry, so that the hydrogen-bonding relay is absolutely conserved.

The effect that these two active-site residues have on the function of the enzyme can be tested by their selective replacement. This work presents the X-ray crystallographic structures of three active-site mutants, Y34F, Q146H and Q146L. While this work was in progress, structural and functional studies were published by other groups on Y34F and Q143N mutants of human mitochondrial MnSOD [168, 169], and H145Q and H145E mutants of the FeSOD from *M. tuberculosis* [170]. These studies complement the work reported here and permit a deeper analysis of the role of these residues in enzyme function.

4.1.1. Rationale of mutants

The conservative replacement of the active-site tyrosine with a phenylalanine (Y34F) potentially breaks the hydrogen-bonding relay to the metal by removing the phenolic oxygen. The aromatic ring and general steric bulk are largely unchanged by this substitution.

Replacement of the glutamine by histidine (Q146H) can potentially maintain the hydrogen-bonding relay and approximate steric bulk. This substitution is useful for two reasons. Not only is the amino nitrogen in the correct position to preserve part of the hydrogen-bonding relay, but the amino nitrogen is in a different environment, namely within a five-membered ring. In addition, histidine is the only other amino acid which is naturally selected for in this position. This would confer a primary structure on the active-site of *E. coli* MnSOD similar to that of the cambialistic MnSOD from *Propionibacterium shermanii*. This substitution may have important consequences for metal-ion specificity.

The substitution of glutamine with leucine (Q146L) is designed to replace both hydrogen-bonding groups with methyl groups. The steric bulk of the amino acid is largely maintained, although leucine is one methylene shorter in length than glutamine.

The X-ray crystallographic structures of these mutants should firstly confirm the amino acid substitution. Secondly, they will determine whether or not changes to the structure are limited to the immediate vicinity of the mutation, or whether they cause wider changes to the structure, which could lead to misinterpretation of other biochemical results. Thirdly, by careful examination of the structural consequences of all three mutations, it should be possible to provide a more authoritative interpretation of other bio-

chemical, spectroscopic and structural analyses and, thus, further insight into the function of this enzyme may be obtained.

4.1.2. Characterisation of mutants of Tyr34

MnSOD Y34F, Fe_2MnSOD Y34F [162] and FeSOD Y34F [171] from *E. coli* have all been characterised, as has human mitochondrial MnSOD Y34F [168]. The Y34F mutation of MnSOD and Fe_2MnSOD *E. coli* has a number of effects on function [162], including changing catalytic activity, pH sensitivity of the metal ion, anion affinities and anion coordination, as outlined below:

(i) The Y34F mutation of *E. coli* MnSOD reduces superoxide dismutase activity by about 20 % compared with WT. Both WT and mutant show a slight pH dependence, with the activity decreasing with increasing pH. About 20 % of activity is lost when the pH is increased from 7.8 to 9.0. In contrast, Fe_2MnSOD Y34F shows greater activity and smaller pH sensitivity than Fe_2MnSOD WT over the pH range 6.3 to 9.0. Like MnSOD, the WT and Y34F Fe_2MnSOD both show decreasing activity with increasing pH. Catalytic activities of wild-type and iron-substituted MnSOD and their mutants from *E. coli* at various values of pH are given in Table 4-1.

Table 4-1. Catalytic activities of wild-type and iron-substituted MnSOD and their mutants from *E. coli* at various values of pH [162 and J.Whittaker *unpublished results*]

	Activity (U/mg)				
MnSOD form	pH 6.3	pH 6.5	pH 7.0	pH 7.8	pH 9.0
Mn_2 WT				7300	5900
Mn_2 Y34F				6000	5000
Fe_2 WT	480		140	60	<5
Fe_2 Y34F	1560		1540	850	150
Mn_2 Q146L		-		340	
Fe_2 Q146L		-		120	
Mn_2 Q146H		590		600	
Fe_2 Q146H		1050		430	
apo-Q146E		-		-	

(ii) The active-site metal centre of the Y34F mutant is less sensitive to pH than the wild-type. Structural changes in the metal site can be probed using absorption spectroscopy. Changes of pH are communicated to the metal ion *via* the coordinated metal ligands, and the effects can be observed by following changes in absorption of the Mn(III) ion at 480 nm. The Mn(III) A_{480} band of WT decreases by 30 % on increasing the pH from 5 to 10,

with pKa's of 6.93 and 9.72. The mutant is less sensitive, changing by only 6 % over the same pH range and having only one pKa (pKa ~ 7) below pH 11. The pH sensitivity of Fe_2MnSOD Y34F can also be followed in the optical spectrum. Fe_2MnSOD WT has both a high and a low pH form, with a pKa of 6.4. Fe_2MnSOD Y34F also has high and low pH forms but the transition is shifted by 1.5 pH units to a pKa of 7.9.

(iii) The Y34F mutant has different anion binding properties. On binding of azide, MnSOD WT is five-coordinate at room temperature and six-coordinate at low temperature. MnSOD Y34F is six-coordinate at both temperatures. Binding of cyanate (OCN^-) which, like N_3^-, can act as an electronic analog of the hydroperoxide anion, is, however, five-coordinate to MnSOD Y34F. Fe_2MnSOD WT and Y34F have higher affinities for azide than their Mn equivalents. Azide affinity is increased for the low pH forms, and for Y34F over WT (see Table 4-2).

Table 4-2. Anion affinities of wild-type and iron-substituted MnSOD and their Y34F mutants from *E. coli* at various values of pH [162, 200]

	K_d (mM)				
MnSOD form	pH 5.0	pH 6.0	pH 7.0	pH 7.8	pH 9.0
Mn_2 WT			7.2		
Mn_2 Y34F			1.6		
Fe_2 WT	0.015	0.090		0.30	
Fe_2 Y34F	0.010				0.10

Sensitivities to hydrogen peroxide are also affected by the mutation. Both WT and Y34F MnSOD are insensitive to hydrogen peroxide at pH 7.0. On the other hand Fe_2MnSOD WT is sensitive to inactivation by hydrogen peroxide, and the Y34F Fe_2MnSOD mutant even more so. Inactivation of Y34F Fe_2MnSOD by hydrogen peroxide is pH dependent, being more pronounced at pH 9.0.

The function of the Y34F mutant of human mitochondrial MnSOD (hMnSOD) has also been investigated [168]. Thermal stability, kinetics and product inhibition were studied in conjunction with the crystal structure, determined to a resolution of 1.9 Å. The Y34F mutant of hMnSOD was shown to have increased thermal stability relative to the wild-type enzyme. Differential scanning calorimetry determined values for the melting temperature, T_m, of ~ 89ºC for the native, and 96ºC for Y34F. This is a surprisingly large increase in stability given that the structural changes in the enzyme are negligible and that two hydrogen bonds, both to Tyr34, are *broken*. Guan *et al.* concluded that the reason for conservation of Tyr34 must therefore be for optimisation of function rather than

optimisation of stability. This is consistent with studies on T4 lysozyme which support the theory that residues involved in function are not optimised for stability [172].

Pulse radiolysis experiments were used to follow the rate at which $O_2^{-\cdot}$ is consumed by the enzyme hMnSOD, the decrease in superoxide concentration being followed by its absorbance at 250 nm. The Y34F mutant has a value for k_{cat}, the rate of maximal catalysis under conditions where the substrate is saturating, approximately ten-fold less than that of the wildtype enzyme. However k_{cat}/K_M for the mutant remains the same as the wildtype at about 10^9 $M^{-1}s^{-1}$, which is close to the limiting rate of substrate diffusion to the catalytic centre.

The Y34F mutant of hMnSOD was also found to be more susceptible to product inhibition by peroxide. Catalysis by hMnSOD showed an initial burst, followed by a much slower zero-order decay of superoxide. The slow down may be due to inhibition by binding of product peroxide dianion to the enzyme. The Y34F mutant is more susceptible than the WT to this effect. None the less, multiple turnovers occur before the enzyme is inhibited. The wild-type is less inhibited and has more catalytic cycles before inhibition occurs [168]. The region of zero-order catalysis in WT hMnSOD has a solvent hydrogen isotope effect between 2.2 and 3.1, suggesting a need for proton transfer in the steps in which product is released from the inhibited enzyme [173]. The product inhibition of WT and Y34F hMnSOD could not be overcome by the use of proton-donating buffers, implicating water as the source of protons (or deuterons).

The X-ray crystallographic structure of the hMnSOD Y34F mutant revealed very slight shifts in all metal and ligand positions, but changes are probably within the error limits of the model. The ring plane of His81 showed the most movement with a rotation of 20º in subunit A and 10º in subunit B. The aromatic ring of Phe34 in the mutant superimposes on that of Tyr34 in the WT, and because of the absence of the phenolic oxygen, the hydrogen-bonding relay in Y34F is broken. No additional solvent species permeate the active-site to maintain the relay.

E. coli FeSOD Y34F has also been purified and analysed [171]. In addition to the Y34F mutant, mutants Y34S and Y34C were prepared. The activities (normalised against the WT) for these three mutants are, respectively, 31 %, 1 % and 18 %. The Y34F mutant exhibited decreased thermal stability, which is in contrast to the results found for Y34F hMnSOD. The activity of Y34F was shown to decrease relative to that of the WT on increasing the pH from 7.8 to 11.0. Azide binding was tighter in the mutant, K_d = 0.1 mM, compared with WT, K_d = 2.0 mM.

4.1.3. Characterisation of mutants of Gln146

hMnSOD Q143N has been prepared and analysed with regards to thermal stability,

kinetics and X-ray crystallographic structure [169]. Two mutants of FeSOD from *M. tuberculosis*, H145Q and H145E have been structurally characterised, although no studies of activity or inhibitor binding have been done [170]. MnSOD Q146L, Fe_2MnSOD Q146L, MnSOD Q146H and Fe_2MnSOD Q146H, all from *E. coli*, have been analysed with regards to enzyme activity, pH dependence, ligand binding, and absorption spectroscopy [Whittaker1999, unpublished results]. The structures of the Q146H and Q146L mutants of *E. coli* MnSOD form the subject of this chapter.

The biochemical characterisation of hMnSOD Q143N revealed a number of effects of the mutation [169]. Enzymatic activity is markedly decreased in the mutant. The value of k_{cat} for the mutant is two orders of magnitude lower than that for the WT, and k_{cat}/K_M is three orders of magnitude lower than that for the WT. This contrasts significantly with the Y34F mutant from hMnSOD, which maintained the diffusion-controlled rate of the wildtype enzyme. Q143N is slightly more stable than the wild-type with an increase in T_M of 2ºC. Q143N lacks the typical WT Mn(III) visible absorption spectra. It also has a complex EPR spectrum, suggesting that the redox state of the metal centre is predominantly Mn(II), in comparison to the wildtype which is predominantly Mn(III).

Structurally, hMnSOD Q143N shows significant rearrangement. The mutation to Asn shortens the sidechain by a methylene group. An additional water moves into the cavity created by the effective shortening of this residue. The water lies in a similar position to that for the amido nitrogen of Q143, hydrogen-bonding to both Asn143 ND1 and a shifted Tyr34 OH. The new water also forms a hydrogen bond with the metal-bound solvent. Asn143 OD1 maintains the hydrogen bond to Trp123 NE1. The Tyr34 sidechain shifts by 0.4 Å in subunit B and 0.9 Å in subunit A. The main-chain of residues which connect the two domains shift 0.9 and 0.5 Å for subunits A and B, respectively. There are other subtle but significant differences between the two subunits. The Mn-OH distance is 2.26 Å in subunit A, being slightly longer than the typical distance of 2.0 Å, and indicating a possible change of OH^- to H_2O. Ligand-metal bonds expand in the mutant, consistent with a reduced, Mn(II), redox state for the metal ion.

In an attempt to alter metal ion specificity, H145Q and H145E mutants of *M. tuberculosis* FeSOD have been prepared [170]. The X-ray crystallographic structures of these enzymes were solved at 4.0 Å and 2.5 Å, respectively. Neither mutation revealed any gross effect on the conformation of the active-site. However, a more detailed analysis was limited by the low resolution of the structures.

4.2. Structure determination of Y34F

4.2.1. Crystallisation

Crystals were grown under similar conditions to the wild-type enzyme, i.e. 14 to 24 % w/v PEG 6000, 0.1 M bicine pH 8 - 9, and at protein concentrations of 2.5 or 9 mg/mL.

4.2.2. Data collection and processing

Two MnSOD Y34F data sets were collected. Both were collected at room temperature on a Rigaku R-Axis IIC image plate detector, using Cu-Kα radiation from a Rigaku RU-200B rotating anode generator. The first crystal on which data were collected was grown from 20 % w/v PEG 6000, 0.1 M bicine pH 8.3 at a protein concentration of 2.5 mg/mL. This crystal diffracted to a resolution of 2.6 Å. The second crystal, on which data were collected to 2.3 Å, was grown from 20 % w/v PEG 6000, 0.1 M bicine pH 8.3 at a protein concentration of 9.0 mg/mL, and in the presence of 25 mM NaN_3. Data were processed and scaled using the programs DENZO [146], and SCALEPACK [146]. The data were put on an approximately absolute scale using the scale factor taken from a Wilson plot. Relevant data collection and processing statistics are given in Table 4-3 (below).

4.2.3. Structure solution, model building and refinement

An initial model for refinement was created from the model of native MnSOD. The model was modified before refinement by removing the metal ions, all solvent water molecules, and the sidechains of all residues within a 10 Å sphere of Phe34. Rigid-body refinement of this model in TNT, with the four subunits of the asymmetric unit being treated as the rigid bodies, resulted in only small rotations and shifts and an increase in the value of R_{free} from 0.373 to 0.394. Rigid-body refinement was therefore abandoned, and an initial 30 cycles of restrained reciprocal space least-squares minimisation in TNT were carried out, decreasing R_{free} to 0.365. Two rounds of model building and refinement bought R_{free} to 0.325 and the R-factor to 0.294, at which point individual B-factor refinement saw the R_{free} drop a further 2.4 % to 0.301. A further 10 cycles of model building and refinement, including the addition of the metal ion and associated ligands, and some 231 solvent water molecules, created a model with a value for R_{free} of 0.231 and an R-factor of 0.199. Refinement and model statistics for Y34F MnSOD are given in Table 4-4 (below).

4.3. Structure determination of Q146L

4.3.1. Data collection and processing

Data were collected from two crystals at room temperature on a Rigaku R-Axis IIC image plate detector, using Cu-Kα radiation from a Rigaku RU-200B rotating anode

Table 4-3. Data collection and reduction statistics for *E. coli* Y34F, Q146H and Q146L MnSOD

Crystal	Y34F MnSOD	Q146H MnSOD	Q146L MnSOD
Space group	$C222_1$	$C222_1$	$C222_1$
Z (Z')	32(4)	32(4)	32(4)
Unit cell	*a*=100.845 Å	*a*=100.766 Å	*a*=101.698 Å
	b=108.893 Å	*b*=109.239 Å	*b*=109.297 Å
	c=182.882 Å	*c*=180.889 Å	*c*=181.722 Å
V(m), $Å^3$/Da	2.79	2.79	2.81
Solvent content	56 %	56 %	56 %
Mosaicity	0.30º	0.20º	0.21º
Data collection temperature	293 K	293 K	293 K
Data processing			
Resolution limits (of last shell)	40 - 2.3 Å	40 - 2.0 Å	40 - 2.0 Å
	(2.33 - 2.30)	(2.05 -2.00)	(2.05 -2.00)
Unique reflections	45092	68276	68589
Observed reflections	348981	400712	812160
Observed reflections after averaging	242697	227560	609197
Observed reflections after averaging $I > 1\sigma_I$	241639	220099	609136
Observed reflections after merging	43949	65122	66399
Observations deleted manually	116	210	3423
Redundancy	5.5	3.5	9.2
Completeness	97.5 % (79.2)	95.4 % (86.0)	96.8 % (87.4)
R_{merge} on intensities[1]	0.087 (0.298)	0.051 (0.327)	0.067 (0.255)
Overall I/σ	17.2 (3.2)	19.8 (4.5)	34.4 (4.7)

[1] $R_{merge} = \Sigma|I-\langle I\rangle|/\Sigma I$, where $\langle I\rangle$ is the mean of individual observations of intensities I.

generator. The second crystal was large enough to translate once in the X-ray beam when radiation damage of the exposed part of the crystal became too great. Data from the two crystals were indexed and integrated separately using the program DENZO [146]. Images from the first crystal were processed between 50.0 and 2.3 Å resolution. Images from the second crystal were processed between 4.0 and 2.0 Å resolution. Because the exposure times for these images were increased by a factor of four, the reflections from the second crystal were more intense. The processing was therefore truncated at 4.0 Å resolution to avoid having to increase the spot integration size to fit the low resolution reflections. Increasing the spot integration size would have the effect of introducing excessive number of overlaps to the integration of the high resolution data. The program

SCALEPACK [146] was used to scale and merge the resulting data from both crystals. The data were then put on an approximately absolute scale using the scale factor taken from a Wilson plot. Relevant data collection and processing statistics are given in Table 4-3 (opposite).

Table 4-4. Refinement and model statistics for *E. coli* Y34F, Q146H and Q146L MnSOD

Model	Y34F	Q146H	Q146L
PDB ID	-	-	-
No. of residues	820	820	820
No. of protein atoms	6508	6516	6528
No. of water molecules	303	444	300
No. of Mn ions	4	4	4
Average B-factors, $Å^2$			
Main-chain atoms	24.1	25.8	29.9
Side-chain atoms	25.6	25.1	31.9
Water molecules	27.4	34.4	35.5
Mn	11.6	13.5	16.9
Overall	25.0	26.0	31.0
Refinement			
Refinement program	CNS v0.5 [131]	CNS v0.4 [131]	CNS v0.5 [131]
Reflections used in refinement	43928	65109	66352
Reflections used in calculation of R_{free}	2220 (5.1 %)	3182 (4.9 %)	3258 (4.9 %)
Resolution limits	40.0-2.3 Å	40.0 - 2.0 Å	40.0 - 2.0 Å
R.M.S bond lengths	0.005 Å	0.005 Å	0.006 Å
R.M.S bond angles	1.19º	1.16º	1.13º
R-factor (all data)	0.164	0.192	0.189
R_{free} (all data)	0.192	0.211	0.214

4.3.2. Structure solution, model building and refinement

The structure was solved using molecular replacement with the structure of native dimeric MnSOD as the search model. The molecular replacement solution was shifted to the same asymmetric unit as the native structure. Rigid-body refinement was carried out in CNS generating a starting model for refinement having a value for R_{free} of 0.305 and an R-factor of 0.294. Five cycles of model building and refinement in CNS gave a model with a value for R_{free} of 0.214 and an R-factor of 0.189. Refinement and model statistics for Q146L MnSOD are given in Table 4-4.

4.4. Structure determination of Q146H

4.4.1. Data collection and processing

Data were collected from a single crystal at room temperature on a Rigaku R-Axis IIC image plate detector, using Cu-Kα radiation from a Rigaku RU-200B rotating anode generator. Use was made of the fact that the crystal was reasonably large (0.25 x 0.3 x 1.2 mm) in that the crystal was translated during data collection when the X-ray exposed part of the crystal had suffered significant radiation damage. The images were subsequently indexed and integrated to 2.0 Å using the program DENZO [146]. The program SCALEPACK [146] was used to scale and merge the resulting data. The data were then put on an approximately absolute scale using the scale factor taken from a Wilson plot. Relevant data collection and processing statistics are given in Table 4-3 (above).

4.4.2. Structure solution, model building and refinement

The structure of MnSOD Q146L was used as the starting model for refinement of MnSOD Q146H, having a value for R_{free} and a R-factor against the MnSOD Q146H data of 0.332 and 0.323, respectively. An initial round of automated torsion-angle dynamics simulated-annealing refinement against maximum-likelihood targets was carried out in CNS. This procedure starts with 200 conjugate-gradient minimisation steps to gain initial estimates of σ_A and the weight for the maximum-likelihood target. Torsion angle molecular dynamics in combination with simulated annealing is then started from a temperature of 2500 K and decreased to 0 K in 25 K steps. Finally, two cycles of 100 steps of conjugate-gradient minimisation are carried out, between which the σ_A and weight values are updated. This automated simulated annealing protocol produced a model having a value for R_{free} of 0.300 and an R-factor of 0.272. Four further rounds of model building and refinement, including the addition of 444 waters, produced a final model having a value for R_{free} and a R-factor of 0.211 and 0.192. Refinement and model statistics for Q146H MnSOD are given in Table 4-4 (above).

4.5. Structural description of Y34F

4.5.1. Structural effects of the Y34F mutation

Tyr34 is absolutely conserved in all Fe and MnSODs. The phenolic oxygen of this residue lies 5.4 Å from the metal, and forms part of the hydrogen-bonding relay linking the metal with solvent in the substrate-access funnel *via* Gln146 and the metal bound hydroxide. Its mutation to phenylalanine causes only small rearrangements of the residues in and around the active-site. The mutation breaks the 3.0 Å hydrogen bond with the NE2 nitrogen of Gln146, and the hydrogen bond with the water in the substrate-access funnel. No water is observed to move into or near the site vacated by the OH of

Tyr34 in the Y34F mutant. The loss of these position-restraining hydrogen bonds, coupled with the change in steric and polar character for this residue, causes a small change in the rotamer of Phe34. The ring plane of Phe34 swings around chi1 by 3 - 4° toward Gln146, which corresponds to a shift of 0.37 Å for the CZ carbon of the phenyl ring (Figure 4-1). The average chi1 of Tyr34 and Phe34 for the four subunits in there respective structures is -65.8° (esd = 0.6°), and -69.3° (esd = 1.0°), respectively. The main-chain of helix A1 is slightly offset from the corresponding position in the native structure, being further away from A2 and the active-site. The shift starts around Phe34 and extends to the end of the helix, with main-chain atoms shifting by between 0.1 and 0.2 Å. This movement of A1 also contributes to the change of position of Phe34 relative to Tyr34 in the native structure.

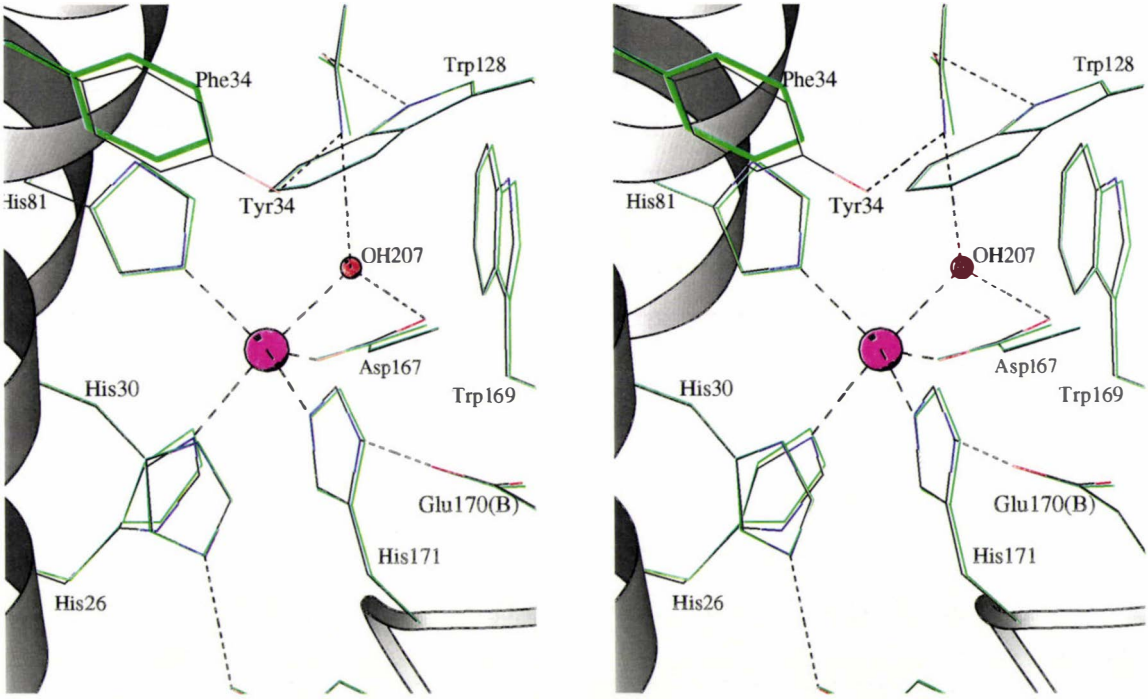

Figure 4-1. A stereo diagram showing an overlay of Y34F and the native structure in the region of the mutation

A stereo diagram showing an overlay of Y34F subunit A (green) and the native subunit A (coloured by atom-type) in the region of the mutation. The mutated residue Phe34 is shown in thick green lines. The largest change is in Phe34, undergoing rotation in chi1 by 3 - 4°. The Mn ion is represented by the larger purple sphere, and its coordinated solvent by the smaller red sphere. Figure drawn with MOLSCRIPT [1].

The active-site geometry of the mutant is very similar to that of the native. There are small differences in the bond lengths and angles of ligands associated with the metal. All

metal bond lengths (averaged over the four subunits) decrease by between 0.02 and 0.08 Å, with standard deviations ranging between 0.01 and 0.05 Å. This may represent a higher proportion of Mn(III) in the Y34F mutant. The hydrogen bond between Gln146_NE2 and the metal-bound solvent decreases in the mutant structure by 0.12 Å to 2.88 Å, but also shows the most variability having a standard deviation of 0.10 Å, averaged over the four subunits. Metal ligand rotamers also show more variability in Y34F than the native. In the native structure the standard deviations for the chi1 and chi2 torsion angles range between 0.1° and 2.6°, with the largest deviation shown in the chi2 of Asp167. In the mutant structure, these standard deviations range between 0.5° and 5.1°. The largest deviation is again shown by the chi2 of Asp167, but significant deviations of 3.1° and 3.5° are shown by the chi2 angles of His26 and His81.

The hydrogen bond of Tyr34 to the water in the substrate-access funnel is also broken by the mutation. Of the 16 waters in the substrate-access funnel of Y34F, 15 can be found in equivalent positions in the native structure (see Figure 4-2 opposite). The extra water in the Y34F structure is found in chains B, C and D, and is near the edge of the substrate-access funnel. There are 17 waters in the substrate-access funnel of the native structure, two of which do not have a corresponding fully occupied water in the Y34F structure. In the native structure the water involved in the hydrogen bond with Tyr34 is present in all four subunits, and is well ordered, having an average B-factor of 18.0 $Å^2$ (compared with the average solvent B-factor in the structure of 31.6 $Å^2$). In Y34F this water is only seen at an occupancy of close to 1.0 in subunit C, having a B-factor of 28.0 $Å^2$, being preserved by its hydrogen bonds with neighbouring waters in the substrate-access funnel. However, residual electron density in subunit D suggests the possibility of a low occupancy water in an equivalent position in this subunit. The native structure also has another water in contact with Tyr34. This water is 3.48 Å from the phenolic oxygen, and is in a poor geometry for a hydrogen bond. It is only seen in subunits B and D of the native structure.

The position of Phe34 does not leave sufficient room for a water to hydrogen bond directly with the NE2 nitrogen of Gln146. Such a water would have 2.7 - 3.0 Å contacts with carbon atoms on Phe34 and Trp169. Subunit D however does have some residual diffuse electron density in this position at the 2 - 3σ level in a 1|Fo-Fc| electron density map. The peak of the diffuse electron density corresponds to a position ~ 2.1 Å from Phe34_CZ and ~ 3.0 Å from the Gln146_NE2. Similar residual density, also in subunit D, indicates the possibility of a low occupancy water 2.6 Å from the ND1 nitrogen of His30.

4.5.2. Tertiary structure

Pairwise RMS deviations for the monomers of Y34F range between 0.15 and 0.35 Å for

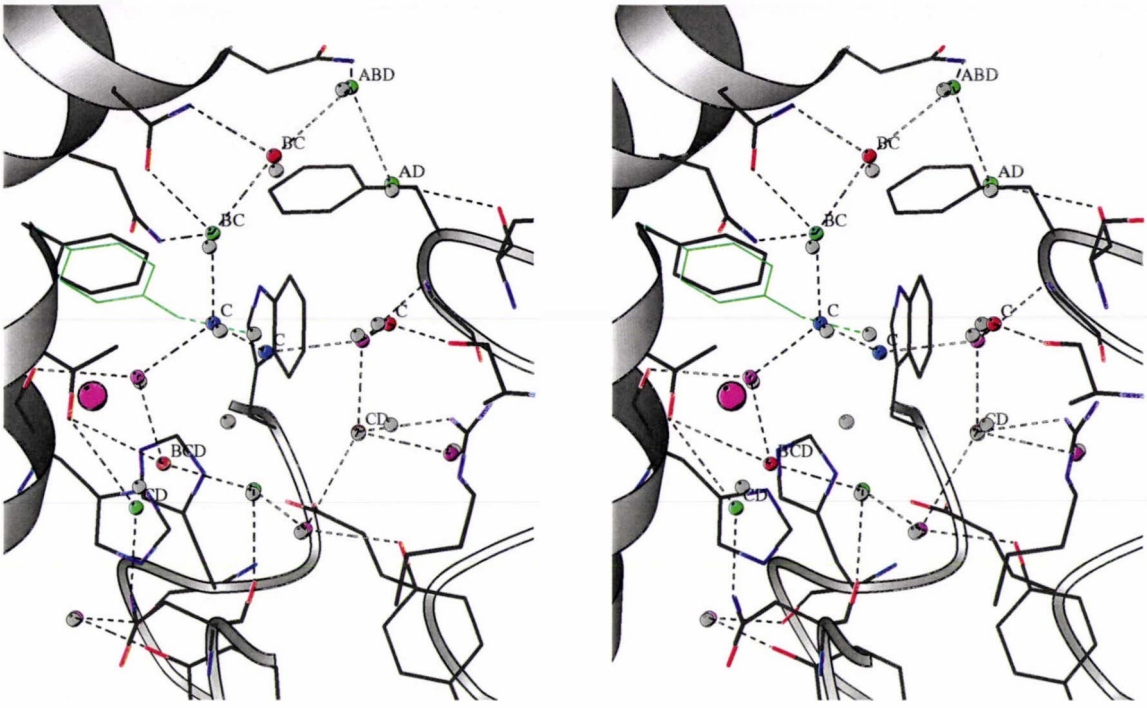

Figure 4-2. A stereo diagram of the waters in the substrate-access funnel of Y34F MnSOD

The 16 waters in the substrate-access funnel of Y34F are coloured by B-factor. B < 25 $Å^2$, purple; 26 - 30 $Å^2$, blue; 31 - 35 $Å^2$, green; 35+ $Å^2$, red. The average B for solvent in the protein is 28 $Å^2$, and for the 16 waters in the substrate-access funnel, 30 $Å^2$. The unique waters in the substrate-access funnel of the native structure are superimposed for comparison, and drawn as grey spheres. Tyr34 of the native structure is shown in green, along with its hydrogen bond to a water in the substrate-access funnel. Labels on water molecules indicate that an ordered water molecule was *not* found in all four subunits at this position. The label lists the subunits in which ordered water molecules *were* found. No label indicates the water was present in all four subunits. The Mn ion is represented by the larger purple sphere. Figure drawn with MOLSCRIPT [1].

superpositions based on all 820 main-chain (C, CA, N, O) atoms in the dimer. If atom pairs are excluded when their deviation is greater than 3.0 times the overall standard deviation, the pairwise RMS deviations range between 0.02 (for a subset of 420 main-chain atoms) and 0.06 Å (for a subset of 600 mainchain atoms). The greatest deviations occur at the N-terminal region, the loop between A1 and A2, and for residues 134 - 136.

Consistent with the facts that the mutation is conservative, interior to the enzyme, and not directly involved in the dimer interface, the tertiary structures of the native and mutant are highly similar. Figure 4-3 (below) shows an overlay of the Cα trace of the native and Y34F mutant structures. Pairwise RMS deviations for the dimers of Y34F superimposed on the dimers of the native structure range between 0.15 and 0.35 Å for superpositions based on all 820 main-chain (C, CA, N, O) atoms in the dimer.

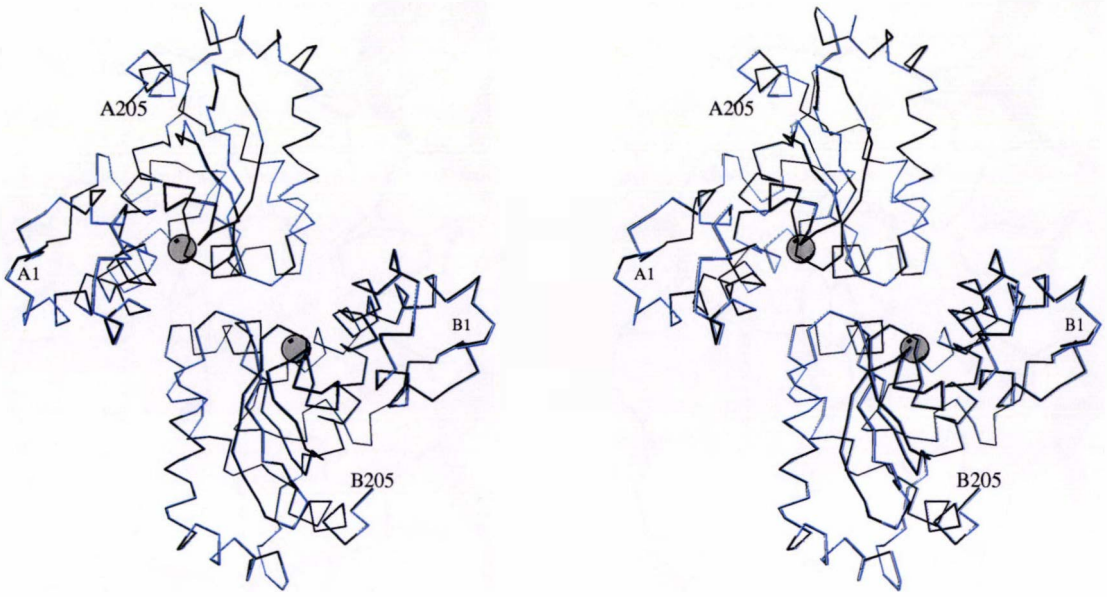

Figure 4-3. A stereo plot of the Cα main-chain trace of the native and Y34F AB dimers, overlaid using the A subunit of each dimer

The 820 main-chain (C, CA, N, O) atoms of subunit A were used to perform the overlay. Using only one subunit in the overlay has the effect of showing the extent of the reorientation of subunit B with respect to subunit A. Native structure in black, and Y34F in blue. The two grey spheres represent the Mn ions in the active sites. Figure drawn with MOLSCRIPT [1].

4.6. Structural description of Q146H

4.6.1. Structural effects of the Q146H mutation

Gln146, whilst not a metal ligand, is an important inner-sphere residue. The hydrogen bond between the metal-coordinated solvent molecule and a nitrogen atom on either a Gln or His is conserved in all Fe and MnSODs. In the native structure, Gln146 is involved in four hydrogen bonds. The NE2 nitrogen of Gln146 is the donor in hydrogen bonds with the metal-coordinated solvent (2.95 Å), and the phenolic oxygen of Tyr34 (2.97 Å). The OE1 oxygen of Gln146 is an acceptor in a hydrogen bond with the NE1 nitrogen of Trp128 (2.97 Å) and a weaker hydrogen bond (3.34 Å) with the ND2 nitrogen of Asn80 (see Figure 4-4 opposite). In the mutation to histidine, three of these four hydrogen bonds are broken, with only the hydrogen bond to the metal-coordinated solvent remaining.

The rotamer adopted by His146 would create 2.3 Å contacts between the histidine CE1 carbon and the CZ and OH atoms on Tyr34. The steric repulsion of these close contacts coupled with the loss of the hydrogen bond to residue 146 causes a rotation of the Tyr34 side-chain into the substrate-access funnel. This rotation of 17.3° in chi1, and 8.8° in chi2

(native Tyr34 average chi1,chi2 = -65.8°, -49.0°; Q146H Tyr34 average chi1,chi2 = -48.5°, -40.2°; and a shift of the phenolic oxygen by 1.5 Å), causes changes in the positions of ordered solvents within the substrate-access funnel, but does not affect the positions of any other residue side-chains. The sidechain of Tyr34 forms a 2.8 Å hydrogen bond with an ordered water in the substrate-access funnel, the hydrogen bond being present in all four subunits. In the mutant structure the phenolic oxygen lies only 3.7 Å from the ND1 nitrogen of His30, but the proximity of the tyrosine to the histidine does not affect the position of His30.

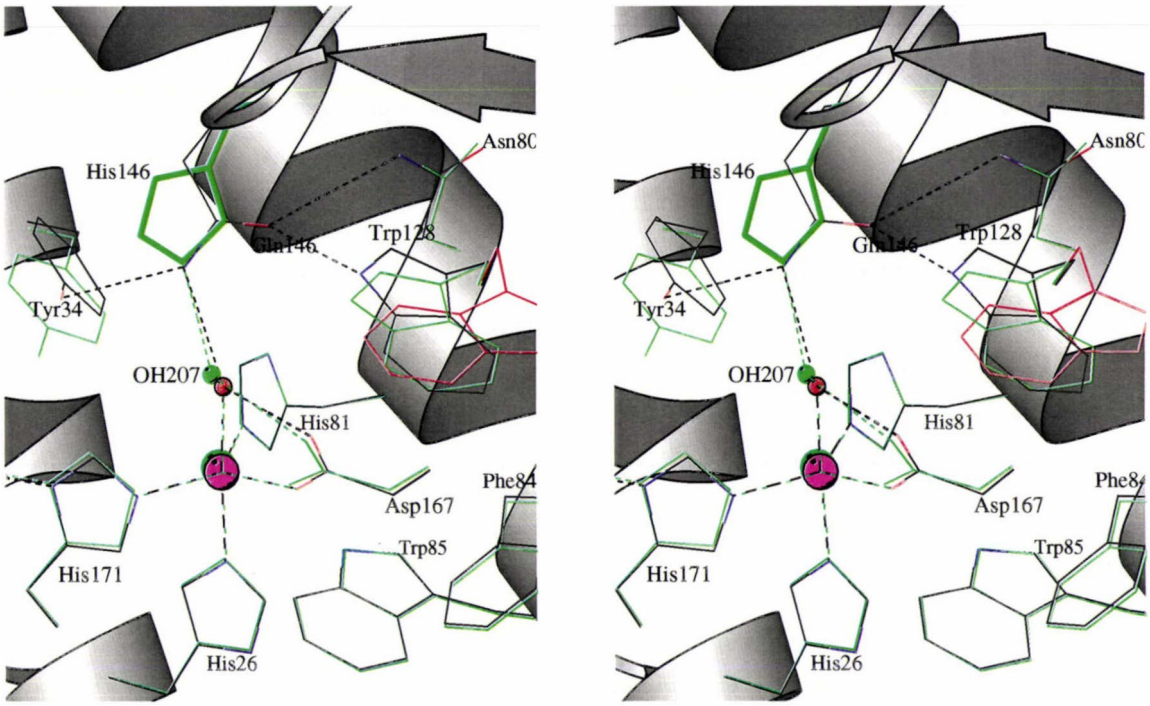

Figure 4-4. A stereo diagram showing an overlay of Q146H and the native structure in the region of the mutation

Q146H structure in green (alternate conformation of Trp128 in red), and native structure coloured by atom-type. The Mn ion of the native structure is coloured purple. Figure drawn with MOLSCRIPT [1].

The hydrogen bonds between the OE1 oxygen of Gln146 and residues Asn80 and Trp128 are not conserved on the mutation of Gln146 to histidine. In the native structure, the side-chain of Asn80 forms two hydrogen bonds. Both hydrogen bonds are formed *via* the ND2 nitrogen which acts as the donor in a 3.34 Å hydrogen bond to Gln146, and the donor in a 2.93 Å hydrogen bond with the main-chain oxygen of Gln146. The mutation of residue 146 to a histidine removes the acceptor for the first hydrogen bond, and the

Asn80 side-chain undergoes a rotation. The chi2 angle of Asn80 changes, on average over the four subunits, from -17.5° (s.d. = 1.2°) in the native to 0.6° (s.d. = 3.8°) in the mutant. The rotation lengthens the hydrogen bond to the main-chain oxygen of Gln146 to 3.40 Å, and allows the ND2 nitrogen of the side-chain to act as a donor in a hydrogen bond to the main-chain oxygen of Asp147. The OD1 oxygen of Asn80 forms a hydrogen bond with a buried water that is conserved in the mutant. The hydrogen bond between Gln146 and the side-chain of Trp128 is also broken because of the loss of the Gln146 OE1 oxygen acceptor on mutation. In this case the effect on the tryptophan is quite dramatic, occupying at approximately 50 % occupancy a discrete alternate conformation. Trp128 lies in a large solvent-excluded cavity, and the alternate conformation adopted is an approximately 180° rotation around chi2. The chi1, chi2 angles for the native Trp128 side-chain are -66.4° and 72.7°, and for the alternate conformation in the mutant, -131.4° and -87.0°. In the alternate conformation of Trp128 no hydrogen bonds are formed with the side-chain. The movement of Trp128 causes a slight rotation of Trp130 around chi2 (95.2° in native and 87.8° in mutant) due to steric repulsion.

The main-chain of the first half of helix A2 in the Q146H structure deviates from the native structure. The shift at the start of the helix (residue 66) is up to 1.0 Å, but drops back to normal deviations (0.1 - 0.2 Å) by residue 77. The main-chain shift allows the 2.98 Å hydrogen bond between Asn73_O and His146_ND1. The side-chain of Phe124 also shifts to reoptimise its packing against the side-chain of Asn73. The altered position of the Phe124 is a result of both movement of its main-chain, and rotations of its chi2 side-chain torsion angle (chi2 native, 73.5°; chi2 mutant 85.4°). Phe124 forms part of the lip of the substrate-access funnel.

Metal-ligand bond lengths in the mutant and native structures are very similar with the differences in the bond lengths ranging from -0.03 to 0.06 Å, being in the same range as the standard deviations of the values when compared over the four subunits. The bond angles differ slightly on account of the movement of the metal-coordinated solvent. The His26_NE2-Mn-OH207_O angle of 174.6° in the native is 177.9° in the mutant structure, becoming more linear. The Asp167_OD1-Mn-OH207_O angle changes the most, being 53.6° in the native structure and 63.1° in the Q146H.

4.6.2. Tertiary structure

Pairwise RMS deviations for the monomers of Q146H range between 0.14 and 0.43 Å for superpositions based on all 820 main-chain (C, CA, N, O) atoms in the dimer. If atom pairs are excluded when their deviation is greater than 3.0 times the overall standard deviation, the pairwise RMS deviations then range between 0.02 (for a subset of 420 main-chain atoms) and 0.07 Å (for subsets of 500 - 600 mainchain atoms). The greatest deviations occurring at the N-terminal region, the loop between A1 and A2, residues 134

- 136, and at the C-terminus.

Figure 4-5 shows an overlay of the Cα trace of the native, Q146H and Q146L AB dimers. Pairwise RMS deviations for the dimers of Q146H superimposed on the dimers of the native structure range between 0.38 and 0.61 Å for superpositions based on all 1640 main-chain (C, CA, N, O) atoms in the dimer. The regions of largest deviation are the N-terminus, the loop between A1 and A2, the A3 - A4 loop, residues 134 - 136, and the loop between B2 and B3.

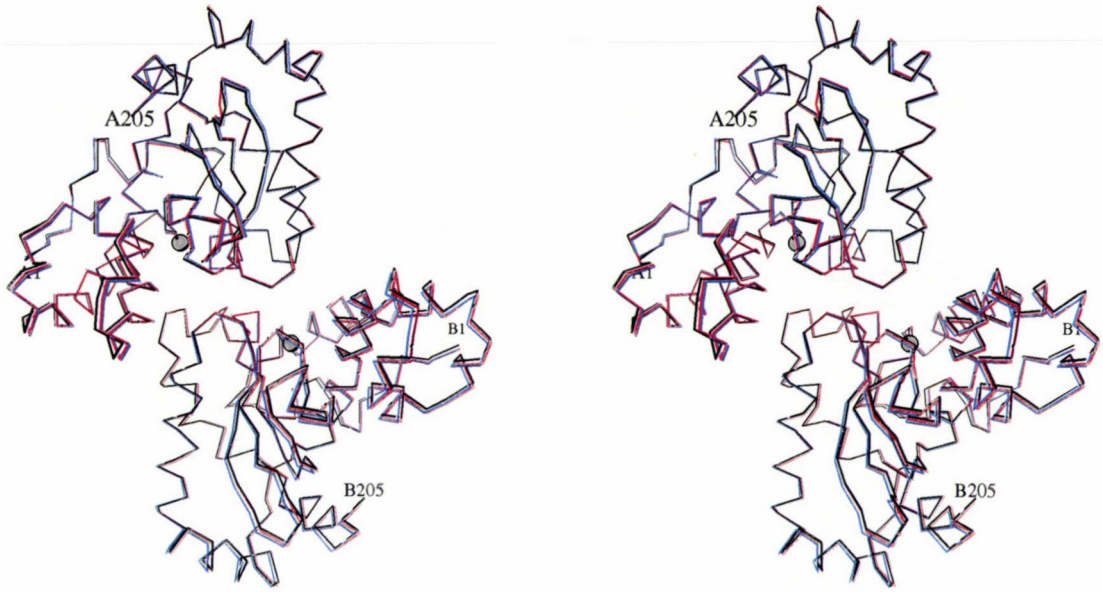

Figure 4-5. A stereo plot of the Cα main-chain trace of the native, Q146H, and Q146L AB dimers

The 1640 main-chain (C, CA, N, O) atoms of the dimer were used to perform the overlay. Native structure in black, Q146H in blue and Q146L in red. The two grey spheres represent the Mn ions in the active sites. Figure drawn with MOLSCRIPT [1].

4.6.3. Comparison with natural His146 MnSOD from *P. shermanii*

The only structure determined having a histidine naturally present at position 146, and that is active with manganese, is the cambialistic SOD from *P. shermanii*. An overlay of the active-site of *E. coli* Q146H MnSOD and *P. shermanii* MnSOD (PDB ID: 1AR5) reveals the primary metal protein-ligands to occupy similar geometries. The bond length of the metal-bound solvent molecule to metal bond is longer in Q146H by ~ 0.2 Å (2.3 as opposed to 2.1 Å). More extensive differences in the hydrogen-bonding patterns around the active-sites of these two enzymes exist due to subtle differences in positions of residues His146, Trp128 and Tyr34.

In *P. shermanii* MnSOD, the orientation of the His 146 ring-plane is not clearly defined in that it may be subject to a flip of ~ 180° around chi1, completely reorienting its hydrogen bond donors and acceptors [138]. Potential hydrogen bonds with His146 in both enzymes are shown in Table 4-5. At the pH for which Q146H MnSOD was crystallised (8.5), the ND1 nitrogen of His146 is likely to be de-protonated or partially protonated at best. Thus, there may only be a partial hydrogen-bond with the main-chain oxygen of Asn73, even considering the favourable geometry. In contrast with *P. shermanii* MnSOD, the orientation of the His146 ring-plane is defined in *E. coli* Q146. The modelled orientation is likely to be the correct one due to the strong hydrogen bond between His146_NE2 and the solvent bound water molecule. Weaker hydrogen bonds to Trp128_NE1 (3.6 Å) and Tyr34_OH (3.6 Å), and a less favourable His146_CE1 ... OH207 interaction, make adoption of the other orientation unlikely.

Table 4-5. Selected inter-atomic contacts associated with His146 in *E. coli* Q146H MnSOD and *P. shermanii* MnSOD

Residue numbering for *P. shermanii* MnSOD given in parentheses. The covalent bond distance between the metal and its bound solvent is also given.

				Q146H	*P. sher*
Mn206	MN	OH207	O	2.3	2.1
His146 (His146)	NE2	OH207	O	2.8	3.2
His146 (His146)	ND1	Asn73 (Phe67)	O	3.0	3.7
His146 (His146)	CD2	Trp128 (Trp126)	NE1	3.6	3.0
His146 (His146)	CE1	Tyr34 (Tyr35)	OH	3.6	3.1

4.7. Structural description of Q146L

4.7.1. Structural effects of the Q146L mutation

The leucine side-chain has no hydrogen bond acceptor or donor atoms, so the four hydrogen bonds that Gln146 makes in the native structure cannot be made when the glutamine is mutated to leucine. Leucine is one methyl carbon shorter in length than glutamine, but has sp^3 hybridisation of its CG carbon as compared with the sp^2 hybridisation of the CD carbon of glutamine, affording the leucine a similar steric bulk. The leucine is, however, a hydrophobic residue, so would be expected to prefer different residue packing contacts to that of the polar glutamine. Leu146 adopts a similar rotamer (see Figure 4-6 opposite) to Gln146, having a similar value for the chi1 torsion angle of -67.0°, and -67.6°, respectively. The chi2 torsion angle is largely determined by residue packing contacts of which there are nine between 3.1 and 3.8 Å.

The sidechain of Tyr34 is rotated away from Leu146 due to steric repulsion by the CD1

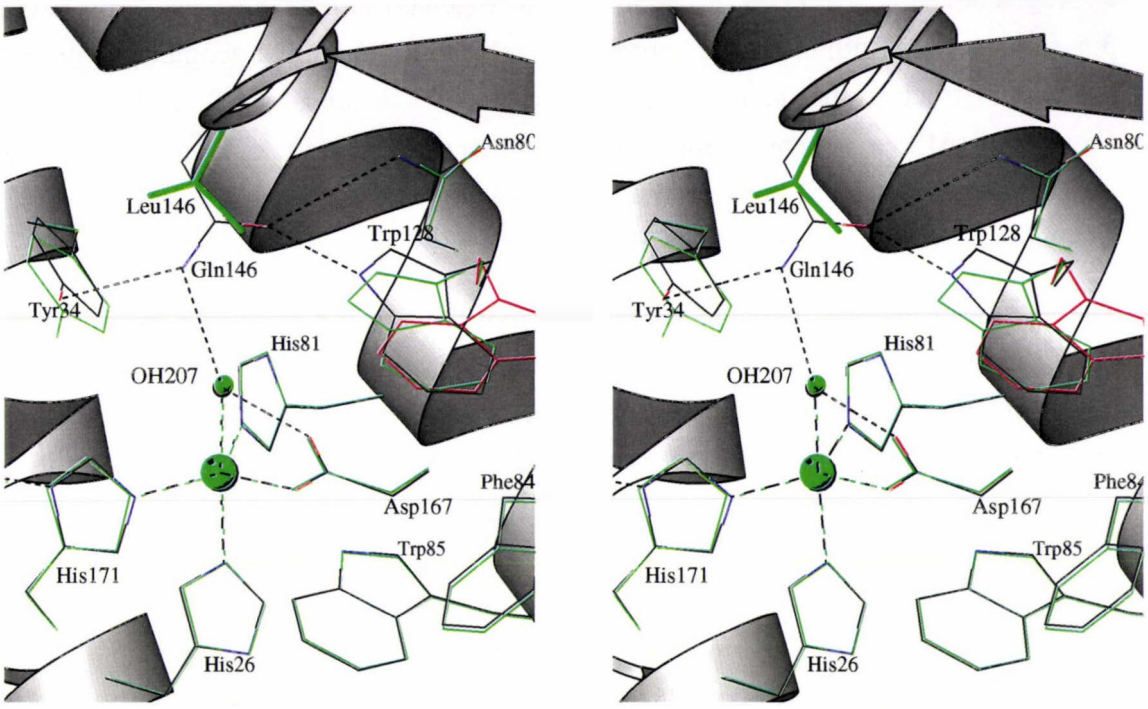

Figure 4-6. A stereo diagram showing an overlay of Q146L and the native structure in the region of the mutation

Q146L structure in green (alternative conformation of Trp128 in red), native structure coloured by atom-type. Figure drawn with MOLSCRIPT [1].

carbon of Leu146. If the native conformation of Tyr34 were to be maintained, the Leu146 CD1 to Tyr34 CZ, CE1 and OH contracts would be 2.95, 3.15 and 3.11 Å, respectively. Instead, rotation of 11.3° (native chi1, chi2 are -65.8°, -49.0°; Q146L chi1, chi2 are -54.5°, -44.4°) around chi1 and a small rotation around the ring plane extend these contact distances to 3.52, 3.59 and 3.81 Å.

Asn80 and Trp128 both rearrange their side-chain rotamers as a result of losing their hydrogen bonds to the residue 146. Asn80 rotates in chi2 (native chi2, -65.2°; Q146L chi2, -68.7°). The rotation allows the ND2 nitrogen of Asn80 to form a 2.9 Å hydrogen bond with the main-chain oxygen of Asp147 as also occurs for Q146H. This new hydrogen bond forms at the expense of the existing hydrogen bond between Asn80_ND2 and the mainchain oxygen of residue 146, which lengths from 2.9 Å in the native structure to 3.3 Å Q146L. Trp128 without the hydrogen bond to residue 146 is more flexible. It undergoes a rotation of 19.1° in chi1 and 23.3° in chi2 to accommodate the change in position of Asn80, the 3.4 Å contact between Asn80_ND2 and Trp128_NE1 being extended to 4.1 Å. Without the hydrogen bond with residue 146 to hold the Trp128 side-chain in place, the side-chain becomes disordered, adopting the same alternate conformation seen in Q146H. In the Q146L mutant, the NE1 nitrogen of Trp128 forms no

hydrogen bonds in either conformation. The hydrogen on Trp128_NE1 may have a weak 3.5 Å interaction with the metal-coordinated solvent, although the geometry is poor. In the native structure the same Trp128_NE1 to OH207 distance is 4.0 Å. The disorder shown by Trp128 is not consistent in all four subunits. In subunit A, the tryptophan sidechain is split about 50:50 between the native and alternate conformations. In subunits B, C and D, this ratio is closer to 80:20.

The active-site ligands maintain very similar positions to the native structure, varying less from the native structure than those in Q146H (see Figure 4-6 above). Bond lengths in Q146L show the same variability as those in Q146H with respect to the native structure, with differences between the mean bond lengths of the Q146L and native structures, calculated over the four subunits, ranging from -0.04 to 0.05 Å.

4.7.2. Tertiary Structure

Pairwise RMS deviations for the monomers of Q146L range between 0.16 and 0.48 Å for superpositions based on all 820 main-chain (C, CA, N, O) atoms in the dimer. If atom pairs are excluded when their deviation is greater than 3.0 times the overall standard deviation, the pairwise RMS deviations range between 0.06 (for a subset of 505 main-chain atoms) and 0.14 Å (for subsets of 500 - 600 mainchain atoms).

Pairwise RMS deviations for the dimers of Q146L superimposed on the dimers of the native structure range between 0.39 and 0.55 Å for superpositions based on all 1640 main-chain (C, CA, N, O) atoms in the dimer (see Figure 4-5 above). The regions of largest deviation are the same as those in Q146H; the N-terminus, the loop between A1 and A2, the A3 - A4 loop, residues 134 - 136, and the loop between B2 and B3.

4.8. Discussion

4.8.1. Y34F

Residues in the secondary coordination sphere of catalytic metal ions are well known to modulate the behaviour of the metal via their interactions with metal-ligands. These residues catalytically fine-tune the enzyme by correctly orienting critical residues, modifying the redox properties of the metal system, altering substrate-metal binding properties and affecting metal-charge stabilisation, all of which affect catalytic activity [174, 175, 139, 176, 177, 178, 179].

The structural effects of the Y34F mutation are subtle, the most noticeable being a rotation of the phenylalanine sidechain and that no additional solvent diffuses into the active site to maintain the hydrogen-bond relay linking the Tyr34 to the metal ion via Gln146, and the metal-bound solvent molecule.

The Y34F mutation causes the loss of hydrogen bonds to Gln146 and solvent in the substrate-access funnel, and is coupled to a rotation of the phenylalanine side-chain around chi1, displacing the CZ atom of the phenyl ring ~ 0.4 Å from its corresponding position in the wildtype tyrosine. The Gln146_NE2 ... OH207 hydrogen bond is stronger in the mutant but also shows the most variability over all four subunits of the mutant. Solvent structure in the substrate-access funnel is very similar except the water that forms a hydrogen bond with Tyr34_OH in the wildtype is less ordered in the Y34F mutant. Importantly it can be confirmed that no ordered water diffuses into the active-site on any significant scale. This confirms that the proposed hydrogen-bond relay from the substrate-access funnel to the metal is completely disrupted by the mutation. However, this disruption is accompanied by only ~ 20 % loss of activity at pH 7.8 and 9.0. Either the proton shuttle is not particularly important to catalytic activity, or highly dissociated water replaces the Tyr OH group to maintain the proton shuttle.

Redox potentials of Y34F mutants of MnSOD and FeSOD have not been measured, so the effect of this mutation on the thermodynamic stability of the metal-ligand complex is not known.

Azide affinities have been measured at a variety of pH values for both wildtype and Y34F mutant MnSOD and Fe_2MnSOD. In all cases azide affinity for the Y34F mutant structures increases by 1.5 - 4 times over the wildtype (see Table 4-2 above). Substrate binding is affected by both steric and electrostatic factors, including charge stabilisation of the metal, and substrate-protein interactions. Tighter binding of the negatively charged substrate analog in Y34F mutants could be due to an overall more positive charge on the metal centre, or stabilisation of the azide-enzyme complex by more favourable interactions with protein residues.

The structure of azide complexed to MnSOD from *T. thermophilus* (PDB ID: 1MNG) shows azide binding in the sixth, vacant coordination site, with the linear azide molecule pointing toward the substrate-access funnel and Tyr34, and lying close and parallel to the ring-plane of the coordinated histidine ligand (His171, *E. coli* numbering scheme) [6]. The coordinated azide forms hydrogen bonds with Tyr34_OH (2.6 Å) and His30_ND1 (3.2 Å, *E. coli* numbering scheme). In contrast, in FeSOD-azide structures from *E. coli* (PDB ID: 1ISC) and *P. shermanii* (PDB ID: 1AVM), the azide points away from the substrate-access funnel, into the cavity around the active-site and forms no hydrogen bonds.

Azide has been shown to bind to both wildtype and Y34F *E. coli* MnSOD. However, X-ray crystallographic structures of this complex could not be determined. Crystals of wildtype and Y34F grown using azide-complexed enzyme, and crystals soaked in azide both fail to show azide at the active site, or anywhere else in the structure. It cannot be determined from the Y34F mutant structure alone why this apparent anomaly exists

between azide complexing to the solution-state as determined spectroscopically, and the solid-state crystallographic results. The pH of crystallisation (8.5) is higher than the pH at which the dissociation constant of azide was measured (7.0). In the iron-substituted enzyme, azide affinities decrease with increasing pH. The pH dependence of azide binding to wildtype and Y34F MnSOD has not been determined. The increasing ionisation of the tyrosine side-chain in the wildtype would likely destabilise the binding of the azide molecule if it were to bind in a geometry similar to that of MnSOD from *T. thermophilus,* as the hydrogen bond between Tyr34 and azide would be replaced by a negatively charged dipole on ionisation of Tyr34. However, azide is also absent from the active site of Y34F MnSOD, and as Phe34 has no negatively-charged dipole, the absence of azide in the crystallographic structures cannot be solely a consequence of the effect of pH of crystallisation on Tyr34.

4.8.2. Q146H

The activity of Q146H MnSOD is 10 % of that of the wildtype. A small number of Mn and FeSOD naturally have histidine at this position and are, or presumed to be, biologically active. The naturally occurring His146 enzymes all have a glycine at position 77. Typically in FeSODs residue 77 is a glutamine. The glutamine and histidine substitutions are mutually exclusive in that steric requirements would otherwise see these two residues occupying the same space. All MnSODs have a glycine at position 77 so the single-point Q146H mutation of *E. coli* MnSOD is sterically feasible.

The histidine side-chain of residue 146 adopts a conformation sterically similar to that of the wildtype glutamine it substitutes. Because of the different types and positions of hydrogen-bonding groups on the histidine, the hydrogen-bonding network of the wildtype is disrupted, leading to movement of Tyr34 and disorder of Trp128.

Both hydrogen bonds formed between Gln146_OE1 in the wildtype and the residues Asn80 and Trp128 are broken by the Q146H mutation. In the wildtype, Asn80 and Trp128 orient the glutamine, and also possibly modulate its character. These roles can be further examined in future mutation studies. The loss of the hydrogen bond with Trp128 causes conformational disorder of this residue, which adopts two positions in equal amounts, the wildtype orientation and another in which the Trp128 side-chain rotates ~180º around chi1. The NE1 nitrogen of Trp128 in the new orientation seen in the Q146H mutant is not involved in any hydrogen bonds. The orientation of the His146 ring-planes in X-ray crystallographic structures where residue 146 is a naturally occurring histidine, differ. The two FeSODs (*M. tuberculosis* PDB ID: 1IDS, *S. solfataricus* PDB ID: 1SSS) with a histidine at position 146 share the same orientation. The CE1 of the histidine points toward OH207, the NE2 at Tyr34, and the ND1 at Trp128. The analogous histidine of the cambialistic MnSOD (*P. shermanii* PDB ID: 1AR5) and the

Q146H *E. coli* mutant share the opposite orientation to that of the two iron structures. If the histidine is involved in modulating the character of the metal ion via the metal bound solvent, then the orientation of His146, and its hydrogen bonds, becomes important.

In the cambialistic *P. shermanii* MnSOD, the orientation of the histidine ring-plane could not be determined unambiguously [138]. Suitable hydrogen bond lengths (3.0 -3.2 Å) occur for three of the four possible hydrogen bonds formed when both orientations are considered. The possibility that the histidine changes its ring-plane orientation depending on pH, metal-ligand environment, or metal oxidation state can not be discounted. High-pH protonation of the histidine in the orientations modelled for the FeSODs is not possible without rearrangments of residues because Trp128_NE1 must act as the hydrogen bond donor. Involvement of the histidine in a proton-transfer relay in an analogous fashion to that proposed for the Gln146 of *E. coli* MnSOD [162] is not possible with either of the static orientations, but could be accommodated by a mechanism where a histidine ring flip promotes the ND1 hydrogen bond donor alternately to Tyr34 and the metal-bound solvent.

The orientation of His146 in the *E. coli* Q146H mutant can be assigned unambiguously, in contrast with the *P. shermanii* structure. Both hydrogen bonds in the alternate orientation of Trp128_NE1 and Y34_OH are very weak at 3.6 Å. In the orientation as modelled, both ND1 and NE2 make reasonable hydrogen bonds at 2.8 and 3.0 Å respectively. In both hydrogen bonds the histidine acts as the hydrogen donor. Because of the arrangement of strong hydrogen bonds in the modelled orientation and weak hydrogen bonds in the alternate conformation, the inactive Q146H *E. coli* MnSOD is unlikely to undergo any dynamic flipping of is His146 ring.

4.8.3. Q146L

The Q146L mutation is nearly isosteric being one methylene carbon shorter. Not being completely isosteric makes it more difficult to distinguish between changes due to the loss of all hydrogen-bonding groups, and those due to steric repulsion from the different atomic arrangement.

Rearrangements occur for Tyr34, Asn80 and Trp128, largely due to the loss of hydrogen bonds between these residues and Leu146. Tyr34 moves towards the substrate-access funnel due to repulsion from the CD1 carbon of leucine. In both the Q146H and Q146L mutants, the rotation of Tyr34 can be determined to be entirely due to steric repulsion from residue 146, rather than loss of a hydrogen bond to the same residue. Movement due to loss of the hydrogen bond can be discounted as Phe34 in the Y34F mutant undergoes very little rotation, and in fact rotates toward residue Gln146. Trp128 exhibits disorder in the same way that occurs in the Q146H mutant, and Asn80 reorients to

maximise its hydrogen bonding potential.

The position of the metal-bound solvent is largely unaffected by both the Q146H and Q146L mutations, having bond distances (2.31 and 2.30 Å respectively) comparable to the native (2.27 Å). Thus residue 146 appears not to modify the ligand-field strength of the metal-bound solvent appreciably.

Both the Q146H and Q146L mutations, while drastically reducing activity to 10 % and 5 % of that of wild-type MnSOD, respectively, do not completely stop superoxide dismutase activity. Gln146 is therefore not essential for activity, but must act to optimise the dismutation reaction. Optimisation of the reaction may occur in proton transfer to the product, stabilisation of ligand displacement [162], or in modifying the stability of the metal iron and therefore its redox potential. The latter can be examined by determining the redox potentials of these mutants.

4.9. Conclusions

The proposed hydrogen-bond relay from the substrate access funnel to the metal is completely disrupted by the Y34F mutation. Any role this relay may have in catalysis is therefore not critical, but acts to optimise the reaction.

Gln146 is not essential for activity, but has an important role in optimising the reaction. Unlike the naturally active His146-containing MnSOD and FeSOD enzymes, the mutation of *E. coli* MnSOD Gln146 to histidine largely inactivates the enzyme. The inactivity may be a consequence of the greater inflexibility of the mutated histidine when compared with its more mobile natural counterparts.

5 Crystal Structures of Gateway Mutants in *Escherichia coli* Manganese Superoxide Dismutase

5.1. Introduction

The catalytic efficiency of an enzyme is only as good as the slowest step in its reaction mechanism. MnSOD has a maximal catalytic rate that approaches the diffusion-controlled limit of 10^8-10^9 $M^{-1}s^{-1}$ [168]. This implies that access of substrate and product to and from the active-site is relatively unimpeded if not actually facilitated by the protein structure. In the Mn and FeSODs, substrate access to the active site occurs *via* a solvent-filled funnel that leads from the outside surface towards the manganese site of each monomer [109]. For each metal site the funnel is formed by residues from both monomers and leads towards the metal-bound solvent molecule. Four residues at the bottom of the funnel partly shield the active site from the bulk solvent. A small hole between them allows small anions and solvent to enter the active site. Because access to the active site for substrate must occur *via* these residues, they have been termed 'gateway' residues [162].

His30 is highly conserved. In a sequence alignment of 87 Fe and MnSOD sequences (see Appendix C), only two species had anything other than His at this residue, and both of those had Asn (FeSOD from *P. aeruginosa* [181], and MnSOD from maize [182]). In the same sequence alignment, Tyr174 is absolutely conserved across all Fe and MnSODs, although the sequences of some 14 MnSOD species did not extend as far as this residue. In all Fe and Mn structures, Tyr174 forms a hydrogen bond across the dimer interface with His30 of the other subunit in the dimer. Thus the position and orientation of His30 is strongly determined by this interaction. A predetermined orientation for His30 may be beneficial for proton interactions in the catalytic mechanism or in interactions with the substrate as it enters the active site. Mutants of H30A and Y174F have been prepared to investigate the role of these gateway residues in the enzymatic mechanism.

5.2. Structure determination of H30A

5.2.1. Crystallisation

Crystals of H30A were grown in sitting drops. The well solution contained 16 - 20 % PEG 6000, and 0.1 M bicine titrated between pH 8.0 and 8.3. Crystals formed as hexagonal blocks rather than the elongated blocks of the wildtype enzyme. Only with polypropylene wells (instead of the more common polyethylene wells) was crystalline material obtained.

5.2.2. Data collection and processing

Data were collected from a single crystal at room temperature on a Rigaku R-Axis IIC image plate detector, using Cu-Kα radiation from a Rigaku RU-200B rotating anode generator. Many crystals were tried before one suitable for data collection could be found as this crystal form is very much more fragile than the wildtype crystal form. After an initial 90º wedge of data was collected using the 0.1 mm collimator, the crystal was translated and a second 90º wedge of data was collected using the 0.3 mm collimator. The 2θ stage of the detector was swung out 6.7º to collect the higher resolution data. The images were subsequently indexed and integrated to 2.2 Å using the program DENZO [146], and the program SCALEPACK [146] was used to scale and merge the resulting data. The data were then put on an approximately absolute scale using the scale factor taken from a Wilson plot. Approximately 5 % of the reflections were flagged for use in calculating the value of R_{free}. The R_{free} reflections, chosen for this and for all other mutant datasets sharing the same cell and spacegroup, corresponded to R_{free} reflections from the native dataset. Relevant data collection and processing statistics are given in Table 5-1 (opposite).

5.2.3. Structure solution, model building, and refinement

Calculations based on the expected solvent content of protein crystals [145] gave a Matthews' coefficient, Vm, of 2.76 $Å^3$/Dalton and a solvent content of 55 %, for a crystal having two MnSOD dimers in the asymmetric unit. A starting model for molecular replacement was generated from the dimeric structure of Q146L MnSOD chains A and B. The model was modified by removing all solvent waters, the metal ion and the solvent-bound hydroxide, and changing Leu146 to Gln, and His30 to Ala. The program AMORE [149] was used to search for two copies of the dimeric search model. The two highest unique peaks in the rotation function had correlation coefficients of 0.20. A translation function was calculated for the first rotation, and a solution was found having a correlation coefficient of 0.35 and an R-factor of 0.48. The rotation and translation of this dimer was fixed, and a suitable translation for the second rotation peak was searched for. A solution was found which increased the correlation coefficient to 0.64 and

Table 5-1. Data collection and reduction statistics for *E. coli* H30A and Y174F MnSOD

Crystal	H30A MnSOD	Y174F MnSOD
Space group	$C222_1$	$P2_1$
Z (Z')	32(4)	4(2)
Unit cell	*a*=100.681 Å *b*=109.110 Å *c*=181.072 Å	*a*=46.893 Å *b*=46.017 Å *c*=95.993 Å β=98.40º
V(m), $Å^3$/Da	2.76	2.28
Solvent content	55 %	40 %
Mosaicity	0.25º	0.21º
Data collection temperature	293 K	110 K
Data processing		
Resolution limits (of last shell)	40 - 2.2 Å (2.25 -2.20)	50 - 1.35 Å (1.37 -1.35)
Unique reflections	50905	89143
Observed reflections	458707	561459
Observed reflections after averaging	255035	373356
Observed reflections after averaging $I > 1\sigma_I$	254625	372430
Observed reflections after merging	48514	89109
Observations deleted manually	666	142
Redundancy	5.3	4.2
Completeness	95.3 % (73.0)	100.0 % (99.9)
R_{merge} on intensities[1]	0.059 (0.259)	0.027 (0.071)
Overall I/σ	22.4 (4.0)	52.5 (18.3)

[1] $R_{merge} = \Sigma|I-\langle I\rangle|/\Sigma I$, where $\langle I\rangle$ is the mean of individual observations of intensities I.

improved the R-factor to a value of 0.37. Rigid-body fitting of the rotation and translation values was carried out in AMORE, further improving the correlation coefficient and R-factor to 0.79 and 0.31, respectively. The choice of asymmetric unit was changed to be the same as that for the native MnSOD structure. Simulated annealing by torsion-angle molecular dynamics and slow-cooling from 5000 K to 0 K in 50 steps was carried out using CNS [131] (development version 0.3c) on the model resulting from molecular replacement. The starting R_{free} and R-factor of 0.42 and 0.42 were improved to 0.297 and 0.269 by the end of the simulated annealing. Five cycles of model building and refinement were required to complete the model. The four Mn atoms, the four metal-bound solvent molecules, and some 250 waters were added to the model during these

five cycles. Model building was carried out using the graphics program TURBO [150, 183]. Refinement of both atom coordinates and atomic B-factors against maximum-likelihood target functions [184] was carried out using CNS (development version 0.5) [131]. The final model has a R_{free} of 0.211 for 2456 reflections in the test set and an R-factor of 0.184 for 46048 reflections in the working set in the resolution range 40.0 - 2.2 Å. Refinement and model statistics are given in Table 5-2.

Table 5-2. Refinement and model statistics for *E. coli* H30A and Y174F MnSOD

Model	H30A MnSOD	Y174F MnSOD
PDB ID	-	-
No. of residues	820	410
No. of protein atoms	6492	3254
No. of water molecules	255	498
No. of manganese ions	4	2
Average B-factors, $Å^2$		
Main-chain atoms	23.9	9.5
Side-chain atoms	25.3	10.8
Water molecules	28.3	18.1
Manganese ions	14.5	6.1
Overall	24.7	11.2
Refinement		
Refinement program	CNS v5.0 [131]	SHELXL [180]
Reflections used in refinement	48504	84648
Reflections used in calculation of R_{free}	2456 (5.1 %)	4444 (5.2 %)
Resolution limits	40.0 - 2.2 Å	50.0 - 1.35 Å
RMS bond lengths	0.005 Å	0.005 Å
RMS bond angles	1.16º	1.34º
R-factor (all data)	0.184	0.170
R_{free} (all data)	0.211	0.196

5.3. Structure determination of Y174F

5.3.1. Data collection and processing

Synchrotron data were collected as described in Chapter 6. Data collected from the non-reduced, non-azido, crystal were indexed and integrated to 1.35 Å using the program DENZO [146], and the program SCALEPACK [146] was used to scale and merge the resulting data. The data were processed only to 1.35 Å rather than the limit of 0.90 Å to which data were collected, for two reasons. Firstly, the version of the program SCA-

LEPACK [146] (version 1.9.1) used to scale the data was unable to scale all the data, between 50.0 and 0.90 Å successfully. Secondly, for point of comparison with the structural changes of the other mutants, a structure to 1.35 Å is adequate, and requires a lot less time to model than would the structure to 0.90 Å.

For the purposes of indexing and integration, the data were treated as two individual batches, representing the low and medium resolution passes of the data collection. The low resolution pass extended between 50.0 and 2.55 Å, and the medium resolution pass between 10.0 and 1.35 Å. The procedure used for indexing and integration was the same for both passes. An initial frame was indexed, appropriate crystal and detector parameters were chosen, and these parameters were refined to convergence. All parameters (crystal orientation, direct beam position, cassette orientation, unit cell, radial and angular offsets, and crossfire), except for crystal to detector distance, were refined. This distance was not refined because of its close correlation to the unit cell and radial offset parameters at medium to low resolution. Once these starting parameters had been determined, the remaining frames in the pass were integrated automatically by the program in a batch mode. The integrated frames in the pass were then scaled and the reflections merged. Post-refinement of the cell and mosaicity parameter was done to determine more accurate values for these parameters. The integration of all frames in the pass was then repeated using the updated values for the cell and mosaicity parameters, and with the additional restraint that the cell parameters were fixed during refinement to the post-refinement values. After both the low and medium resolution passes had been integrated individually, all frames from both passes were scaled together. Multiple rounds of scaling, averaging and reflection outlier rejection were done before the reflections were finally merged. The relevant data collection and processing statistics are presented in Table 5-1 (above). The data were then put on an approximately absolute scale using a Wilson plot. Approximately 5 % of the reflections were flagged for use in calculating the value of R_{free}. R_{free} reflections were chosen which corresponded to R_{free} reflections from the native and other mutant data sharing the same cell and spacegroup.

5.3.2. Model building and refinement

The model of Y174F MnSOD, which was originally refined against data collected to 1.5 Å on the in-house Rigaku R-Axis IIC image plate detector (see Chapter 6 for data collection, processing and refinement of this model), was used as the starting model for refinement of the 1.35 Å data. The two Mn metal ions and all solvent waters were removed from the starting model, and the B-factors of all atoms were reset to the Wilson B of 8.0 $Å^2$. SHELXL (Release 97-2) [180] was used to refine the structure. The refinement protocol is given in Table 5-3 (below). Refinement and model statistics are given in Table 5-2 (opposite).

Table 5-3. Summary of refinement protocol of the 1.35 Å model of Y174F MnSOD

Job	Action	Cycles	N res.[1]	N par.[2]	R-factor	R_{free}
0	*Starting model:* No metal or solvent molecules, B-factor reset to Wilson B of 8.0 Å^2					
1	SWAT	CGLS 10	13391	13027	0.277	0.296
2	*Rebuild:* added 322 waters	CGLS 6	13409	14323	0.205	0.228
3	*Rebuild:* added 176 waters	CGLS 12	13402	15027	0.188	0.212
4	HOPE	CGLS 4	13404	15039	0.175	0.198
5	ANIS waters, ISOR waters	CGLS 4	16393	17529	0.170	0.196

[1]. Number of restraints.

[2]. Number of parameters.

5.4. Structural description of H30A

5.4.1. Structural effects of the H30A mutation

His30 is part of helix A1 and forms a hydrogen bond across the dimer interface to Tyr174 of the other subunit. The mutation of the histidine to an alanine breaks this hydrogen bond. Because of the strong internal hydrogen bonding of helices, the main-chain in the region of His30 is not affected by the mutation. Tyr174, however, is part of the loop between β-strand B3 and helix A5, and the breaking of the hydrogen bond has a greater effect on the main-chain of this loop. There are shifts of up to 0.5 Å in the main-chain of the loop containing this residue. The space vacated by the mutation of the histidine to alanine is not occupied by waters. In fact, the region around Tyr174 is subject to some considerable disorder with Tyr174, Asn179 and, to a lesser extent, Gln178, Arg180 and Leu175 all showing difference density corresponding to alternative conformations. Positions for partially occupied waters are also apparent. Difference density indicates Asn179 rotates 160º in chi1 to form an alternative conformation where the terminal atoms of the Asn side-chain lie in the approximate position of the NE2 of His30. This is accompanied by a concerted rotation of about 15º around chi1 for Tyr174, due to steric repulsion. The tyrosine shifts into the cavity which is occupied by water Ow1741M in the native structure. A stereo plot of the H30A mutant and native structures in the region of the mutation is shown overlaid in Figure 5-1 (opposite).

The secondary, tertiary and quaternary structure remain mostly unchanged by the mutation. Superimposing the dimers of the mutant structure onto the native dimer results in RMS differences between 1640 (C, CA, N, O) main-chain atoms in a pairwise comparison of between 0.2 and 0.3 Å. The largest differences between the mutant main-chain and the native main-chain occur in the variable loop region. Variation also occurs at the

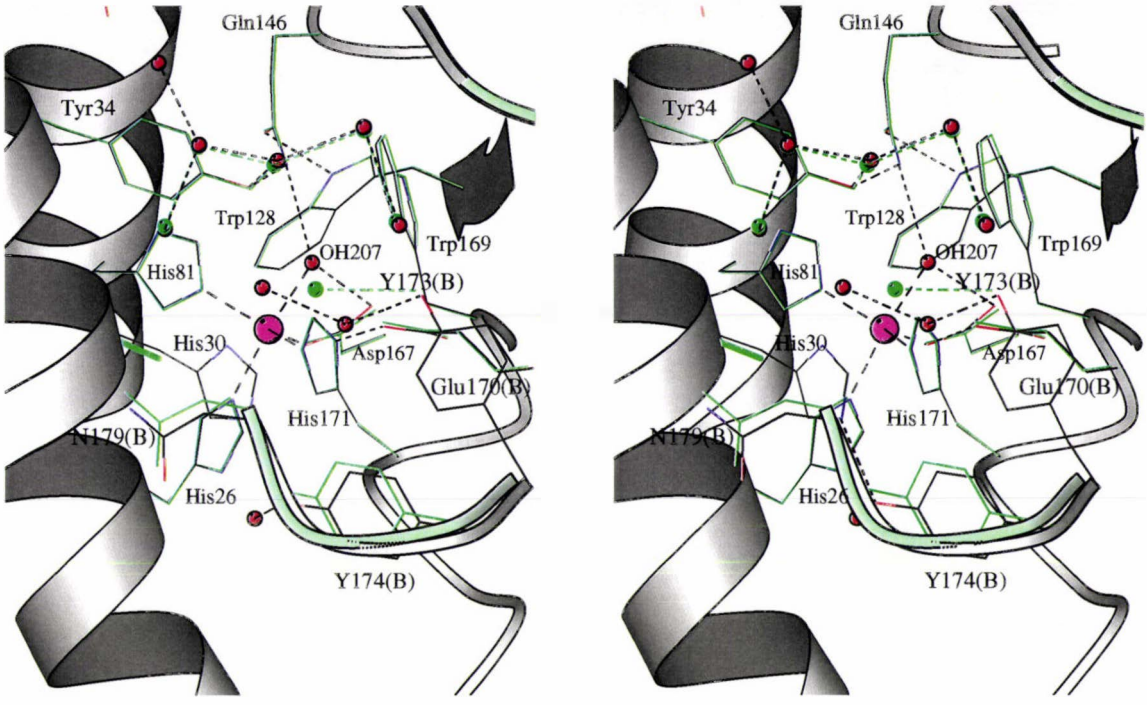

Figure 5-1. A stereo plot showing an overlay of H30A and the native structure in the region of the mutation

H30A MnSOD (subunit A active site) is drawn in green, and the native structure (subunit A active site) coloured by atom-type. Subunit B of H30A, drawn in light-green, shifts relative to subunit B of the native structure. The Mn ion is represented by the purple sphere. Figure drawn with MOLSCRIPT [1].

N-terminus, in helices A3 and A4, and in residues 174 - 180 in the loop between B3 and A5. Figure 5-2 (below) shows an overlay of dimers from the native, H30A and Y174F structures superimposed using the main-chain residues of subunit A.

The active-site bond lengths and angles are unchanged by the mutation.

5.5. Structural description of Y174F

5.5.1. Structural effects of the Y174F mutation

Mutation of Tyr174 to a phenylalanine breaks the 2.6 Å hydrogen bond between Tyr174 of one subunit and His30 of the other subunit. This hydrogen bond between two conserved residues is one of seven (four unique) spanning the dimer interface. The same hydrogen bond is broken in the H30A mutant; however, disruption to the dimer interface and subunit orientations within the dimer are far more extensive for the Y174F mutation. In the H30A mutant, where the histidine is replaced with a much smaller, non-flexible alanine residue, the position of Tyr174 hardly changes. In the Y174F mutant the tyrosine, a large polar residue, is replaced with a phenylalanine, a similarly sized but entirely

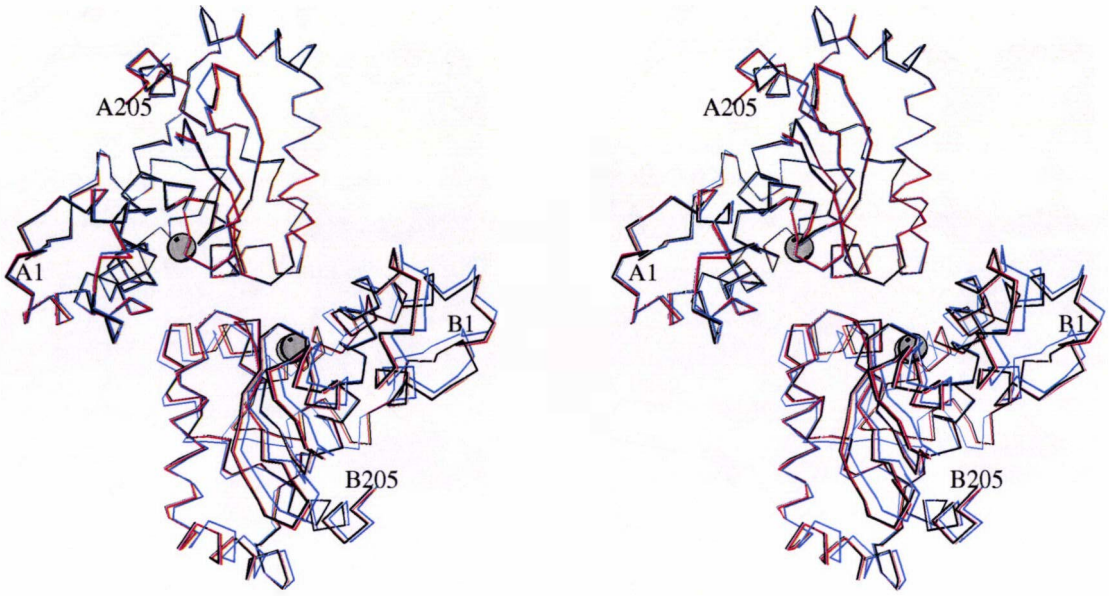

Figure 5-2. A stereo plot of the Cα main-chain trace of the native, H30A and Y174F dimers, overlaid using the A subunit of each dimer

The 820 main-chain (C, CA, N, O) atoms of subunit A were used to perform the superposition. Using only one subunit in the superposition has the effect of showing the extent of the reorientation of subunit B with respect to subunit A. Native structure in black, H30A in red and Y174F in blue. The grey spheres represent the Mn ions. Figure drawn with MOLSCRIPT [1].

hydrophobic residue. The change in side-chain nature from polar to hydrophobic causes a reorientation of F174 that maximises hydrophobic contacts. This simple side-chain movement stimulates extensive rearrangements of neighbouring residues in the dimer interface, and subsequently, large concerted shifts of the main-chain as the subunits within the dimer reorientate to accommodate the changes. A stereo plot of the mutant and native structures in the region of the Y174F mutation are shown overlaid in Figure 5-3 (opposite).

On the atomic level, the mutation represents the removal of a single oxygen atom. This phenolic oxygen of Tyr174 in the native structure is involved in two hydrogen bonds, being the likely acceptor in a hydrogen bond with His30, and a donor or acceptor in a hydrogen bond with a lone solvent water molecule (Ow1741M) sitting in an adjacent cavity.

The removal of the phenolic oxygen in the mutation of the tyrosine to a phenylalanine, breaks both hydrogen bonds. Without the strong 2.6 Å hydrogen bond with His30 to orient the Phe174 side-chain, and to maximise hydrophobic contacts, Phe174 undergoes a rotation. The rotation of the chi1 torsion angle, is ~ 30°. The chi2 torsion angle does not

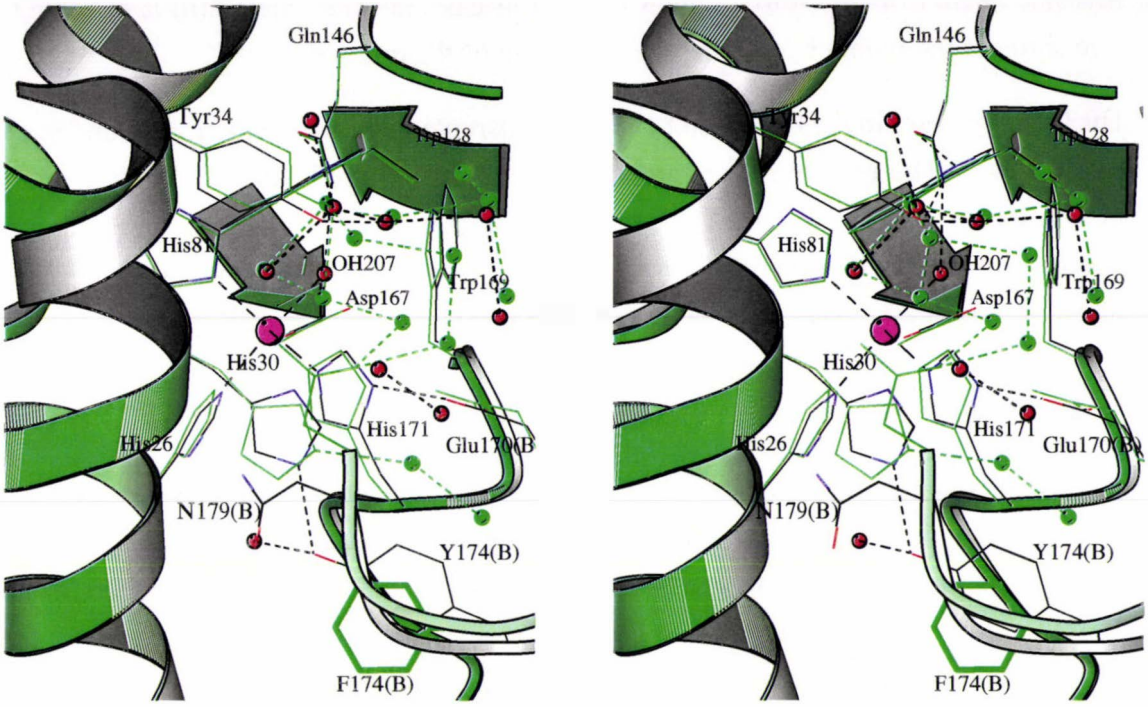

Figure 5-3. A stereo plot showing an overlay of Y174F and the native structure in the region of the mutation

Y174F MnSOD is drawn in green, and the native structure is coloured by atom-type. Subunit B of Y174F, drawn in light-green, shifts relative to subunit B of the native structure. The Mn ion is represented by the purple sphere. Figure drawn with MOLSCRIPT [1].

change; however, the ring plane of Phe174 has an effective rotation relative to the A subunit of ~ 30° due to the movement of the entire B subunit relative to the A subunit. The rotation in chi1 is toward the adjacent, largely hydrophobic cavity. This cavity in the native structure contained the solvent water molecule Ow1741M. The position of Ow1741M was maintained in this cavity by two hydrogen bonds, one being a 2.9 Å hydrogen bond with Tyr174, and the other a 2.9 Å hydrogen bond with the main-chain oxygen of His171. The loss of one of these hydrogen bonds in the mutant structure coupled with an increased hydrophobic environment and steric repulsion from Phe174, causes this solvent molecule to abandon the cavity. In its new orientation, Phe174 makes hydrophobic contacts between 3.8 and 4.6 Å with Leu175 from the same subunit, and Ile25, Leu175, the CB of His 171, and Phe174, all from the other subunit. The NCS axis relating the two subunits of the dimer is close to Tyr174. In the native structure the CD2 atoms of Tyr174 are 5.3 Å apart, whereas in the mutant structure the CD2 atoms of Phe174 are only 3.8 Å apart. The movement of Phe174 toward the NCS axis brings this residue close enough to its counterpart in the other subunit to share hydrophobic contacts around the axis. Leu175 also undergoes a side-chain shift, bringing the CD2 atoms of

this side-chain from 4.3 Å to within 3.7 Å. In this case, the side-chain shift is due to relative shifts of the main-chain rather than a change of the rotamer.

His30, the partner in the hydrogen bond being disrupted by the mutation, also undergoes reorientation. The residue rotates around the chi2 torsion angle by ~ 150°, flipping the histidine ring. The native His30 side-chain orientation is defined by its 2.6 Å hydrogen bond with Tyr174. At basic pH the NE2 nitrogen atom of histidine is more usually protonated rather than the ND1 nitrogen [185]. Also, the potential hydrogen on the NE2 nitrogen is pointing directly at the phenolic oxygen of Tyr174. It is likely therefore that the NE2 nitrogen of His30 is protonated, and is the donor in the hydrogen bond with Tyr174.

It is unlikely, at the pH of crystallisation, that this histidine is charged. The flipped His30 ring of the mutant forms a 2.77 Å hydrogen bond *via* its NE2 nitrogen with an ordered water molecule (Ow101L) in the substrate-access funnel. This water molecule is not present in the native structure. The ND1 nitrogen may form a potential, albeit weak, 3.6 Å hydrogen bond with the main-chain oxygen of Ile25. If the histidine ring were flipped 180° to conform to the approximate orientation of His30 in native MnSOD, the 2.77 Å hydrogen bond to water Ow101L would be broken, and a 3.14 Å hydrogen bond would be formed between the ND1 nitrogen and another ordered water molecule (Ow198L) in the substrate-access funnel. Of these two possibilities, the modelled orientation seems the most likely.

The side-chain of Asn179 also undergoes a conformational change. In the native structure Asn179 forms part of the lip of the substrate-access funnel, with its sidechain pointing out toward the surface of the dimer. In the Y174F mutant structure the sidechain undergoes a 220° rotation around the chi1 torsion angle, pointing the sidechain into the substrate-access funnel. Two waters occupy the space vacated by the change in rotamer. The new position of the side-chain lies above His30, such that His30 is no longer directly visible to bulk solvent outside the dimer. The movement of this sidechain into the substrate-access funnel is accentuated by a shift of the main-chain in the region of this residue, which affects the position and order of solvent in the funnel. Asn179 in the Y174F mutant makes three hydrogen bonds to waters in the funnel: Asn179_ND2...Ow61L (2.88 Å); Asn179_OD1...Ow70M (2.72 Å); Asn179_OD1...Ow69M (2.79 Å). The conformation of Asn179 in the Y174F mutant does not correspond to the conformations seen in the native and the H30A mutant.

Comparison of the ordered solvent structure of the Y174F mutant with the ordered solvent structure of the native MnSOD must take into consideration the much tighter crystal packing of Y174F, as highlighted by its lower percentage of bulk-solvent (40 % in Y174F, and 55 % in native MnSOD), the appreciably higher resolution of the Y174F structure, and the fact that the native structure was determined at ambient temperature

while the Y174F structure was determined at 110 K. These differences will markedly affect the number and order of the external solvent molecules involved in intermolecular contacts. Moreover, the functionally more interesting solvent molecules internal to the dimer and in the substrate-access funnel may also show discrepancies in their number and order. Those in the substrate-access funnel may be particularly affected by changes in crystal packing and temperature. An additional ordered solvent appears in the Y174F mutant structure that is not present in the native structure. This water, Ow198L, is positioned between the phenolic oxygen of Tyr34, and the CD2 of His30. In the native structure the Tyr34_OH to His30_ND1 distance is 5.1 Å. The equivalent distance to His30_CD2 in the Y174F mutant structure is 5.7 Å, the distance increasing due to small rotations of these two residues away from each other. In the mutant structure Tyr34 undergoes a 2° rotation around chi1, which shifts the position of the phenolic oxygen by 0.4 Å. This shift, however, shortens insignificantly the Tyr34_OH...Gln146_NE2 hydrogen bond from 2.97 Å in the native to 2.90 Å in the mutant structure. The rotations of Tyr34 and His30 in the mutant structure increase the distance between these two residues enough for a water to occupy the space between them. Water Ow198L forms three hydrogen bonds with other solvent waters, and a 2.60 Å hydrogen bond with Tyr34.

Table 5-4. Temperature factor ($Å^2$) statistics for the two chains of Y174F

	Chain A	Chain B
Average main chain	8.3	10.8
Sigma main chain	4.0	3.9
Average side chain	9.5	12.2
Sigma side chain	5.1	5.1
Average protein	8.9	11.5
Average solvent (number)	17.3 (259)	19.0 (239)
Metal ion	5.3	6.9
Metal-bound solvent	5.5	8.2

5.5.2. NCS analysis

No non-crystallographic symmetry restraints were applied to the 1.35 Å refinement in SHELXL. NCS geometry restraints would have the advantage of increasing the effective data to parameter ratio, necessary if anisotropic refinement were attempted at this resolution. NCS B-factor restraints, restraining B-factors of NCS-equivalent atoms to be approximately equal could not be employed because of the large difference in average temperature factors between the two NCS-related chains. The average temperature factor for both main-chain and side-chain atoms of chain B is ~ 30 % higher than those of chain A (see Table 5-4). This can be appreciated visually: when viewing the electron density

via TURBO, that for chain B is noticeably more diffuse and disordered than that for chain A. A plot of Cα temperature factors by residue for the two chains is shown in Figure 5-4.

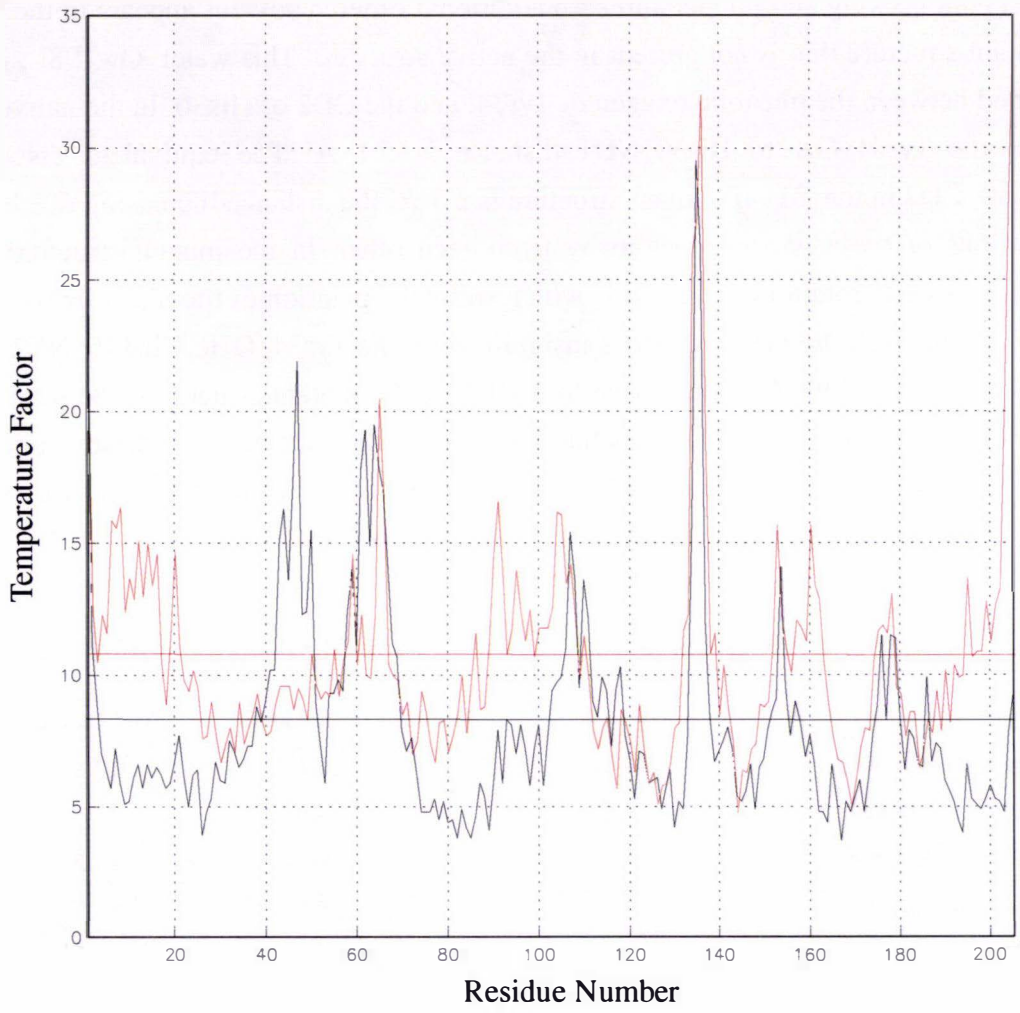

Figure 5-4. Plot of temperature factor of Cα atoms by residue number for the two chains of Y174F

Cα temperature factors for chain A are drawn in black, and for chain B in red. The average main-chain temperature factor for subunit A is 8.3 $Å^2$ (horizontal black line), and the average main-chain temperature factor for subunit B is 10.8 $Å^2$ (horizontal red line).

To highlight differences in the main-chain dihedral angles between the two NCS-related subunits, the standard deviation of psi and phi is plotted as a function of residue number (Figure 5-5 opposite). Fifteen residues show appreciable deviation from the RMS difference: Ser1, Tyr2, Leu7, Lys20, Phe48, Asn50, Glu55, Asp61, Gly91, Thr92, Gly135, Asp136, Ile163, Lys204 and Lys205. The deviations shown by these residues can be

attributed to differences in their inter- or intramolecular contacts and in the solvent environment as a result of crystal packing. The greatest deviation occurs for the C-terminus residues Lys204 and Lys205. In chain A Lys205 is well defined, folding back on chain A, and forming contacts *via* ordered solvents to a symmetry-related chain A N-terminus. Lys205 in chain B is less well defined and adopts a completely different conformation as a result of not having the equivalent symmetry-related contacts of chain A.

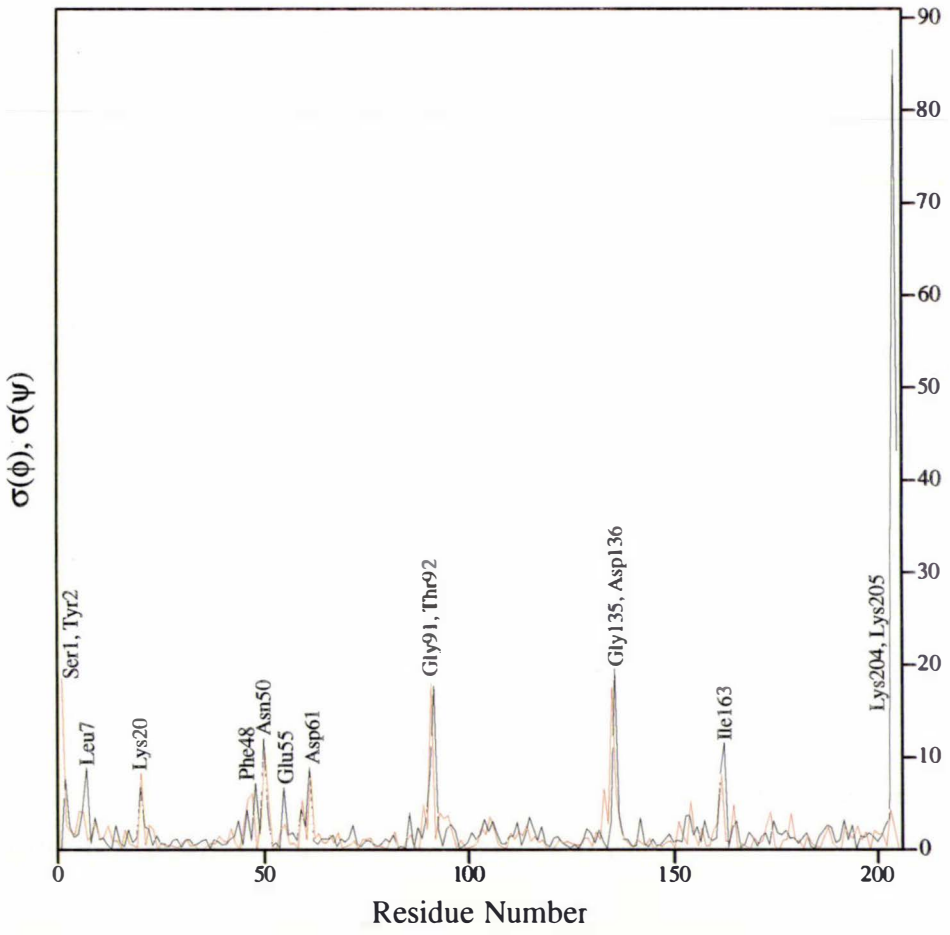

Figure 5-5. Standard deviation of phi and psi plotted as a function of residue number for Y174F

The black curve shows the standard deviation of the phi angles of corresponding residues in the two NCS-related subunits. The red curve shows the standard deviation of the psi angles.

In a similar fashion, the standard deviations of side-chain torsion angles, chi1 and chi2, are plotted as a function of residue number. Some twenty-four residues show significantly different side-chain torsion angles between the subunits. Side-chains of residues

having a corresponding deviation in the phi-psi plot are assumed to deviate for the same reason that the main-chain torsion angles deviate. Deviations of side-chains in the variable loop region (residues Glu43 - Lys48) are attributed to the extensive crystal-packing contacts, high main-chain variability, and disorder exhibited in this region. An additional five residues, Glu21, Lys118, Pro149, Gln178 and Asn179, show deviations. Differences within the subunits between the side-chains of Glu21, Lys118, Gln178 and Asn179 can be attributed to disorder and/or symmetry contacts. Pro149 has a different ring-pucker, possibly mediated *via* a symmetry contact.

The program SUPPOS was used to superimpose the two NCS-related subunits of Y174F. In all superpositions involving Y174F, residues Lys204 and Lys205 are excluded as the large distances between these residues (~ 10 Å) skews the RMS differences. The RMS difference for the overlay of subunit B on subunit A using all 812 main-chain (CA, C, N, O) atoms in each subunit, is 0.28 Å. This is comparable with the values for the pairwise overlay of the native subunits which range from 0.14 - 0.35 Å. However differences in the native subunits are confined to three main areas, the N-terminus, the variable loop region and residues 134 - 136. In addition the RMS differences for the native are overstated because of the large differences of residues 134 - 136. In fact the Y174F subunits show less similarity with each other than do the native subunits. The major differences between the Y174F subunits are at the N-terminus, the variable loop region, particularly residues 49 - 51, residues 85 - 100, particularly Gly91, residues 134 - 136 and the C-terminus.

5.5.3. Comparisons of Y174F with native

There are few differences in phi and psi angles between subunits of the native structure. Such differences are clearly shown by plotting sigma of phi and sigma of psi as a function of residue number in a phi-psi sigma plot. The phi-psi sigma plot for subunits of the native structure is very clean, having only a single major peak ($\sigma = 80°$) for residues 134 - 136, which are involved in a crystal packing contact. Smaller peaks where sigma is less than 10° are located in two other regions, the N-terminus, and the variable loop region centred around residue Asn50. The remarkably clean plot is in part a consequence of reasonably tight NCS restraints applied during refinement, and few disruptive main-chain crystal packing contacts. The phi-psi sigma plot (Figure 5-5 above) for Y174F shows more residues having significant deviations in their main-chain phi and psi angles. Y174F has 15 residues having sigma of phi or psi around the 10° level or higher. The larger number of differences in Y174F compared with the native structure may be in part due to the absence of NCS restraints in refinement, but also to the more extensive nature of the crystal packing-contacts.

A phi-psi sigma plot of the estimated standard deviation for the scatter of phi and psi

angles of a given residue about their respective means (sigma) can be generated using all subunits from both the native and Y174F structures. Ignoring peaks in this plot that have been contributed from differences in either the native or Y174F structures alone leaves only three peaks corresponding to residues Asn145, Phe177 and Asn179. The sigma values for these peaks are all less than 10° indicating only small differences in phi and psi torsion angles. Phe177 and Asn179 are part of a surface loop and Asn179 is disordered in Y174F. Asn145 is an important internal residue in the tight turn which holds the highly conserved active-site residue Gln146.

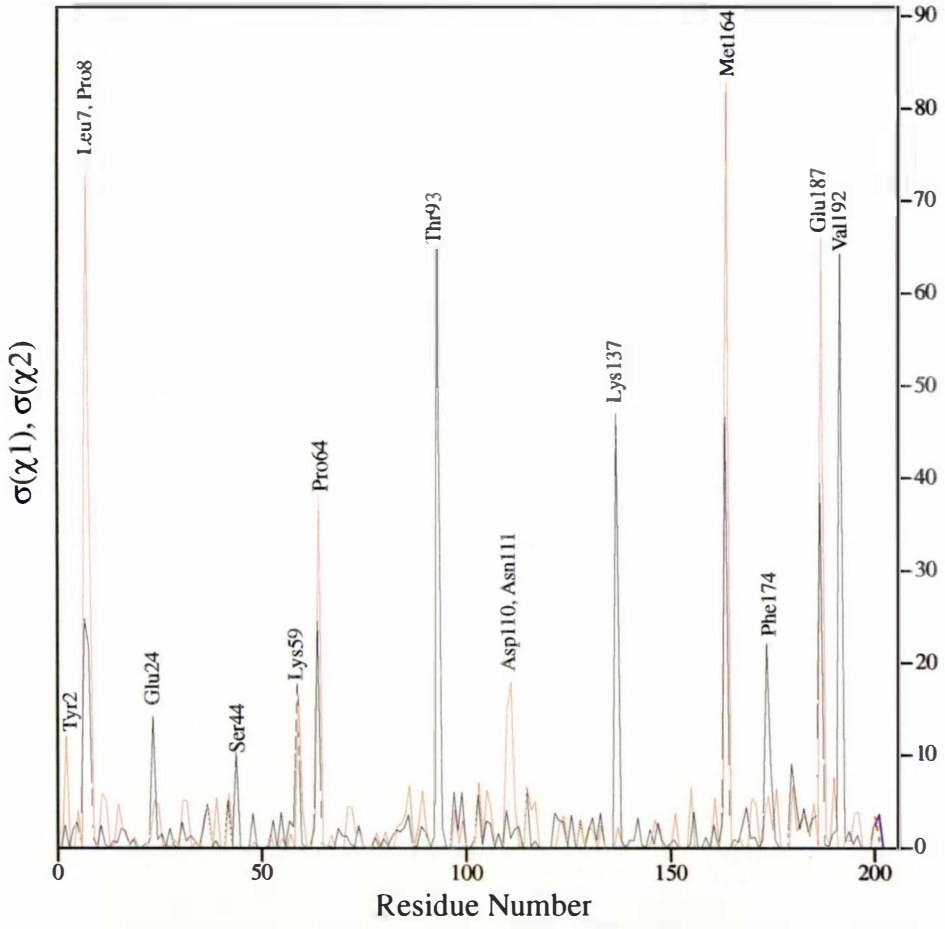

Figure 5-6. Sigma of the chi1 and chi2 angles plotted as a function of residue number

Sigma of chi1 is plotted in black, and sigma of chi2 in red.

In a similar way differences in side-chain rotamers can be determined from chi1-chi2 sigma plots. The sigma of chi1 and chi2 angles among all the subunits of the native and Y174F structures can be plotted as a function of residue number. Residues whose

sidechains deviate significantly within the subunits of either the native or Y174F structure are removed from the plot. Such residues have different chi1 and chi2 angles because of either intermolecular contacts or disorder. The chi1-chi2 sigma plot shows 15 residues in Y174F have side-chain conformations that are significantly different from the equivalent residues in the native structure (Figure 5-6 above). The rotation of F174 is picked up in this analysis. Residues Thr93, Met164, and Val192 may be better modelled in the native structure by imposing the rotamer of their better defined Y174F counterpart.

Of all the mutant structures, Y174F shows the greatest changes in tertiary structure from the native. Overlaying the two native dimers on the Y174F dimer gives RMS differences of 0.98 Å for the 1624 main-chain atoms of the native AB dimer, and 0.85 Å for the CD dimer. This is significantly higher than the RMS difference of 0.25 Å (1618 main-chain atoms) for the overlay of the native AB dimer with the native CD dimer. Figure 5-2 (above) shows a Cα trace of the native AB dimer and the Y174F dimer, superimposed using main-chain atoms only in the A subunit. This shows the extent to which subunit orientation is affected by the mutation.

The active-site bond lengths and angles are unchanged by the mutation.

Table 5-5. Details of the crystal packing contacts for the primitive orthorhombic lattice of Y174F

Buried surface ($Å^2$)	Subunits involved in contact	Region of subunit involved in contact
2 x 1130	B	Variable loop near top of A2 with start of A3 and A6.
		Residues 135 - 136 with N-terminal arm.
2 x 1030	A	C-terminal helix with bottom of N-terminal arm.
		A2 - A3 loop (90 - 91) with end of A1 (50 - 52).
2 x 520	B	A4 with top of A1 and variable loop region.
2 x 230	A	A3 with A5.
		A3 - A4 loop with B1 - B2 loop.
2 x 180	A,B	Residues Gln21, Asp61, Ala154 and Lys20.

5.5.4. Crystal packing

Crystals of MnSOD Y174F formed as large elongated blocks in space-group $P2_1$. The crystalline structure is formed from two alternating layers of dimeric molecules. The layers form in the *ab*-plane at *c*=0 and 0.5 (see Figure 5-7 opposite). Dimers within one layer are related to those in the adjacent layer by the two-fold rotation component of the 2_1-screw axes parallel to the *b*-axis. Molecules within the planes form into columns running parallel to the *a*- and *b*-axes. The dimers in the columns parallel to the *b*-axis pack closely, with only a small solvent channel forming parallel to the *b*-axis. A similar sol-

vent channel running parallel to the *a*-axis forms between the dimers within a layer. These solvent channels are kept compact because of both the tight packing of the dimers within the column and the overlapping nature of the alternating layers in the *ab*-plane. No solvent channels form along the *c*-axis because of the offset (along both the *a*- and *b*-axes) of the alternating layers.

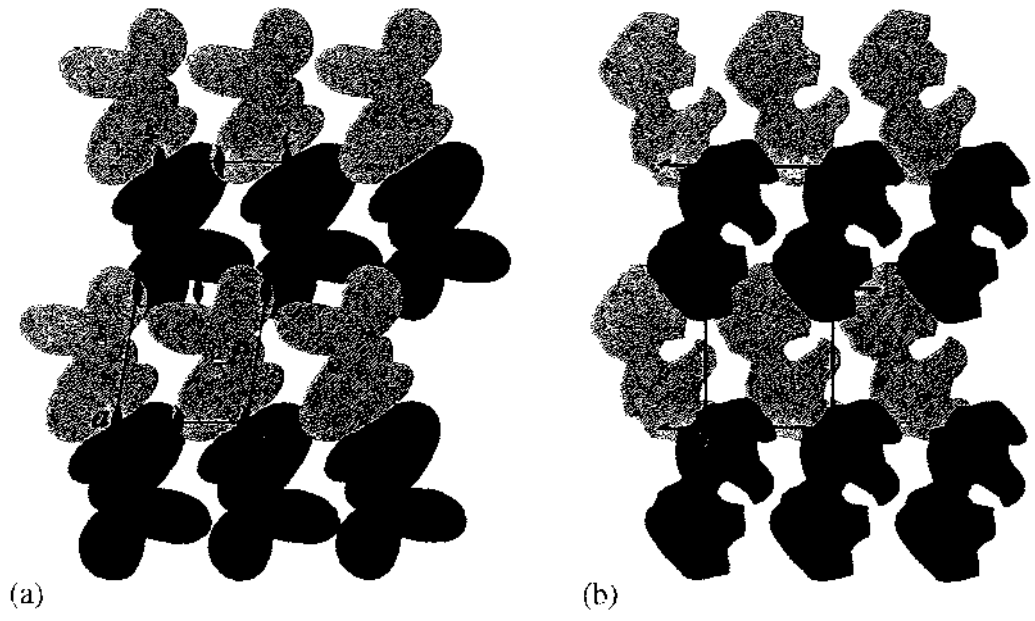

Figure 5-7. Schematic diagram of the packing of dimeric MnSOD Y174F within the crystal lattice

Layers of dimers are shown running left to right, and form in the *ab*-plane. The layer of light grey molecules are translated relative to the layer of dark grey molecules by 0.5 in *b* due to the 2_1-screw axes. In (b), the solvent channels forming parallel to the *b*-axis are shown. In (a), the solvent channels forming parallel to the *a*-axis are shown. No solvent channels form parallel to the *c*-axis due to the overlapping of the alternating layers of dimers.

The solvent-accessible surface area of the dimer was calculated as 17200 $Å^2$ using the program ASC [158, 159]. Approximately 6300 $Å^2$ (37 %) of this surface is buried by symmetry-related molecules. The contributions to the buried surface area by the individual crystal-packing contacts are given in Table 5-5 (opposite), and are shown schematically in Figure 5-8 (below). The two most extensive crystal-packing contacts are created between dimers in the alternating layers. Subunit A of the dimer has 10 hydrogen bonds forming with residues in the A subunit of a symmetry-related molecule. These contacts, between residues in the variable loop near the top of helix A2, the start of helix A3 and helix A6, bury ~ 2260 $Å^2$ of solvent-accessible surface. Subunit B also has 10 hydrogen

bonds to residues in symmetry-related B subunits. The crystal-packing contacts in the B subunit form in two areas: between the C-terminal helix and the lower half of the N-terminal arm, and between the A2 - A3 loop and the variable loop near the end of helix A1. These contacts bury ~ 2060 $Å^2$ of solvent-accessible surface. Further close contacts are formed between molecules within the layers. Subunit B-subunit B contacts bury ~ 1040 $Å^2$ of solvent-accessible surface and include one hydrogen bond. Subunit A-subunit A (~ 460 $Å^2$) and subunit A-subunit B (~ 360 $Å^2$) also form contacts between molecules lying within the plane. The Cα overlay of the native dimer and MnSOD Y174F, superimposed using only the Cα atoms in the A subunit (see Figure 5-2 above), shows the regions of greatest deviation are also those involved in the most extensive crystal-packing contacts.

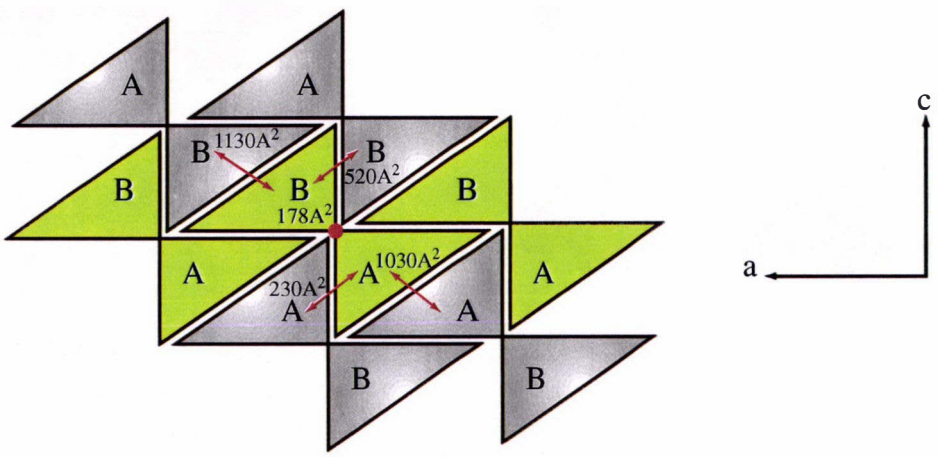

Figure 5-8. A schematic diagram showing the packing of the dimers into planes of identical subunits

The dimers shaded in yellow are at y+1/2 relative to the dimers shaded in gray. Crystal-packing contacts between subunits are shown with the red arrows, and the corresponding buried surface area is given in $Å^2$. The two major contacts form between the planes. The red circle in the center represents the 180 $Å^2$ contact. This contact is along *b* in the *ac* plane, and is made with a molecule related by a translation of one cell length along *b*. Axes are orthogonalised for clarity.

5.6. Discussion

Tyr174 is absolutely conserved in Fe and MnSODs, and His30 is highly conserved, being replaced by asparagine in only two of 87 sequences examined (see Appendix C). The side-chains of these two residues are provided from different subunits to form a hydrogen bond which spans the dimer interface.

Mutation of His30 to alanine reduces the catalytic activity to 30 % of wildtype, and substitution of Tyr174 by phenylalanine to 40 % of wildtype. Neither of these residues is directly linked with the active-site metal ion. Careful examinations of the structural consequences of these mutations are necessary inorder to explain the loss of activity when these non-active-site residues are mutated.

Two structural elements are disrupted by the H30A and Y174F mutations. In both mutants, the hydrogen bond spanning the dimer interface is broken. This hydrogen bond is one of seven connecting the subunits across the dimer, four of which are unique, and the other three being related by the NCS symmetry of the dimer. The second element being disrupted is the gateway residue His30, one of four residues forming the entrance to the active site at the base of the substrate-access funnel.

The H30A mutation does not affect the active site, or even the residues in the secondary coordination sphere. The largest structural changes are the movements of Tyr174 and its main-chain loop, which also changes the position of Asn179(B). Asn179, a residue at the edge of the substrate-access funnel, exhibits disorder in H30A. The Y174F mutation creates more extensive disruption both to the dimer interface and the active-site. Including the flipping of the His30 ring, and a different conformation for Asn179.

5.6.1. H30A

The active-site of the H30A mutant is unperturbed by the mutation. Even Glu170(B) a secondary coordination sphere residue, which, like Tyr174, is provided by the 'other' subunit, is not significantly affected by the mutation. The only significant structural changes, other than the loss of His30, is the exposure of the Tyr174 phenolic oxygen, and the effect of the alternate conformation of Asn179(B). The hydrogen-bonding potential of Tyr174 is maintained in part by hydrogen-bond formation with a partially occupied water molecule in the cavity toward which Tyr174 shifts, and the alternate conformation of Asn179(B). In the *T. thermophilus* MnSOD-azide complex, the metal-ligated azide molecule interacts with both Tyr34 and His30. The His30_ND1 ... N_3^-_N2 and N_3^-_N3 distances are 3.5 and 3.1 Å respectively. Whilst the alternate conformation of Asn179(B) is in the approximate steric position of the deleted histidine, any potential Asn179(B)_ND2 ... N_3^-_N3 interaction would be weak at ~ 4.6 Å.

5.6.2. Y174F

Structural changes due to the Y174F mutation are far more pervasive than those due to the H30A mutation, even though the same dimer-interface hydrogen bond is broken in both cases. The driving force for the rearrangement of the dimer interface of Y174F appears to be the change in character of residue 174 from a polar tyrosine to a hydrophobic phenylalanine. The propensity of hydrophobic residues to pack into solvent-

excluded, non-polar environments causes Phe174 of the Y174F mutant to undergo a greater conformational change than that which occurs for Tyr174 in the H30A mutant.

The resulting movements of residues and main-chain atoms in the dimer interface permeates through the structure to cause changes at the active-site. Because of the changes at the active site of the Y174F mutant, it is not as simple to differentiate the loss of activity from modifications occurring at the active site as was able to be done for the H30A mutant whose active site was essentially unchanged. The changes in the primary coordination sphere of the Y174F mutant are, however, limited to barely significant shifts and rotations of residue side-chains. More significant is the effect the mutation has on the position and orientation of His30.

The ring-plane of His30 is effectively flipped, modifying the positioning of its hydrogen-bonding groups. The orientation of His30 then is largely determined by its hydrogen bond with Tyr174. In the native orientation of His30, the ND1 nitrogen is projected toward the both the active-site and Tyr34, while the NE2 nitrogen is involved in the strong hydrogen bond with Tyr174. The position of His30_ND1 may therefore be important for optimising the catalytic reaction. Roles for the ND1 nitrogen could revolve around its ability to become protonated. Tyr174 may therefore not only orient His30, but act to modify its effective pKa. The ND1 nitrogen of His30 could be involved in protonation of product, interactions with and orientation of incoming substrate, or to provide a positive (if protonated) charge at the base of the substrate-access funnel.

The movement of His30 also allows for a solvent water to diffuse into the space between His30 and Tyr34. This water is also present in the inactive iron-substituted MnSOD structure, but is not seen in the active wildtype enzyme.

Asn179(B) is the only other residue to adopt a significantly different conformation. Asn179(B) flips into the substrate-access funnel, fully occupying a conformation that lies above His30, effectively creating both a steric and electrostatic shield between His30 and the bulk solvent. This new position for Asn179(B) also narrows the substrate-access funnel, but probably not enough to sterically hinder substrate diffusion into the active-site.

5.7. Conclusions

The lack of any changes in both the primary and secondary coordination shells of the H30A mutant active-site, coupled with a 70 % reduction in catalytic activity, indicate an important role for His30 in optimising the catalytic mechanism.

It is likely that the 60 % reduction in catalytic activity of the Y174F mutant is due to a different orientation, and possibly different effective pKa of His30, although a loss of

activity due to the slight differences of the primary and secondary coordination spheres can not be entirely ruled out.

Structural evidence supports a role for Tyr174 in orienting and possibly also modifying the pK of His30. The involvement of His30, in particular *via* its ND1 nitrogen, with aspects of the catalytic mechanism including interaction or protonation of substrate, can be postulated based on its structural behaviour.

6 Atomic Resolution Crystal Structure of *Escherichia coli* Y174F Manganese Superoxide Dismutase

6.1. Introduction

The structural detail of X-ray crystallographic investigations of protein structures is largely limited by the quality of the crystals from which data are collected. The quality of crystals, as measured in these studies by the resolution to which they diffract, is an inherent property of the molecular packing, and of the solvent content within the crystal. In general, because of the large size and flexible nature of macromolecules, the protein crystalline lattice is represented by few inter-molecular packing contacts and by large regions of diffuse solvent. This has the effect of reducing the order of the crystalline lattice and, therefore, the resolution to which the crystal diffracts. Unfortunately such properties of protein crystals are not easily engineered, and although experimental techniques at both the crystallisation and data collection stages can improve the quality of data obtained, the discovery of a protein crystal which diffracts to atomic resolution (<1.2 Å) is still regarded as fortuitous.

Whilst the number of atomic resolution structures is steadily increasing, largely due to advances in experimental technique, and the rate at which protein structures in general are being solved, few protein crystals diffract to < 1.0 Å resolution, and most that do have less than 100 residues in the asymmetric unit. The $P2_1$ crystalline form of the Y174F mutant of *E. coli* MnSOD is therefore unusual in that not only does it diffract to a resolution of 0.90 Å, but it is a dimer of 410 residues in the asymmetric unit. The advantages of atomic resolution data to X-ray crystallographic investigations stem from the accuracy with which the positions of individual protein atoms can be determined. The higher number of reflections recorded at atomic resolutions also improves the ratio of data to model parameters; in the case of Y174F MnSOD the data to parameter ratio is further improved by the presence of non-crystallographic symmetry within the dimer.

The discovery of a crystal of a superoxide dismutase that diffracts to atomic resolution will be a considerable benefit to both mechanistic and modelling aspects of Mn and Fe superoxide dismutases, and may lead to the advancement of techniques in the crystallo-

graphic investigation of protein structures in general.

6.2. Data collection and processing

Data have been collected from five crystals of MnSOD Y174F using differing X-ray sources and data collection strategies. The fundamental differences between these data collections are summarised in Table 6-1.

Table 6-1. Data collections of Y174F MnSOD with various oxidation states and ligands

Data set	Description	Res. (Å)	Temp. (K)	X-ray source	Wavelength (Å)	File identifier
MnSOD Y174F	native oxidation state	1.50	113	lab source	1.5418	mnsod22
MnSOD Y174F	native oxidation state	1.10	113	lab source	1.5418	mnsod24
MnSOD Y174F	native oxidation state	0.90	110	DESY X11	0.9058	mnsod44
redMnSOD Y174F	reduced	0.90	110	DESY X11	0.9058	mnsod47
redMnSOD-azide Y174F	reduced, 100mM NaN_3	1.25	110	DESY X11	0.9058	mnsod50

6.2.1. Crystal mounting and freezing

All data were collected at a temperature of between 110 to 113 K. The cryoprotectant used to protect the crystal during freezing was the same as that used for the low temperature data collections of WT MnSOD, 25 % PEG 6000, 15 % MPD, and the same concentration and pH of buffer used in the crystallisation, usually 0.1 M bicine pH 8.5. All crystals were frozen by the same procedure. A series of different diameter 20 µM nylon loops are mounted on supporting bases. The loops are glued to one end of 14 mm long, 0.65 mm diameter, stainless steel tubes. The other end of the tube is glued into a plastic support platform which contains an iron base. The support platform is designed to be fixed by magnetic attraction to a matching goniometer head. A single crystal or fragment is selected. A mounted loop is chosen such that the diameter of the loop will completely encompass the selected crystal without deformation of the loop. The loop and supporting base are then mounted on the goniometer, and the goniometer adjusted to align the loop with the dry liquid nitrogen stream which will be used to flash freeze the crystal. The crystal is scooped out of its drop using the loop and immediately released into the cyroprotectant. The action of retrieving the crystal from the cyroprotectant, back into the loop, takes between 30 and 60 s. During this time the crystal is pushed through the cyroprotectant and much of its surrounding mother liquor is replaced by cryoprotectant. Once the crystal is back in the loop, the loop and supporting base are immediately mounted on the goniometer head, and the crystal is flash frozen by the stream of dry liquid nitrogen blowing around it.

6.2.2. Data collection and processing *in-house*

Two data sets were collected from crystals of Y174F MnSOD *in-house*. Data were collected on a Rigaku R-Axis IIC image plate detector, using Cu-Kα radiation from a Rigaku RU-200B rotating anode generator. The Cu radiation was collimated using a 0.3 mm collimator. Selected crystallographic data statistics are given in Table 6-2 (below). The initial data collected to 1.5 Å suffered from poor redundancy and completeness. To collect the high resolution data it is necessary to swing the two-theta stage of the detector away from the path of the direct beam in order to collect the higher angle reflections. Because these high-angle reflections are intense enough to be collected, the effective size of the reciprocal lattice required for collection is increased relative to a lower resolution data collection with the same detector geometry. In effect, many more frames have to be collected to obtain comparable redundancy and completeness to lower resolution data collections. A second data set was collected to 1.1 Å resolution, to both extend the resolution of the data, and to improve on the redundancy and completeness.

The data were collected in two batches, a high resolution batch (2.3 - 1.1 Å) and a low resolution batch (50.0 - 1.5 Å). The 1.1 Å limit of this data is the highest possible resolution obtainable on the R-AxisIIC with this crystal cell. The detector was positioned as close as possible (100.0 mm) to the crystal without incurring excessive overlapping of reflections. Potential overlaps were further reduced by collecting small (0.25º) oscillations. Given that the mosaicity of these crystals is about 0.5º, no reflections were fully recorded on any one image. The 2θ stage on which the detector is mounted was swung out as far as possible (45.6º), to the edge of the detector table. A total of 1140 0.25º, 10-minute exposure oscillations were collected in the high resolution batch. The low resolution batch, 50.0 - 1.5 Å was collected in two passes. In the first pass to 1.5 Å, 386 0.75º, 10-minute exposure oscillations were collected. The crystal to film distance was 140.0 mm and 2θ was 27º. A second, quicker pass to 2.3 Å was made to improve the redundancy and completeness of the low resolution data. In this pass, 90 2.0º, 10-minute exposure oscillations were collected. The crystal to film distance was 205.0 mm and 2θ was 13.0º. An additional high-resolution pass was made after reorienting the crystal in order to improve the completeness in the 2.3 - 1.1 Å shell. During the reorientation the crystal experienced a thaw-freeze cycle, leading to an increase in mosaicity. The data subsequently collected only diffract to 1.5 Å resolution. A further 240 oscillations (0.25º, 10 minute exposure) oscillations were collected with a crystal to film distance of 100.0 mm and 2θ of 45.7º.

Data were integrated, scaled and merged using the programs DENZO and SCALEPACK [146]. Because the number of frames collected (1616) exceeded the number of frames that SCALEPACK (version 1.9.1) was able to scale at any one time, data were first

scaled in the batches in which they were collected. The scaled, un-merged and outlier-rejected data from these six batches were then scaled and merged together, using the six scale and B factors calculated between the batches.

Table 6-2. Data collection and reduction statistics for *E. coli* Y174F MnSOD. Data were collected on an RaxisIIC *in-house*

Crystal	MnSOD Y174F	MnSOD Y174F
Space group	$P2_1$	$P2_1$
Z (Z')	4(2)	4(2)
Unit cell	*a*=46.75 Å	*a*=46.874 Å
	b=45.78 Å	*b*=45.830 Å
	c=95.68 Å	*c*=95.947 Å
	β=98.1º	β=98.29º
V(m), $Å^3$/Da		
Solvent content		
Mosaicity	0.42º	0.48º
Data collection temperature	113 K	113 K
Data processing		
Resolution limits (of last shell)	50 - 1.5 Å	50 - 1.1 Å
	(1.55 - 1.50)	(1.12 - 1.10)
Unique reflections	64794	163425
Observed reflections	379947	1409498
Observed reflections after averaging	148829	472953
Observed reflections after averaging $I > 1\sigma_I$	143835	438341
Observed reflections after merging	56826	149343
Observations deleted manually	10149	-
Redundancy	2.53	3.2
Completeness	87.7 % (68.2)	91.4 % (67.5)
R_{merge} on intensities[1]	0.043 (0.058)	0.039 (0.216)
Overall I/σ	-	31.5 (4.0)

[1] $R_{merge} = \Sigma|I-\langle I\rangle|/\Sigma I$, where $\langle I\rangle$ is the mean of individual observations of intensities I.

6.2.3. Collection and processing of *synchrotron* data

Atomic resolution data were collected on the X11 beamline of the European Molecular Biology Laboratory (EMBL) Hamburg Outstation at the Deutsches Elektronen-Synchrotron (DESY), Hamburg, Germany. The synchrotron source for the X11 beamline is the DORIS Storage Ring, with a positron energy of 4.45 GeV. The X11 beamline is a fixed

wavelength (0.91 Å) beamline with a bent single-crystal germanium triangular monochromator and segmented mirror. The detector used was a Mar345 imaging plate. An Oxford cryogenic cooling system was used to maintain the crystals at cryogenic temperatures.

Crystals were harvested, frozen and tested on the R-AxisIIC at Massey. The crystals were then transferred to the cryogenic storage dewer used to transport them to Germany. In addition a number of crystals were harvested and transferred to Eppendorf tubes surrounded in their mother liquor. The Eppendorfs containing the crystals were packed into an additional container and packed with foam to act as both a barrier to vibration and sudden temperature changes. These crystals were transported to Germany at ambient temperatures.

Three data sets were collected during the five days of allotted beam time on X11. The first was collected from a crystal that had been tested at Massey, and transported in the cryogenic storage dewer. This crystal, in its native oxidation state diffracted to 0.90 Å. The second data set collected was from a crystal transported at ambient temperature. The crystal was reduced by the addition of 1 part 10 % H_2O_2 with 40 parts mother liquor. The pale violet colour of the crystal was visibly bleached out over a period of a few minutes as the reduced form of the enzyme was produced within the crystal lattice. This reduced crystal was then frozen *in situ* and data collected to 0.90 Å. A third crystal was reduced in the same way, and subjected to the addition of 0.1 M NaN_3 slowly over a period of a few hours. This crystal diffracted to 1.25 Å resolution.

For the data to 0.90 Å, three separate passes were collected, a high, medium and low resolution pass (see Table 6.3 below for data collection parameters). Because of the intensity of the reflections in the low resolution pass, it was necessary to add an attenuator into the path of the X-ray beam. A piece of folded aluminium foil taped in front of the X-ray shutter acted as the attenuator. For the data to 1.25 Å resolution only high and low resolution passes were needed. After collection of the three datasets, the several hours of the remaining beam time were utilised by putting the reduced MnSOD Y174F crystal back into the beam and collecting an additional low resolution pass. The crystal orientation was changed from that of the original data collection by offsetting its rotation on the goniometer by ~ 10º around the axis perpendicular to both the X-ray beam, and the spindle axis.

Data collected from the non-reduced crystal form of Y174F MnSOD were indexed and integrated using the program DENZO [146]. The high, medium and low resolution passes were all processed independently. Each of the high and medium resolution passes was processed in batches of between 50 and 100 frames to facilitate better use of computing resources. The autoindexing routine in DENZO was used to index 1325 reflection

Table 6-3. Data collection parameters for data collected on beamline X11 at DESY

Data collection parameter	MnSOD Y174F	redMnSOD Y174F	redMnSOD-N_3^- Y174F
High resolution pass			
Effective resolution range (Å)	2.40 - 0.90		2.80 - 1.25
Oscillation range (º)	0.4	0.8	1.0
Exposure time (s)	120	100	200
Crystal to film distance (mm)	96	96	160
Degrees collected (º)	179.2	188.4	154
Med resolution pass			
Effective resolution range (Å)	10.0 - 1.35		35.0 - 1.50
Oscillation range (º)	0.7	1.4	1.4
Exposure time (s)	50	50	60
Crystal to film distance (mm)	180	180	210
Degrees collected (º)	179.9		197.4
Low resolution pass			
Effective resolution range (Å)	50.0 - 2.55		45.0 - 2.20
Oscillation range (º)	2.0	2.5	2.2
Exposure time (s)	20	12	30
Crystal to film distance (mm)	400	340	320
Degrees collected (º)	196	545	193.6

in frame two of the high resolution pass. The highest symmetry Bravais lattice requiring the least distortion to fit the lattice as determined by the data was primitive monoclinic, with a metric tensor distortion index of 0.01 %. The higher symmetry C-centred orthorhombic lattice showed the next least-highest distortion of 2.16 %. The indexing was confirmed by first refining all parameters to convergence, then using the refined parameters to index an image collected with a significantly different value of phi. The indexing parameters of frame two were then used to index the first frame in each of the batches of the high resolution pass, and the parameters for each of these frames were refined to convergence. The individual batches in the high resolution pass were then indexed and integrated automatically using the batch mode of the program. The refined parameters from the first frame of each batch were used as the starting parameters for indexing of that batch. Only reflections falling between the resolution limits given in Table 6-3 for each resolution pass, were integrated. Parameters refined were: the crystal orientation; the unit cell dimensions; the position of the image plate; the crystal to image-plate distance; the position of the direct X-ray beam; the spiral scanner alignment corrections, radial and angular offset; and the divergence and focusing (crossfire) of the X-ray

beam. The medium and low resolution passes were processed in the same manner except that the distance parameter was not refined, but fixed at the measured value from the detector geometry.

Table 6-4. Data collection and reduction statistics for native oxidation state, and reduced-MnSOD-N_3^-, Y174F MnSODs from *E. coli*

Data were collected on the X11 beamline at DESY, and scaled using SCALEPACK version 1.9.1.

Crystal	MnSOD Y174F	redMnSOD-N_3^- Y174F
Space group	$P2_1$	$P2_1$
Z (Z')	4(2)	4(2)
Unit cell	*a*=46.893 Å	*a*=46.707 Å
	b=46.017 Å	*b*=45.972 Å
	c=95.993 Å	*c*=95.993 Å
	β=98.40º	β=97.96º
V(m), Å^3/Da		
Solvent content		
Mosaicity	0.24º	0.70º
Data collection temperature	110 K	110 K
Data processing		
Resolution limits (of last shell)	50 - 0.90 Å	50 - 1.25 Å
	(0.91 - 0.90)	(1.26 - 1.25)
Unique reflections	298677	111733
Observed reflections	2448558	1359380
Observed reflections after averaging	1324166	679506
Observed reflections after averaging $I > 1\sigma_I$	1272901	678939
Observed reflections after merging	287514	108342
Observations deleted manually(low,med,high)	7+179+2022	1045
Redundancy	4.6	6.27
Completeness	96.3 % (68.0)	97.0 % (94.8)
R_{merge} on intensities[1]	0.033 (0.355)	0.041 (0.335)
Overall I/σ	43.0 (2.5)	33.1 (4.0)

[1] $R_{merge} = \Sigma|I-\langle I\rangle|/\Sigma I$, where $\langle I\rangle$ is the mean of individual observations of intensities I.

Scaling, merging and post-refinement of each resolution pass was carried out using the program SCALEPACK [146] in order to determine accurate values of the unit cell parameters and of mosaicity. Scale and B factors were calculated for each of the frames

in the high resolution pass. In an iterative procedure, multiple rounds of scaling and outlier rejection were carried out until all significant outliers had been rejected. In the final round of this iterative procedure, post-refinement of the unit cell parameters, crystal orientation, and mosaicity were carried out, and the scaled and averaged reflections merged. The high, medium and low resolution passes were then reprocessed. The updated values of the mosaicity for each pass were used in the reprocessing. The unit cell parameters were fixed at those determined by post-refinement of the high-resolution pass, and were not allowed to refine during the reprocessing. The program SCALEPACK (version 1.9.1) was unable to simultaneously scale, or merge, all frames of the reprocessed data, due to the large number of parameters involved. For this reason, the scaling was separated into smaller batches, and the smaller batches were then scaled together. The individual resolution passes were firstly scaled using the reprocessed data with multiple rounds of scaling and outlier rejection being carried out. The scaled data were then averaged but not merged and three sets of scaled, outlier-rejected, and non-merged data were then output corresponding to the high, medium and low resolution data collection passes. In a final round of scaling, three sets of scale and B factors were calculated between the three passes, and the data merged. Data from the redMnSOD-N_3^- crystal form were also indexed, integrated, scaled and merged using this protocol. Because of the lower resolution (1.25 Å) of the redMnSOD-N_3^- data and, therefore, the fewer number of parameters, the scaling and merging of all frames of this data were able to be carried out in a single batch. Selected data collection and processing statistics are given for the data scaled using version 1.9.1 of SCALEPACK in Table 6-4 (above).

With the subsequent development of a new version of SCALEPACK (version 1.12), all three data sets were able to be rescaled in a single batch. Selected data collection and processing statistics are given for the data scaled using version 1.12 of SCALEPACK in Table 6-5 (opposite).

6.3. *Synchrotron* X-ray data quality

6.3.1. Accuracy of cell dimensions

One problem with some atomic resolution structures whose data were collected at Hamburg has been the accuracy of the cell dimensions used in refinement [186]. Validation of these structures using the programs WHATCHECK [187], SQUID [188] and PROVE [189] all suggested cell dimensions were in error by up to 0.5 %. Errors in the cell dimensions lead to systematic deviations of the refined atomic parameters, which is how the validation programs detect this problem. For the structures having this problem, the cell dimensions had been calculated during data reduction using the program DENZO, and the estimated values of wavelength and crystal to detector distance. The experimental dimensions as calculated in this manner all appeared to be too short by about 0.5 % on

Table 6-5. Data collection and reduction statistics for native and reduced oxidation states of Y174F MnSOD and for a Y174F reduced-MnSOD-N_3^- derivative from *E. coli*

Data were collected on the X11 beamline at DESY, and scaled using SCALEPACK version 1.12.

Crystal	MnSOD Y174F	redMnSOD Y174F	redMnSOD-N_3^- Y174F
Space group	$P2_1$	$P2_1$	$P2_1$
Z (Z')	4(2)	4(2)	4(2)
Unit cell	*a*=46.893 Å	*a*=46.815 Å	*a*=46.707 Å
	b=46.017 Å	*b*=45.832 Å	*b*=45.973 Å
	c=95.993 Å	*c*=96.187 Å	*c*=95.980 Å
	β=98.40°	β=98.20°	β=97.97°
V(m), $Å^3$/Da			
Solvent content			
Mosaicity	0.24°	0.41°	0.70°
Data collection temperature	110 K	110 K	110 K
Data processing			
Resolution limits (of last shell)	50.0 - 0.90 Å (0.91 - 0.90)	45.0 - 0.90 Å (0.91 - 0.90)	45.0 - 1.25 Å (1.26 - 1.25)
Unique reflections	298677	297741	111733
Observed reflections	2446982	2588590	1367429
Observed reflections after averaging	1273711	1535891	681878
Observed reflections after averaging $I > 1\sigma_I$	1264359	1533647	681304
Observed reflections after merging	287455	274173	108370
Observations deleted manually	2189	1050	1772
Redundancy	4.4	5.6	6.3
Completeness	96.2 % (67.8)	92.1 % (81.7)	97.0 % (94.8)
R_{merge} on intensities[1]	0.033 (0.355)	0.030 (0.395)	0.043 (0.335)
Overall I/σ	41.5 (2.5)	56.8 (2.6)	38.0 (4.0)

1. $R_{merge} = \Sigma|I-\langle I\rangle|/\Sigma I$, where $\langle I\rangle$ is the mean of individual observations of intensities I.

average, leading to an underestimate of cell volume of 1 to 2 %. The errors were determined to be due to poor definition of both the absolute wavelength and the crystal to detector distance. In response to this, the estimation of wavelength and crystal to detector distance were subsequently improved at Hamburg. The wavelength of the radiation used to collect the Y174F MnSOD data was calibrated during the data collection at 0.9058 Å, and as such is sufficiently accurate. The method used to determine the unit cell dimensions for Y174F MnSOD, as described above (see 6.2.3 *Collection and processing of*

synchrotron data), was by post-refinement of the integrated, high-resolution (2.4 - 0.90 Å) data, where the crystal to detector distance parameter was allowed to refine during the parameter refinement stage of the reflection integration. It may be that using the fixed value for the crystal to detector distance recorded during data collection at Hamburg will lead to more accurate estimates of cell dimensions. Calculations using the program WHATCHECK showed no systematic deviations in bond lengths in the 1.35 Å structure of Y174F MnSOD, as presented in Chapter 5, indicating that the values for the unit cell are sufficiently accurate for refinement at this resolution.

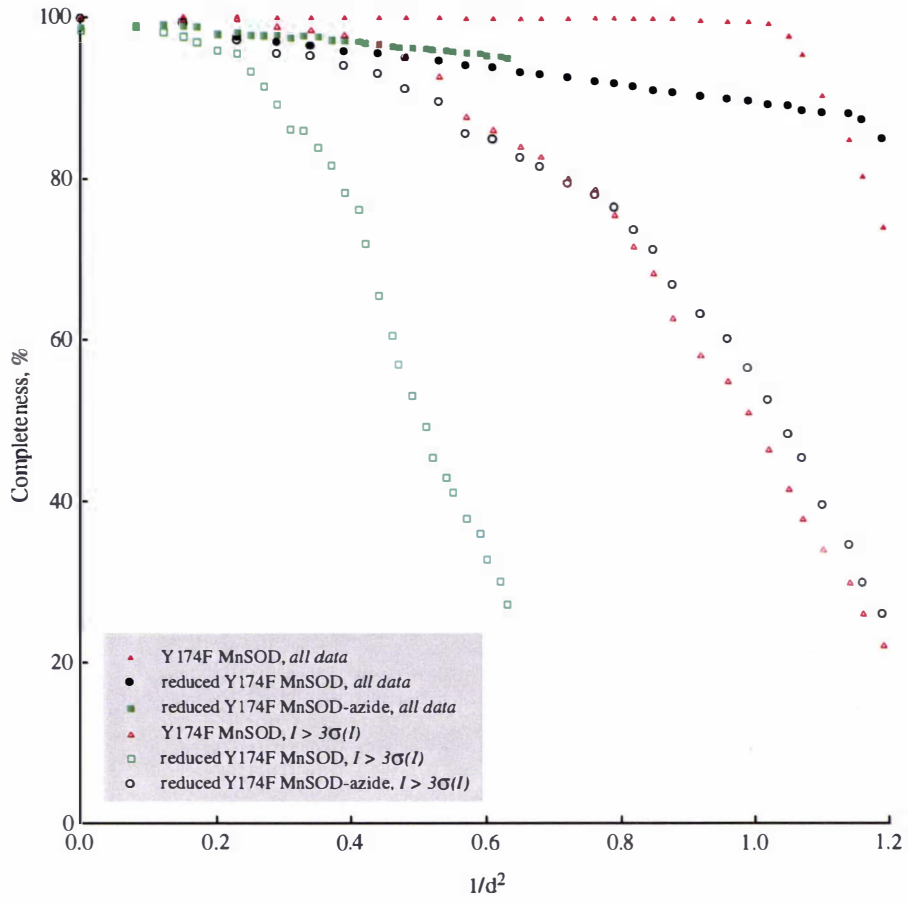

Figure 6-1. Completeness of data plotted against resolution for the three synchrotron data sets of Y174F MnSOD

Percentage of theoretical completeness plotted with, filled symbols for all reflections, and unfilled symbols for reflections with I > 3σ(I). Native oxidation state crystal form represented by red triangles, reduced form by black circles and reduced form with azide by green squares.

6.3.2. Diffraction limits and effective resolution

Diffraction of crystals of Y174F MnSOD was observed to the edge of the Mar345 imaging plate at a crystal to film distance of 96.0 mm, corresponding to a resolution of 0.90 Å. Data at a lower resolution than 50 Å were obscured by the X-ray beam stop. The diffraction limits of this study are therefore 50.0 - 0.90 Å.

The effective resolution of X-ray crystallographic data is the resolution to which the data is considered statistically meaningful. The choice of the value of the effective resolution is usually based on statistical analyses of the data, the criteria involved in this decision being quite variable amongst crystallographers, but usually considering the variation over the data of the ratio of I to σ(I), the merging R(I)-factor for symmetry-related reflections, and percentage of theoretical completeness. In some cases, data are used for refinement or structure solution to a resolution higher than the effective resolution [190].

In Figure 6-1 (opposite) the percentage of theoretical completeness is plotted as a function of resolution for the three synchrotron data sets, firstly, for all reflections (filled symbols), and, secondly, for reflections having $I > 3\sigma(I)$ (hollow symbols). In Figure 6-2 (below), the merging R(I)-factor for symmetry-related reflections is plotted as a function of resolution for the three synchrotron data sets, again separately for all reflections, and for reflections having $I < 3\sigma(I)$. Inspection of these plots allows critical evaluation of the effective resolution of these data.

6.4. Benefits of atomic resolution data of *E. coli* Y174F MnS●D

6.4.1. In investigations of Mn and Fe superoxide dismutases

The structure of Y174F MnSOD is the first Fe or MnSOD structure at atomic resolution, the previous highest resolution structure being that of *P. shermanii* cambialistic FeSOD [191] at 1.35 Å resolution. Atomic resolution structures of MnSOD will have several benefits for studies on Fe and MnSODs.

Firstly, the accurate determination of the active-site metal geometry. As the mechanism of superoxide dismutation used by these enzymes is a cyclic redox mechanism, the enzyme alternates between the reduced and oxidised states. The atomic resolution structures of both the resting oxidation state and the reduced oxidation state will allow the accurate description of differences between them, be that different coordination states of the metal, or more subtly in the positions of ligands in the secondary coordination sphere. The accurate determination of bond lengths and angles of the metal ion will allow the application of more accurate restraints in the refinement of similar structures at lower resolution. Additionally, it will be possible, given the high data to parameter ratio and the inherent thermal order observed in the region of the metal ion, to refine the occu-

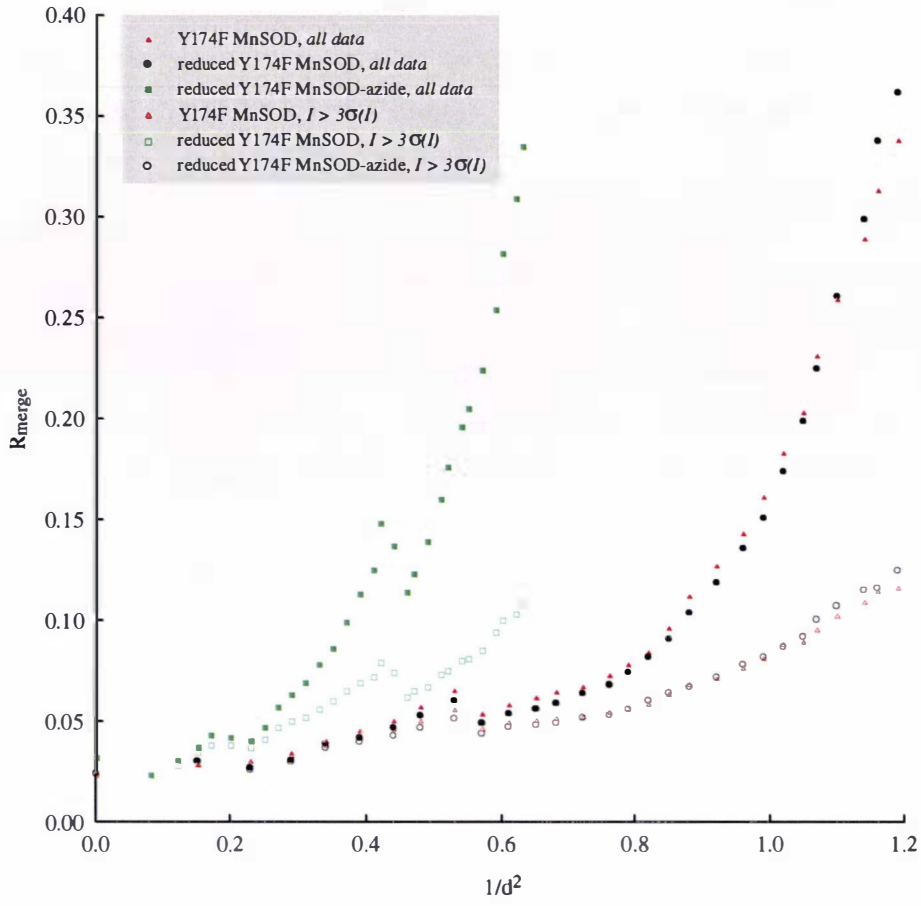

Figure 6-2. R_{merge} plotted against resolution for the three synchrotron data sets of Y174F MnSOD

R_{merge}, where $R_{merge} = \Sigma|I-\langle I\rangle|/\Sigma I$, and $\langle I\rangle$ is the mean of individual observations of intensities I, is plotted with, filled symbols for all reflections, and unfilled symbols for reflections with $I > 3\sigma(I)$. Native oxidation state crystal form represented by red triangles, reduced form by black circles and reduced form with azide by green squares.

pancy of the metal ion, which has been shown experimentally to have an occupancy of less than one metal per active site.

Secondly, atomic resolution data can in some cases reveal the atomic positions of hydrogen atoms, which at lower resolutions are generally not observed due to their low (single-electron) X-ray scattering power. The mechanism of superoxide dismutation requires that two protons be taken up per cycle. At what stage the protons are picked up by departing substrate is still unclear. If the atomic positions of hydrogen atoms can be observed within the active-site of the enzyme and on key residues, their likelihood of involvement in the mechanism may be inferred from their positions and orientations. Key residues include the metal-bound solvent molecule, residues involved in the putative hydrogen-bonding relay from the metal to bulk solvent (Gln146, Tyr34), the gate-

way residue His30, and the conserved solvent molecule at the entrance to the active site.

Thirdly, the protonation states of catalytic residues can be determined experimentally at different values of pH. The activity and ligand-binding properties of Fe and MnSODs is dependent on pH [125, 115, 9, 199]. Structural studies on the cambialistic SOD of *P. shermanii* at different values of pH have been reported [191]. The advantage of doing such studies at atomic resolution is that the protonation state of residues can be determined experimentally and related to the pH-dependent activity of the enzyme.

6.4.2. Advancement of crystallographic techniques and protocols

The combination of diffraction to atomic resolution and large number of atoms for the Y174F MnSOD structure is quite unique. The data can therefore be used in testing the effectiveness of crystallographic programs for atomic resolution, many-atom models. In particular, structure solution by *ab initio* methods may be investigated (see 6.4.3 *Ab initio structure solution*).

Atomic resolution protein structures, while becoming increasingly more common, are still very much the exception rather than the norm. However, this small subset of structures is used in designing appropriate geometric and conformational restrains for application in refinement of structures at lower resolutions. Atomic resolution structures have also been used to check and aid in the development of protein structure validation programs such as PROCHECK, PROVE, SQUID and WHATCHECK [186].

6.4.3. *Ab initio* structure solution

Ab initio methods, also commonly known as direct methods, are the most common method for solving structures with fewer than 100 non-hydrogen atoms. This method for overcoming the phase problem utilizes the relationship between the phases of structure factors and the distribution of normalized structure factors. For protein molecules these distributions are more complicated and less apparent because of the larger number of non-hydrogen atoms and non-atomicity (non atomic resolution) of most data sets. Atomic resolution data has the advantage over lower resolution data for similarly sized protein structures in that the number of reflections is greatly increased, allowing for more relationships to be found between reflections. Data to better than 1.2 Å resolution is required for *ab initio* structure solution using direct methods [192]. The program SnB [193] has been used to successfully solve structures with between 100 and 1000 non-hydrogen atoms [194], including the 1001 non-hydrogen atom structure of triclinic lysozyme at 1.0 Å resolution [195]. SnB uses a variation on the conventional direct-methods procedure, called shake-and-bake. In the shake-and-bake method, triplet invariants are first generated from the normalized structure-factor magnitudes. A trial structure of randomly positioned atoms is used to calculate initial phases, and this is followed by

cycles of phase refinement alternated with real-space density modification. The program SHELXS implements a similar scheme of automatic Fourier recycling to improve and extend a trial structure [196]. SHELXS uses a peaklist optimization procedure to improve the starting phases from a trial structure. The trial structure is generated from either a direct methods solution, or from tangent expansion of a partial structure. Slightly better than random phases can be used initially if the positions of any heavy atoms in the structure can be located by interpretation of the Patterson function.

Solution of the Y174F MnSOD structure by direct methods is not essential to the refinement, as molecular replacement techniques have already provided a structure solution. Nonetheless, structure solution by *ab initio* methods offers the advantage that no previously refined model was ever used in the calculation of the phases of the atomic resolution refinement, thereby eliminating any possibility of phase bias. In addition, a completely different set of R_{free} reflections could be chosen to avoid those that are related to the reflections in the working set by the NCS-relationships within the data [197].

7 Perspectives

7.1. Concluding remarks

A detailed mechanism of superoxide dismutation by the Mn- and Fe-containing superoxide dismutases is far from complete. Although the basic mechanism of this metal-catalysed redox reaction is known, many aspects still remain undetermined. Key amongst them is the binding mode of superoxide in each state of the reaction, where, when and how the protonation events occur, and how the enzyme structure controls the redox potential of the metal ion. Currents efforts revolve around both biochemical and structural studies including pH-dependent activity, substrate analog binding, and redox potential measurements, and structure determination by both X-ray crystallography and NMR techniques. The same studies on mutants of these enzymes will prove useful in determining roles for individual residues in the enzyme.

A key aspect of this enzyme's behaviour now appears to be the pH dependence exhibited by many of its biochemical characteristics. Biochemical measurements conducted at a single pH can be misleading. Hence, a precise understanding of the protonation events of this enzyme requires biochemical measurements, including activity and redox potential, to be made over a range of pH values, on both the wildtype enzyme and site-directed mutants.

The necessary inter-relation of biochemical and structural data therefore requires that the structural studies likewise be concerned with accurate pH determination. Other aspects of this enzyme also require particular attention if structural analysis, in particular by the X-ray crystallographic technique, are to be meaningful. Primary concerns are metal-ion content, redox state and pH.

Metal-ion content, both in the type of metal and the occupancy of the metal site, if not controlled, must at least be accurately known. Clearly single active-site, mixed-metal species should be avoided due to complications arising in liganding states. Likewise incomplete metal occupancy of the active-site would require that multiple ligand conformations be modelled. Such models lead to a more difficult and less accurate determination of active-site parameters, at least at modest resolution. The oxidation state of the

active-site is equally important, with mixed redox species giving rise to similar problems as described for mixed-metal or partial occupancy species. Knowing accurately the pH of the structure determination is important if structural explanations of protonation behaviour are to be related to equivalent biochemical evidence.

The complete structural determination of a Mn- or Fe-containing superoxide dismutase, native or mutant, should therefore consider the above aspects. In practical terms the metal type and active-site contents of the enzyme solution must be determined. The possibility of non-active-site metal binding has to be considered [10]. Multiple structure determinations at different pH values based around important enzymic pK's could prove useful at tracking structural changes due to these protonation events. The pH of the crystallisation buffer solutions can not be taken as an accurate value for the pH of the crystal. If crystal behaviour allows, titration of crystals by soaking in a pseudo mother liquor of adequate volume for accurate pH determination, would allow for more accurate estimates of the pH of crystallisation. The same consideration would be required for solutions of cyroprotectant. Whilst not always easy to achieve, preferred redox states for the crystal would be either fully reduced or fully oxidised. The complete structural determination may therefore require a number of individual structure determinations at varying pH values and in different redox states.

The roles of secondary and even tertiary coordination sphere residues will need to be examined before all aspects of the mechanism are determined. The influence in particular of such residues as Asn80 and Trp128 on the secondary coordination sphere residue Gln146 could be carefully examined in mutagenesis studies. Mutants of the gateway residues, including the naturally occurring H30N substitution may also prove beneficial. Further mutation of Tyr174, in the hope of a substitution which correctly orients His30 without modifying its effective pK, a seemingly difficult prospect, would distinguish further the roles of these two gateway residues.

A Selected active-site bond lengths and angles

Native *E. coli* MnSOD Bond Lengths (Å)

				A	B	C	D	Avg.	S.D.
34	OH	146	NE2	2.98	3.08	2.98	2.98	3.00	0.04
146	NE2	207	OH	2.95	2.92	2.89	2.86	2.91	0.03
146	OE1	128	NE1	2.97	3.00	3.06	2.97	3.00	0.03
206	MN	26	NE2	2.21	2.20	2.19	2.18	2.19	0.01
206	MN	81	NE2	2.25	2.20	2.24	2.22	2.22	0.02
206	MN	167	OD1	3.53	3.56	3.53	3.52	3.54	0.02
206	MN	167	OD2	1.98	2.02	2.01	1.96	1.99	0.02
206	MN	171	NE2	2.21	2.28	2.24	2.26	2.25	0.03
206	MN	207	OH	2.24	2.26	2.30	2.29	2.27	0.02

E. coli Fe_2MnSOD Bond Lengths (Å)

				A	B	Avg.	S.D.
34	OH	146	NE2	3.10	3.05	3.08	0.03
34	OH	208	OH	-	2.88	-	-
146	NE2	207	OH	2.65	2.60	2.63	0.02
146	OE1	128	NE1	2.93	2.88	2.90	0.03
206	FE	26	NE2	2.20	2.20	2.20	0.00
206	FE	81	NE2	2.03	2.15	2.09	0.06
206	FE	167	OD1	3.63	3.47	3.55	0.08
206	FE	167	OD2	2.02	1.98	2.00	0.02
206	FE	171	NE2	2.31	2.28	2.30	0.01
206	FE	207	OH	2.10	2.22	2.16	0.06
206	FE	208	OH	-	2.05	-	-

Native *E. coli* MnSOD Bond Angles (º)

						A	B	C	D	Avg.	S.D.
26	NE2	206	MN	81	NE2	93.8	91.8	91.8	91.6	92.2	0.9
26	NE2	206	MN	167	OD1	121.6	120.8	121.5	123.1	121.7	0.8
26	NE2	206	MN	167	OD2	90.3	88.3	88.6	91.4	89.7	1.3
26	NE2	206	MN	171	NE2	90.1	90.1	90.1	89.5	89.9	0.3
26	NE2	206	MN	207	OH	173.6	173.4	174.9	176.7	174.6	1.3
81	NE2	206	MN	167	OD1	116.1	117.7	116.6	118.1	117.1	0.8
81	NE2	206	MN	167	OD2	109.0	114.7	112.0	110.0	111.6	2.1
81	NE2	206	MN	171	NE2	133.1	131.2	132.9	128.8	131.4	1.7
81	NE2	206	MN	207	OH	91.1	92.9	90.0	89.9	91.0	1.2
167	OD1	206	MN	167	OD2	34.3	33.7	34.4	34.5	34.2	0.3
167	OD1	206	MN	171	NE2	100.9	102.6	102.0	103.4	102.1	0.9
167	OD1	206	MN	207	OH	52.3	52.7	53.6	53.6	53.0	0.6
167	OD2	206	MN	171	NE2	117.8	114.2	115.1	120.2	116.8	2.4
167	OD2	206	MN	207	OH	84.2	85.5	86.3	85.2	85.3	0.8
171	NE2	206	MN	207	OH	89.6	90.3	92.2	92.0	91.0	1.1

E. coli Fe_2MnSOD Bond Angles (º)

						A	B	Avg.	S.D.
26	NE2	206	FE	81	NE2	86.9	91.9	89.4	2.5
26	NE2	206	FE	167	OD1	115.7	123.2	119.4	3.8
26	NE2	206	FE	167	OD2	87.0	87.8	87.4	0.4
26	NE2	206	FE	171	NE2	89.4	90.4	89.9	0.5
26	NE2	206	FE	207	OH	174.0	178.1	176.0	2.1
26	NE2	206	FE	208	OH	-	89.9	-	-
81	NE2	206	FE	167	OD1	117.3	109.5	113.4	3.9
81	NE2	206	FE	167	OD2	103.8	108.6	106.1	2.4
81	NE2	206	FE	171	NE2	148.1	148.0	148.0	0.1
81	NE2	206	FE	207	OH	98.4	89.2	93.8	4.6
81	NE2	206	FE	208	OH	-	69.7	-	-
146	NE2	34	OH	208	OH	-	92.0	-	-
167	OD1	206	FE	167	OD2	32.2	36.0	34.1	1.9
167	OD1	206	FE	171	NE2	92.7	95.6	94.2	1.4
167	OD1	206	FE	207	OH	59.4	54.9	57.2	2.2
167	OD1	206	FE	208	OH	-	146.6	-	-
167	OD2	206	FE	171	NE2	107.6	103.3	105.4	2.2
167	OD2	206	FE	207	OH	89.1	90.4	89.8	0.7
167	OD2	206	FE	208	OH	-	177.1	-	-
171	NE2	206	FE	207	OH	87.5	89.6	88.5	1.0
171	NE2	206	FE	208	OH	-	78.4	-	-
207	OH	206	FE	208	OH	-	91.9	-	-

B Surface Area of Interface Residues

Interface atoms of native *E. coli* MnSOD and FeSOD as defined by the decrease in SA ($Å^2$) of residues on dimerization of chain A and chain B.

MnSOD				FeSOD			
Residue		Chain A	Chain B	Residue		Chain A	Chain B
Gln	21	-3.0	-3.1	Glu	21	-18.5	-16.6
Ile	25	-40.2	-41.2	Tyr	25	-51.4	-51.4
Lys	29	-28.2	-28.6	Lys	29	-24.8	-23.8
His	30	-38.2	-37.1	His	30	-40.0	-40.4
Thr	33	-1.7	-0.7				
Tyr	34	-11.8	-12.1	Tyr	34	-11.4	-10.8
				Asn	65	-38.2	-38.4
				Asn	66	-2.2	-2.8
Asn	73	-38.2	-38.0				
Asn	74	-4.2	-4.0				
				Gln	69	-2.5	-2.4
Phe	124	-136.9	-138.7	Phe	118	-135.2	-135.4
Gly	125	-46.5	-45.8	Gly	119	-41.7	-43.2
Ser	126	-28.2	-29.1	Ser	120	-28.9	-28.6
Asn	145	-29.7	-29.8	Ser	139	-7.8	-8.2
Gln	146	-3.0	-3.0	Asn	140	-50.2	-47.2
				Ala	141	-2.1	-2.0
Trp	169	-44.1	-44.1	Trp	158	-45.8	-45.3
Glu	170	-90.4	-91.1	Glu	159	-92.6	-91.4
His	171	-38.1	-39.1	His	160	-33.3	-33.4
Tyr	174	-96.7	-95.6	Tyr	163	-89.6	-91.8
Leu	175	-62.0	-61.7	Ile	164	-37.9	-37.3
Gln	178	-40.3	-40.5	Arg	167	-88.7	-88.5
Asn	179	-65.4	-66.8	Asn	168	-68.8	-71.5
Arg	181	-1.0	-1.2				

C Mn and FeSOD Sequence Alignments

Species codes for FeSOD sequence alignment

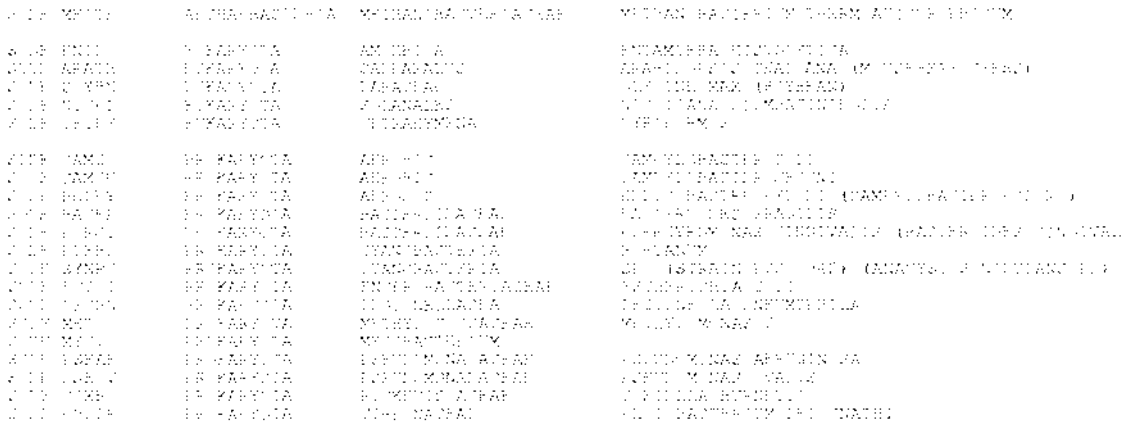

Iron superoxide dismutase sequence alignment

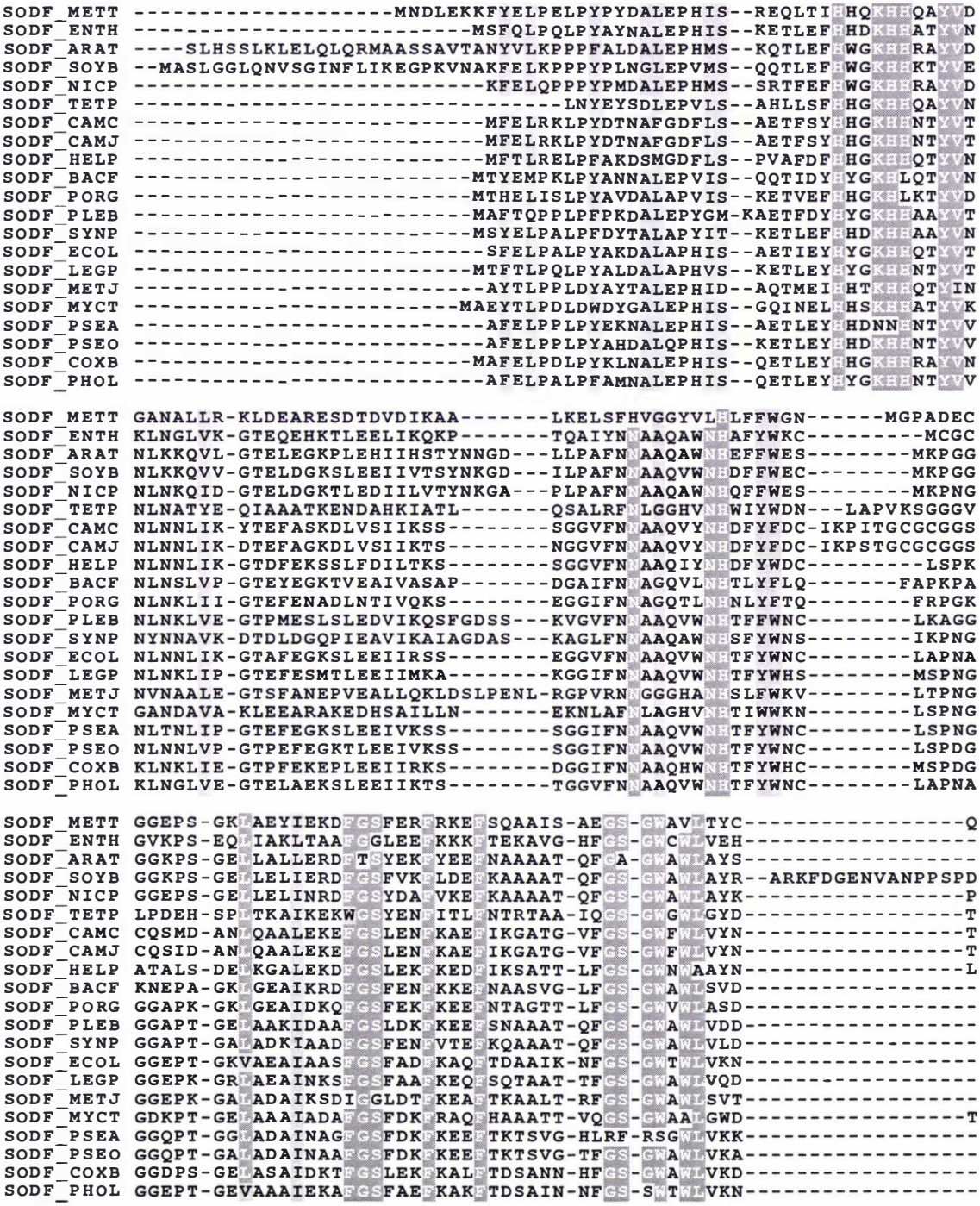

Iron superoxide dismutase sequence alignment

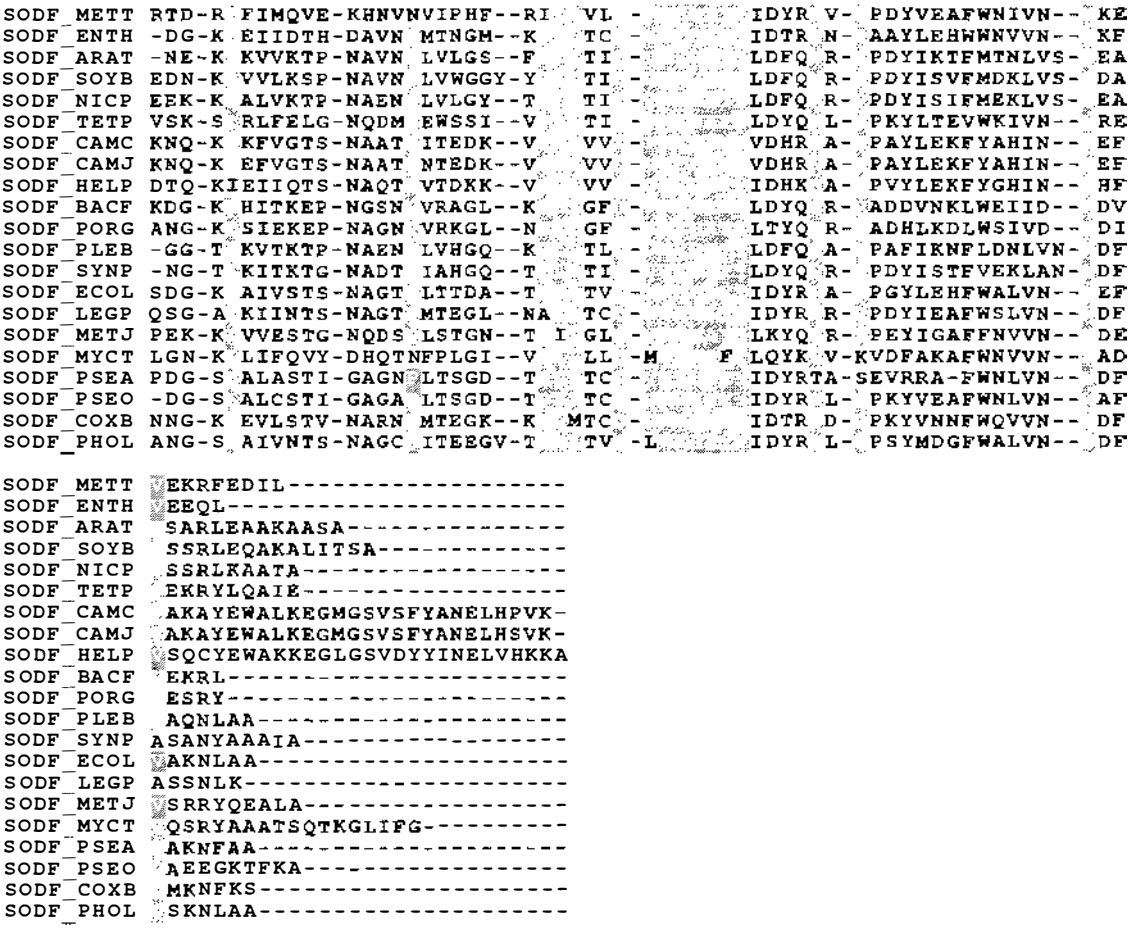

Species codes for MnSOD sequence alignment

SODM_HUMAN	MN	HOMO SAPIENS (HUMAN).
SODM_BOVIN	MN	BOS TAURUS (BOVINE).
SODM_MOUSE	MN	MUS MUSCULUS (MOUSE).
SODM_RAT	MN	RATTUS NORVEGICUS (RAT).
SODM_RABIT	MN	ORYCTOLAGUS CUNICULUS (RABBIT).
SODM_CAVPO	MN	CAVIA PORCELLUS (GUINEA PIG).
SODM_PEA	MN	PISUM SATIVUM (GARDEN PEA).
SODM_NICPL	MN	NICOTIANA PLUMBAGINIFOLIA (LEADWORT-LEAVED TOBACCO).
SODM_HEVBR	MN	HEVEA BRASILIENSIS (PARA RUBBER TREE).
SODM_CAEEL	MN	CAENORHABDITIS ELEGANS.
SODN_CAEEL	MN	CAENORHABDITIS ELEGANS.
SODM_MAIZE	MN	ZEA MAYS (MAIZE).
SODN_MAIZE	MN	ZEA MAYS (MAIZE).
SODO_MAIZE	MN	ZEA MAYS (MAIZE).
SODP_MAIZE	MN	ZEA MAYS (MAIZE).
SODM_DROME	MN	DROSOPHILA MELANOGASTER (FRUIT FLY).
SODM_BRAFL	MN	BRANCHIOSTOMA FLORIDAE (FLORIDA LANCELET) (AMPHIOXUS).
SODM_PIG	MN	SUS SCROFA (PIG).
SODM_PETMA	MN	PETROMYZON MARINUS (SEA LAMPREY).
SODM_PARCL	MN	PARASTICHOPUS CALIFORNICUS (SEA CUCUMBER).
SODM_PALVU	MN	PALINURUS VULGARIS (EUROPEAN SPINY LOBSTER).
SODM_EPTST	MN	EPTATRETUS STOUTII (PACIFIC HAGFISH).
SODM_ECOLI	MN	ESCHERICHIA COLI.
SODM_SALTY	MN	SALMONELLA TYPHIMURIUM.
SODM_BACST	MN	BACILLUS STEAROTHERMOPHILUS.
SODM_BACSU	MN	BACILLUS SUBTILIS.
SODM_BACCA	MN	BACILLUS CALDOTENAX.
SODM_LACLA	MN	LACTOCOCCUS LACTIS (SUBSP. LACTIS) (STREPTOCOCCUS LACTIS).
SOD1_PLEBO	MN	PLECTONEMA BORYANUM.
SOD2_PLEBO	MN	PLECTONEMA BORYANUM.
SOD3_PLEBO	MN	PLECTONEMA BORYANUM.
SODM_THETH	MN	THERMUS AQUATICUS (SUBSP. THERMOPHILUS).
SODM_THEAQ	MN	THERMUS AQUATICUS.
SODM_LISMO	MN	LISTERIA MONOCYTOGENES.
SODM_LISIV	MN	LISTERIA IVANOVII.
SODM_BORPE	MN	BORDETELLA PERTUSSIS.
SODM_HAEIN	MN	HAEMOPHILUS INFLUENZAE.
SODM_XANCP	MN	XANTHOMONAS CAMPESTRIS (PV. CAMPESTRIS).
SODM_PSEAE	MN	PSEUDOMONAS AERUGINOSA.
SODM_HALHA	MN	HALOBACTERIUM HALOBIUM, AND HALOBACTERIUM CUTIRUBRUM.
SOD1_HALCU	MN	HALOBACTERIUM CUTIRUBRUM.
SOD1_HALSG	MN	HALOBACTERIUM SP. (STRAIN GRB).
SOD2_HALSG	MN	HALOBACTERIUM SP. (STRAIN GRB).
SODM_HALMA	MN	HALOARCULA MARISMORTUI (HALOBACTERIUM MARISMORTUI).
SOD1_HALVO	MN	HALOBACTERIUM VOLCANII (HALOFERAX VOLCANII).
SOD2_HALVO	MN	HALOBACTERIUM VOLCANII (HALOFERAX VOLCANII).
SODM_PROFR	MN	PROPIONIBACTERIUM FREUDENREICHII SHERMANII.
SODM_NOCAS	MN	NOCARDIA ASTEROIDES.
SODM_MYCLE	MN	MYCOBACTERIUM LEPRAE.
SODM_MYCAV	MN	MYCOBACTERIUM AVIUM.
SODM_MYCCE	MN	MYCOBACTERIUM CELATUM.
SODM_MYCCH	MN	MYCOBACTERIUM CHELONAE.
SODM_MYCIT	MN	MYCOBACTERIUM INTRACELLULARE.
SODM_MYCKA	MN	MYCOBACTERIUM KANSASII.
SODM_MYCMA	MN	MYCOBACTERIUM MALMOENSE.
SODM_MYCMR	MN	MYCOBACTERIUM MARINUM.
SODM_MYCPA	MN	MYCOBACTERIUM PARATUBERCULOSIS.
SODM_MYCPH	MN	MYCOBACTERIUM PHLEI.
SODM_MYCSC	MN	MYCOBACTERIUM SCROFULACEUM.
SODM_MYCSZ	MN	MYCOBACTERIUM SZULGAI.
SODM_MYCSM	MN	MYCOBACTERIUM SMEGMATIS.
SODM_CORDI	MN	CORYNEBACTERIUM DIPHTHERIAE.
SODM_ONCVO	MN	ONCHOCERCA VOLVULUS.
SODM_YEAST	MN	SACCHAROMYCES CEREVISIAE (BAKER'S YEAST).
SODF_SULAC	MN	SULFOLOBUS ACIDOCALDARIUS.
SODM_YEREN	MN	YERSINIA ENTEROCOLITICA.

Manganese superoxide dismutase sequence alignment

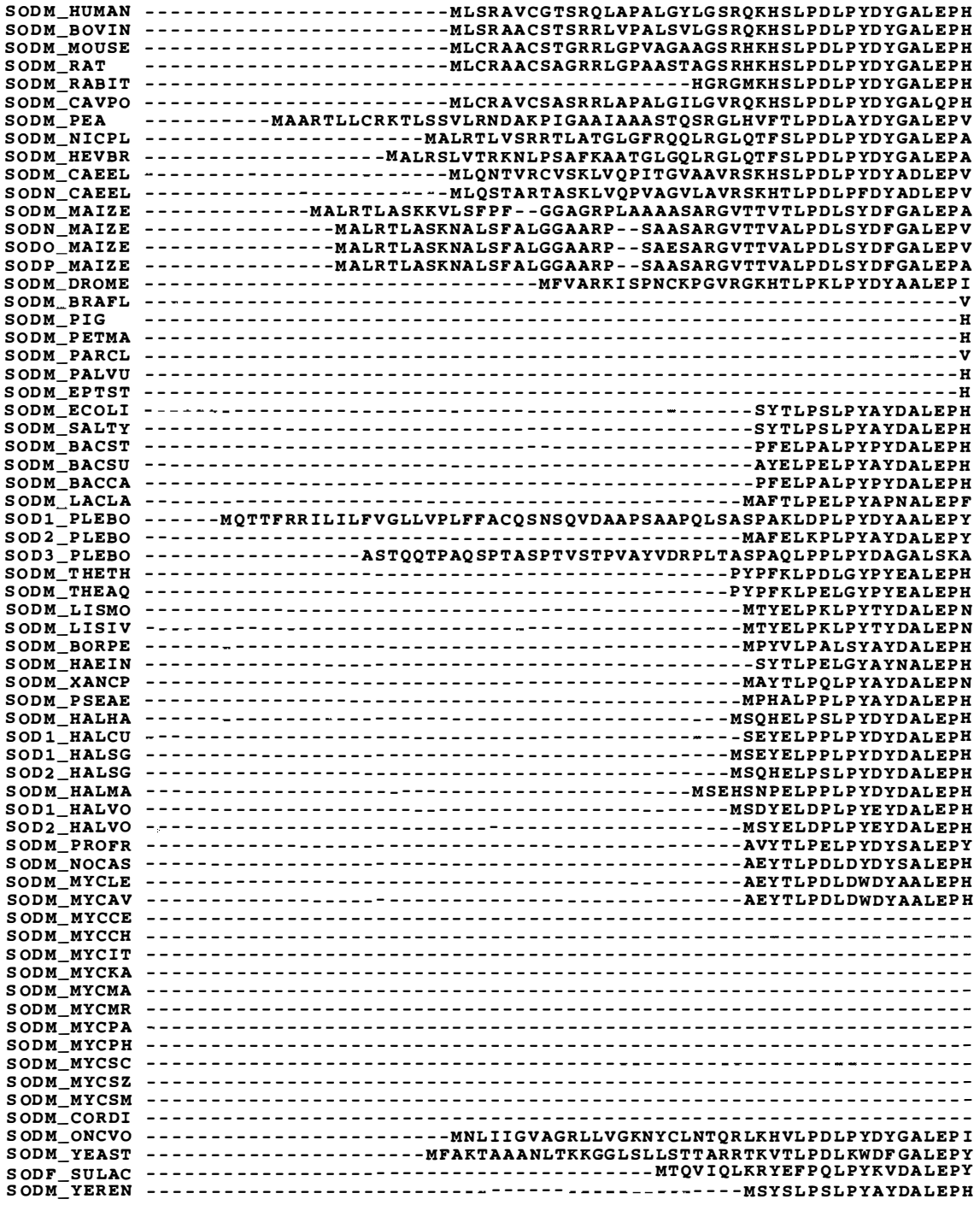

Manganese superoxide dismutase sequence alignment

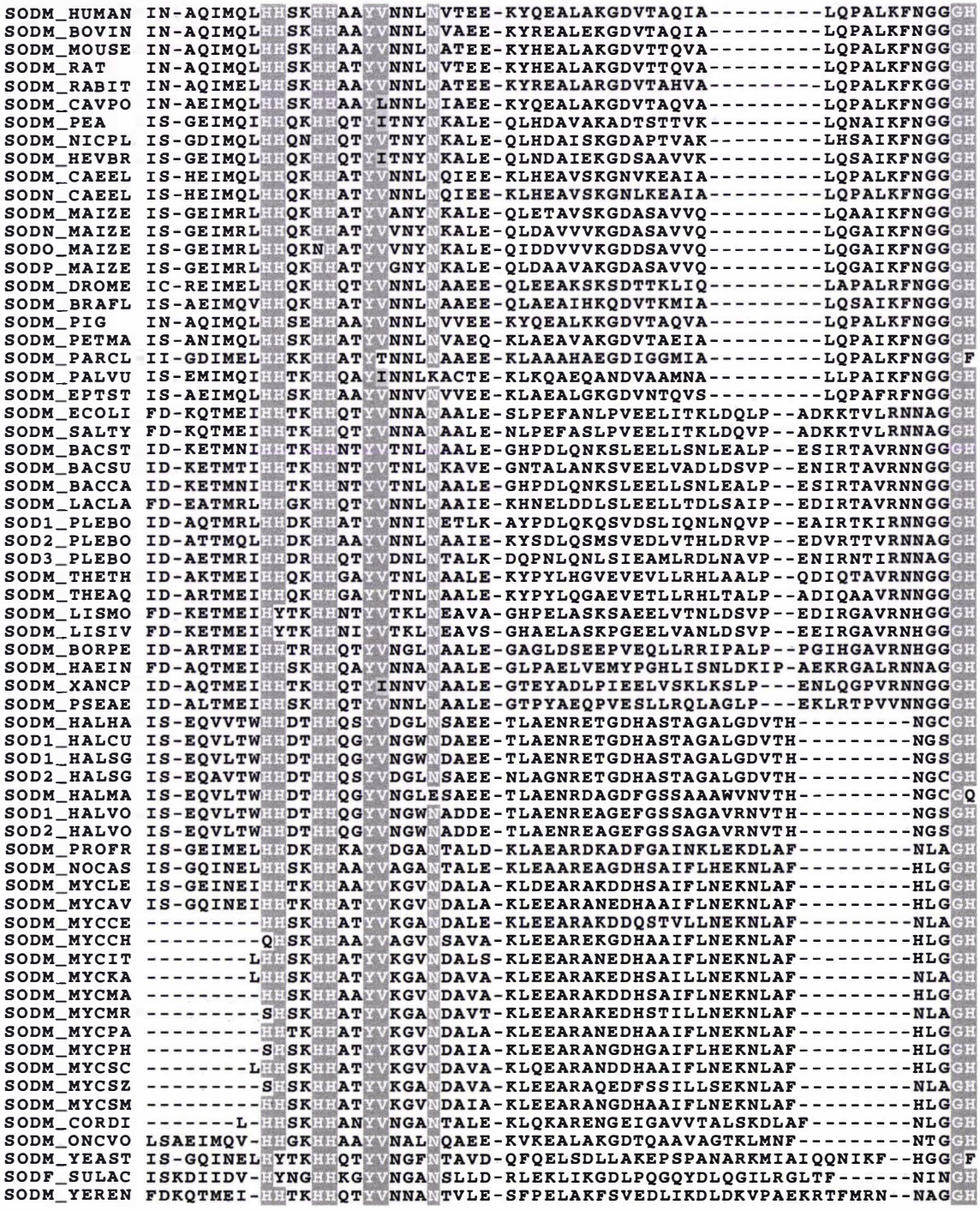

Manganese superoxide dismutase sequence alignment

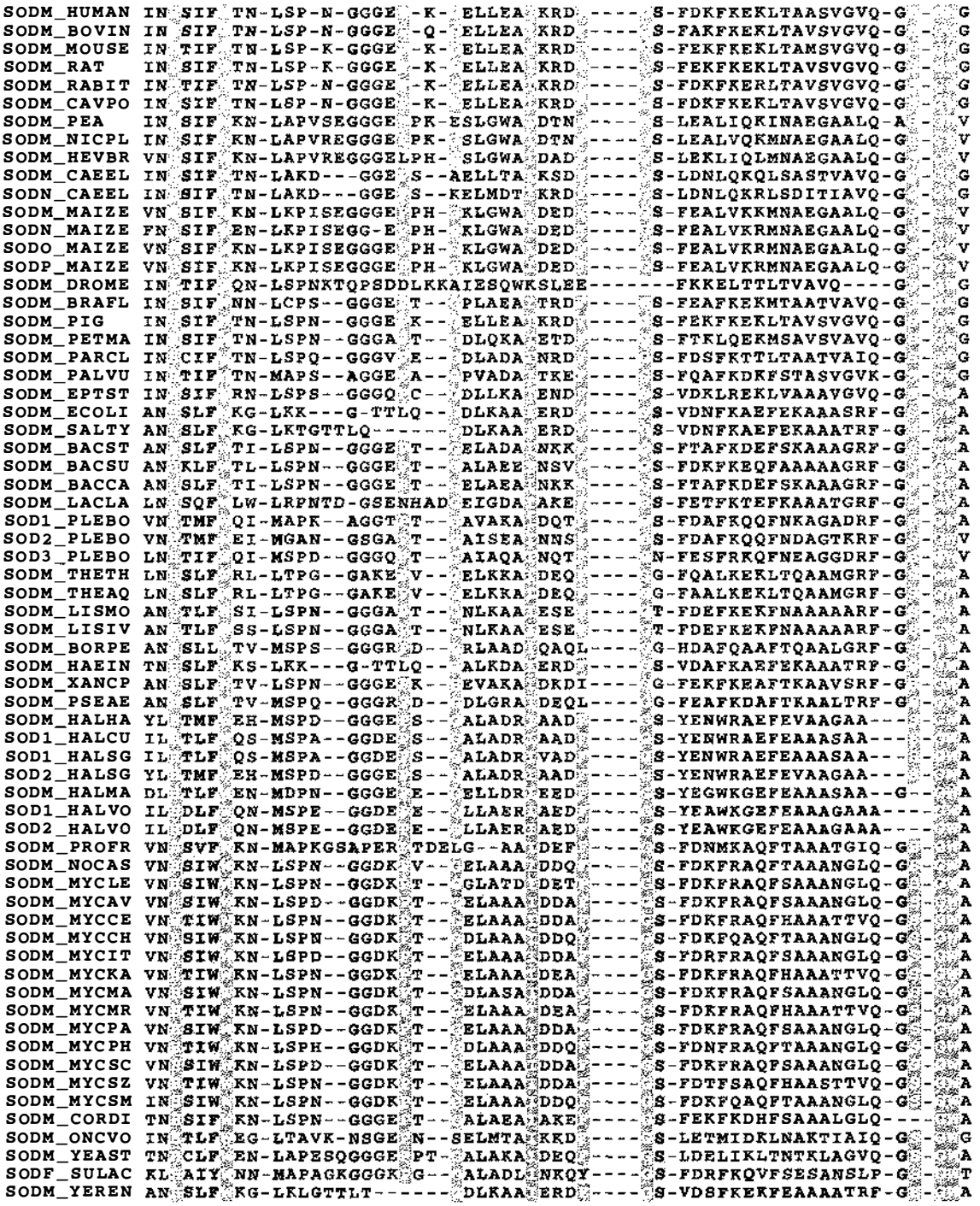

Manganese superoxide dismutase sequence alignment

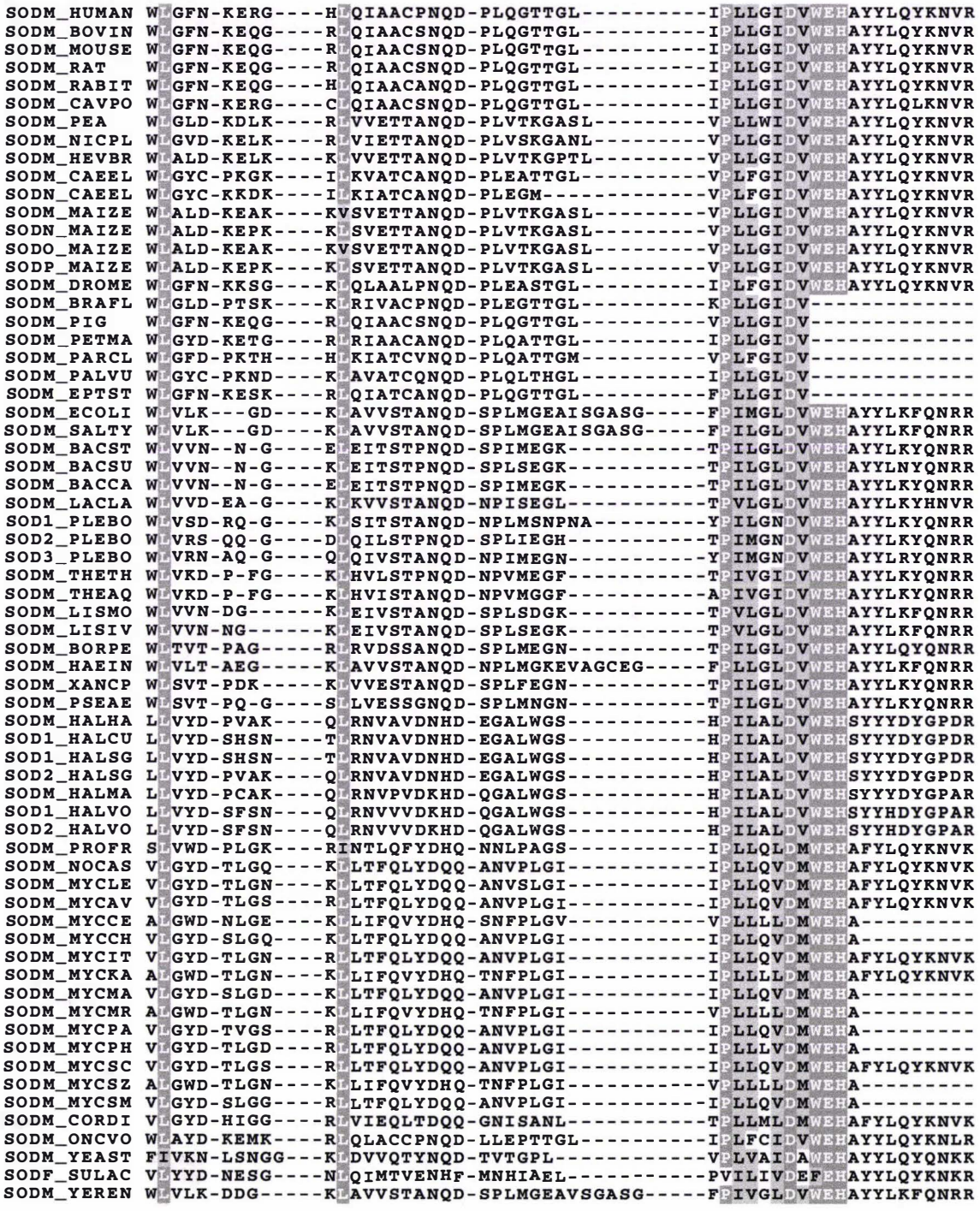

Manganese superoxide dismutase sequence alignment

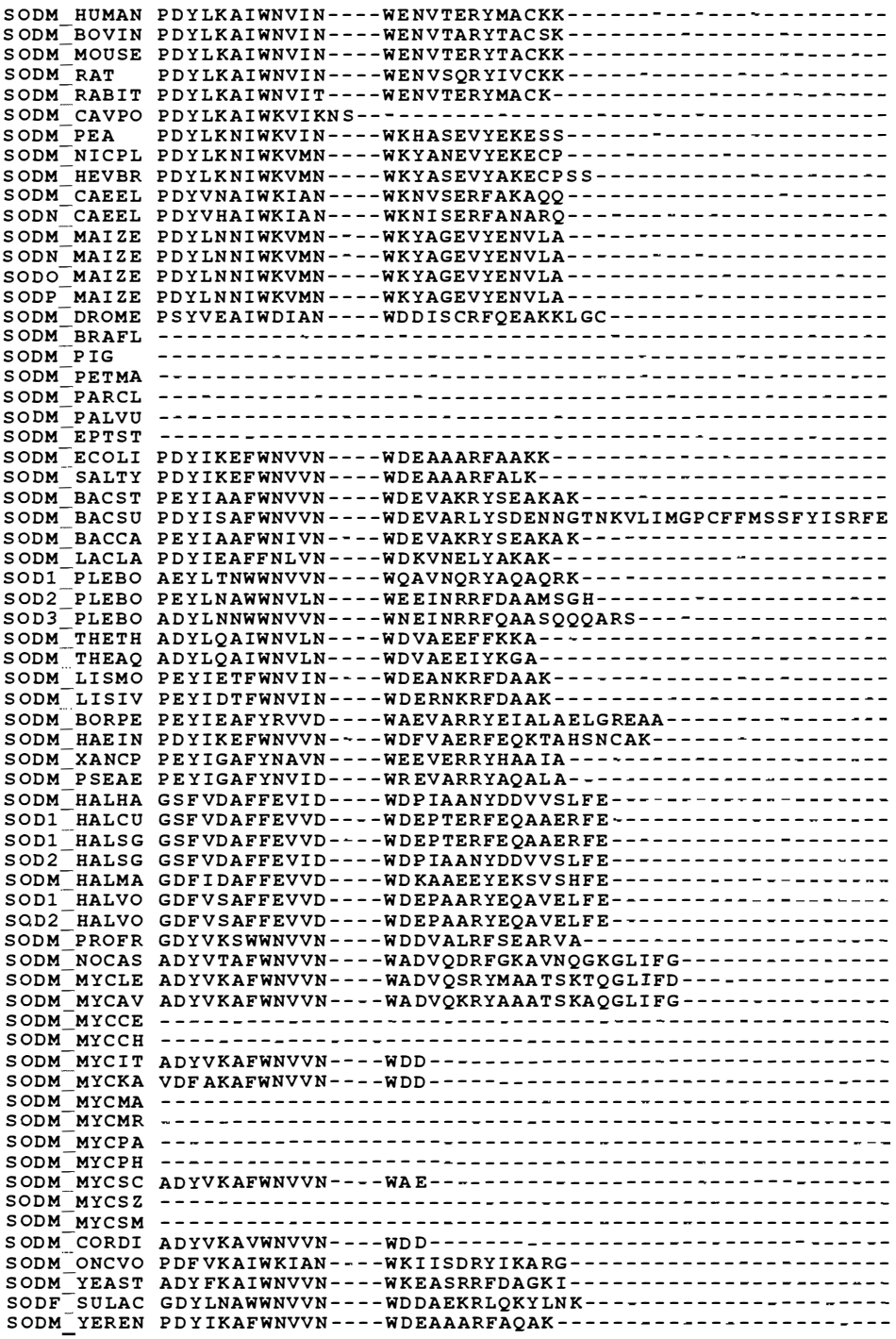

Bibliography

[1] P. J. Kraulis. MOLSCRIPT: A program to produce both detailed and schematic plots of protein structures. *Journal of Applied Crystallography*, **24**:946–950, 1991.

[2] F. C. Bernstein, T. F. Koetzle, G. J. Williams, E. E. Meyer Jr, M. D. Brice, J. R. Rodgers, O. Kennard, T. Shimanouchi, and M. Tasumi. The protein data bank: a computer-based archival file for macromolecular structures. *Journal of Molecular Biology*, **112**(3):535–542, 1977.

[3] Research collaboratory for structural bioinformatics, PDB. *http://www.rcsb.org/pdb*

[4] W. F. Beyer Jr, J. A. Reynolds, and I. Fridovich. Differences between the manganese- and the iron-containing superoxide dismutases of *Escherichia coli* detected through sedimentation equilibrium, hydrodynamic and spectroscopic studies. *Biochemistry*, **28**(10):4403–4409, 1989.

[5] J. W. Whittaker and M. M. Whittaker. Active site spectral studies on manganese superoxide dismutase. *Journal of the American Chemical Society*, **113**:5528–5540, 1991.

[6] M. S. Lah, M. M. Dixon, K. A. Pattridge, W. C. Stallings, J. A. Fee, and M. L. Ludwig. Structure-function in *Escherichia coli* iron superoxide dismutase: Comparisons with the manganese enzyme from *Thermus thermophilus*. *Biochemistry*, **34**(5):1646–1660, 1995.

[7] C. Bull, E. C. Niederhoffer, T. Yoshida, and J. A. Fee. Kinetic studies of superoxide dismutases: Properties of the manganese-containing protein from *Thermus thermophilus*. *Journal of the American Chemical Society*, **113**(11):4069–4076, 1991.

[8] M. M. Whittaker and J. W. Whittaker. Low-temperature thermochromism marks a change in coordination for the metal ion in manganese superoxide dismutase. *Biochemistry*, **35**(21):6762-6770, 1996.

[9] F. Yamakura, K. Kobayashi, S. Tagawa, A. Morita, T. Imai, D. Ohmori and T. Matsumoto. pH-dependent activity change of superoxide dismutase from *Mycobacterium smegmatis*. *Biochemistry and Molecular Biology International*, **36**(2):233-240, 1995.

[10] C. K. Vance and A.-F. Miller. A simple proposal that can explain the inactivity of metal-substituted superoxide dismutases. *Journal of the American Chemical Society*, **120**(3):461–467, 1998.

[11] Y. A. Ilan, G. Czapski, and D. Meisel. One-electron transfer redox potentials of free-radicals. 1. oxygen-superoxide system. *Biochimica et Biophysica Acta*, **430**(2):209–224, 1976.

[12] D. T. Sawyer and J. S. Valentine. How super is superoxide? *Accounts of Chemical Research*, **14**:393–400, 1981.

[13] P. B. Merkel and D. R. Kearns. Radiationless decay of singlet molecular oxygen in solution. Experimental and theoretical study of electronic-to-vibrational energy transfer. *Journal of the American Chemical Society*, **94**(21):7244–7253, 1972.

[14] P. E. Cade, R. F. W. Bader, and J. Pelletier. Molecular charge distributions and chemical bonding. V. Molecular excitation, ionization, and electron attachment. *Journal of Chemical Physics*, **54**(8):3517–3533, 1971.

[15] M. Momenteau and C. A. Reed. Synthetic heme dioxygen complexes. *Chemical Reviews*, **94**(3):659–698, 1994.

[16] P. F. Knowles, J. F. Gibson, F. M. Pick, and R. C. Bray. Electron-spin-resonance evidence for enzymic reduction of oxygen to a free radical, the superoxide ion. *Biochemical Journal*, **111**(1):53–58, 1969.

[17] W. Kanzig and M. H. Cohen. Paramagnetic resonance of oxygen in alkali halides. *Physical review letters*, **3**(11):509–510, 1959.

[18] G. Czapski. Radiation chemistry of oxygenated aqueous solutions. *Annual Review of Physical Chemistry*, **22**:171–208, 1971.

[19] B. H. J. Bielski and J. M. Gebicki. Species in irradiated oxygenated water. *Advances in Radiation Chemistry*, **2**:177–279, 1970.

[20] J. Petlicki and T. G. M. van de Ven. The equilibrium between the oxidation of hydrogen peroxide by oxygen and the dismutation of peroxyl or superoxide radicals in aqueous solutions in contact with oxygen. *Journal of the Chemical Society, Faraday Transactions*, **94**:2763–2767, 1998.

[21] D. Behar, G. Czapski, J. Rabani, L. M. Dorfman, and H. A. Schwarz. Acid dissociation constant and decay kinetics of the perhydroxyl radical. *Journal of Physical Chemistry*, **74**(17):3209–3213, 1970.

[22] M. Ardon. *Oxygen*. W. A. Benjamin, N.Y., 1965.

[23] P. M. Wood. Redox potential of the system oxygen-superoxide. *FEBS Letters*, **44**(1):22–24, 1974.

[24] D. Meisel and G. Czapski. One-electron transfer equilibriums and redox potentials of radicals studied by pulse radiolysis. *Journal of Physical Chemistry*, **79**(15):1503–1509, 1975.

[25] J. William C. Barrette, D. T. Sawyer, J. A. Fee, and K. Asada. Potentiometric titrations and oxidation-reduction potentials of several iron superoxide dismutases. *Biochemistry*, **22**(3):624–627, 1983.

[26] J. Stein, J. J. P. Fackler, G. J. McClune, J. A. Fee, and L. T. Chan. Superoxide and manganese(III). Reactions of Mn-edta and Mn-cydta complexes with $O_2^{\cdot-}$ X-ray structure of KMn-edta.H_2O. *Inorganic Chemistry*, **18**(12):3511–3519, 1979.

[27] J. A. Fee and J. S. Valentine. *Chemical and Physical Properties of Superoxide*, pages 19–60. Academic Press, 1977.

[28] G. Schwarzenbach and J. Heller. Complexons. XVIII. Iron(II) and iron(III) complexes of ethylenediaminetetraacetic acid and their oxidation-reduction equilibria. *Helv. Chim. Acta*, **34**:576–591, 1951.

[29] H. Taube. Mechanisms of oxidation with oxygen. *J. Gen. Physiol.*, **49**(1):29–52, 1965.

[30] W. Beyer, J. Imlay, and I. Fridovich. Superoxide dismutases. *Progress in Nucleic Acid Research and Molecular Biology*, **40**:221–253, 1991.

[31] I. Fridovich. Superoxide radical: An endogenous toxicant. *Annual Review of Pharmacology and Toxicology*, **23**:239–257, 1983.

[32] I. Fridovich. Superoxide radical and superoxide dismutases. *Ann. Rev. Biochem.*, **64**:97–112, 1995.

[33] H. J. H. Fenton. *Journal of the Chemical Society*, **65**:899, 1894.

[34] D. M. Williams, G. R. Lee, and G. E. Cartwright. Role of superoxide anion radical in reduction of ferritin by xanthine oxidase. *Journal Of Clinical Investigation*, **53**:665–667, 1974.

[35] P. Biemond, H. G. van Eijk, A. F. Swaak, and J. F. Koster. Iron mobilization from ferritin by superoxide derived from stimulated polymorphonuclear leukocytes: Possible mechanism in inflammation diseases. *Journal Of Clinical Investigation*, **73**:1576–1579, 1984.

[36] F. Haber and J. Weiss. The catalytic decomposition of hydrogen peroxide by iron salts. *Proceedings of the Royal Society of London. Series A*, **A147**:332–351, 1934.

[37] C. E. Thomas, L. A. Morehouse, and S. D. Aust. Ferritin and superoxide-dependent lipid peroxidation. *Journal of Biological Chemistry*, **260**(6):3275–3280, 1985.

[38] B. H. J. Bielski. Reevaluation of the spectral and kinetic properties of hydroperoxo and superoxide anion free radicals. *Photochem. Photobiol.*, **28**(4-5):645–649, 1978.

[39] B. H. J. Bielski, R. L. Arudi, and M. W. Sutherland. A study of the reactivity of HO_2/O_2^- with unsaturated fatty acids. *Journal of Biological Chemistry*, **258**:4759–4761, 1983.

[40] J. M. Gebicki and B. H. J. Bielski. Comparison of the capacities of the perhydroxyl and the superoxide radicals to initiate chain oxidation of linoleic acid. *Journal of the American Chemical Society*, **103**:7020–7022, 1981.

[41] A. Samuni, M. Chevion, and G. Czapski. Roles of copper and $O_2^{-\cdot}$ in the radiation-induced inactivation of T7-bacteriophage. *Radiation Research*, **99**(3):562–572, 1984.

[42] G. Czapski. On the use of $OH^{\cdot}$ scavengers in biological systems. *Israel Journal of Chemistry*, **24**(1):29–32, 1984.

[43] C. S. Moody and H. M. Hassan. Mutagenicity of oxygen free radicals. *Proceedings of the National Academy of Sciences, USA*, **79**(9):2855–2859, 1982.

[44] S. B. Farr, R. D'Ari, and D. Touati. Oxygen-dependent mutagenesis in *Escherichia coli* lacking superoxide dismutase. *Proceedings of the National Academy of Sciences, USA*, **83**(21):8268–8272, 1986.

[45] J. A. Imlay and S. Linn. Bimodal pattern of killing of DNA-repair-defective or anoxically grown *Escherichia coli* by hydrogen peroxide. *Journal of Bacteriology*, **166**(2):519–527, 1986.

[46] J. A. Imlay, S. M. Chin, and S. Linn. Toxic DNA damage by hydrogen peroxide through the Fenton reaction *in vivo* and *in vitro*. *Science*, **240**:640-642, 1988.

[47] W. Bors, M. Saran, and G. Czapski. The nature of intermediates during biological oxygen activation. *Dev. Biochem.*, **11B**:1–31, 1980.

[48] E. F. Elstner. Oxygen activation and oxygen toxicity. *Annu. Rev. Plant. Physiol.*, **33**:73–96, 1982.

[49] R. J. Youngman. Oxygen activation: Is the hydroxyl radical always biologically relevant? *Trends in Biochemical Science*, **9**:280–283, 1984.

[50] H. Ding and B. Demple. Glutathione-mediated destabilization *in vitro* of [2Fe-2S] centers in the SoxR regulatory protein. *Proceedings of the National Academy of Sciences, USA*, **93**(18):9449-9453, 1996.

[51] B. Demple. Redox signaling and gene control in the *Escherichia coli* soxRS oxidative stress regulon–a review. *Gene*, **179**(1):53–57, 1996.

[52] I. Fridovich. Superoxide anion radical ($O_2^{-\cdot}$), superoxide dismutases, and related matters. *The Journal of Biological Chemistry*, **272**(30):18515–18517, 1997.

[53] M. Sono. The roles of superoxide anion and methylene blue in the reductive activation of indoleamine 2,3-dioxygenase by ascorbic acid or by xanthine oxidase-hypoxanthine. *Journal of Biological Chemistry*, **264**(3):1616–1622, 1989.

[54] N. Shimizu, K. Kobayashi, and K. Hayashi. The reaction of superoxide radical with catalase. *The Journal of Biological Chemistry*, **259**(7):4414–4418, 1984.

[55] A. J. Kettle, D. F. Sangster, J. M. Gebicki, and C. C. Winterbourn. A pulse radiolysis investigation of the reactions of myeloperoxidase with superoxide and hydrogen peroxide. *Biochimica et Biophysica Acta*, **956**:58–62, 1988.

[56] J. Butler, W. H. Koppenol, and E. Margoliash. Kinetics and mechanism of the reduction of ferricytochrome *c* by the superoxide anion. *The Journal of Biological Chemistry*, **257**(18):10747–10750, 1982.

[57] D. L. Olson and A. Scheeline. The peroxidase-NADH biochemical oscillator. 2. Examination of the roles of hydrogen peroxide and superoxide. *Journal of Physical Chemistry*, **99**:1212–1217, 1995.

[58] D. L. Olson, E. P. Williksen, and A. Scheeline. An experimentally based model of the peroxidase-NADH biochemical oscillator: An enzyme-mediated chemical switch. *Journal of the American Chemical Society*, **117**:2–15, 1995.

[59] T. Mann and D. Keilin. Hemocuprein and hepatocuprein: Copper-protein compounds of blood and liver in mammals. *Proceedings of the Royal Society of London. Series B*, **B126**:303–315, 1939.

[60] M. S. Mohamed and D. M. Greenburg. Isolation of purified copper protein from horse liver. *Journal of General Physiology*, **37**:433–439, 1954.

[61] H. Porter, J. Folch-Pi, J. Beggrovs, and S. Ainsworth. Cerebrocuprein. I. A copper-containing protein isolated from brain. *J. Neurochem.*, **1**:260–271, 1957.

[62] H. Markowitz, G. E. Cartwright, and M. M. Wintrobe. Copper metabolism. XXVII. Isolation and properties of an erythrocyte cuproprotein (erythrocuprein). *Journal of Biological Chemistry*, **234**:40–45, 1959.

[63] J. M. McCord and I. Fridovich. The reduction of cytochrome *c* by milk xanthine oxidase. *Journal of Biological Chemistry*, **243**(21):5753–5760, 1968.

[64] B. B. Keele Jr, J. M. McCord, and I. Fridovich. Superoxide dismutase from *Escherichia coli* B. *Journal of Biological Chemistry*, **245**(22):6176–6181, 1970.

[65] F. J. Yost Jr and I. Fridovich. An iron-containing superoxide dismutase from *Escherichia coli*. *Journal of Biological Chemistry*, **248**(14):4905–4908, 1973.

[66] K. Hjalmarsson, S. L. Marklund, A. Engstrom, and T. Edlund. Isolation and sequence of complementary DNA encoding human extracellular superoxide dismutase. *Proceedings of the National Academy of Sciences, USA*, **84**(18):6340-6344, 1987.

[67] L. Tibell, K. Hjalmarsson, T. Edlund, G. Skogman, A. Engstrom, and S. L. Marklund. Expression of human extracellular superoxide dismutase in Chinese hamster ovary cells and characterization of the product. *Proceedings of the National Academy of Sciences, USA*, **84**(19):6634-6638, 1987.

[68] E. Kusunose, K. Ichihara, Y. Noda, and M. Kusunose. Superoxide dismutase from *Mycobacterium tuberculosis*. *Journal of Biochemistry (Tokyo)*, **80**(6):1343–1352, 1976.

[69] K. Ichihara, I. Kasaoka, E. Kusunose, and M. Kusunose. A manganese and iron-containing superoxide dismutase from *Rhodococcus bronchialis*. *Journal Of General And Applied Microbiology*, **26**(6):387–393, 1980.

[70] D. E. Ose and I. Fridovich. Superoxide dismutase: Reversible removal of manganese and its substitution by cobalt, nickel, or zinc. *Journal of Biological Chemistry*, **251**(4):1217–1218, 1976.

[71] D. E. Ose and I. Fridovich. Manganese-containing superoxide dismutase from *Escherichia coli*: Reversible resolution and metal replacement. *Archives Of Biochemistry And Biophysics*, **194**(2):360–364, 1979.

[72] C. T. Privalle and I. Fridovich. Inductions of superoxide dismutases in *Escherichia coli* under anaerobic conditions. *The Journal of Biological Chemistry*, **263**(9):4274–4279, 1988.

[73] W. F. Beyer Jr and I. Fridovich. *In vivo* competition between iron and manganese by occupancy of the active site region of the manganese superoxide dismutase of *Escherichia coli*. *The Journal of Biological Chemistry*, **266**(1):303–308, 1991.

[74] C. T. Privalle and I. Fridovich. Transcriptional and maturational effects of manganese and iron on the biosynthesis of manganese-superoxide dismutase in *Escherichia coli*. *The Journal of Biological Chemistry*, **267**(13):9140–9145, 1992.

[75] B. Meier, A. P. Sehn, M. E. Schinina, and D. Barra. *In vivo* incorporation of copper into the iron-exchangable and manganese-exchangable superoxide dismutase from *Propionibacterium shermanii*. *European Journal of Biochemistry*, **219**:463–468, 1994.

[76] B. Meier, A. P. Sehn, M. Sette, M. Paci, A. Desideri, and G. Rotilio. *In vivo* incorporation of cobalt into *Propionibacterium shermanii* superoxide dismutase. *FEBS Letters*, **348**:283–286, 1994.

[77] C. D. Pennington and E. M. Gregory. Isolation and reconstitution of iron- and manganese-containing superoxide dismutases from *Bacteroides thetaiotaomicron*. *Journal of Bacteriology*, **166**(2):528–532, 1986.

[78] B. Meier, A. P. Sehn, C. Michel, and M. Saran. Reactions of hydrogen peroxide with superoxide dismutase from *Propionibacterium shermanii* - an enzyme which is equally active with iron or manganese - are independent of the prosthetic metal. *Archives of Biochemistry and Biophysics*, **313**(2):296–303, 1994.

[79] R. A. Edwards, H. M. Baker, M. M. Whittaker, J. W. Whittaker, G. B. Jameson, and E. N. Baker. Crystal structure of *Escherichia coli* manganese superoxide dismutase at 2.1 Å resolution. *Journal of Biological Inorganic Chemistry*, **3**:161–171, 1998.

[80] E. M. Gregory and C. H. Dapper. Chemical and physical differentiation of superoxide dismutases in anaerobes. *Journal of Bacteriology*, **144**(3):967–974, 1980.

[81] J.-Y. Juan, S. N. Keeney, and E. M. Gregory. Reconstitution of the *Deinococcus radiodurans* aposuperoxide dismutase. *Archives Of Biochemistry And Biophysics*, **286**(1):257–263, 1991.

[82] B. Meier, D. Barra, F. Bossa, L. Calabrese, and G. Rotilio. Synthesis of either iron or manganese- superoxide dismutase with an apparently identical protein moiety by an anaerobic bacterium dependent on the metal supplied. *Journal of Biological Chemistry*, **257**(23):13977–13980, 1982.

[83] M. E. Martin, B. R. Byers, M. O. J. Olson, M. L. Salin, J. E. L. Arceneaux, and C. Tolbert. A *Streptococcus mutans* superoxide dismutase that is active with either manganese or iron as a cofactor. *Journal of Biological Chemistry*, **261**(20):9361–9367, 1986.

[84] A. Amano, S. Shizukuishi, H. Tamagawa, K. Iwakura, S. Tsunasawa, and A. Tsunemitsu. Characterization of superoxide dismutases purified from either anaerobically maintained or aerated *Bacteroides gingivalis*. *Journal of Bacteriology*, **172**(3):1457–1463, 1990.

[85] T. Matsumoto, K. Terauchi, T. Isobe, K. Matsuoka, and F. Yamakura. Iron-manganese-containing superoxide dismutases from *Methylomonas J*: Identity of the protein moiety and amino acid sequence. *Biochemistry*, **30**:3210–3216, 1991.

[86] E. M. Gregory. Characterization of the O_2-induced manganese-containing superoxide dismutase from *Bacteroides fragilis*. *Archives of Biochemistry and Biophysics*, **238**:83–89, 1985.

[87] A. Amano, S. Shizukuishi, A. Tsunemitsu, and S. Tsunasawa. Identity of amino acid sequences of superoxide dismutase purified from both anaerobically maintained and aerated *Porphyromonas gingivalis*. *Oral Microbiology Immunology*, **7**:368–371, 1992.

[88] K. Asada, K. Yoshikawa, M. Takahashi, Y. Maeda, and K. Enmanji. Superoxide dismutases from a blue-green alga, *Plectonema boryanum*. *Journal of Biological Chemistry*, **250**(8):2801–2807, 1975.

[89] R. C. Bray, S. A. Cockle, E. M. Fielden, P. B. Roberts, G. Rotilio, and L. Calabrese. Reduction and inactivation of superoxide dismutase by hydrogen peroxide. *Biochemical Journal*, **139**(1):43–48, 1974.

[90] F. Yamakura. Destruction of tryptophan residues by hydrogen peroxide in iron-superoxide dismutase. *Biochemical and Biophysical Research Communications*, **122**(2):635–641, 1984.

[91] W. F. Beyer and I. Fridovich. Effect of hydrogen peroxide on the iron-containing superoxide dismutase of *Escherichia coli*. *Biochemistry*, **26**(5):1251–1257, 1987.

[92] E. K. Hodgson and I. Fridovich. The interaction of bovine erythrocyte superoxide dismutase with hydrogen peroxide: inactivation of the enzyme. *Biochemistry*, 14(24):5294–5299, 1975.

[93] E. K. Hodgson and I. Fridovich. The interaction of bovine erythrocyte superoxide dismutase with hydrogen peroxide: chemiluminescence and peroxidation. *Biochemistry*, 14(24):5299–5303, 1975.

[94] W. F. Beyer and I. Fridovich. Effect of hydrogen peroxide on the iron-containing superoxide dismutase of *Escherichia coli*. *Biochemistry*, **26**(5):1251–1257, 1987.

[95] D. A. Clare, J. Blum, and I. Fridovich. A hybrid superoxide dismutase containing both functional iron and manganese. *Journal of Biological Chemistry*, **259**(9):5932–5936, May 1984.

[96] K. Puget and A. M. Michelson. Isolation of a new copper-containing superoxide dismutase: Bacteriocuprein. *Biochemical and Biophysical Research Communications*, **58**:830–838, 1974.

[97] H. M. Steinman. Copper-zinc superoxide dismutase from *Caulobacter crescentus* CB15. *Journal of Biological Chemistry*, **257**(17):10283–10293, 1982.

[98] J. V. Bannister and M. W. Parker. The presence of a copper/zinc superoxide dismutase in the bacterium *Photobacterium leiogathi*: A likely case of gene transfer from eukaryotes to prokaryotes. *Proceedings of the National Academy of Sciences, USA*, **82**:149–152, 1985.

[99] D. C. Weatherburn. Structure and function of manganese-containing biomolecules. *Perspectives on Bioinorganic Chemistry*, **3**:1–113, 1996.

[100] M. W. Parker and C. C. F. Blake. Crystal structure of manganese superoxide dismutase from *Bacillus stearothermophilus* at 2.4 Å resolution. *Journal of Molecular Biology*, **199**:649–661, 1988.

[101] W. C. Stallings, K. A. Pattridge, R. K. Strong, and M. L. Ludwig. Manganese and iron superoxide dismutases are structural homologs. *Journal of Biological Chemistry*, **259**(17):10695–10699, 1984.

[102] M. E. McAdam, R. A. Fox, F. Lavelle, and E. M. Fielden. A pulse-radiolysis study of the manganese-containing superoxide dismutase from *Bacillus stearothermophilus*. A kinetic model for the enzyme action. *Biochemical Journal*, **165**(1):71–79, 1977.

[103] J. A. Fee, G. J. McClune, P. O. O'Neill, and E. M. Fielden. Saturation behaviour of superoxide dismutase catalyzed by the iron-containing superoxide dismutase of *Escherichia coli* B. *Biochemical and Biophysical Research Communications*, **100**(1):377–384, 1981.

[104] J. A. Fee, G. J. McLune, A. C. Lees, R. Zidovetski, and I. Pecht. The pH dependence of the spectral and anion binding properties of iron-containing superoxide dismutase from *Escherichia coli* B: An explanation for the azide inhibition of dismutase activity. *Israel Journal Of Chemistry*, **21**(1):54–58, 1981.

[105] C. Bull and J. A. Fee. Steady-state kinetic studies of superoxide dismutases: Properties of the iron-containing protein from *Escherichia coli*. *Journal of the American Chemical Society*, **107**(11):3295–3304, 1985.

[106] A. Terech, J. Purcheault, and C. Ferredini. Saturation behaviour of the manganese-containing superoxide dismutase from *Paracoccus denitrificans*. *Biochemical and Biophysical Research Communications*, **113**(1):114–120, 1983.

[107] J. Benovic, T. Tillman, A. Cudd, and I. Fridovich. Electrostatic facilitation of the reaction catalyzed by the manganese-containing and iron-containing superoxide dismutase. *Archives of Biochemistry and Biophysics*, **221**:329–332, 1983.

[108] C. L. Borders Jr, P. J. Horton, and W. F. Beyer Jr. Chemical modification of iron-containing and manganese-containing superoxide dismutases from *Escherichia coli*. *Archives of Biochemistry and Biophysics*, **268**(1):74-80, 1989.

[109] M. L. Ludwig, A. L. Metzger, K. A. Pattridge, and W. C. Stallings. Manganese superoxide dismutase from *Thermus thermophilus*: A structural model refined at 1.8 Å resolution. *Journal of Molecular Biology*, **219**:335–358, 1991.

[110] M. Pick, J. Rabani, F. Yost, and I. Fridovich. The catalytic mechanism of the manganese-containing superoxide dismutase of *Escherichia coli* studied by pulse radiolysis. *Journal of the American Chemical Society*, **96**:7329–7333, 1974.

[111] F. Lavelle, M. E. McAdam, E. M. Fielden, P. B. Roberts, K. Puget, and A. M. Michelson. A pulse-radiolysis study of the catalytic mechanism of the iron-containing superoxide dismutase from *Photobacterium leiognathi*. *Biochemical Journal*, **161**(1):3–11, 1977.

[112] M. E. McAdam, F. Lavelle, R. A. Fox, and E. M. Fielden. A pulse-radiolysis study of the manganese-containing superoxide dismutase from *Bacillus stearothermophilus*. *Biochemical Journal*, **165**(1):81–87, 1977.

[113] D. Ringe, G. A. Petsko, F. Yamakura, K. Suzuki, and D. Ohmori. Structure of iron superoxide dismutase from *Pseudomonas ovalis* at 2.9 Å resolution. *Proceedings of the National Academy of Sciences, USA*, **80**:3879–3883, 1983.

[114] B. Gray and A. J. Carmichael. Kinetics of superoxide scavenging by dismutase enzymes and manganese mimics determined by electron spin resonance. *The Biochemical Journal*, **281**(3):795–802, 1992.

[115] B. Meier, C. Michel, M. Saran, J. Huttermann, F. Parak, and G. Rotilio. Kinetic and spectroscopic studies on a superoxide dismutase from *Propionibacterium shermanii* that is active with iron or manganese: pH-dependence. *The Biochemical Journal*, **310**(3):945–950, 1995.

[116] J. A. Fee and C. Bull. Steady-state kinetic studies of superoxide dismutases. Saturative behavior of the copper- and zinc-containing protein. *Journal of Biological Chemistry*, **261**(28):13000–13005, 1986.

[117] W. C. Stallings, C. Bull, J. A. Fee, M. S. Lah, and M. L. Ludwig. Iron and manganese superoxide dismutases: Catalytic inferences from the structures. *Current Communications in Cell and Molecular Biology*, **5**:193–211, 1992. Cold Spring Harbour Laboratory Press, Plainview, New York J.G.Scandalios.

[118] J. Sines, S. Allison, A. Wierzbicki, and J. A. McCammon. Brownian dynamics simulation of the superoxide-superoxide dismutase reaction: Iron and manganese enzymes. *Journal of Physical Chemistry*, **94**:959–961, 1990.

[119] E. C. Niederhoffer, J. A. Fee, V. Papaefthymiou, and E. Munck. INC annual report, Los Alamos National Laboratory, 1987.

[120] J. A. Fee, T. Yoshida, C. Bull, P. O'Neill, and M. E. Fielden. On the mechanism of the iron-containing superoxide dismutase from *E. coli*. In *Superoxide and Superoxide Dismutase in Chemistry, Biology and Medicine. Proceedings of the 4th International Conference, 1985*, pages 205–211, 1986. (G.Rotilio,Ed) Elsevier, Amsterdam, North Holland.

[121] D. L. Tierney, J. A. Fee, M. L. Ludwig, and J. E. Penner-Hahn. X-ray absorption spectroscopy of the iron site in *Escherichia coli* Fe(III) superoxide dismutase. *Biochemistry*, **34**:1661–1668, 1995.

[122] G. D. Lawrence and D. T. Sawyer. Potentiometric titrations and oxidation-reduction potentials of manganese and copper-zinc superoxide dismutases. *Biochemistry*, **18**(14):3045–3050, 1979.

[123] H. J. Forman and I. Fridovich. Superoxide dismutase: A comparison of rate constants. *Archives of Biochemistry and Biophysics*, **158**(1):396–400, 1973.

[124] W. C. Stallings, A. L. Metzger, K. A. Pattridge, J. A. Fee, and M. L. Ludwig. Structure-function relationships in iron and manganese superoxide dismutases. *Free Radical Research Communications*, **12-13**(1):259–268, 1991.

[125] B. Meier, C. Scherk, M. Schmidt, and F. Parak. pH-dependent inhibition by azide and fluoride of the iron superoxide dismutase from *Propionibacterium shermanii*. *Biochemical Journal*, **331**(2):403–407, 1998.

[126] H. M. Hassan and I. Fridovich. Enzymatic defenses against the toxicity of oxygen and of streptonigrin in *Escherichia coli*. *Journal of Bacteriology*, **129**(3):1574–1583, 1977.

[127] H. W. Dougherty, S. J. Sadowski, and E. E. Baker. A new iron-containing superoxide dismutase from *Escherichia coli*. *Journal of Biological Chemistry*, **253**(14):5220–5223, 1978.

[128] T. O. Slykhouse and J. A. Fee. Physical and chemical studies on bacterial superoxide dismutases. *Journal of Biological Chemistry*, **251**(18):5472–5477, 1976.

[129] K. A. Hopkin, M. A. Papazian, and H. M. Steinman. Functional differences between manganese and iron superoxide dismutases in *Escherichia coli* K-12. *Journal of Biological Chemistry*, **267**(34):24253–24258, 1992.

[130] D. E. Tronrud and B. W. Matthews. Conjugate-direction minimization: An improved method for the refinement of macromolecules. *Acta Crystallographica*, **A48**:912–916, 1992.

[131] A. T. Brunger, P. D. Adams, G. M. Clore, W. L. DeLano, P. Gros, R. W. Grosse-Kunstleve, J.-S. Jiang, J. Kuszewski, M. Nilges, N. S. Pannu, R. J. Read, L. M. Rice, T. Simonson, and G. L. Warren. Crystallography and NMR system: A new software suite for macromolecular structure determination. *Acta Crystallographica*, **D54**:905–921, 1998.

[132] W. Kabsch and C. Sander. Dictionary of protein secondary structure: Pattern recognition of hydrogen-bonded and geometrical features. *Biopolymers*, **22**:2577–2637, 1983.

[133] A. Nicholls, K. A. Sharp, and B. Honig. Protein folding and association: Insights from the interfacial and thermodynamic properties of hydrocarbons. *Proteins: Structure, Function, and Genetics*, **11**:281–296, 1991.

[134] G. E. O. Borgstahl, H. E. Parge, M. J. Hickey, W. F. Beyer Jr, R. A. Hallewell, and J. A. Tainer. The structure of human mitochondrial manganese superoxide dismutase reveals a novel tetrameric interface of two 4-helix bundles. *Cell*, **71**(1):107–118, October 1992.

[135] J. B. Cooper, K. McIntyre, M. O. Badasso, S. P. Wood, Y. Zhang, T. R. Garbe, and D. Young. X-ray structure analysis of the iron-dependent superoxide dismutase from *Mycobacterium tuberculosis* at 2.0 angstroms resolution reveals novel dimer-dimer interactions. *Journal of Molecular Biology*, **246**:531–544, 1995.

[136] H.-D. Youn, E.-J. Kim, J.-H. Roe, Y. C. Hah, and S.-O. Kang. A novel nickel-containing superoxide dismutase from *Streptomyces spp*. *Biochemical Journal*, **318**:889–896, 1996.

[137] B. L. Stoddard, P. L. Howell, D. Ringe, and G. A. Petsko. The 2.1-Å resolution structure of iron superoxide dismutase from *Pseudomonas ovalis*. *Biochemistry*, **29**:8885–8893, 1990.

[138] M. Schmidt, B. Meier, and F. Parak. X-ray structure of the cambialistic superoxide dismutase from *Propionibacterium shermanii* active with Fe or Mn. *Journal of Biological Inorganic Chemistry*, **1**:532–541, 1996.

[139] J. A. Tainer, E. D. Getzoff, K. M. Beem, J. S. Richardson, and D. C. Richardson. Determination and analysis of the 2 Å structure of copper,zinc superoxide dismutase. *Journal of Molecular Biology*, **160**:181–217, 1982.

[140] E. M. Gregory and I. Fridovich. Induction of superoxide dismutase by molecular oxygen. *Journal of Bacteriology*, **114**:543–548, 1973.

[141] K. M. Beem, J. S. Richardson, and D. C. Richardson. Manganese superoxide dismutases from *Escherichia coli* and from yeast mitochondria: Preliminary X-ray crystallographic studies. *Journal of Molecular Biology*, **105**:327–332, 1976.

[142] H. M. Steinman, L. Weinstein, and M. Brenowitz. The manganese superoxide dismutase of *Escherichia coli* K-12 associates with DNA. *Journal of Biological Chemistry*, **269**(46):28629–28634, 1994.

[143] K. A. Hopkin. Physiological functions of iron and manganese superoxide dismutases in *Escherichia coli* K-12. *Einstein Quarterly Journal of Biology and Medicine*, **10**:2–13, 1992.

[144] D. Touati. Cloning and mapping of the manganese superoxide dismutase gene (sodA) of *Escherichia coli*. *Journal of Bacteriology*, **155**:1078–1087, 1983.

[145] B. Matthews. Solvent content of protein crystals. *The Journal of Molecular Biology*, **33**:491–497, 1968.

[146] Z. Otwinowski and W. Minor. Processing of X-ray diffraction data collected in oscillation mode. *Methods in Enzymology*, **276**:307–326, 1997.

[147] S. French and K. Wilson. On the treatment of negative intensity observations. *Acta Crystallographica*, **A34**:517–525, 1978.

[148] Collaborative Computational Project, Number 4. The ccp4 suite: Programs for protein crystallography. *Acta Crystallographica*, **D50**:760–763, 1994.

[149] J. Navaza. Amore: An automated package for molecular replacement. *Acta Crystallographica*, **A50**:157–163, 1994.

[150] A. Roussel and C. Cambillau. *Silicon Graphics Geometry Partners Directory*, pages 77–78. Silicon Graphics, Mountain View, CA, 1991.

[151] P. C. Moews and R. H. Kretsinger. Refinement of the structure of carp muscle calcium-binding parvalbumin by model building and difference fourier analysis. *Journal of Molecular Biology*, **91**:201–228, 1975.

[152] R. A. Engh and R. Huber. Accurate bond and angle parameters for X-ray protein structure refinement. *Acta Crystallographica*, **A47**:392–400, 1991.

[153] R. Laskowski, M. MacArthur, D. Moss, and J. Thomton. Procheck: A program to check the stereochemical quality of protein structures. *Journal of Applied Crystallography*, **26**:283–291, 1993.

[154] C. M. Wilmot and J. M. Thomton. Beta-turns and their distortions: A proposed new nomenclature. *Protein Engineering*, **3**(6):479–493, 1990.

[155] G. J. Kleywegt. Use of non-crystallographic symmetry in protein structure refinement. *Acta Crystallographica*, **D52**:842–857, 1996.

[156] A. L. Morris, M. W. MacArthur, E. G. Hutchinson, and J. M. Thomton. Stereochemical quality of protein structure coordinates. *Proteins*, **12**:345–364, 1992.

[157] S. Jones and J. M. Thornton. Protein-protein interactions: A review of protein dimer structures. *Progress in Biophysics and Molecular Biology*, **63**:31–65, 1995.

[158] F. Eisenhaber and P. Argos. Improved strategy in analytic surface calculation for molecular systems: Handling of singularities and computational efficiency. *Journal of Computational Chemistry*, **14**(11):1272–1280, 1993.

[159] F. Eisenhaber, P. Lijnzaad, P. Argos, C. Sander, and M. Scharf. The double cube lattice method: Efficient approaches to numerical integration of surface area and volume and to dot surface contouring of molecular assemblies. *Journal of Computational Chemistry*, **16**:273–284, 1995.

[160] D. C. Rees, M. Lewis, and W. N. Lipscomb. Refined crystal structure of carboxypeptidase A at 1.54 Å resolution. *Journal of Molecular Biology*, **168**:367–387, 1983.

[161] O. Herzberg and M. James. Common structural framework of the two Ca^{2+}/Mg^{2+} binding loops of troponin *c* and other Ca^{2+} binding proteins. *Biochemistry*, **24**:5298–5302, 1985.

[162] M. M. Whittaker and J. W. Whittaker. Mutagenesis of a proton linkage pathway in *Escherichia coli* manganese superoxide dismutase. *Biochemistry*, **36**(29):8923–8931, 1997.

[163] O. Farver and I. Pecht. Electron transfer in proteins: In search of preferential pathways. *FASEB Journal*, **5**:2554–2559, 1991.

[164] I. M. Kolthoff and W. J. Tomsicek. The oxidation potential of the system potassium molybdocyanide-potassium molybdicyanide, and the effect of neutral salts on the potential. *Journal of Physical Chemistry*, **40**:247, 1936.

[165] R. L. Kingston, H. M. Baker, and E. N. Baker. Search designs for protein crystallization based on orthogonal arrays. *Acta Crystallographica*, **D50**:429–440, 1994.

[166] J. Jancarik and S.-H. Kim. Sparse matrix sampling: a screening method for crystallization of proteins. *Journal of Applied Crystallography*, **24**:409–411, 1991.

[167] F. Yamakura, T. Matsumoto, and K. Kobayashi. Analysis of the metal-specific activity of Fe- and Mn-superoxide dismutase by using Mn-substituted Fe-SOD and Fe-substituted MnSOD. In K. Asada and T. Yoshikawa, editors, *Frontiers of reactive oxygen species in biology and medicine*, pages 115–118. Elsevier Scientific Publishers, B. V., Amsterdam, 1994.

[168] Y. Guan, M. J. Hickery, G. E. O. Borgstahl, R. A. Hallewell, J. R. Lepock, D. O'Connor, Y. Hsieh, H. S. Nick, D. N. Silverman, and J. A. Tainer. Crystal structure of Y34F mutant human mitochondrial manganese superoxide dismutase and the functional role of tyrosine 34. *Biochemistry*, **37**:4722–4730, 1998.

[169] Y. Hsieh, Y. Guan, C. Tu, P. J. Bratt, A. Angerhofer, J. R. Lepock, M. J. Hickery, J. A. Tainer, H. S. Nick, and D. N. Silverman. Probing the active site of human manganese superoxide dismutase: The role of glutamine 143. *Biochemistry*, **37**:4731–4739, 1998.

[170] K. Bunting, J. B. Cooper, M. O. Badasso, I. J. Tickle, M. Newton, S. P. Wood, Y. Zhang, and D. Young. Engineering a change in metal-ion specificity of the iron-dependent superoxide dismutase from Mycobacterium tuberculosis. *European Journal of Biochemistry*, **251**:795–803, 1998.

[171] T. Hunter, K. Ikebukuro, W. H. Bannister, J. V. Bannister, and G. J. Hunter. The conserved residue tyrosine 34 is essential for maximal activity of iron-superoxide dismutase from *Escherichia coli*. *Biochemistry*, **36**:4925–4933, 1997.

[172] B. K. Shoichet, W. A. Baase, R. Kuroki, and B. W. Matthews. A relationship between protein stability and protein function. *Proceedings of the National Academy of Sciences, USA*, 92(2):452–456, 1995.

[173] J. L. Hsu, Y. Hsieh, C. Tu, D. O'Connor, H. S. Nick, and D. N. Silverman. Catalytic properties of human manganese superoxide dismutase. *Journal of Biological Chemistry*, **271**(30):17687–17691, 1996.

[174] L. L. Kiefer, S. A. Paterno, and C. A. Fierke. Hydrogen bond network in the metal binding site of carbonic anhydrase enhances zinc affinity and catalytic efficiency. *Journal of the American Chemical Society*, **117**:6831–6837, 1995.

[175] D. B. Goodin and D. E. McRee. The Asp-His-Fe triad of cytochome *c* peroxidase controls the reduction potential, electronic structure, and coupling of the tryptophan free radical to the heme. *Biochemistry*, **32**:3313–3324, 1993.

[176] L. Banci, I. Bertini, D. E. Cabelli, R. A. Hallewell, J. W. Tung, and M. S. Viezzoli. A characterization of copper/zinc superoxide dismutase mutants at position 124. zinc-deficient proteins. *European Journal of Biochemistry*, **196**(1):123–128, 1991.

[177] J. M. Wang, M. Mauro, S. L. Edwards, S. J. Oatley, L. A. Fishel, V. A. Ashford, N. H. Xuong, and J. Kraut. X-ray structures of recombinant yeast cytochrome *c* peroxidase and three heme-cleft mutants prepared by site-directed mutagenesis. *Biochemistry*, **29**(31):7160–7173, 1990.

[178] L. B. Vitello, J. E. Erman, M. A. Miller, J. M. Mauro, and J. Kraut. Effect of Asp-235–Asn substitution on the absorption spectrum and hydrogen peroxide reactivity of cytochrome *c* peroxidase. *Biochemistry,* **31**:11524-11535, 1992.

[179] C. A. Lesburg and D. W. Christianson. X-ray crystallographic studies of engineered hydrogen bond networks in a protein-zinc binding site. *Journal of the American Chemical Society*, **117**:6838–6844, 1995.

[180] G. M. Sheldrick and T. R. Schneider. SHELXL: High-resolution refinement. *Methods in Enzymology*, **277B**:319–343, 1997.

[181] D. J. Hassett, W. A. Woodruff, D. J. Wozniak, M. L. Vasil, and M. S. Cohen and D. E. Ohman. Cloning and characterization of the pseudomonas aeruginosa sodA and sodB genes encoding manganese- and iron cofactored superoxide dismutase: Demonstration of increased manganese superoxide dismutase activity in alginate-producing bacteria. *Journal of Bacteriology*, **175**(23):7658–7665, 1993.

[182] D. Zhu and J. G. Scandalios. Maize mitochondrial manganese superoxide dismutases are encoded by a differentially expressed multigene family. *Proceedings of the National Academy of Sciences, USA*, **90**:9310–9314, 1993.

[183] A. Roussel and C. Cambillau. Turbo-Frodo, Silicon Graphics applications directory. Silicon Graphics, Mountain View, CA, 1991.

[184] N. S. Pannu and R. J. Read. Improved structure refinement through maximum likelihood. *Acta Crystallographica*, **A52**:659–668, 1996.

[185] W. F. Reynolds, I. R. Peat, M. H. Freedman, and J. R. Lyerla Jr. Determination of the tautomeric form of the imidazole ring of l-histidine in basic solution by carbon-13 magnetic resonance spectroscopy. *Journal of the American Chemical Society*, **95**(2):328–331, 1973.

[186] EU 3-D Validation Network. Who checks the checkers? Four validation tools applied to eight atomic resolution structures. *Journal of Molecular Biology*, **276**:417–436, 1998.

[187] R. W. W. Hooft, C. Sander, G. Vriend, and E. E. Abola. Errors in protein structures. *Nature*, **381**:272, 1996.

[188] T. J. Oldfield. SQUID: A program for the analysis and display of data from crystallography and molecular dynamics. *Journal of Molecular Graphics*, **10**:247–252, 1992.

[189] J. Pontius, J. Richelle, and S. Wodak. Deviations from standard atomic volumes as a quality measure for protein crystal structures. *Journal of Molecular Biology*, **264**:121–136, 1996.

[190] C. Frazao, C. M. Soares, M. A. Carrondo, E. Pohl, Z. Dauter, K. S. Wilson, M. Hervas, J. A. Navarro, M. A. D. La Rosa, and G. M. Sheldrick. *Ab initio* determination of the crystal structure of cytochrome c6 and comparison with plastocyanin. *Structure*, **3**:1159–1169, 1995.

[191] M. Schmidt. Manipulating the coordination number of the ferric iron within the cambialistic superoxide dismtutase of *Propionibacterium shermanii* by changing the pH-value. *European Journal of Biochemistry*, **262**:117–126, 1999.

[192] G. M. Sheldrick. Phase annealing in SHELX-90: Direct methods for larger structures. *Acta Crystallographica*, **A46**:467–473, 1990.

[193] C. M. Weeks, G. T. DeTitta, H. A. Hauptman, P. Thuman, and R. Miller. Structure solution by minimal-function phase refinement and fourier filtering. II. Implementation and applications. *Acta Crystallographica*, **A50**:210–220, 1994.

[194] S. E. Ealick. Now we're cooking: new successes for shake-and-bake. *Nature Structural Biology*, **5**:469–472, 1997.

[195] A. M. Deacon, C. M. Weeks, R. Miller, and S. E. Ealick. The shake-and-bake structure determination of triclinic lysozyme. *Proceedings of the National Academy of Sciences, USA*, **95**:9284–9289, 1998.

[196] G. M. Sheldrick and R. O. Gould. Structure solution by iterative peaklist optimization and tangent expansion in spacegroup P1. *Acta crystallographica*, **B51**:423–431, 1995.

[197] G. J. Kleywegt and T. A. Jones. Where freedom is given, liberties are taken. *Structure*, **3**:535–540, 1995.

[198] J. M. McCord and I. Fridovich. Superoxide dismutase. An enzymic function for erythrocuprein (hemocuprein). *Journal of Biological Chemistry*, **244**(22):6049-6055, 1969.

[199] F. Yamakura, K. Kobayashi, H. Ue, and M. Konno. The pH-dependent changes of the enzymic activity and spectroscopic properties of iron-substituted manganese superoxide dismutase - A study on the metal-specific activity of Mn-containing superoxide dismutase. *European Journal of Biochemistry*, **227**(3):700-706, 1995.

[200] C. K. Vance and A-F. Miller. Spectroscopic comparisons of the pH dependencies of Fe-substituted (Mn)Superoxide dismutase and Fe-superoxide dismutase. *Biochemistry*, **37**:5518-5527, 1998.